Graphene/elastomer nanocomposites

A thesis submitted to

The University of Manchester

for the degree of

Doctor of Philosophy

in the

Faculty of Science and Engineering

2019

Mufeng Liu

Department of Materials

School of Natural Sciences

Contents

Word count: 39,579

List of Tables

List of Figures

9

List of Symbols

A	Fitting parameter without physical meaning for mechanical percolation based on jamming theory
A_c	Area of the crystalline peaks for X-ray diffraction measurement
A_α	Area of the amorphous halo for X-ray diffraction measurement
b	Fitting parameter without physical meaning for mechanical percolation based on jamming theory
c	Volume concentration of spherical particles in an emulsion
c_k	Kraus filler parameter of carbon blacks
D	Diffusion coefficient
d_e/d_0	Diameter of a disc-shape sample at equilibrium of the swelling/prior to the swelling
$E_\parallel/E_\perp$	Uniaxial modulus of the composite parallel/perpendicular to the filler orientation
E_1	Modulus at the percolation threshold
E_c	Modulus of composite
E_{eff}	Effective modulus of the filler in a nanocomposite
e_f/e_m	Strain of the filler/matrix in a model composite
E_m	Modulus of matrix
E_R	Effective modulus determined by Raman band shift
f	Shape factor of a rod-like filler, equal to width/breadth of the rod
G_m	Shear modulus of the matrix
h_e/h_0	Thickness of a disc-shape sample at equilibrium of the swelling/prior to the swelling
I_0	Amplitude of Raman band assuming the surface normals are uniformly distributed around the Z-axis
I_{sample}	Amplitude of Raman band at different rotation angles
l	Lateral size of a graphene flake

18

$l_1/l_2/l_3$	Extension ratio of the final equilibrium swollen state referred to the original unit length at unswollen state in the direction of 1/2/3
m	Kraus fitting parameter in Kraus' theory
$M(\infty)$	Mass uptake at the saturation point of the absorption
$M(t)$	Mass uptake at time t
M_1/M_2	Mass uptake at 1/2-th measurement
M_c	Molecular weight between crosslinks for a rubber
n	Mechanical reinforcing efficiency
n_1/n_2	Numbers of moles of the solvent/elastomer in the swollen gel at equilibrium
p	Vapour pressure of the liquid component at equilibrium within the mixture (swollen rubber)
p_0	Saturation vapour pressure of pure liquid
R	The gas constant
s	Aspect ratio of graphene
s_{eff}	Effective aspect ratio of graphene that contributes to mechanical reinforcement in a bulk composite
t	Thickness of graphene employed
T	Thickness of the matrix surrounding the graphene flakes in a composite
t_1/t_2	Time of diffusion at 1/2-th measurement
Tan δ	The ratio of the viscous to elastic response of a viscoelastic material
T_g	Glass transition temperature
T_m	Melting point of a polymer
t_i	Time of diffusion at i-th measurement
T_K	Kelvin temperature
v_1/v_2	Molar volumes of the solvent/the elastomer
V_e/V_0	Volume of the sample for swelling measurement at equilibrium/unswollen state
V_f	Volume fraction of filler
V_f	Volume fraction of matrix

19

vol%	Volume fraction
V_p	Volume fraction of the filler at percolation threshold
w_f/w_m	Mass of the filler/matrix
wt%	Mass fraction
$W_\perp$	Work done by the out-of-plane force
$W(t)$	Weight of a specimen after an exposure time t
$W(0)$	Weight of a specimen at time $t=0$
x	Position along the flake
X_c	Degree of crystallinity of a polymer
$\sigma_\perp$	Out-of-plane stress from the GNPs contributes to the plane of the matrix
ε	Strain
$\varepsilon_\parallel/\varepsilon_\perp$	Strain of the composite parallel/perpendicular to the filler orientation at equilibrium of swelling
η	Viscosity of a liquid
η^*	Viscosity of an emulsion
η_o	Orientation factor
v	Poisson's ratio
v_{matrix}	Poisson's ratio of the matrix
$v_{graphene}$	Poisson's ratio of graphene
v_e	Crosslinking density
ρ	Density
ρ_f/ρ_m	Density of the filler/matrix
σ_f	Axial stress of the filler
Φ	Rotation angle of polarised Raman spectroscopy measurement
ϕ_1/ϕ_2	Volume fraction of the solvent/rubber (or composite) in the swollen rubber
$\phi_{2\ neat}$	Volume fraction of the neat rubber in the swollen rubber
ϕ_{2f}	Volume fraction of the rubber in the swollen composite (excluding the filler volume)
Φ_X/Φ_Z	Rotation angle-laser parallel to the X/Z axis

χ	Dimensionless parameter representing the polymer-solvent interaction
ω_{2D}	Raman 2D band shift
Π	Osmotic pressure from the solvent to the elastomer
$\Pi_{\parallel}/\Pi_{\perp}$	Osmotic (swelling) pressure (Π) from the solvent to the elastomers in the direction parallel/perpendicular to the plane
$<P_2(\cos\theta)>$ (P_2)/ $<P_4(\cos\theta)>$ (P_4)	Fitting parameters of polarised Raman spectroscopy in determining orientation factor of graphene in bulk composites
$\Delta A_{\perp}$	Change in the Helmholtz free energy due to change of the dimension in the direction perpendicular to the plane
ΔG	Gibbs free energy change
ΔG_{def}	Change of free energy of elastic deformation
ΔG_{mix}	Change of free energy of mixing (or dilution)
ΔH_f	Enthalpy of fusion of the sample measured
ΔH_f^0	Enthalpy of fusion of 100% crystalline polymers
2θ	Angle between the incident and the diffracted beam of X-ray diffraction

List of Abbreviations

0D	Zero dimensional
1D	One dimensional
2D	Two dimensional
3D	Three dimensional
AFM	Atomic force microscopy
CB	Carbon black
CBS	n-cyclohexyl-2-benzothiazole sulfenamide
CNT	Carbon nanotube
CT	Computer tomography
CVD	Chemical vapour deposition
DMTA	Dynamic mechanical thermal analysis
DSC	Differential scanning calorimetry
EPDM	Ethylene propylene diene monomer
FEGSEM	Field emission gun scanning electron microscopy
fGO	Functionalised graphene oxide
GGS	Guth-Gold-Smallwood
GNP	Graphene nanoplatelets
GO	Graphene oxide
HAF	High abrasion furnace
hBN	Hexagonal boron nitride
HXNBR	Hydrogenated carboxylated nitrile–butadiene rubber
MoS_2	Molybdenum disulphide
MWCNT	Multi-wall carbon nanotubes
NBR	Nitrile-butadiene rubber
NR	Natural rubber
ODA	Octadecylamine
PA	Polyamide

PDA   Polydopamine

PU   Polyurethane

rGO   Reduced graphene oxide

SBR   Styrene-butadiene rubber

SEM   Scanning electron microscopy

SMR   Standard Malaysian Rubber

TEM   Transmission electron microscopy

TGA   Thermogravimetric analysis

TMTD   Tetramethylthiuram disulfide

TPE   Thermoplastic elastomer

TPU   Thermoplastic Polyurethane

UT   Unfilled Translucent

VV   Vertical-vertical

XNBR   Carboxylated nitrile–butadiene rubber

XRD   X-ray diffraction

Abstract

The University of Manchester

Doctor of Philosophy

Mufeng Liu

2019

Graphene/elastomer nanocomposites

The mechanisms of mechanical reinforcement of elastomers by graphene have been studied in detail. The study comprises two aspects primarily: uniaxial and biaxial reinforcement by the graphene nanoplatelets (GNPs). The effects of the filler morphologies, filler orientation and filler/matrix interfaces on the mechanical reinforcement were investigated. Raman spectroscopy and analytical modelling have been demonstrated to be useful in studying graphene/elastomer nanocomposites.

The graphene/elastomer nanocomposites employed were prepared using melt mixing using three sizes of GNPs and a range of different elastomers, including thermoplastic elastomers, natural rubber and nitrile butadiene rubber. It was revealed that the GNPs were generally oriented in-plane due to the pressure involved in the moulding processes. Another morphology of the GNPs within the elastomeric matrices was loops/folds that existed prior to the processing of the nanocomposites.

The evaluation of the mechanical reinforcement by the GNPs using tensile testing suggested that the addition of the GNPs improved the stiffness and strength of the materials significantly. Raman *in situ* band shift measurements indicated that the stress transfer efficiency from the elastomers to the GNPs was low. The study using analytical modelling indicated that the reinforcement of graphene in graphene/elastomer nanocomposites is dependent upon the orientation, aspect ratio and volume fraction of the filler and independent of the filler modulus.

When exposed to solvents, graphene/elastomer nanocomposites show an interesting anisotropic swelling phenomenon, induced by the in-plane orientation of the GNPs. The dimensional swelling can be predicted accurately by the theory proposed. The theoretical analysis and the Raman band shift during biaxial deformation of the nanocomposites indicated that graphene was able to provide constraining in-plane biaxial force through the interface when the GNPs are oriented in-plane.

Declaration

No portion of the work referred to in the thesis has been submitted in support of an application for another degree or qualification of this or any other university or other institute of learning.

Copyright Statement

i. The author of this thesis (including any appendices and/or schedules to this thesis) owns certain copyright or related rights in it (the "Copyright") and s/he has given The University of Manchester certain rights to use such Copyright, including for administrative purposes.

ii. Copies of this thesis, either in full or in extracts and whether in hard or electronic copy, may be made only in accordance with the Copyright, Designs and Patents Act 1988 (as amended) and regulations issued under it or, where appropriate, in accordance with licensing agreements which the University has from time to time. This page must form part of any such copies made.

iii. The ownership of certain Copyright, patents, designs, trademarks and other intellectual property (the "Intellectual Property") and any reproductions of copyright works in the thesis, for example graphs and tables ("Reproductions"), which may be described in this thesis, may not be owned by the author and may be owned by third parties. Such Intellectual Property and Reproductions cannot and must not be made available for use without the prior written permission of the owner(s) of the relevant Intellectual Property and/or Reproductions.

iv. Further information on the conditions under which disclosure, publication and commercialisation of this thesis, the Copyright and any Intellectual Property and/or Reproductions described in it may take place is available in the University IP Policy (see http://documents.manchester.ac.uk/DocuInfo.aspx?DocID=24420), in any relevant Thesis restriction declarations deposited in the University Library, The University Library's regulations (see https://www.library.manchester.ac.uk/about/regulations/) and in The University's policy on Presentation of Theses.

Acknowledgements

First I would like to appreciate my supervisors, Professor Robert J. Young and Professor Ian A. Kinloch, who gave me the precious opportunity to study in Manchester. Their guidance is my fortune for a lifetime.

I would also like to express my greatest appreciation to Dr. Dimitrios G. Papageorgiou for his mentoring throughout the 3 years, for both aspects of experiments and academics. Moreover, I would like to thank Dr. Suhao Li for his experimental guidance at the beginning of my study.

I would like to acknowledge all the colleagues and staff in University of Manchester for the help with different techniques employed in my study.

I am thankful for the financial support from China Scholarship Council and Graphene Flagship.

Last but not least, I would express my appreciation to my wife, other family members and all my friends for their support.

Objective and Structure of the Thesis

Since the isolation of monolayer graphene was reported in 2004, graphene and graphene-related materials have been attracting a lot of interest in both industry and the academic community. Amongst the related studies, there is a growing body of literature that recognises the applicability of graphene to be used for reinforcement in polymer nanocomposites. Graphene possesses exceptional mechanical properties and a large aspect ratio (large specific surface area), which makes it a perfect candidate to be employed as mechanical reinforcement. Besides, its unique two-dimensional (2D) geometry is advantageous to impart multifunctionality to the nanocomposites, such as electrical conductivity, thermal conductivity and barrier properties. Extensive research of graphene also drives the development of its derivatives and other 2D materials that can be used as fillers in polymer nanocomposites, such as graphene oxide (GO), reduced graphene oxide (rGO), functionalised graphene oxide (fGO), hexagonal boron nitride (hBN), molybdenum disulphide (MoS_2) and many other 2D materials for different purposes. Each type of filler has its own advantages, but they are also accompanied with disadvantages. As a result, the selection of the filler depends on the specific application.

Elastomers are a type of polymer that require the aid of fillers, mainly due to their relatively poor mechanical properties. Graphene, owing to its excellent properties and unique geometry, has therefore been employed as a filler and studied in a variety of elastomer matrices. In the light of many reports in the past decade, it was found, however, the reinforcement of graphene in elastomer nanocomposites is overall not as efficient as expected. The mechanisms that underpin the reinforcement of graphene in elastomers are not fully understood. The aim of this research project has therefore been to investigate the mechanisms of reinforcement associated with properties of graphene and polymer matrix. It is hoped that this research will contribute to a deeper understanding and a general evaluation of mechanical enhancement by graphene in elastomeric matrices from a mechanics point of view.

The overall structure of the thesis takes the form of seven chapters:

Chapter 1 gives a review of graphene and graphene-based elastomer nanocomposites. It is composed of general preparation methods of both graphene and graphene/elastomer nanocomposites. Characterisation techniques and the performance of the nanocomposites regarding mechanical reinforcement and liquid barrier properties are reviewed. The key factors of graphene that control the reinforcing efficiency are discussed, including orientation, interfaces, aspect ratio and morphology. Chapter 2 reviews analytical theories that exist in the literature, explaining mechanical reinforcement and enhancement of liquid barrier properties of filler-reinforced elastomers.

Chapter 3 & 4 study uniaxial reinforcement of graphene-reinforced thermoplastic elastomers. The shear-lag model for 2D materials is introduced to understand the mechanical reinforcement under tension. A number of microstructural and interfacial characterisations are used to investigate the effects of morphologies, orientation and volume fraction of the filler on reinforcing efficiency.

Chapter 5 & 6 study the biaxial reinforcement of elastomer nanocomposites filled with aligned graphene, through swelling in liquids. In Chapter 5, a number of different elastomers and solvents were employed to study swelling behaviour of the nanocomposites. A novel and comprehensive theory was established, based on the theory of Flory, Rehner and Treloar's statistical mechanics. In Chapter 6, microscopic characterisation methods were employed to study biaxial reinforcement of the elastomer by aligned graphene, in order to fully understand the mechanisms of biaxial reinforcement of elastomers by aligned 2D materials.

Chapter 7 gives conclusions to the studies accomplished in this thesis and recommendations for future work.

Chapter 1. Graphene-reinforced Elastomer Nanocomposites

1.1 Graphene

The isolation of monolayer graphene was reported for the first time in 2004 by Geim and Novoselov in Manchester [1]. The name of graphene is given by its atomic structure, which consists of a flat monolayer of sp^2-hybridized carbon atoms densely packed into a two-dimensional (2D) honeycomb lattice [2]. It is the building block of other carbon allotropes, such as 0D wrapped fullerenes, 1D rolled nanotubes or 3D stacked graphite [2].

1.1.1   Preparation

Preparation of graphene can be classified into 'top-down' and 'bottom-up' methods. Top-down is defined as an exfoliation route to prepare graphene from bulky graphite. Bottom-up refers to building a graphene structure from small molecules. Each method has its advantages and disadvantages. The selection of the preparation method of graphene depends on the target application.

The first isolation of single-layer graphene was accomplished by means of mechanical cleavage from highly oriented pyrolytic graphite [1]. The specific approach involves repeated peeling from the graphite using a 'Scotch' tape. This method can control the number of the graphene layers and the lateral dimensions of the graphene films are from 10 µm for few-layer graphene to 100 µm for thicker flakes [1]. Mechanical exfoliation is highly reliable for preparing high-quality graphene films. However, it is limited in producing graphene for research purposes and not available for scale-up for applications in bulk composites [3, 4].

Due to the demand of large amounts of graphene, more approaches aiming at large-scale exfoliation have been explored. One of the most successful routes is liquid-phase exfoliation. This technique involves several steps including dispersion, exfoliation and purification of graphite in organic solvents, such as dimethylformamide [5] or N-methyl-pyrrolidone [6]. Sonication is usually employed to assist the progress of exfoliation followed by centrifugation. The mechanism underpinning this method is that the selected solvent possesses an equal or higher surface tension than the interaction energy between the graphene layers. The pioneering work of Paton *et al.* has found that high-shear mixing of graphite in appropriate liquid can also contribute to the excellent exfoliation of graphene [7]. Graphene prepared by this method is relatively defect-free and not oxidised. Nevertheless, although liquid-phase exfoliation has many advantages and is presumed to meet the needs of many commercial applications with its scalability, it is currently not used by industries, because the lateral sizes of graphene layers are generally at most a few microns, and furthermore, it involves expensive chemicals, which is also not environmentally friendly. Likewise, electrochemical exfoliation can also be used to prepare graphene [8].

Thermal exfoliation is another successful path to produce graphene. The theoretical basis is to use heat (microwave) to vaporize the acid in acid-intercalated natural graphite, which can contribute to a fast and considerable expansion of the graphite gallery [9]. The lateral dimensions of graphene produced from this approach are from 1 to 15 µm, and the thickness is around 10 nm. This method can produce few-layer and multi-layer graphene with a satisfactory level of productivity, making it the most common method to produce large amounts of graphene for nanocomposites.

The term 'bottom-up' for graphene preparation refers to synthesis of graphene molecules from small and atomically-precise building blocks [10]. Chemical vapour deposition (CVD) is one of the most useful techniques that can produce graphene of high quality. However, there are issues unsolved and it is currently only at the research stage [3]. Furthermore, the production of graphene by CVD has been targeted mainly on electronic devices [4].

1.1.2   Characterisation

A variety of microscopic techniques including optical microscopy, scanning electron microscopy (SEM), transmission electron microscopy (TEM), atomic force microscopy (AFM) have been extensively used to characterise graphene for its nanostructure and morphology. Although the graphene is one atom thick, it is found to absorb a significant fraction (2.3%) of the visible light and this absorption is independent of wavelength [11]. It can be seen from **Figure 1.1** (a) that the number of layers of graphene can be differentiated visually by optical microscopy [12]. Scanning electron microscopy is a useful way to characterise the morphological and microstructural characteristics of graphene. In **Figure 1.1** (b), exfoliated graphene is characterised by SEM. It can be found that isolated thin sheets are formed indicating efficient exfoliation, while the flakes are wrinkled forming porous structures [13].
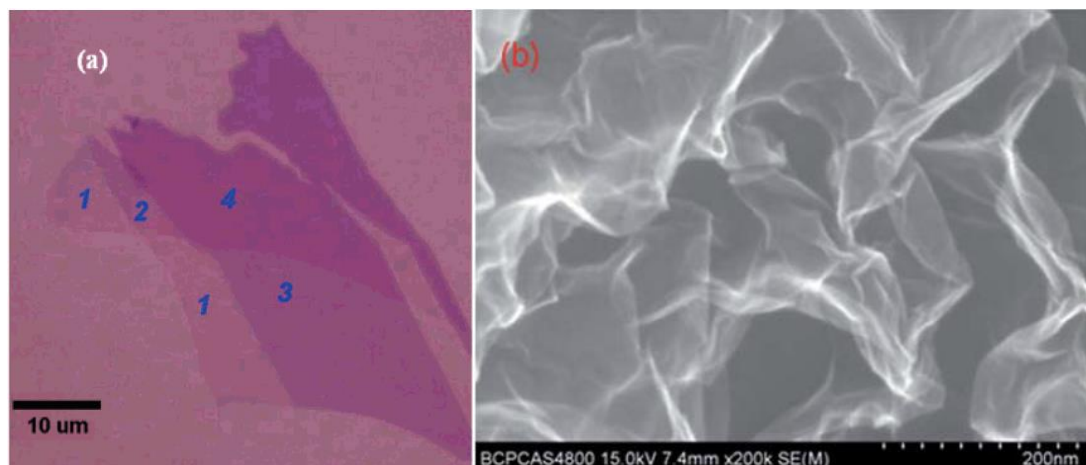
Figure 1.1 (a) Optical image of graphene with marked layer numbers [12]; (b) Scanning electron microscope image of exfoliated graphene [13].

More advanced and complex microscopic methods are also effective ways to characterise graphene, including AFM and TEM aimed at determining the size, thickness and layer numbers of the graphene flakes, etc [3].

X-ray diffraction (XRD) can be used to characterise exfoliation state of graphene. Pure graphite has a (002) reflection sharp Bragg peak at $2\theta \approx 26°$ under a general XRD measurement parameters (Cu Kα radiation, λ=0.154nm). With decreasing number of layers, this peak becomes broader and eventually disappears when the material is single-layer graphene [14]. The advantage of this method is that it can give an average number of layers for bulk samples.

Raman spectroscopy is one of the most crucial and useful techniques of characterisation of graphene, due to the strong resonance Raman scattering in sp^2-hybridized carbon atoms [15]. The major peaks of graphene in Raman spectrum are G band at approximately 1580 cm^{-1} and 2D band (also known as G' band) at around 2680 cm^{-1}. The G band results from the stretching of C-C bond in graphitic materials, which is signature for all kinds of sp^2 carbon systems. The 2D band is a second-order two-phonon process presenting a strong peak, the position of which depends on the laser energy. In addition, the 2D band can be used to determine the number of layers of graphene. The 2D band of monolayer graphene exhibits a sharp peak at ~2650 cm^{-1} with a relatively high intensity. With the increase of the layer numbers, the 2D (G') band becomes broader, more asymmetric and less intense, while the 2D wavenumber becomes higher, as shown in the **Figure 1.2** (a) [16]. When the number of layers is more than 5, the 2D Raman band becomes similar as that of graphite. Furthermore, single-layer, bilayer, trilayer graphene and multi-layer graphene can be characterised by their 2D Raman fingerprints [15] as shown in **Figure 1.2** (b-e). Apart from the major bands, D band (~1350 cm^{-1}) and D' band (~1620 cm^{-1}) may be present in the Raman spectra and are induced by defects [15]. The D band indicates the presence of disorder in the sp^2-hybridized carbon systems, while impurities or surface charges in the graphene result in a D' band [15, 17], which splits from the G band. The extended Raman spectrum in **Figure 1.2** (a) exhibits no presence of D or D' bands indicating the graphene produced from the mechanical exfoliation has a high level of perfection [15, 16].
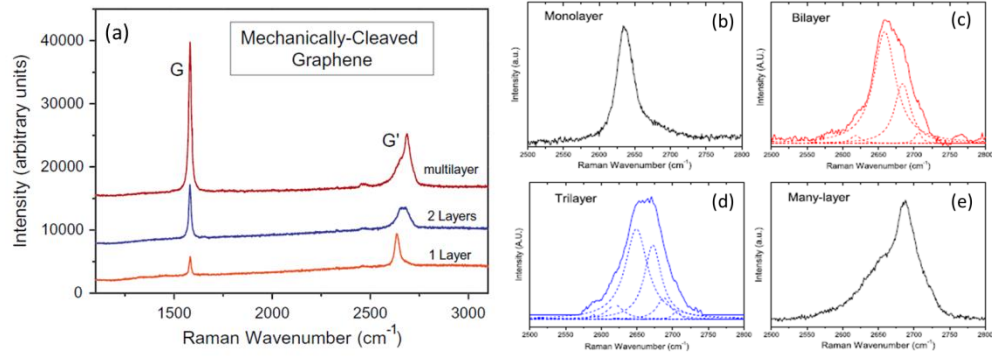
Figure 1.2 (a) Raman spectra of mechanically exfoliated graphene with single-layer, bilayer and multilayer [16]; (b-e) 2D Raman spectra of monolayer, bilayer, trilayer and many-layer graphene [15].

Other spectroscopies have also been utilized in characterising graphene on its chemical structure, including UV-vis spectroscopy [18] and X-ray photoelectron spectroscopy (XPS) [19, 20].

1.1.3   Mechanical Properties

Graphene has excellent mechanical properties that are superior to bulk graphite. The extraordinary specific stiffness and strength come from the long-range π-conjugation given by the sp^2 carbon hybridization [21]. The mechanical properties of the single-layer graphene were first measured by Lee et.al [22], using nanoindentation under an atomic force microscope (AFM). The results showed graphene is the strongest materials ever measured with Young's modulus of 1 TPa and intrinsic strength of 130 GPa. These values are approximately consistent with the theoretical *ab initio* calculations [23] as shown in **Figure 1.3** (a). Such exceptional mechanical properties of graphene make it a perfect candidate as a reinforcement of polymer nanocomposites.

Raman spectroscopy has been mentioned as a powerful technique to characterise graphitic materials, particularly graphene regarding the number of layers, degree of

perfection, etc. It is also a significant characterisation method to detect the molecular deformation of graphene by the investigation of the stress-induced Raman band shifts as shown in **Figure 1.3** (b).
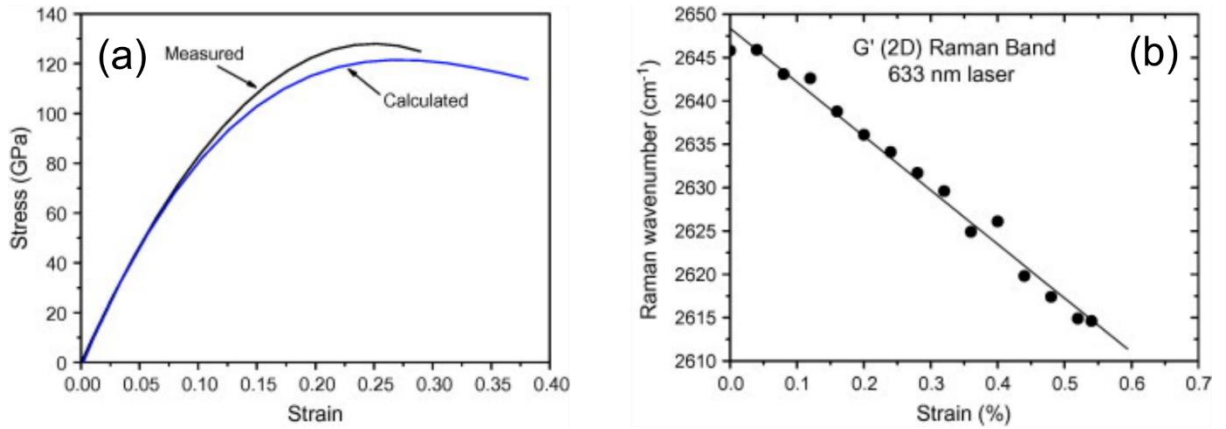
Figure 1.3 (a) Stress-strain curves of a monolayer graphene from theoretical calculations and mechanical measurements [16]; (b) 2D Raman band shifts induced by stress [16].

It was discovered previously that the rate of the 2D Raman band shift per strain is related to the Young's modulus of high-performance fibres [24]. For instance, regarding carbon fibres under tensile deformation, the band (G and 2D) positions shift to lower wavenumber almost linearly with strain. Previous research by Cooper et al. has proven that the rate of the 2D Raman band shift per strain increases with increasing modulus of carbon fibres, and furthermore, this shift rate is related linearly to modulus. It suggests that there is a universal dependence of 2D band shift on stress (-5cm^{-1}/GPa) for graphitic forms of carbon [25], which can be used as a universal calibration for the calculation of the modulus of graphene [3, 16].

A high degree of stress-induced band shifts has been found for both the G and 2D bands when graphene is deformed due to the strong bond stretching and distortion of monolayer crystal lattice [26]. The elastic modulus of monolayer graphene can be calculated by introducing the slope of the Raman wavenumber against the strain (-60 cm^{-1}/% strain),

using carbon fibres as a calibration. The value is equal to 1200 ± 100 GPa [27] which is similar to that from the direct measurement [22] and from the theoretical calculation [23]. Gong *et al.* [28] revealed that monolayer and bilayer graphene gave similar band shifts under strain, but when the number of layers is more than two, the rate of the 2D band shift per unit strain decreases with increasing layer number of the graphene (**Figure 1.4**). It is indicative of good stress transfer at polymer-graphene interface but poorer stress transfer efficiency between graphene layers [28].
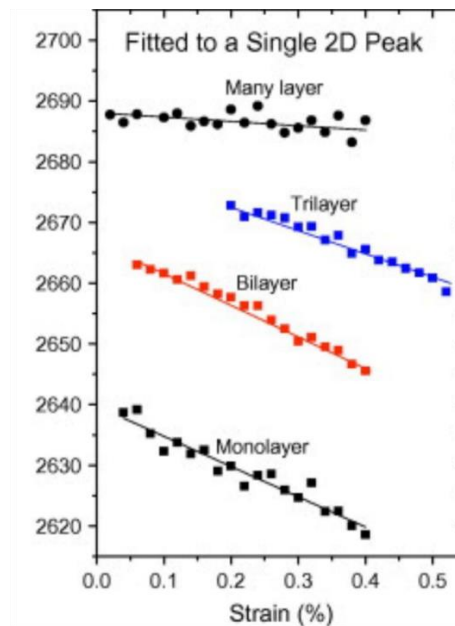
Figure 1.4 2D band shift against strain for adjacent monolayer, bilayer, trilayer and many-layer graphene on the same specimen [28].

1.1.4 Nomenclature of Graphene-based Materials

Given that the graphene-based nanomaterials are being extensively studied, a universal classification of different types of graphene is needed. This section will give a general classification of graphene substances.

A standardised nomenclature of the graphene family is crucial, in order to eliminate the confusion and misunderstanding in the global scientific community. Significant effort was made by Bianco et al. [29] followed by a clearer and recommended classification framework of graphene-based materials by Wick et al. [30] as shown in **Figure 1.5**. There are three elementary properties used to categorise the graphene-based materials: number of graphene layers, average lateral size and atomic carbon/oxygen ratio. For the exfoliated graphene, the classification is mostly determined by the number of layer (or thickness). The name 'graphene nanosheet' can only be used to define single-layer hexagonal sp^2 carbon lattice. Few-layer graphene refers to 2-5 layers of carbon atomic sheets. When the number of layers increases to 5-10, the name of multilayer graphene can be applied. Graphite (or graphene) nanoplatelets are the graphitic materials which has a lateral dimension/thickness (especially thickness) less than 100 nm.
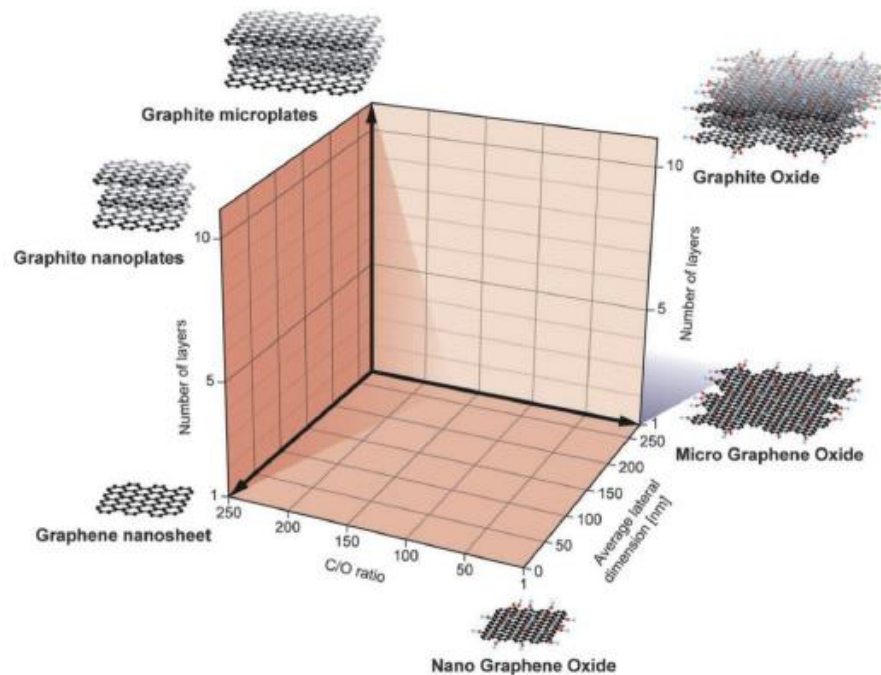
Figure 1.5 Classification grid for different graphene types based on number of graphene layers, average lateral dimension, and atomic C/O ratio [30].

1.2   Graphene/elastomer Nanocomposites

This section reviews general preparation methods, characterisation methods, mechanical properties and liquid barrier properties of elastomers reinforced by graphene that have been reported.

1.2.1   Preparation

The key to preparing graphene/polymer nanocomposites is to make graphene homogeneously dispersed in the polymer matrix so that the properties of the materials can be enhanced effectively by improving the matrix-filler and filler-filler interactions [3, 4]. There are generally three methods [3] to prepare graphene/elastomer nanocomposites including melt mixing, solution/latex blending, and *in situ* polymerisation. Melt mixing is to make use of a shear force to disperse the fillers in the elastomer matrix in the molten state. Solution or latex blending involves solving the graphene into solution or latex with high-speed shear mixing, ultra-sonication or stirring. *In situ* polymerisation of polymer, nanocomposites need to be completed by mixing the filler with monomer and undergoing *in situ* polymerisation. The advantages and disadvantages of these methods are listed below in **Table 1.1**.

Table 1.1 Comparison between three major preparation methods of graphene/elastomer nanocomposites.

Method	Dispersion	Popularity	Advantages	Disadvantages
Melt mixing	Poor	Industry	Low cost; Fast; Environmentally friendly	Poor dispersion; Need high temperature; May cause breakage of the nanosheets
Solution/latex blending	Good	Academia	Good dispersion and exfoliation of the filler; No further processing	High costs, removal and disposal of the solvents; Environmental problems
In situ polymerisation	Good	Successful but not popular	Excellent matrix-filler and filler-filler interactions; Excellent mechanical reinforcement	Demands low viscosity of the matrix; Lower electrical conductivity values

1.2.2 Characterisation

A number of major techniques for characterising graphene/elastomer nanocomposites are briefly reviewed.

1.2.2.1 Electron Microscopy

Electron Microscopy is one of the most useful ways to examine the microstructure of graphene reinforced elastomer nanocomposites. The key factors that control the reinforcement including dispersion, orientation and morphologies of the fillers and filler/matrix interface in nanocomposites can be generally characterised. Araby et al. [31] have studied melt mixed EPDM with GNPs using scanning electron microscopy (SEM) and the microstructural characteristics of the nanocomposites were characterised thoroughly by SEM, as can be seen in **Figures 1.6**. It can be seen from **Figure 1.6** (b) and (f-h) that the overall dispersion of the GNPs in the EPDM matrix is reasonably satisfactory up to volume fraction of 26.7% of the GNPs. The orientation of the filler is quite random. With higher magnification in **Figure 1.6** (c) and (d), the morphologies of the GNPs in the EPDM can be found in various geometries, along with good interfaces between the filler and the matrix. SEM is a widely-used method characterising the microstructure of polymer nanocomposites reinforced by graphene that is related to the processing methods employed. Transmission electron microscopy (TEM), on the other hand, can provide higher magnification and information of the internal compositions of the nanocomposites [31, 32]. However, electron microscopies are limited in only visually characterising the sample and the orientation of the filler is not quantifiable.
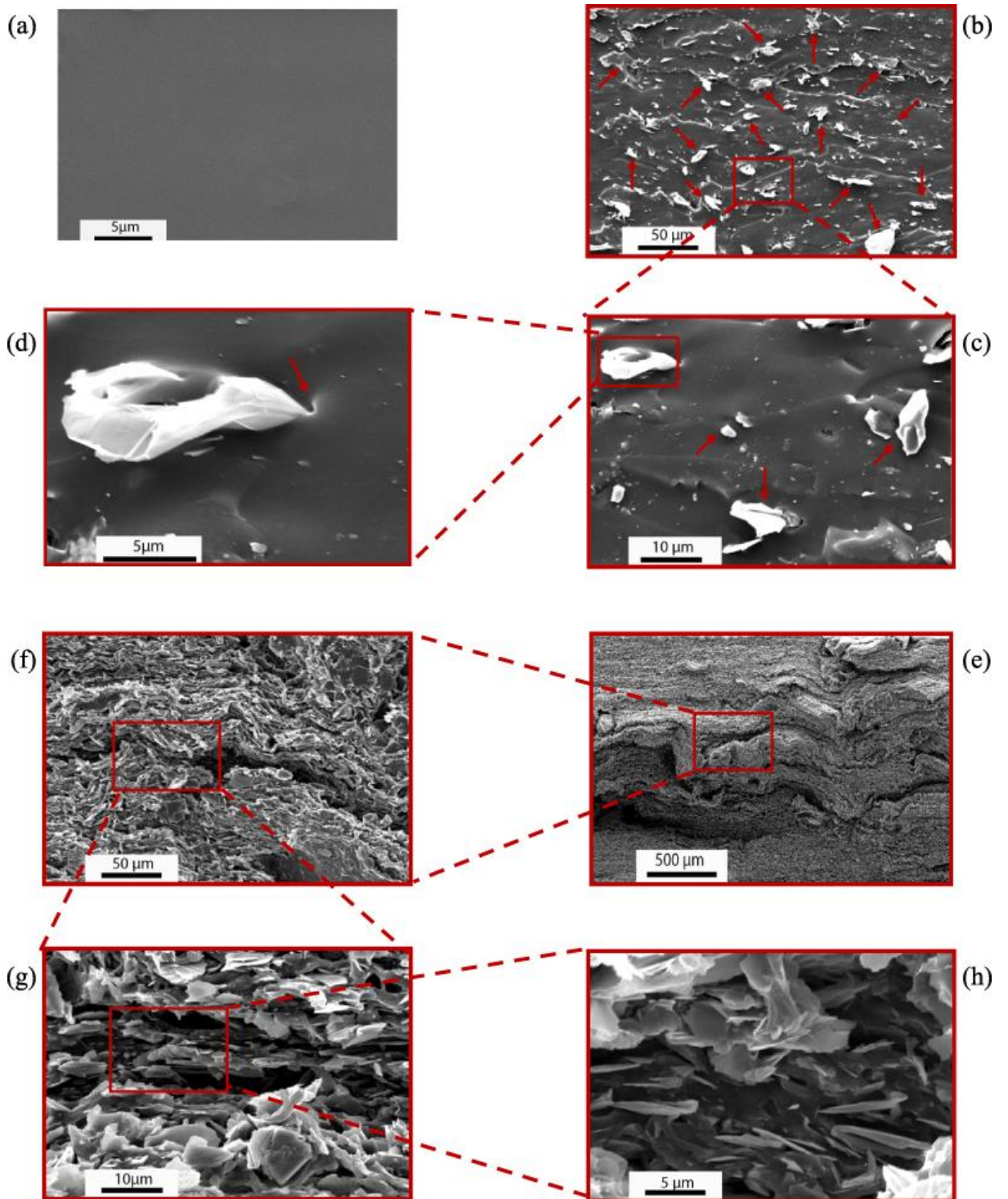
Figure 1.6 SEM micrographs of (a) neat EPDM, (b-d) 2.8 vol% and (e-h) 26.7 vol% of GNP reinforced EPDM [31].

41

1.2.2.2   Thermal Analysis

Major thermal analyses that have been employed in literatures for characterisation of graphene/elastomer nanocomposites, include thermogravimetric analysis (TGA), dynamic mechanical thermal analysis (DMTA) and differential scanning calorimetry (DSC).

TGA measures the percentage of mass loss of samples at elevated temperature, which can detect the compositions of the samples. Regarding graphene/elastomer nanocomposites, TGA is a generally employed to determine the actual loadings of the fillers and thermal stability of the samples [33-50].

DMTA provides information on molecular mobility and viscoelastic properties of elastomers reinforced by graphene through investigation of mechanical relaxation of the matrix, which is particularly useful for analysing mechanical reinforcement by graphene in elastomeric matrices [31, 33-35, 39, 41, 44, 46, 47, 49-61]. Generally, the storage modulus of polymers can be increased with the addition of graphene which provides reinforcement. Moreover, the glass transition temperature of the nanocomposites can also be increased with increasing graphene content, indicating that the mobility of the polymer chains is restricted. Graphene, with high aspect ratio, can create a high interfacial area in the nanocomposites and therefore restricts molecular movement of the polymers effectively. This effect of nanofillers, such as graphene, is particularly remarkable and has been interpreted as a nanoconfinement [3].

Araby et al. [31, 53] reported EPDM and styrene-butadiene rubber (SBR) reinforced by GNPs and carried out characterisations using DMTA (**Figure 1.7**). From both (a) and (b) in **Figure 1.7**, it can be seen that storage modulus was improved efficiently suggesting high level of filler-matrix interactions as a result of satisfactory dispersion of the filler. Additionally, the glass transition (indicated by the tan δ peak) shifts to higher temperature since graphene restrains the mobility of the macromolecular chains.
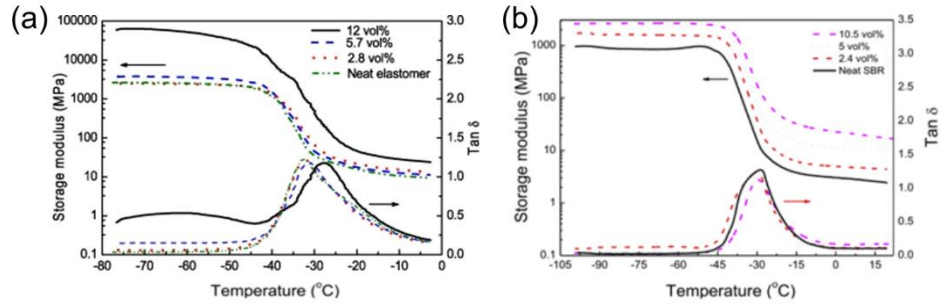
Figure 1.7 Storage modulus and loss factor (tan δ) of the nanocomposites as a function of temperature for (a) EPDM reinforced by GNPs [31] and (b) SBR reinforced by GNPs [53].

DSC is another common and useful technique for determining the important parameters of the polymers, including glass transition temperature (T_g), melting point (T_m), and degree of crystallinity, by probing heat flow with increasing temperature [33, 39, 46, 50, 61]. As for composites, DSC has been particularly employed to determine the crystallinity of the polymers, since it was reported that the addition of nanofillers could exert nucleation effect to the matrix polymers and therefore affect the mechanical reinforcement [39, 62, 63].

In summary, due to the importance and reliability of the information obtained from thermal analysis, the methods mentioned in this section have become routine techniques for studies on graphene/elastomer nanocomposites. Measurement of thermal conductivity is another thermal analysis method that is important for elastomers. However, it is used to determine a specific property (thermal conductivity) and therefore is not included in this section of the review.

1.2.2.3   *X-ray Diffraction*

X-ray diffraction (XRD) is a useful technique that can characterise graphene/elastomer nanocomposites regarding the exfoliation and intercalation level of the graphene layers. The exfoliation and intercalation level of the graphene-based fillers can be estimated by

the change of the Bragg peak of graphite as reviewed in section 1.1.2. An advantage of XRD is that the results obtained from XRD reflect the overall status of graphene in the bulk composites. Bai *et al.* [59] used XRD to characterise the dispersion of exfoliated graphene oxide (GO) in the matrix of hydrogenated carboxylated nitrile–butadiene rubber (HXNBR) as shown in **Figure 1.8** (left). The typical graphite peak at $2\theta \approx 26.6°$ shifted to $11.2°$ after functionalization and exfoliation, followed by an absence of the peak of graphitic materials for the HXNBR/GO nanocomposite. It has been attributed to substantial exfoliation of the GO into monolayer or few layers during the compounding process [59]. Similar experiments using XRD have been employed in other studies, but aiming at characterising the physically-mixed exfoliated graphite nanoplatelets (GNPs) in a polymer matrix [64, 65]. An example is the work of Bandla *et al.* [64], in which the GNPs was mixed into PET matrix and processed through injection moulding. The XRD patterns (in **Figure 1.8**, right) show no broadening or position shift of the graphite peak, indicating the graphite nanoplatelets were not well-exfoliated.
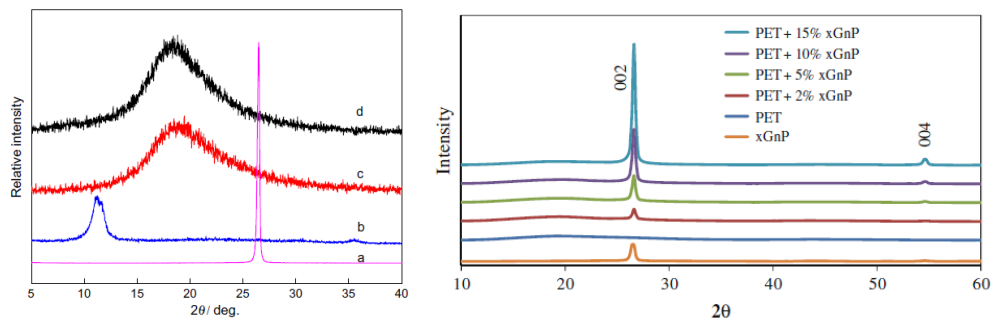
Figure 1.8 Left: XRD patterns of (a) graphite, (b) GO, (c) GO/HXNBR (1.3 vol%) and (d) HXNBR [59]; Right: XRD patterns of exfoliated GNPs, neat PET and composites of PET/GNPs with a series of different GNPs loading [64].

Further information that can be obtained from XRD patterns is the crystallinity of the polymer matrices of the graphene reinforced nanocomposites that can be used to confirm the results from DSC.

Overall, XRD is a useful and efficient characterisation method to provide information on bulk nanocomposites and this method has been well-applied in the analysis of graphene/elastomer nanocomposites [3].

1.2.2.4   *Raman Spectroscopy*

Raman spectroscopy is a particularly powerful characterisation method for graphene reinforced elastomer nanocomposites. Important information regarding chemical composition and dispersion of graphene [66] in the composites systems can be obtained from the Raman spectrum and by Raman mapping. In terms of mechanical reinforcement, crucial parameters of nanocomposites can be evaluated, including orientation of graphene [67-71] and interfaces between the elastomeric matrix and graphene [68, 72], in order to fully understand the mechanisms of reinforcement.

A series of papers that built a systematic methodology characterising orientation of graphene in graphene/polymer nanocomposites with polarised Raman spectroscopy were accomplished by Li *et al.* [69-71]. This method has its well-defined parameters that can determine the effect of degree of orientation of graphene on the mechanical reinforcement of the eventual nanocomposites quantitatively. The experimental arrangement of the method is shown in **Figure 1.9** (a). The Raman laser was 'VV' (vertical-vertical) polarised and was propagated in either X axis (in-plane) or Z axis (out-of-plane). The intensity of G band (or 2D band) was recorded while the sample (or the laser) was rotated. The angular dependence of the Raman intensities on the rotating angles (Φ_X or Φ_Z) can be fitted by the following equation (1.1) [70, 71]:

$$I_{\text{sample}}(\Phi) = I_0 \left\{ \frac{8}{15} + \left\langle P_2\left(\cos\theta\right)\right\rangle \left(-\frac{16}{21} + \frac{8}{7}\cos^2\Phi \right) + \left\langle P_4\left(\cos\theta\right)\right\rangle \left(\frac{8}{35} - \frac{8}{7}\cos^2\Phi + \cos^4\Phi \right) \right\} \ (1.1)$$

where I_{sample} and I_0 are the Raman intensity recorded at angle of Φ and 0, respectively; $<P_2(\cos\theta)>$ and $<P_4(\cos\theta)>$ are fitting parameters that can be determined by measured

45

Raman intensities and the corresponding angles of the incident light. Based on the $<P_2(\cos\theta)>$ and $<P_4(\cos\theta)>$ values obtained above, the orientation factor that determines the mechanical reinforcement is then given by [70, 71]:

$$\eta_O = \frac{8}{15} + \frac{8}{21}\left\langle P_2\left(\cos\theta\right)\right\rangle + \frac{3}{35}\left\langle P_4\left(\cos\theta\right)\right\rangle \tag{1.2}$$

Based on the work of Li *et al.* [69-71], the orientation factor (η_o) was determined as 0.53 and 1 for 3D randomly oriented and perfectly in-plane oriented graphene flakes, respectively.

Li *et al.* also employed polarised Raman spectroscopy to characterise the filler orientation of graphene/elastomer nanocomposites for the first time [68]. In **Figure 1.9** (b-d), the Raman intensity of G band of the GNPs (M5, M15 and M25) against the rotating angles from 0° to 90° in the natural rubber matrix was fitted using equation (1.1). It can be seen from the figures that the Raman intensity remains unchanged with the angle of incident laser when the laser was propagated along Z axis (out-of-plane). On the other hand, there was a clear angular dependence of the G band intensity on the rotating angles when the laser was propagated along X axis (in-plane). The orientation factors (η_o) for the GNPs were then calculated with the P_2 and P_4 values using equation (1.2) and the corresponding values are around 0.8, 0.7 and 0.6 for M5, M15 and M25 GNPs in natural rubber nanocomposites.
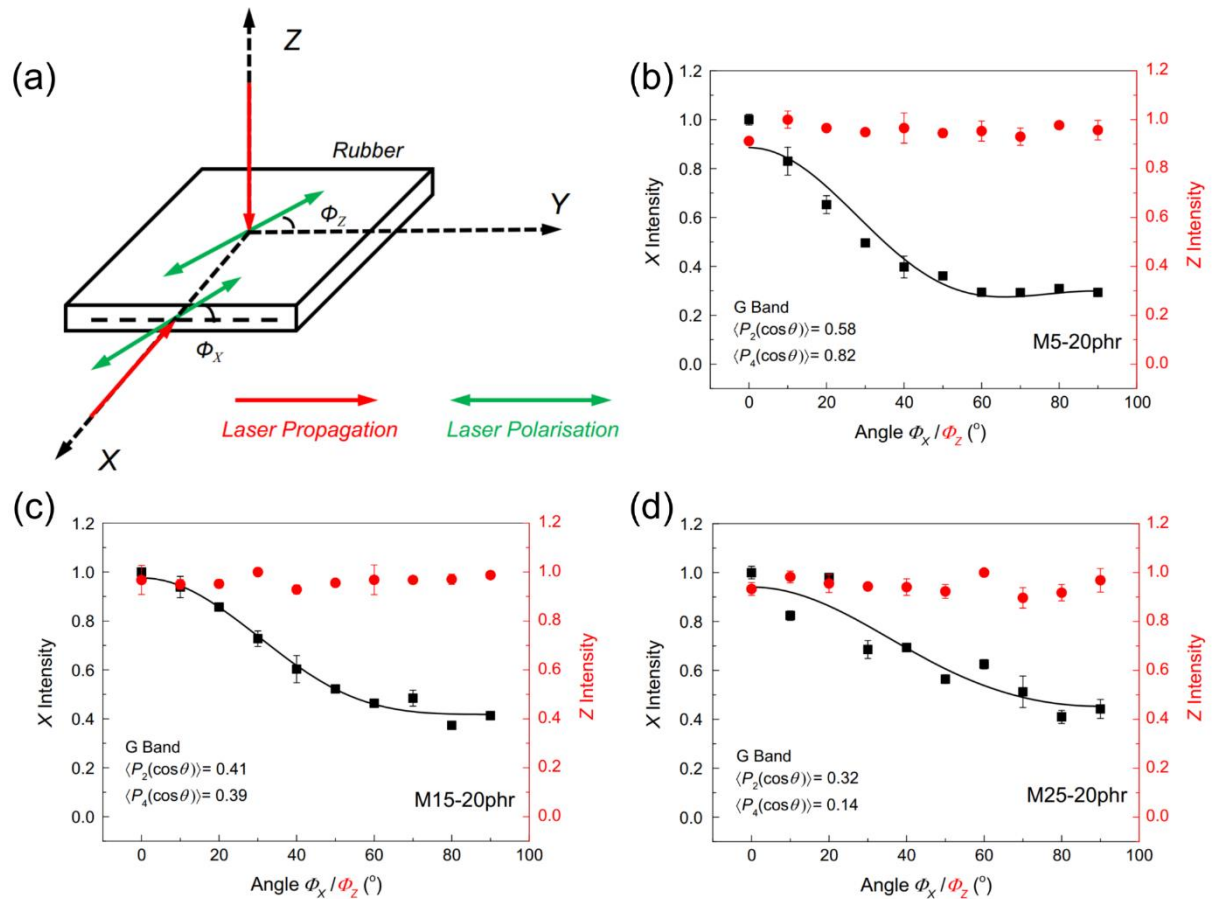
Figure 1.9 (a) Experimental method for the study of orientation of graphene using polarised Raman spectroscopy; (b-d) Normalized Raman intensity of G band as a function of the rotating angles from 0 to 90 degrees for M5, M15 and M25 GNPs, measured along *X* (black) and *Z* (red) axis [68].

Another useful way of characterisation using Raman spectroscopy is for the measurement of strain-induced Raman band shifts, that can evaluate the interfacial bonding and therefore provide information of stress transfer which is related to the shear modulus of the matrix [72]. The principle of this method is to record Raman band shift (usually G or 2D) relative to the strain applied on the nanocomposites. Taking the 2D band Raman band shift as an example (as 2D band shift is twice as sensitive as the G band in applied strain [73]), the slope of the curve fitting of 2D band shift against the composite strain gives an indication of the stress transfer efficiency from the matrix to the measured flake. The

effective modulus of the reinforcement from Raman 2D band shift measurement is then given by:

$$E_R = -\frac{d\omega_{2D}}{d\varepsilon} \cdot \frac{1050}{-60} \text{GPa} \tag{1.3}$$

where $-d\omega_{2D}/d\varepsilon$ is the measured Raman band shift against the applied composite strains, in the unit of $cm^{-1}/\%$; 1050 is the modulus of monolayer graphene, in the unit of GPa; -60 is the Raman 2D band shift of monolayer graphene under uniaxial strain [74], in the unit of $cm^{-1}/\%$.

The experiment of strain-induced Raman band shifts is particularly difficult to carry out for soft matrices such as elastomer. Li *et al.* [68] performed this experiment, again for the first time, on natural rubber/GNP nanocomposites, by probing laser spot on individual flakes while the samples was under tensile strain (**Figure 1.10**). The Raman band shift of the GNPs in the natural rubber matrix shows a relatively low slope for the graphene 2D band and the effective modulus values were determined using equation (1.3) as 67 MPa, 54 MPa and 58 MPa for M5, M15 and M25 GNPs. These modulus values are extremely low for graphene, which possesses a modulus of 1 TPa. The reason for this is that elastomers, such as natural rubber, have very low Young's modulus and therefore a low shear modulus [72]. The stress transfer through the shear stress at the interface is consequently very low compared with stiffer polymers [72].
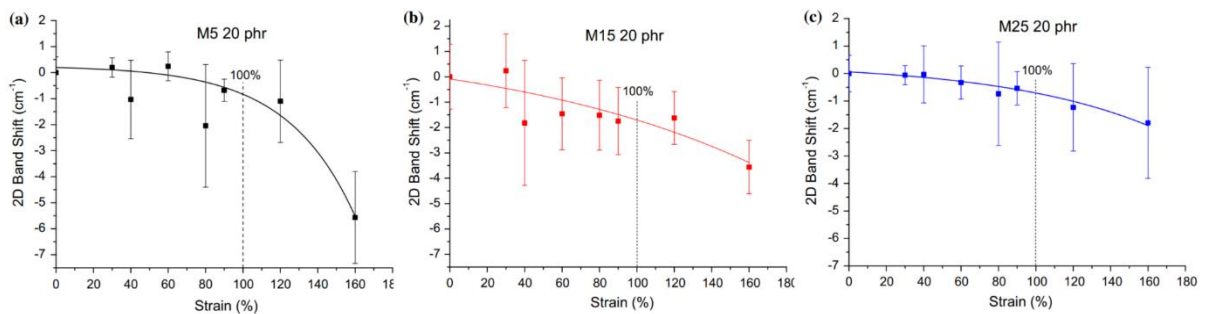
Figure 1.10 Raman 2D band shift with strain for the nanocomposites with 20 phr of (a) M5, (b) M15 and (c) M25 [68].

In conclusion, Raman spectroscopy can give very useful information on the analysis of the mechanisms of reinforcement of elastomers by graphene.

1.2.2.5   *Other Characterisation Methods*

A number of other characterisation methods have been employed in the studies of graphene/elastomer nanocomposites, including Fourier Transform InfraRed (FTIR) [51, 55, 75], XPS (X-ray Photoelectron Spectroscopy) [51, 55] and X-ray computed tomography (CT) [68]. FTIR and XPS are particularly useful in characterising chemical interaction between graphene and the elastomeric matrix and are applied widely in nanocomposites that involve chemical functionalization. X-ray CT is a new characterisation technology in materials science, although it has been used in medical science for decades. The application of CT to characterisation of graphene/polymer nanocomposites enables clear visualization of microstructural characteristics, especially the various morphologies of graphene-based fillers inside the bulk composites, such as flat, curved, fractured, multi-layer and agglomerate flakes [68, 76]. The utilization of CT scan can aid the mechanical reinforcement of graphene in nanocomposites to be analysed and understood. However, the main challenge of this method is its relatively low resolution that limits its accuracy in determining thickness of the graphene substances used [76].

1.2.3   Tensile Properties

There are a large number of reports in the literature that employ graphene-based fillers to reinforce mechanical properties of elastomers [31-33, 35, 37, 39, 42, 43, 46, 47, 49-60, 68, 75, 77-105].

Araby *et al.* prepared EPDM nanocomposites reinforced by graphene nanoplatelets (GNPs) [31] using melt compounding and the mechanical properties were examined. It was found that GNP induced a steady improvement (up to ~27 vol% GNP loading) in the

tensile modulus and strength of the material, which indicated both good dispersion and interface between the GNPs and the EPDM matrix. Further work by Araby *et al.* [53] compared the mechanical reinforcement of SBR (Styrene-Butadiene-Rubber)/GNP nanocomposites prepared by melt mixing and solution blending. It was shown that GNPs gave better mechanical enhancement to SBR using solution blending than melt mixing, as a result of a better dispersion of GNPs.

Nawaz et al. functionalised graphene oxide (GO) with octadecylamine (ODA) and conducted solution blending with polyurethane to prepare nanocomposites [75]. The Young's modulus was increased from 9.6 MPa for neat TPU to 335 MPa for ~30 vol% of GO (more than 30 times higher modulus). However, the elastomer became more brittle and therefore exhibited lower tensile strength and strain at failure when the volume fraction reached higher than 2%. The stiffening efficiency of functionalised GO in the nanocomposites prepared by solution blending was considerably higher than non-functionalised filler reinforced elastomer prepared by melt mixing, due to better filler dispersion and filler/matrix interaction [75]. Similar phenomena were also found in other reports [101-104].

Yang *et al.* functionalised graphene sheets with polydopamine (PDA) and carried out solution blending with a polyurethane [101]. The modulus of the nanocomposites with only 0.94 vol% improved from 10 MPa to 60 MPa. The tensile strength increased from 30 MPa (neat) to 50 MPa (0.24 vol%) and then reduced to 30 MPa (0.94 vol%), similar to the work of Nawaz et al. [75]. In the work of Yang *et al.* [101], the effect of the orientation of the filler on mechanical reinforcement was analysed using the Halpin-Tsai model and it was found that the graphene provided higher stiffening effect than 3D random-oriented 2D materials, due to the compression moulding inducing a preferred orientation of graphene in the in-plane direction. Similar results were found in PU/GNP nanocomposites in another study [35].

Li *et al.* [68] prepared natural rubber nanocomposites reinforced by GNPs and it was found the modulus increased with increasing GNP loadings. The tensile strength of natural rubber, however, was not improved, because natural rubber is intrinsically a very strong material due to its crystallization during the tensile tests. For the first time, the orientation of the GNPs was quantified using polarised Raman spectroscopy for elastomer/graphene nanocomposites to analyse the mechanical reinforcement of the GNPs. The preferred in-plane orientation of the GNPs was demonstrated clearly and was owing to the compression moulding that provided compression force on the materials. It was found that the GNPs with smaller lateral sizes showed higher degree of in-plane orientation than larger flakes. The modulus of the nanocomposites was analysed using modified rule-of-mixtures and it was indicated that GNPs exerted relatively low effective modulus in such a soft material (natural rubber) due to the low shear modulus of the matrix that provided a low efficiency of stress transfer.

Generally, the factors that determine the reinforcement of graphene in elastomers include the morphologies, dispersion, orientation of the fillers and filler-matrix interfaces. Filler morphologies depends on the type of graphene employed and can determine the average aspect ratio value of the filler in the matrix, which is crucial for mechanical reinforcement. Filler dispersion and filler-matrix interfaces are highly dependent upon preparation routes and can be enhanced by chemical functionalization [39, 47, 51, 56, 75, 81, 85-87, 93, 97], while filler orientation depends mainly on the moulding method used [3, 35, 68, 101].

There are still issues remaining unsolved in the existing literature, such as quantification of effective aspect ratio of the filler. The effective aspect ratio mentioned herein refers to an average aspect ratio in the bulk nanocomposites that provides mechanical reinforcement, which is difficult to be fully characterised by microscopy or CT scan.

1.2.4   Liquid Barrier Properties

Resistance to organic liquids is an important property that is highly-relevant to several applications of elastomers, since such materials find extensive use in seals, O-rings, gaskets and flexible pipes. Elastomers, possessing large free volume, usually display relatively poor liquid barrier properties, allowing small molecules of liquids to diffuse into the materials quite easily [106]. The diffusion of liquid molecules into elastomers results in the swelling of the materials that affects their mechanical properties significantly [106], and hence makes the materials lose their serviceability. When inorganic fillers are incorporated into elastomers, both the diffusion of the small molecules and the swelling of the elastomers can be restrained as a result of the reinforcement due to stress transfer at the elastomer-filler interface [107]. This reinforcement is controlled principally by the area of the filler/matrix interface and the adhesion of the filler. Graphene, possessing high aspect ratio and therefore providing large specific interfacial area in the composites, is very promising for improving the barrier properties of the elastomers in liquids.

Liquid barrier properties of the elastomer nanocomposites reinforced by graphene can be determined by swelling test and related studies have been reported extensively [31, 41, 46, 50, 51, 53, 78, 79, 84, 94, 99, 105, 108-114]. According to these studies, the volumetric swelling of the elastomer nanocomposites in organic solvents was determined by measurements of the dimensions of dry samples and after the samples were swollen (at equilibrium). The volume swelling ratios were then analysed using Flory-Rehner theory [115, 116], which can determine the crosslinking density of the elastomers. Based on Flory-Rehner equation, the crosslinking density is given by:

$$\nu_e = -\frac{\ln(1-\phi_2)+\phi_2+\chi\phi_2^2}{\nu_1\left(\sqrt[3]{\phi_2}-0.5\phi_2\right)} \tag{1.4}$$

where v_1 is the molar volume of solvent, χ is a dimensionless factor dependent upon the polymer-solvent interaction and v_2 is the volume fraction of the rubber or nanocomposites in the swollen gel.

The volume swelling ratio and the calculated crosslinking density for a number of studies [31, 46, 78, 99, 105, 112] upon different elastomers reinforced by different types of graphene are shown in **Figure 1.11**. Generally, the volume swelling ratio of the samples was reduced by the addition of graphene-based fillers and the constraining effect of the graphene was attributed to increasing crosslinking density due to increasing the number of 'physical crosslinks' with the increasing filler loadings. The so-called increased 'physical crosslinks' by graphene in fact resulted from the stress built up at the interfaces between the filler and the matrix during the swelling process, as suggested by a classical theory proposed by Kraus for filled vulcanizates [107]. In these studies, the actual crosslinking densities of the elastomers, however, were not characterised using chemical characterisation methods. Given that the elastomers were mixed with same amount (phr) of crosslinking agents for all the samples, as suggested by the formulations in these works, the chemical crosslinking densities of the elastomers might remain unchanged for the samples with different graphene loadings.
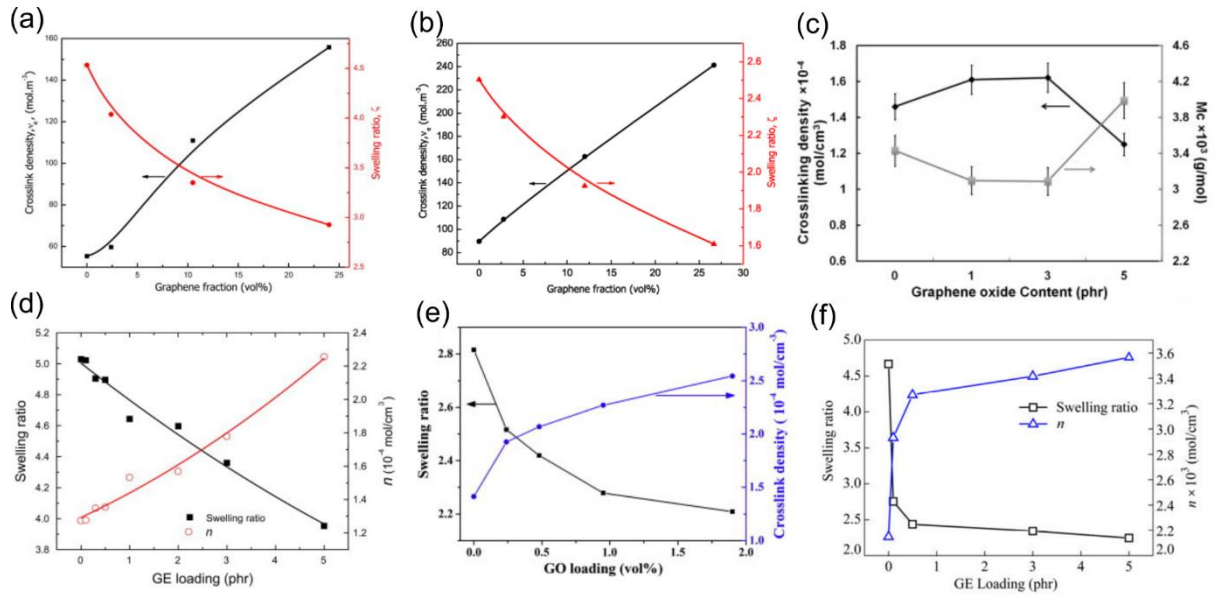
Figure 1.11 Swelling ratio and calculated crosslinking density against graphene loading of (a) SBR-GNP [105], (b) EPDM-GNP [31], (c) EPDM-GO [78], (d) NR-rGO [46], (e) carboxylated acrylonitrile butadiene rubber (XNBR)-GO [99] and (f) SBR-rGO [112].

Nevertheless, the dimensional swelling in different directions has been overlooked for swelling test of graphene-reinforced elastomer. The results that were reported [31, 41, 46, 50, 51, 53, 78, 79, 84, 94, 99, 105, 108-114] only included volume swelling ratios rather than dimensional swellings in different directions. Graphene is a type of filler possessing highly-asymmetric geometries and therefore its orientation in the nanocomposites can provide anisotropic reinforcement of the samples. The consequent anisotropic mechanical properties of the composites induced by orientation of graphene may alter the swelling behaviour of the nanocomposites in different directions, as swelling is dependent upon the modulus of the materials [107]. As suggested by section 1.3, graphene, as a filler, can be oriented in-plane by compression moulding. As a result, there may be anisotropic swelling for the elastomers reinforced by graphene. It was observed previously by Coran et al. [117] that the rubber filled with unidirectionally-aligned carbon fibres exhibited anisotropic swelling, where the swelling along the fibre was reduced and in contrast, the swelling in the transverse direction of the fibres was even greater compared with unfilled rubber. Hence, it is of great interest to conduct deeper studies in anisotropic swelling of

graphene/elastomer nanocomposites and the mechanisms of reinforcement by graphene in the swelling of elastomers.

1.3 Conclusion

Graphene can be used as an efficient reinforcement in elastomers to improve the tensile properties and liquid barrier properties. Progress in terms of graphene/elastomer nanocomposites suggests that the preparation and characterisation have been well-developed after studies during the past decade. It will be demonstrated in this thesis, however, that further studies are needed to understand the mechanisms of reinforcement fully.

References

[1] Novoselov KS, Geim AK, Morozov SV, Jiang D, Zhang Y, Dubonos SV, Grigorieva IV, Firsov AA. Electric field effect in atomically thin carbon films. Science. 2004;306(5696):666-9.

[2] Geim AK, Novoselov KS. The rise of graphene. Nanoscience and Technology: A Collection of Reviews from Nature Journals: World Scientific; 2010. p. 11-9.

[3] Papageorgiou DG, Kinloch IA, Young RJ. Graphene/elastomer nanocomposites. Carbon. 2015;95:460-84.

[4] Papageorgiou DG, Kinloch IA, Young RJ. Mechanical properties of graphene and graphene-based nanocomposites. Progress in Materials Science. 2017;90:75-127.

[5] Blake P, Brimicombe PD, Nair RR, Booth TJ, Jiang D, Schedin F, Ponomarenko LA, Morozov SV, Gleeson HF, Hill EW, Geim AK. Graphene-based liquid crystal device. Nano Letters. 2008;8(6):1704-8.

[6] Hernandez Y, Nicolosi V, Lotya M, Blighe FM, Sun Z, De S, McGovern IT, Holland B, Byrne M, Gun'Ko YK, Boland JJ. High-yield production of graphene by liquid-phase exfoliation of graphite. Nature Nanotechnology. 2008;3(9):563.

[7] Paton KR, Varrla E, Backes C, Smith RJ, Khan U, O'Neill A, Boland C, Lotya M, Istrate OM, King P, Higgins T. Scalable production of large quantities of defect-free few-layer graphene by shear exfoliation in liquids. Nature Materials. 2014;13:624.

[8] Abdelkader AM, Kinloch IA, Dryfe RA. Continuous electrochemical exfoliation of micrometer-sized graphene using synergistic ion intercalations and organic solvents. ACS Applied Materials & Interfaces. 2014;6(3):1632-9.

[9] Xiang J, Drzal LT. Thermal conductivity of exfoliated graphite nanoplatelet paper. Carbon. 2011;49(3):773-8.

[10] Tour JM. Top-down versus bottom-up fabrication of graphene-based electronics. Chemistry of Materials. 2013;26(1):163-71.

[11] Nair RR, Blake P, Grigorenko AN, Novoselov KS, Booth TJ, Stauber T, Peres NM, Geim AK. Fine structure constant defines visual transparency of graphene. Science. 2008;320(5881):1308-1308.

[12] Ni Z, Wang H, Kasim J, Fan H, Yu T, Wu Y, Feng Y, Shen Z. Graphene thickness determination using reflection and contrast spectroscopy. Nano Letters. 2007;7(9):2758-63.

[13] Xu B, Yue S, Sui Z, Zhang X, Hou S, Cao G, Yang Y. What is the choice for supercapacitors: graphene or graphene oxide? Energy & Environmental Science. 2011;4(8):2826-30.

[14] Khanra P, Kuila T, Bae SH, Kim NH, Lee JH. Electrochemically exfoliated graphene using 9-anthracene carboxylic acid for supercapacitor application. Journal of Materials Chemistry. 2012;22(46):24403-10.

[15] Ferrari AC, Meyer JC, Scardaci V, Casiraghi C, Lazzeri M, Mauri F, Piscanec S, Jiang D, Novoselov KS, Roth S, Geim AK. Raman spectrum of graphene and graphene layers. Physical Review Letters. 2006;97(18):187401.

[16] Young RJ, Kinloch IA, Gong L, Novoselov KS, Roth S, Geim AK. The mechanics of graphene nanocomposites: a review. Composites Science and Technology. 2012;72(12):1459-76.

[17] Malard L, Pimenta M, Dresselhaus G, Dresselhaus M. Raman spectroscopy in graphene. Physics Reports. 2009;473(5-6):51-87.

[18] Li D, Müller MB, Gilje S, Kaner RB, Wallace GG. Processable aqueous dispersions of graphene nanosheets. Nature Nanotechnology. 2008;3(2):101.

[19] Paredes JI, Villar-Rodil S, Martínez-Alonso A, Tascon JM. Graphene oxide dispersions in organic solvents. Langmuir. 2008;24(19):10560-4.

[20] Xu Y, Bai H, Lu G, Li C, Shi G. Flexible graphene films via the filtration of water-soluble noncovalent functionalized graphene sheets. Journal of the American Chemical Society. 2008;130(18):5856-7.

[21] Allen MJ, Tung VC, Kaner RB. Honeycomb carbon: a review of graphene. Chemical Reviews. 2009;110(1):132-45.

[22] Lee C, Wei X, Kysar JW, Hone J. Measurement of the elastic properties and intrinsic strength of monolayer graphene. Science. 2008;321(5887):385-8.

[23] Liu F, Ming P, Li J. Ab initio calculation of ideal strength and phonon instability of graphene under tension. Physical Review B. 2007;76(6):064120.

[24] Young RJ. Monitoring deformation processes in high-performance fibres using Raman spectroscopy. Journal of the Textile Institute. 1995;86(2):360-81.

[25] Cooper CA, Young RJ, Halsall M. Investigation into the deformation of carbon nanotubes and their composites through the use of Raman spectroscopy. Composites Part A: Applied Science and Manufacturing. 2001;32(3-4):401-11.

[26] Young RJ, Gong L, Kinloch IA, Riaz I, Jalil R, Novoselov KS. Strain mapping in a graphene monolayer nanocomposite. ACS Nano. 2011;5(4):3079-84.

[27] Frank O, Tsoukleri G, Riaz I, Papagelis K, Parthenios J, Ferrari AC, Geim AK, Novoselov KS, Galiotis C. Development of a universal stress sensor for graphene and carbon fibres. Nature Communications. 2011;2:255.

[28] Gong L, Young RJ, Kinloch IA, Riaz I, Jalil R, Novoselov KS. Optimizing the reinforcement of polymer-based nanocomposites by graphene. ACS nano. 2012;6(3):2086-95.

[29] Bianco A, Cheng H-M, Enoki T, Gogotsi Y, Hurt RH, Koratkar N, Kyotani T, Monthioux M, Park CR, Tascon JM, Zhang J. All in the graphene family–A recommended nomenclature for two-dimensional carbon materials. Carbon. 2013;65:1-6.

[30] Wick P, Louw-Gaume AE, Kucki M, Krug HF, Kostarelos K, Fadeel B, Dawson KA, Salvati A, Vázquez E, Ballerini L, Tretiach M. Classification framework for graphene-based materials. Angewandte Chemie International Edition. 2014;53(30):7714-8.

[31] Araby S, Zaman I, Meng Q, Kawashima N, Michelmore A, Kuan HC, Majewski P, Ma J, Zhang L. Melt compounding with graphene to develop functional, high-performance elastomers. Nanotechnology. 2013;24(16):165601.

[32] Liu S, Tian M, Yan B, Yao Y, Zhang L, Nishi T, Ning N. High performance dielectric elastomers by partially reduced graphene oxide and disruption of hydrogen bonding of polyurethanes. Polymer. 2015;56:375-84.

[33] Barrett JS, Abdala AA, Srienc F. Poly (hydroxyalkanoate) elastomers and their graphene nanocomposites. Macromolecules. 2014;47(12):3926-41.

[34] Chen B, Ma N, Bai X, Zhang H, Zhang Y. Effects of graphene oxide on surface energy, mechanical, damping and thermal properties of ethylene-propylene-diene rubber/petroleum resin blends. RSC Advances. 2012;2(11):4683-9.

[35] Chen Z, Lu H. Constructing sacrificial bonds and hidden lengths for ductile graphene/polyurethane elastomers with improved strength and toughness. Journal of Materials Chemistry. 2012;22(25):12479-90.

[36] Dao TD, Lee H-i, Jeong HM. Alumina-coated graphene nanosheet and its composite of acrylic rubber. Journal of Colloid and Interface Science. 2014;416:38-43.

[37] Gan L, Shang S, Yuen CWM, Jiang S-x, Luo NM. Facile preparation of graphene nanoribbon filled silicone rubber nanocomposite with improved thermal and mechanical properties. Composites Part B: Engineering. 2015;69:237-42.

[38] Kim JS, Yun JH, Kim I, Shim SE. Electrical properties of graphene/SBR nanocomposite prepared by latex heterocoagulation process at room temperature. Journal of Industrial and Engineering Chemistry. 2011;17(2):325-30.

[39] Lee YR, Raghu AV, Jeong HM, Kim BK. Properties of waterborne polyurethane/functionalized graphene sheet nanocomposites prepared by an in situ method. Macromolecular Chemistry and Physics. 2009;210(15):1247-54.

[40] Lian H, Li S, Liu K, Xu L, Wang K, Guo W. Study on modified graphene/butyl rubber nanocomposites. I. Preparation and characterization. Polymer Engineering & Science. 2011;51(11):2254-60.

58

[41] Matos CF, Galembeck F, Zarbin AJ. Multifunctional and environmentally friendly nanocomposites between natural rubber and graphene or graphene oxide. Carbon. 2014;78:469-79.

[42] Mensah B, Kim S, Arepalli S, Nah C. A study of graphene oxide-reinforced rubber nanocomposite. Journal of Applied Polymer Science. 2014;131(16).

[43] Stanier DC, Patil AJ, Sriwong C, Rahatekar SS, Ciambella J. The reinforcement effect of exfoliated graphene oxide nanoplatelets on the mechanical and viscoelastic properties of natural rubber. Composites Science and Technology. 2014;95:59-66.

[44] Valentini L, Bolognini A, Alvino A, Bon SB, Martin-Gallego M, López-Manchado MA. Pyroshock testing on graphene based EPDM nanocomposites. Composites Part B: Engineering. 2014;60:479-84.

[45] Verdejo R, Barroso-Bujans F, Rodriguez-Perez MA, De Saja JA, Lopez-Manchado MA. Functionalized graphene sheet filled silicone foam nanocomposites. Journal of Materials Chemistry. 2008;18(19):2221-6.

[46] Wu J, Xing W, Huang G, Li H, Tang M, Wu S, Liu Y. Vulcanization kinetics of graphene/natural rubber nanocomposites. Polymer. 2013;54(13):3314-23.

[47] Xing W, Wu J, Huang G, Li H, Tang M, Fu X. Enhanced mechanical properties of graphene/natural rubber nanocomposites at low content. Polymer International. 2014;63(9):1674-81.

[48] Xiong X, Wang J, Jia H, Fang E, Ding L. Structure, thermal conductivity, and thermal stability of bromobutyl rubber nanocomposites with ionic liquid modified graphene oxide. Polymer Degradation and Stability. 2013;98(11):2208-14.

[49] Yan D, Zhang HB, Jia Y, Hu J, Qi XY, Zhang Z, Yu ZZ. Improved electrical conductivity of polyamide 12/graphene nanocomposites with maleated polyethylene-octene rubber prepared by melt compounding. ACS Applied Materials & Interfaces. 2012;4(9):4740-5.

[50] Zhan Y, Wu J, Xia H, Yan N, Fei G, Yuan G. Dispersion and exfoliation of graphene in rubber by an ultrasonically-assisted latex mixing and in situ reduction process. Macromolecular Materials and Engineering. 2011;296(7):590-602.

[51] Wei J, Qiu J. Allyl-Functionalization enhanced thermally stable graphene/fluoroelastomer nanocomposites. Polymer. 2014;55(16):3818-24.

[52] Li C, Feng C, Peng Z, Gong W, Kong L. Ammonium-assisted green fabrication of graphene/natural rubber latex composite. Polymer Composites. 2013;34(1):88-95.

[53] Araby S, Meng Q, Zhang L, Kang H, Majewski P, Tang Y, Ma J. Electrically and thermally conductive elastomer/graphene nanocomposites by solution mixing. Polymer. 2014;55(1):201-10.

[54] Luo Y, Zhao P, Yang Q, He D, Kong L, Peng Z. Fabrication of conductive elastic nanocomposites via framing intact interconnected graphene networks. Composites Science and Technology. 2014;100:143-51.

[55] Tang Z, Wu X, Guo B, Zhang L, Jia D. Preparation of butadiene–styrene–vinyl pyridine rubber–graphene oxide hybrids through co-coagulation process and in situ interface tailoring. Journal of Materials Chemistry. 2012;22(15):7492-501.

[56] Liu X, Kuang W, Guo B. Preparation of rubber/graphene oxide composites with in-situ interfacial design. Polymer. 2015;56:553-62.

[57] Potts JR, Shankar O, Du L, Ruoff RS. Processing–morphology–property relationships and composite theory analysis of reduced graphene oxide/natural rubber nanocomposites. Macromolecules. 2012;45(15):6045-55.

[58] Varghese TV, Kumar HA, Anitha S, Ratheesh S, Rajeev R, Rao VL. Reinforcement of acrylonitrile butadiene rubber using pristine few layer graphene and its hybrid fillers. Carbon. 2013;61:476-86.

[59] Bai X, Wan C, Zhang Y, Zhai Y. Reinforcement of hydrogenated carboxylated nitrile–butadiene rubber with exfoliated graphene oxide. Carbon. 2011;49(5):1608-13.

[60] Das A, Kasaliwal GR, Jurk R, Boldt R, Fischer D, Stöckelhuber KW, Heinrich G. Rubber composites based on graphene nanoplatelets, expanded graphite, carbon nanotubes and their combination: A comparative study. Composites Science and Technology. 2012;72(16):1961-7.

[61] Khajehpour M, Sadeghi S, Yazdi AZ, Sundararaj U. Tuning the curing behavior of fluoroelastomer (FKM) by incorporation of nitrogen doped graphene nanoribbons (CNx-GNRs). Polymer. 2014;55(24):6293-302.

[62] Ryan KP, Lipson SM, Drury A, Cadek M, Ruether M, O'Flaherty SM, Barron V, McCarthy B, Byrne HJ, Blau WJ, Coleman JN. Carbon-nanotube nucleated crystallinity

in a conjugated polymer based composite. Chemical Physics Letters. 2004;391(4):329-33.

[63] Coleman JN, Khan U, Blau WJ, Gun'ko YK. Small but strong: a review of the mechanical properties of carbon nanotube–polymer composites. Carbon. 2006;44(9):1624-52.

[64] Bandla S, Hanan JC. Microstructure and elastic tensile behavior of polyethylene terephthalate-exfoliated graphene nanocomposites. Journal of Materials Science. 2012;47(2):876-82.

[65] Inuwa IM, Hassan A, Samsudin SA, Haafiz MM, Jawaid M, Majeed K, Razak NA. Characterization and mechanical properties of exfoliated graphite nanoplatelets reinforced polyethylene terephthalate/polypropylene composites. Journal of Applied Polymer Science. 2014;131(15).

[66] Bissett MA, Kinloch IA, Dryfe RA. Characterization of MoS2–graphene composites for high-performance coin cell supercapacitors. ACS Applied Materials & Interfaces. 2015;7(31):17388-98.

[67] Boland CS, Khan U, Ryan G, Barwich S, Charifou R, Harvey A, Backes C, Li Z, Ferreira MS, Möbius ME, Young RJ. Sensitive electromechanical sensors using viscoelastic graphene-polymer nanocomposites. Science. 2016;354(6317):1257-60.

[68] Li S, Li Z, Burnett TL, Slater TJ, Hashimoto T, Young RJ. Nanocomposites of graphene nanoplatelets in natural rubber: microstructure and mechanisms of reinforcement. Journal of Materials Science. 2017;52(16):9558-72.

[69] Li Z, Young RJ, Kinloch IA. Interfacial stress transfer in graphene oxide nanocomposites. ACS Applied Materials & Interfaces. 2013;5(2):456-63.

[70] Li Z, Young RJ, Kinloch IA, Wilson NR, Marsden AJ, Raju APA. Quantitative determination of the spatial orientation of graphene by polarized Raman spectroscopy. Carbon. 2015;88:215-24.

[71] Li Z, Young RJ, Wilson NR, Kinloch IA, Vallés C, Li Z. Effect of the orientation of graphene-based nanoplatelets upon the Young's modulus of nanocomposites. Composites Science and Technology. 2016;123:125-33.

[72] Young RJ, Liu M, Kinloch IA, Li S, Zhao X, Vallés C, Papageorgiou DG. The mechanics of reinforcement of polymers by graphene nanoplatelets. Composites Science and Technology. 2018;154:110-6.

[73] Mohiuddin TM, Lombardo A, Nair RR, Bonetti A, Savini G, Jalil R, Bonini N, Basko DM, Galiotis C, Marzari N, Novoselov KS. Uniaxial strain in graphene by Raman spectroscopy: G peak splitting, Grüneisen parameters, and sample orientation. Physical Review B. 2009;79(20):205433.

[74] Gong L, Kinloch IA, Young RJ, Riaz I, Jalil R, Novoselov KS. Interfacial stress transfer in a graphene monolayer nanocomposite. Advanced Materials. 2010;22(24):2694-7.

[75] Nawaz K, Khan U, Ul-Haq N, May P, O'Neill A, Coleman JN. Observation of mechanical percolation in functionalized graphene oxide/elastomer composites. Carbon. 2012;50(12):4489-94.

[76] Li Z, Slater TJA, Ma X, Yu Y, Young RJ, Burnett TL. The taxonomy of graphite nanoplatelets and the influence of nanocomposite processing. Carbon. 2019;142:99-106.

[77] Yan N, Xia H, Wu J, Zhan Y, Fei G, Chen C. Compatibilization of natural rubber/high density polyethylene thermoplastic vulcanizate with graphene oxide through ultrasonically assisted latex mixing. Journal of Applied Polymer Science. 2013;127(2):933-41.

[78] Allahbakhsh A, Mazinani S, Kalaee MR, Sharif F. Cure kinetics and chemorheology of EPDM/graphene oxide nanocomposites. Thermochimica Acta. 2013;563:22-32.

[79] Kumar SK, Castro M, Saiter A, Delbreilh L, Feller JF, Thomas S, Grohens Y. Development of poly (isobutylene-co-isoprene)/reduced graphene oxide nanocomposites for barrier, dielectric and sensingapplications. Materials Letters. 2013;96:109-12.

[80] Khan U, May P, O'Neill A, Coleman JN. Development of stiff, strong, yet tough composites by the addition of solvent exfoliated graphene to polyurethane. Carbon. 2010;48(14):4035-41.

[81] Moghaddam SZ, Sabury S, Sharif F. Dispersion of rGO in polymeric matrices by thermodynamically favorable self-assembly of GO at oil–water interfaces. RSC Advances. 2014;4(17):8711-9.

[82] Sadasivuni KK, Saiter A, Gautier N, Thomas S, Grohens Y. Effect of molecular interactions on the performance of poly (isobutylene-co-isoprene)/graphene and clay nanocomposites. Colloid and Polymer Science. 2013;291(7):1729-40.

[83] Zhan Y, Lavorgna M, Buonocore G, Xia H. Enhancing electrical conductivity of rubber composites by constructing interconnected network of self-assembled graphene with latex mixing. Journal of Materials Chemistry. 2012;22(21):10464-8.

[84] Yang H, Liu P, Zhang T, Duan Y, Zhang J. Fabrication of natural rubber nanocomposites with high graphene contents via vacuum-assisted self-assembly. RSC Advances. 2014;4(53):27687-90.

[85] Schopp S, Thomann R, Ratzsch KF, Kerling S, Altstädt V, Mülhaupt R. Functionalized Graphene and Carbon Materials as Components of Styrene-Butadiene Rubber Nanocomposites Prepared by Aqueous Dispersion Blending. Macromolecular Materials and Engineering. 2014;299(3):319-29.

[86] Choi JT, Kim DH, Ryu KS, Lee HI, Jeong HM, Shin CM, Kim JH, Kim BK. Functionalized graphene sheet/polyurethane nanocomposites: effect of particle size on physical properties. Macromolecular Research. 2011;19(8):809-14.

[87] Wei J, Jacob S, Qiu J. Graphene oxide-integrated high-temperature durable fluoroelastomer for petroleum oil sealing. Composites Science and Technology. 2014;92:126-33.

[88] Kumar V, Hanel T, Giannini L, Galimberti M, Giese U. Graphene reinforced synthetic isoprene rubber nanocomposites. Elastomers and Plastics. 2014;67:38-46.

[89] Kim H, Miura Y, Macosko CW. Graphene/polyurethane nanocomposites for improved gas barrier and electrical conductivity. Chemistry of Materials. 2010;22(11):3441-50.

[90] Kumar V, Giese U, Hanel T, Galimberti MS, Giannini L. Graphene/Styrene Butadiene Rubber Nanocomposites. 2014.

[91] Beckert F, Trenkle S, Thomann R, Mülhaupt R. Mechanochemical route to functionalized graphene and carbon nanofillers for graphene/SBR nanocomposites. Macromolecular Materials and Engineering. 2014;299(12):1513-20.

[92] She X, He C, Peng Z, Kong L. Molecular-level dispersion of graphene into epoxidized natural rubber: Morphology, interfacial interaction and mechanical reinforcement. Polymer. 2014;55(26):6803-10.

[93] Ozbas B, O'Neill CD, Register RA, Aksay IA, Prud'homme RK, Adamson DH. Multifunctional elastomer nanocomposites with functionalized graphene single sheets. Journal of Polymer Science Part B: Polymer Physics. 2012;50(13):910-6.

[94] Xing W, Tang M, Wu J, Huang G, Li H, Lei Z, Fu X, Li H. Multifunctional properties of graphene/rubber nanocomposites fabricated by a modified latex compounding method. Composites Science and Technology. 2014;99:67-74.

[95] Hernández M, del Mar Bernal M, Verdejo R, Ezquerra TA, López-Manchado MA. Overall performance of natural rubber/graphene nanocomposites. Composites Science and Technology. 2012;73:40-6.

[96] Dong B, Liu C, Zhang L, Wu Y. Preparation, fracture, and fatigue of exfoliated graphene oxide/natural rubber composites. RSC Advances. 2015;5(22):17140-8.

[97] Ozbas B, Toki S, Hsiao BS, Chu B, Register RA, Aksay IA, Prud'homme RK, Adamson DH. Strain-induced crystallization and mechanical properties of functionalized graphene sheet-filled natural rubber. Journal of Polymer Science Part B: Polymer Physics. 2012;50(10):718-23.

[98] Paszkiewicz S, Szymczyk A, Špitalský Z, Mosnáček J, Kwiatkowski K, Rosłaniec Z. Structure and properties of nanocomposites based on PTT-block-PTMO copolymer and graphene oxide prepared by in situ polymerization. European Polymer Journal. 2014;50:69-77.

[99] Kang H, Zuo K, Wang Z, Zhang L, Liu L, Guo B. Using a green method to develop graphene oxide/elastomers nanocomposites with combination of high barrier and mechanical performance. Composites Science and Technology. 2014;92:1-8.

[100] Araby S, Wang CH, Wu H, Meng Q, Kuan HC, Kim NK, Mouritz A, Ma J. Development of flame-retarding elastomeric composites with high mechanical performance. Composites Part A: Applied Science and Manufacturing. 2018;109:257-66.

[101] Yang L, Phua SL, Toh CL, Zhang L, Ling H, Chang M, Zhou D, Dong Y, Lu X. Polydopamine-coated graphene as multifunctional nanofillers in polyurethane. RSC Advances. 2013;3(18):6377-85.

[102] Yadav SK, Cho JW. Functionalized graphene nanoplatelets for enhanced mechanical and thermal properties of polyurethane nanocomposites. Applied Surface Science. 2013;266:360-7.

[103] Nguyen DA, Lee YR, Raghu AV, Jeong HM, Shin CM, Kim BK. Morphological and physical properties of a thermoplastic polyurethane reinforced with functionalized graphene sheet. Polymer International. 2009;58(4):412-7.

[104] Wu C, Huang X, Wang G, Wu X, Yang K, Li S, Jiang P. Hyperbranched-polymer functionalization of graphene sheets for enhanced mechanical and dielectric properties of polyurethane composites. Journal of Materials Chemistry. 2012;22(14):7010-9.

[105] Araby S, Zhang L, Kuan H-C, Dai J-B, Majewski P, Ma J. A novel approach to electrically and thermally conductive elastomers using graphene. Polymer. 2013;54(14):3663-70.

[106] Young RJ, Lovell PA. Introduction to polymers: CRC press; 2011.

[107] Kraus G. Swelling of filler-reinforced vulcanizates. Journal of Applied Polymer Science. 1963;7(3):861-71.

[108] Araby S, Saber N, Ma X, Kawashima N, Kang H, Shen H, Zhang L, Xu J, Majewski P, Ma J. Implication of multi-walled carbon nanotubes on polymer/graphene composites. Materials & Design (1980-2015). 2015;65:690-9.

[109] Mensah B, Kumar D, Lim D-K, Kim SG, Jeong B-H, Nah C. Preparation and properties of acrylonitrile–butadiene rubber–graphene nanocomposites. Journal of Applied Polymer Science. 2015;132(36).

[110] Pradhan B, Srivastava SK. Synergistic effect of three-dimensional multi-walled carbon nanotube–graphene nanofiller in enhancing the mechanical and thermal properties of high-performance silicone rubber. Polymer International. 2014;63(7):1219-28.

[111] Tang M, Xing W, Wu J, Huang G, Xiang K, Guo L, Li G. Graphene as a prominent antioxidant for diolefin elastomers. Journal of Materials Chemistry A. 2015;3(11):5942-8.

[112] Tang M-z, Xing W, Wu J-r, Huang G-s, Li H, Wu S-d. Vulcanization kinetics of graphene/styrene butadiene rubber nanocomposites. Chinese Journal of Polymer Science. 2014;32(5):658-66.

[113] Tang Z, Zhang L, Feng W, Guo B, Liu F, Jia D. Rational design of graphene surface chemistry for high-performance rubber/graphene composites. Macromolecules. 2014;47(24):8663-73.

[114] Yan Y, Potts M, Jiang Z, Sencadas V. Synthesis of highly-stretchable graphene – poly(glycerol sebacate) elastomeric nanocomposites piezoresistive sensors for human motion detection applications. Composites Science and Technology. 2018;162:14-22.

[115] Flory PJ, Rehner Jr J. Statistical Mechanics of Cross-Linked Polymer Networks II. Swelling. The Journal of Chemical Physics. 1943;11(11):521-6.

[116] Flory PJ, Rehner Jr J. Statistical mechanics of cross-linked polymer networks I. Rubberlike elasticity. The Journal of Chemical Physics. 1943;11(11):512-20.

[117] Coran AY, Boustany K, Hamed P. Unidirectional fiber–polymer composites: Swelling and modulus anisotropy. Journal of Applied Polymer Science. 1971;15(10):2471-85.

Chapter 2. Analytical Models

In materials science, analytical modelling is a way of linking the behaviour of a system to a mathematical model. Compared with numerical models, analytical models are more popular for composites science, due to their simplicity, accuracy and general applicability to different materials. Over the past decades, different models have been proposed to investigate and understand the mechanical reinforcement in elastomeric composite materials and swelling behaviours with an eventual target of predicting the properties of the heterogeneous system. In this chapter, a number of major micromechanical models used to study the reinforcement of elastomer nanocomposites by graphene and models for analysing the swelling process of nanocomposites in liquids are reviewed. The principles and derivations of these models are discussed briefly in order to understand the main principles and evaluating their advantages and disadvantages.

2.1 Composites Micromechanics for Elastomer Nanocomposites

There are generally two points of view in investigating mechanical improvement of polymer-based nanocomposites reinforced by graphene. One is considering graphene as a micro-scale discontinuous reinforcement, such as short fibres. In this case, classical micromechanical models are considered to be applicable for graphene. Another is to consider polymer nanocomposites as quasi-homogeneous molecular blends, suggesting analysis using micromechanical models is not feasible. Although it remains debatable in this aspect, classical micromechanics have been employed widely and proven to be effective in studying the mechanical properties of polymer nanocomposites reinforced by graphene-based fillers, particularly at reasonably low filler loadings. In this section, the classical models including Guth-Gold theory and shear-lag/rule-of-mixtures are reviewed in terms of their application on graphene reinforced elastomer nanocomposites. Semi-empirical theories such as Mori-Tanaka theory [1] and Halpin-Tsai theory [2] are not included in the review, since they have not been used in this thesis.

2.1.1 Guth-Gold Theory

The Guth-Gold theory is a well-accepted theory to evaluate the mechanical reinforcement of elastomers particularly by spherical and rod-like fillers [3]. The theory was developed in 1950s, based on Einstein's viscosity law, Smallwood's theory and hydrodynamics. The simplicity of the Guth-Gold equation drives its wide application in the assessment of the reinforcing efficiency of rubber composites reinforced by carbon blacks. The principle of the analysis of reinforcement by Guth-Gold theory is hereby reviewed. The advantages and disadvantages of the Guth-Gold theory in analysing elastomers reinforced by graphene (or other 2D materials) are briefly discussed.

The theoretical basis of the Guth-Gold theory is the Einstein's viscosity law, as shown below. The viscosity of a emulsion, for rigid spheres suspended in a liquid, is given by [4],

$$\eta^* = \eta(1 + 2.5c) \tag{2.1}$$

where c is the volume concentration of spherical particles and η is the viscosity of the liquid. The Einstein's viscosity law indicates that the viscosity of an emulsion with spheres suspended in a liquid has a linear relationship to the concentration, with a coefficient of 2.5. Coincidentally, a theory proposed by Smallwood also suggests that the modulus of a rubber composite filled with carbon blacks (also spherical filler) is linear to the volume fraction of CB with a coefficient of 2.5 [5], when the CB loading is relatively low (<10 vol%) [3]. The modulus of rubber/carbon black composites is given by,

$$E_c = E_m(1 + 2.5V_f) \tag{2.2}$$

Based on the equations (2.1) and (2.2), the mechanics of an elastomer/CB composite under tension was therefore able to be analogous to the physical properties of suspensions of colloidal particles in a solvent, because in both systems, the matrix or the liquid was

considered as a continuum [3]. The development of the Guth-Gold theory was to consider the polydispersity of the spheres at high concentration in a liquid, where the morphologies of spherical particles forming rod-like geometries, and therefore the viscosity of the emulsion was increased in a higher degree with increasing filler concentration [3] (as shown in **Figure 2.1**). Consequently equation (2.2) was developed further to a quadratic form, in which the modulus of the composites reinforced by a spherical filler is given by,

$$E_c = E_m(1 + 2.5V_f + 14.1V_f^2) \tag{2.3}$$

Guth [3] proposed equation (2.3) based on their results found in fluid and after experiments on CB-filled rubbers, the equation was proven to be effective in studying mechanical reinforcement.
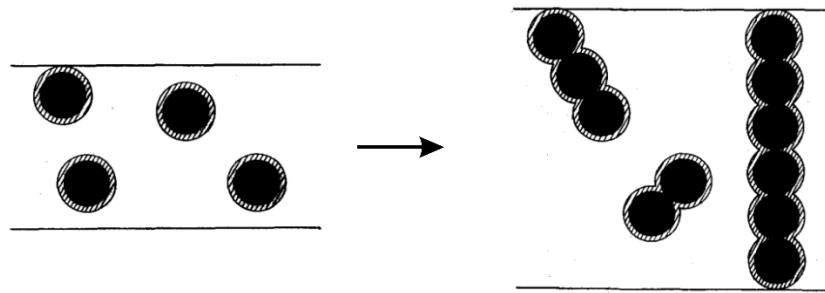
Figure 2.1 Principle of derivation of Guth-Gold equation: analogy of rod-like geometry at high concentration from individual spheres at low concentration [3].

A further development of Guth has indicated that the modulus of the composites reinforced by a rod-like filler is given by [3],

$$E_c = E_m(1 + 0.67fV_f + 1.62f^2V_f^2) \tag{2.4}$$

where E_m is the modulus of the elastomer, V_f is the volume fraction of the rod-like filler used and f is the shape factor of a rod, which is the length/breadth of the rod. It should be noted that Equation (2.3) can be applied theoretically on carbon black (CB) reinforced

elastomers. Empirically, however, the actual equation that predicts the behaviour of CB filled elastomers more accurately is equation (2.4), when the shape factor f is equal to 6 [6].

There has been a number of reports [7-22] in the literature employing the theoretical analysis of Guth-Gold for elastomers reinforced by graphene-based fillers, where the shape factor f was defined as the aspect ratio s of graphene (lateral size/thickness). Overall, the Guth-Gold theory can predict accurately the 'accelerating stiffening' effect, where the modulus against volume fraction of the filler shows a super-linear relationship as suggested by the quadratic equation (2.1). Nevertheless, the fitted shape factor values (for graphene, the aspect ratio) are underestimated for graphene that was used. The values range from around 10 to 30 for graphene nanoplatelets, graphene oxide (GO) and functionalised graphene oxide (fGO) [7-12, 14-17, 20-22], which are known to be significantly lower than those for graphene (theoretically thousands). In terms of typical rod-like fillers, such as fibres-filled or carbon nanotubes-filled elastomers [23-27], the fitted aspect ratio values (also in the order of tens) are quite reasonable. This can then be attributed to the fact that the original derivation of Guth-Gold equation was based on the varied morphologies that were formed by carbon black, which tend to be rods, whereas graphene is a kind of planar material that possesses large areas of planes of very thin thickness. In this case, therefore, it is reasonable to assume that the definition of the aspect ratio (shape factor) between rods and 2D materials is different.

To conclude, Guth-Gold theory is a classical theory with theoretical basis, indicating that the modulus of the composites is related to volume fraction and shape factor (aspect ratio) of the filler and the mechanical improvement is independent of the mechanical properties of the filler. The reason for this is that it was assumed that the inorganic fillers (spheres or rods) were unable to be deformed during the deformation of the elastomers, because elastomers were considered to be extremely soft type of materials. The simplicity of the Guth-Gold equation in analysing mechanical reinforcement of soft matrices by micro- and nano-filler makes it applied widely in composites mechanics for elastomers. Guth-Gold equation is more accurate for rod-like fillers than plate-like fillers due to the

different definition of the shape factor and this is attributed to the analogy of forming rods from spheres, which was used in the derivation of the equation.

2.1.2 Shear-lag Theory and Rule-of-mixtures

Shear-lag theory has been used widely to study mechanical reinforcement for composites reinforced by short fibres [28-34]. It was originally proposed by Cox [35] and subsequently developed by Rosen [36]. It is particularly useful to analyse the mechanics of resins reinforced by short fibres and only until recently it has been employed for polymers reinforced by graphene [37, 38]. Shear-lag model describes the effect of loading on composites, suggesting that the load applied on a matrix is transferred by a shear stress through the interface from the matrix to the reinforcement (short fibres) during the deformation of the composites.

Gong et al. [38] has performed Raman band shift measurement on model composites during the deformation of the materials, probing the laser on different spots of a monolayer graphene above PMMA substrate. Shear-lag theory was used subsequently to analyse the stress transfer. As can be seen from **Figure 2.2** (a), a monolayer graphene was identified and selected for measurement of Raman band shift under tensile strain. **Figure 2.2** (b) shows the schematic diagram of the materials and the measurement. Upon this single-layer graphene model composites, the Raman 2D band shift rate was determined as -60 cm^{-1}/% strain, in agreement with modulus of graphene under uniaxial tension [39]. Based on the shear-lag analysis in this work [38] for platelets, for a given matrix strain (e_m), the variation of graphene strain (e_f) with position (x) across the monolayer graphene is given by,

$$e_f = e_m \left[1 - \frac{\cosh\left(ns\frac{x}{l}\right)}{\cosh(ns/2)} \right] \qquad (2.5)$$

where $n = \sqrt{\dfrac{2G_{\mathrm{m}}}{E_{\mathrm{f}}}\left(\dfrac{t}{T}\right)}$ (2.6)

and G_{m} is the shear modulus of the matrix, E_{f} is the Young's modulus of the monolayer graphene, l is the length of the graphene flake in the direction of x, t is the thickness of the graphene, T is the thickness of the resin around the flake and s is the aspect ratio (l/t) of the graphene in the x direction. The parameter n indicates the stress transfer efficiency and therefore ns is related to both flake morphologies and interfacial interaction. With equation (2.5) and its reasonable agreement with the experimental results from Raman measurements (shown in **Figure 2.2** e and f), the shear-lag approach was proven effective in analysing graphene reinforced polymers in a model composite.
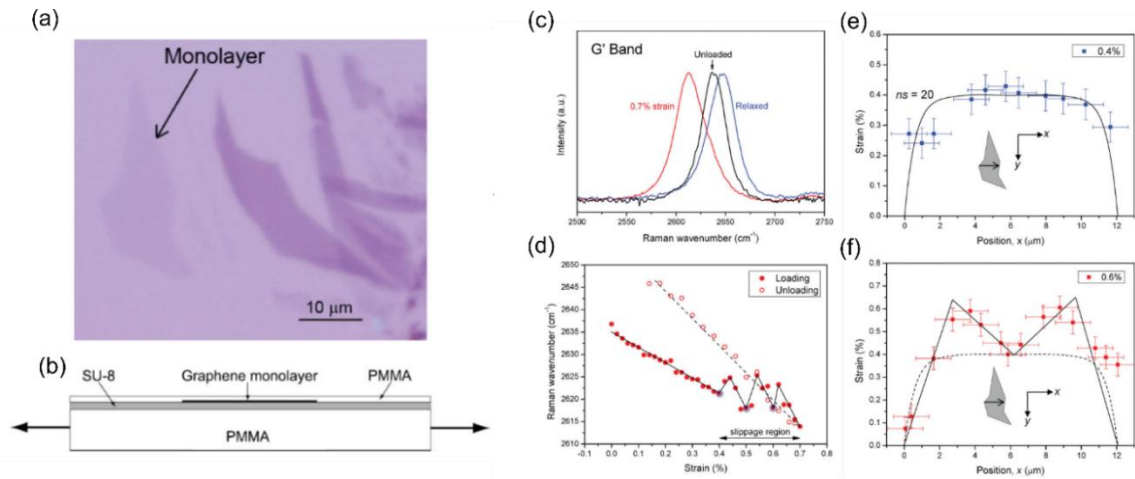
Figure 2.2 (a) Optical micrograph showing the monolayer graphene flake investigated within the model composite; (b) Schematic diagram of the model composite; (c) Change of G'(2D) band spectra with deformation; (d) Band shift of G'(2D) band against strain applied. Distribution of strain in the graphene in the direction of the tensile axis (x) across the single monolayer: (e) Variation of axial strain with position across the monolayer in the x-direction at 0.4% matrix strain. (The curve fitted to the data is equation 2.5) and (f) at 0.6% matrix strain. (The solid lines are fitted to the data to guide the eye. The dashed curve is the shear-lag fit to the data in Fig. 2.2e at 0.4% strain.) Figure reproduced from Ref [39].

Subsequently, Young et al. [37] evaluated reinforcing efficiency of graphene nanoplatelets (GNPs) in a number of different polymers from soft to stiff ones and scaled filler modulus (E_f) with matrix modulus (E_m) (**Figure** 2.3a), where filler modulus was calculated from the simple rule-of-mixtures:

$$E_c = E_f V_f + E_m (1 - V_f) \tag{2.7}$$

where V_f is the volume fraction of the filler. It was found that the stress transfer efficiency from graphene nanoplatelets to polymer matrices is highly dependent upon the shear modulus of the matrix. The principles of the theoretical analysis were based on shear-lag theory. According to equation (2.5), the average axial stress of a flake is given by,

$$\bar{\sigma}_f = E_{eff} e_m \left[1 - \frac{\tanh(ns/2)}{ns/2} \right] \tag{2.8}$$

where $n = \sqrt{\dfrac{2G_m}{E_{eff}}} \left(\dfrac{t}{T} \right)$ $\tag{2.9}$

E_{eff} is the effective modulus of the nanoplatelets and G_m is the shear modulus of the matrix. Assuming uniform strain ($e_f = e_m$), and taking the orientation factor of 2D materials [40, 41] into account equation (2.8) gives,

$$E_f = E_{eff} \eta_o \left[1 - \frac{\tanh(ns/2)}{ns/2} \right] \tag{2.10}$$

It was realized the E_{eff} can only be large when G_m is large. For soft matrices like elastomers when ns is small [37], the hyperbolic equation (2.10) can be expanded using Taylor series and the higher powers can be neglected, equation (2.10) can then be simplified to,

$$E_f \approx \eta_o \frac{s^2}{6} \frac{t}{T} G_m \tag{2.11}$$

and because $G_m = \frac{E_m}{2(1+v)}$, where v is the Poisson's ratio of the matrix, therefore,

$$E_f \approx \eta_o \frac{s^2}{12} \frac{t}{T} \frac{E_m}{(1+v)}$$
(2.12)

Hence, the analysis based on shear-lag theory indicates E_f is proportional to E_m. It can be seen that the reinforcement of graphene is independent of the modulus of graphene, similar to Guth-Gold theory (equation 2.4). With similar theoretical derivation, the effective modulus measured by Raman band shift (E_R) is given by $E_R \approx \eta_o \frac{s^2}{8} \frac{t}{T} \frac{E_m}{(1+v)}$ for elastomers, which is also indicative of $E_f \propto E_m$ (**Figure 2.3**b) .
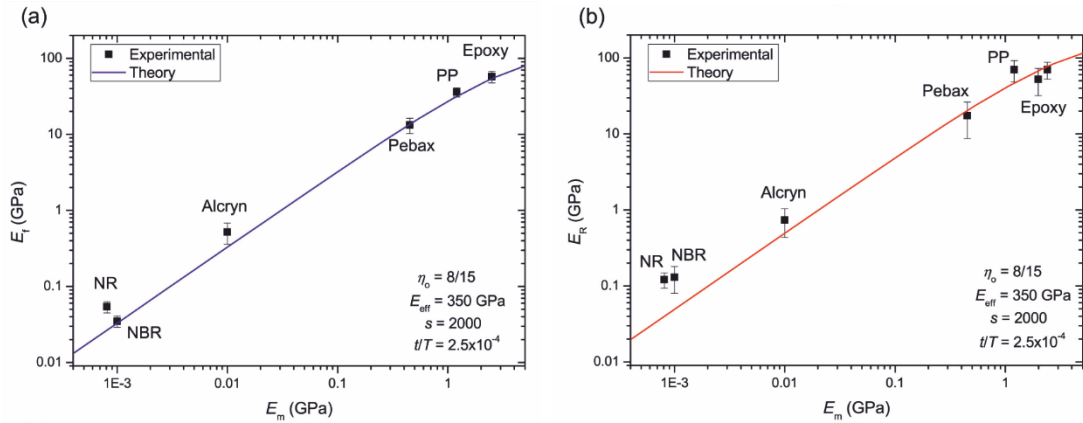
Figure 2.3 (a) E_f of M25 GNPs against different E_m for different polymers with a solid line based on equation (2.10). (b) Filler modulus measured by Raman band shift (E_R) against different E_m for different polymers with a solid line based on the shear-lag equation for Raman band shift measurements [37]. Figures reproduced from Ref. [37].

Combined equation (2.12) with the rule-of-mixtures (2.7), and approximating t/T to the volume fraction of the GNPs (V_f) assuming that the nanoplatelets are sandwiched between layers of the matrix, the elastomeric nanocomposites reinforced by GNPs is given by,

$$E_c \approx E_m [1 - V_f + \eta_o \frac{s^2}{12} \frac{E_m}{(1+v)} V_f^2]$$
(2.13)

74

In summary, equation (2.13) is the shear-lag/rule-of-mixtures theoretical model for elastomers nanocomposites reinforced by graphene. It indicates that the modulus of the nanocomposite is dependent only upon orientation, aspect ratio and volume fraction of the filler and independent of the modulus of the graphene. This equation has a very similar form as Guth-Gold theory mentioned in section 2.1.1. Compared with Guth-Gold theory, the aspect ratio of 2D materials is well-defined and the orientation parameter is included in shear-lag theory.

2.2 Mechanical Percolation of Graphene/elastomer Nanocomposites

Percolation-like phenomenon exist not only in the transport properties of nanocomposites, such as electrical or thermal conductivity, but also in the mechanical properties. For polymer nanocomposites, it is suggested that the reinforcement from a filler to a matrix polymer is in a different degree, above and below a volume fraction of a filler (percolation threshold volume fraction V_p), since when a filler loading is high, there should be a filler network formed. The original theoretical basis is jamming theory [42], analysing the rheological behaviour of a number of polymers in their molten state mixed with carbon blacks. For elastomer-based nanocomposites, a number of studies have introduced mechanical percolation to explain the results [10, 13, 43-47].

In 2007, Shawna *et al.* introduced the concept of mechanical percolation for the first time for a nanoclay-reinforced thermoplastic polyurethane [46]. As can be seen from **Figure 2.4**, the modulus of the nanocomposite materials can be fitted well below ~5 wt%, using the Guth-Gold equation (shown in equation 2.1). The modulus values of the nanocomposites with filler loadings higher than the percolation threshold (V_p in **Figure 2.4**), however, cannot be fitted with Guth-Gold equation as below V_p. Another equation for the modulus $E_c = E_1 + A\left(V_f - V_p\right)^b$ was introduced, in the form of power-law, where E_1 is the modulus at the percolation threshold, *A* and *b* are fitting parameters without any physical meaning. As can be seen in **Figure 2.4**, the fitting results are satisfactory. Similar theoretical analysis was introduced in other reports for graphene and CNT [10, 13, 43-45,

47], with random *A* and *b* values for different materials. One of the disadvantages of this power-law model is its variable and inexplicit parameters (*A* and b) that could fit any random composite system without physical meaning. A micromechanical model with explicit parameters is therefore expected for a better understanding of the mechanical percolation phenomenon for elastomer nanocomposites.
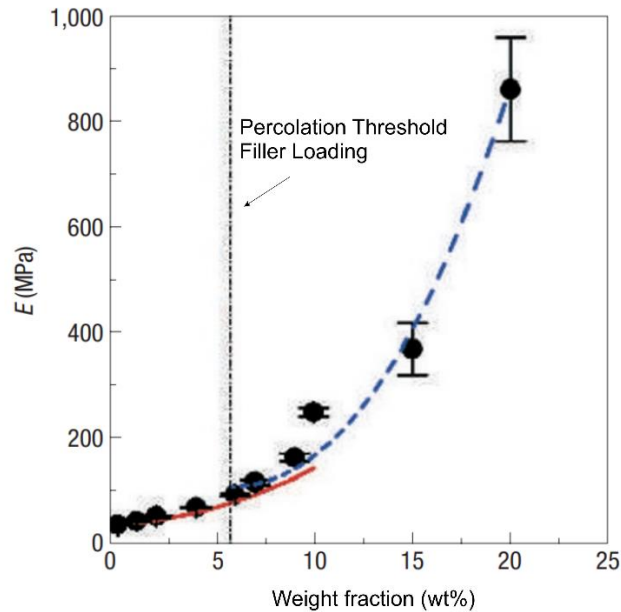
Figure 2.4 Modulus of the nanocomposites against the filler (nanoclay) loading, where a mechanical percolation threshold was found at around 5 wt% [46].

2.3 Liquid Barrier Properties

Elastomers, possessing large free volume, usually display relatively poor liquid barrier properties, allowing small molecules of liquids to diffuse into the materials quite easily. Resistance to organic liquids is also an important property that is highly relevant to a number of applications of elastomers, since such materials find extensive use in seals, O-rings, gaskets and flexible pipes. Two-dimensional nanomaterials such as graphene, possessing a high aspect ratio and therefore providing large specific interfacial area in the nanocomposites, are very promising for improving the barrier properties of the elastomers

in liquids. In this section, a number of theories are reviewed regarding studies of the diffusion and swelling behaviour of elastomers and their nanocomposites.

2.3.1 Gravimetric Diffusion – Fickean Diffusion

There are a number of works reporting the study of gravimetric diffusion of liquid molecules into elastomers or elastomeric nanocomposites [48-53]. The transport of small molecules into polymer specimens with different geometries has been investigated by Cervenka *et al.* [54] based on Fickean diffusion. Relative parameters, such as the diffusion coefficient (D) and the mass uptake at saturation (M_∞), were specified and well-defined for relatively small specimens. Their specific analysis can be also applied to elastomer-based nanocomposites, in order to investigate the effect of the filler on the absorption of small molecules. Herein, the relevant factors controlling the solvent uptake into small specimens are reviewed briefly. For a well-defined small and plate-like specimen (with a diameter of at least 10× the thickness), the relative mass uptake $M(t)$ determined gravimetrically with exposure times is given by,

$$M(t) = \frac{W(t)-W(0)}{W(0)} \tag{2.14}$$

where $W(t)$ is the weight of a specimen after an exposure time t and $W(0)$ is calculated theoretically by determining the intercept of the linear fitting of $W(t)$ against $t^{1/2}$ at $t_i=0$, in order to reduce any systematic error involved in gravimetry [54]. The determination of the diffusion coefficient, D, for a specimen with a length a, width b and height h for short exposure times t_x, can be obtained by [54],

$$\frac{M(t)}{M(\infty)} = 1 - \left(1 - \frac{4}{h}\sqrt{\frac{Dt_i}{\pi}}\right)\left(1 - \frac{4}{a}\sqrt{\frac{Dt_i}{\pi}}\right)\left(1 - \frac{4}{b}\sqrt{\frac{Dt_i}{\pi}}\right) \tag{2.15}$$

and for a plate-like specimen, that is, $a \rightarrow \infty$ and $b \rightarrow \infty$, equation (2.15) can be reduced to the form for experimental determination of the diffusion coefficient, D,

$$\frac{4M(\infty)}{h\sqrt{\pi}}\sqrt{D}=\frac{M_2\text{-}M_1}{\sqrt{t_2}\text{-}\sqrt{t_1}}$$

(2.16)

where h is the thickness of the samples and $M(\infty)$ is the mass uptake at the saturation point of the absorption. On the basis of the equation (2.16), the diffusion coefficient (D) can be determined experimentally for small specimens.

2.3.2 Swelling of Elastomers – Flory-Rehner Theory

In 1940s, Flory and Rehner [55, 56] proposed a comprehensive theory for investigation of the swelling behaviours of crosslinked elastomers in solvents. It is based on Flory-Huggins model [57, 58] for calculating the configurational entropy of mixing between liquid and polymer molecules, and statistical mechanics for deformation of Gaussian network (soft polymer network at low strain) [56].

In this theoretical system, definitions of a number of parameters needs to be given. For a crosslinked elastomer in a solvent at the saturated swollen state, the volume fraction of the solvent in the swollen rubber is given by,

$$\phi_1=\frac{n_1v_1}{n_1v_1+n_2v_2}$$

(2.17)

and the volume fraction of the rubber in the swollen sample is,

$$\phi_2=\frac{n_2v_2}{n_1v_1+n_2v_2}$$

(2.18)

where n_1 and n_2 are the respective numbers of moles of the solvent and the elastomer in the swollen gel at equilibrium; v_1 and v_2 are the molar volumes of the solvent and the elastomer, respectively. It can be shown from equation (2.18) that the volume swelling ratio of the rubber network at saturation is $1/\phi_2$.

78

Based on the Flory-Huggins relationship, the Gibbs free energy of mixing is giving by,

$$\Delta G_{\mathrm{mix}} = R T_K \left[\ln\left(1 - \phi_2\right) + \phi_2 + \chi \phi_2^2 \right] \tag{2.19}$$

where R is the gas constant, T_K is the thermodynamic temperature, and χ is a dimensionless parameter which is dependent upon the polymer-solvent interaction [59, 60]. It should be noted the free energy of mixing obtained from equation (2.19) is the free energy of dilution for the polymers prior to crosslinking.

The process of swelling of elastomers involves elastic deformation of the materials from unswollen state to saturated swollen state of the elastomer networks. The deformation is usually in a small degree and therefore Gaussian network model can be introduced [59, 60]. Assuming isotropic expansion of the network for uniform structure of rubbers, the Gibbs free energy of elastic deformation from unswollen state to saturated swollen state for crosslinked rubbers is given by,

$$\Delta G_{\mathrm{def}} = \frac{\rho R T_K}{M_c} v_1 \phi_2^{\frac{1}{3}} \tag{2.20}$$

where ρ is the density of the elastomer, M_c is molecular weight between crosslinks. It should be noted that the M_c is related to mechanical properties of the elastomer and thus the expression of the shear modulus of the matrix (G_m), $G_m = \rho R T_K / M_c$ [59, 60].

Based on Flory-Rehner theory, the total free energy during swelling process is,

$$\Delta G = \Delta G_{\mathrm{mix}} + \Delta G_{\mathrm{def}} \tag{2.21}$$

At the equilibrium swollen state (saturation), the free energy change equals to zero ($\Delta G = 0$), and based on equations (2.19) and (2.20),

$$\ln\left(1\text{-}\phi_2\right)+\phi_2+\chi\phi_2^2+\frac{\rho v_1}{M_c}\phi_2^{\frac{1}{3}}=0 \tag{2.22}$$

With expansion of the logarithm in equation (2.22) and neglecting high powers of ϕ_2, equation (2.22) can be rewritten in the form,

$$(\rho v_1/M_c)\approx\left(\frac{1}{2}\text{-}\chi\right)\phi_2^{\frac{5}{3}} \tag{2.23}$$

Equation (2.23) is the well-known Flory-Rehner theory for swelling of crosslinked rubbers. As aforementioned, M_c is related to the mechanical properties of the rubbers (shear modulus). Hence, the volume swelling of the crosslinked rubbers is dependent upon the modulus of the rubber and the type of the solvent. Flory [61] used butyl rubbers with different crosslinking degrees (rubbers with varied M_c values) to carry out swelling measurements in cyclohexane and presented the relationship between M_c and ϕ_2 experimentally. In **Figure 2.5** the log-log plot of the modulus for butyl rubbers against the volume swelling ratio ($1/\phi_2$) of the rubbers with various degrees of crosslinking gave data lying on a straight line with a slope of -3/5, indicating a satisfactory agreement with the theory (equation 2.23).
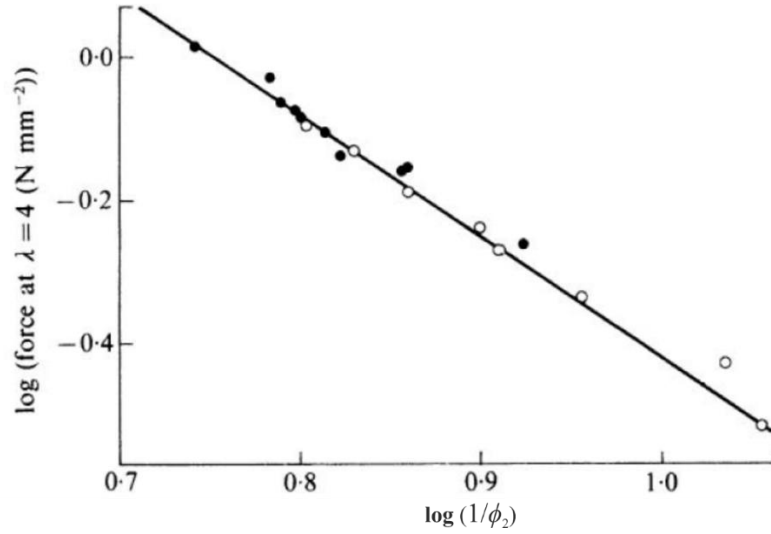
Figure 2.5 Relation between modulus for butyl rubbers with various cross-linking degree and their corresponding equilibrium swelling ratio ($1/\phi_2$) [61].

Based on Flory-Rehner theory, the work of Treloar in 1950 reported that, counterintuitively, the application of tensile strains (uniaxial and biaxial) to rubber samples led to an increased volume swelling ratio in solvents [62]. Treloar successfully quantified the dependence of volume swelling ratio (solvent uptake) on the applied strain either uniaxial (equation 2.24) or biaxial (equation 2.25). As can be seen from **Figure 2.6**, the experimental results were in agreement with equations (2.24 and 2.25). Such a potentially useful theory has, however, yet to be applied for the study of the swelling behaviour of rubber composites.

$$\ln\left(1-\phi_2\right)+\phi_2+\chi\phi_2^2+\frac{\rho v_1}{M_c l_1}=0 \tag{2.24}$$

$$\ln\left(1-\phi_2\right)+\phi_2+\chi\phi_2^2+\frac{\rho v_1}{M_c \phi_2 l_2^4}=0 \tag{2.25}$$

where l_1 and l_2 are defined in Figure 2.6 (a).
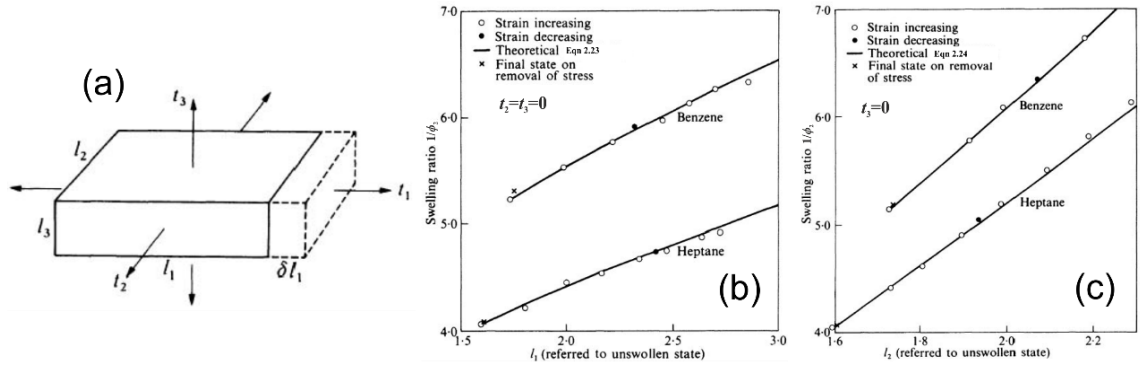
Figure 2.6 (a) Equilibrium of swollen rubber under stress (t_1, t_2 and t_3) in principal axes, which originally in the form of a unit cube, and l_1, l_2 and l_3 are the extension ratios of the final equilibrium swollen state referred to the original unit length at unswollen state. The stresses t_1, t_2 and t_3 are defined as true stresses applied; (b) dependence of swelling on strain under uniaxial extension, correspondent to the case $t_2=t_3=0$ in (a); dependence of swelling on strain under biaxial extension, correspondent to the case $t_3=0$ in (a). Figures reproduced from Ref. [59].

2.3.2 Swelling of Elastomer Composites

Elastomers are usually used with fillers. One of the most common filler is carbon black (CB), which has been used extensively for the purpose of constraining swelling of rubbers and detailed studies were undertaken by Kraus [64], as shown in **Figure 2.7**. For the Kraus theory, the degree of the volume swelling of an elastomer is defined as,

$$\phi_2 = \frac{\text{Volume of rubber}}{\text{Volume of the swollen rubber-solvent gel}} \tag{2.26}$$

same to equation (2.18), and for a CB-filled elastomer,

$$\phi_{2f} = \frac{\text{volume of rubber in composite (total volume minus filler volume)}}{\text{Volume of swollen rubber gel (total swollen volume minus filler volume)}} \tag{2.27}$$

For elastomer composites undergoing swelling, the ratio ϕ_2/ϕ_{2f} is given by,

82

$$\phi_2/\,\phi_{2\mathrm{f}} = 1 - mV_{\mathrm{f}}/(1 - V_{\mathrm{f}}) \tag{2.28}$$

while the parameter *m* is given by,

$$m = 3c_{\mathrm{k}} \cdot (1 - \phi_2^{1/3}) + \phi_2 - 1 \tag{2.29}$$

where c_{k} is the filler parameter, which is a constant of the filler and dependent upon geometry of the filler and adhesion to the matrix. Based on Kraus' theory, higher specific area (surface area per volume) and higher adhesion of the filler give higher values of c_{k}, and consequently higher values of *m*, based on the equation (2.29), where the ϕ_2 remains consistent for the same elastomer and the same solvent. As suggested by the equation (2.28), for adhering filler reinforced elastomers, the plot of the ratio $\phi_2/\,\phi_{2\mathrm{f}}$ against $V_{\mathrm{f}}/(1 - V_{\mathrm{f}})$ should produce a linear line with a slope of less than zero (**Figure 2.7** a) in the case that no filler-filler interaction exists up to a reasonable filler loading. Regarding non-adhering filler reinforced elastomers, the slope of $\phi_2/\,\phi_{2\mathrm{f}}$ against $V_{\mathrm{f}}/(1 - V_{\mathrm{f}})$ should be larger than zero, indicating no restraining effect of the filler on the swelling of elastomers, as shown in **Figure 2.7** (b).
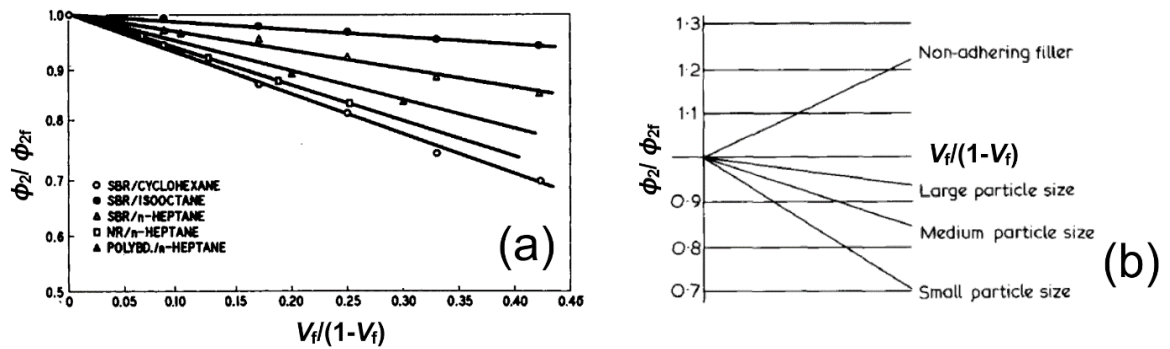
Figure 2.7 (a) dependence of swelling on filler (CB) loading by volume, for different rubber/solvent combinations [63]; (b) dependence of swelling on particle sizes on the filler (CB) [6].

The theory proposed by Kraus has been shown to be applicable to carbon blacks and other types of spherical fillers [6, 63, 64]. However, the parameters c_k and m are not well-defined and therefore the theory provides an empirical equation and is difficult to be modified. The reduced swelling ratio of carbon black-reinforced elastomer composites as the result of an improved stiffness modulus is central to Kraus' theory [63]. However, when elastomers are reinforced by asymmetric fillers with unidirectional orientation such as aligned rods and platelets, the mechanical reinforcement is anisotropic [65, 66]. The anisotropy of modulus leads to anisotropic swelling when the nanocomposites are immersed in liquids [65, 66]. In this case, Kraus' equation is not applicable, because the reinforcement from asymmetric fillers is no longer uniform and leads to complexity in the swelling process. Nevertheless, there are limited number of reports explaining anisotropic swelling for graphene/elastomer nanocomposites and therefore Kraus' theory has been used to model the swelling behaviour of elastomer nanocomposites reinforced by carbon nanotubes (CNT) and graphene and the results [67-69], as shown in **Figure 2.8**. As shown, the plots of the results from asymmetric filler reinforced elastomers did not show linear relationship (equation 2.28), indicating Kraus theory may not be valid for these fillers.
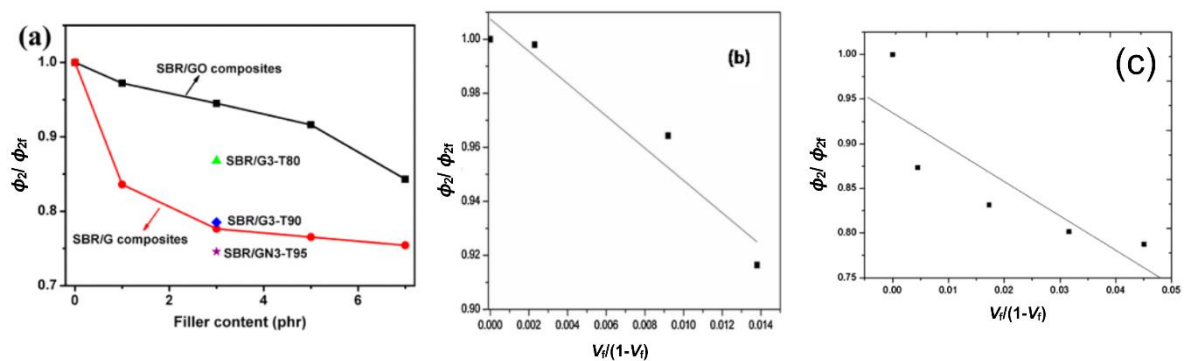
Figure 2.8 Kraus plots for swelling of (a) SBR/GO and SBR/G (G refers to functionalised GO) nanocomposites [67]; (b) natural rubber (NR)/GNP nanocomposites [69] and (c) NR/MWCNT nanocomposites [68].

2.4 Conclusion

A number of analytical models have been reviewed with respect to reinforcement of elastomers by graphene. The micromechanics based in shear-lag and rule-of-mixtures is believed well-developed and it can be developed further by including mechanical percolation phenomenon. Kraus theory, analysing swelling behaviours, however, is neither satisfying nor able to understand the swelling of graphene/elastomer nanocomposites. A new and better theory is yet to be established to understand biaxial reinforcement of graphene in elastomers.

References

[1] Mori T, Tanaka K. Average stress in matrix and average elastic energy of materials with misfitting inclusions. Acta Metallurgica. 1973;21(5):571-4.

[2] Affdl JH, Kardos J. The Halpin-Tsai equations: a review. Polymer Engineering & Science. 1976;16(5):344-52.

[3] Guth E. Theory of filler reinforcement. Journal of Applied Physics. 1945;16(1):20-5.

[4] Einstein A. Eine neue bestimmung der moleküldimensionen. Annalen der Physik. 1906;324(2):289-306.

[5] Smallwood HM. Limiting law of the reinforcement of rubber. Journal of Applied Physics. 1944;15(11):758-66.

[6] Boonstra B. Role of particulate fillers in elastomer reinforcement: a review. Polymer. 1979;20(6):691-704.

[7] Das A, Kasaliwal GR, Jurk R, Boldt R, Fischer D, Stöckelhuber KW, Heinrich G. Rubber composites based on graphene nanoplatelets, expanded graphite, carbon nanotubes and their combination: A comparative study. Composites Science and Technology. 2012;72(16):1961-7.

[8] Fernández-d'Arlas B, Corcuera MA, Eceiza A. Comparison between exfoliated graphite, graphene oxide and multiwalled carbon nanotubes as reinforcing agents of a polyurethane elastomer. Journal of Thermoplastic Composite Materials. 2015;28(5):705-16.

[9] Frasca D, Schulze D, Böhning M, Krafft B, Schartel B. Multilayer graphene chlorine isobutyl isoprene rubber nanocomposites: influence of the multilayer graphene concentration on physical and flame-retardant properties. Rubber Chemistry and Technology. 2016;89(2):316-34.

[10] Kautschuk-Nanocomposite S. Graphene/Styrene Butadiene Rubber Nanocomposite.

[11] Koerner H, Liu W, Alexander M, Mirau P, Dowty H, Vaia RA. Deformation–morphology correlations in electrically conductive carbon nanotube—thermoplastic polyurethane nanocomposites. Polymer. 2005;46(12):4405-20.

[12] Kumar V, Hanel T, Giannini L, Galimberti M, Giese U. Graphene reinforced synthetic isoprene rubber nanocomposites. Elastomers and Plastics. 2014;67:38-46.

[13] Kumar V, Lee DJ. Studies of nanocomposites based on carbon nanomaterials and RTV silicone rubber. Journal of Applied Polymer Science. 2017;134(4).

[14] Lee J-Y, Kumar V, Tang X-W, Lee D-J. Mechanical and electrical behavior of rubber nanocomposites under static and cyclic strain. Composites Science and Technology. 2017;142:1-9.

[15] Lowe DJ, Chapman AV, Cook S, Busfield JJ. Micromechanical models of young's modulus of NR/organoclay nanocomposites. Journal of Polymer Science Part B: Polymer Physics. 2011;49(22):1621-7.

[16] Mensah B, Kim S, Arepalli S, Nah C. A study of graphene oxide-reinforced rubber nanocomposite. Journal of Applied Polymer Science. 2014;131(16).

[17] Mensah B, Kumar D, Lee GB, Won J, Gupta KC, Nah C. Gold functionalized-graphene oxide-reinforced acrylonitrile butadiene rubber nanocomposites for piezoresistive and piezoelectric applications. Carbon Letters (Carbon Lett). 2018;25:1-13.

[18] Potts JR, Shankar O, Du L, Ruoff RS. Processing–morphology–property relationships and composite theory analysis of reduced graphene oxide/natural rubber nanocomposites. Macromolecules. 2012;45(15):6045-55.

[19] Su J, Zhao Z, Huang Y, Liao X, Yang Q. Thermal oxidative and ozone oxidative stabilization effect of hybridized functional graphene oxide in a silica-filled solution styrene butadiene elastomer. Physical Chemistry Chemical Physics. 2016;18(42):29423-34.

[20] Valentini L, Bon SB, Hernández M, López-Manchado MA, Pugno N. Nitrile butadiene rubber composites reinforced with reduced graphene oxide and carbon nanotubes show superior mechanical, electrical and icephobic properties. Composites Science and Technology. 2018;166:109-14.

[21] Wang J, Zhang K, Cheng Z, Lavorgna M, Xia H. Graphene/carbon black/natural rubber composites prepared by a wet compounding and latex mixing process. Plastics, Rubber and Composites. 2018;47(9):398-412.

[22] Zhan Y, Wu J, Xia H, Yan N, Fei G, Yuan G. Dispersion and exfoliation of graphene in rubber by an ultrasonically-assisted latex mixing and in situ reduction process. Macromolecular Materials and Engineering. 2011;296(7):590-602.

[23] Praveen S, Chattopadhyay PK, Jayendran S, Chakraborty BC, Chattopadhyay S. Effect of nanoclay on the mechanical and damping properties of aramid short fibre-filled styrene butadiene rubber composites. Polymer International. 2010;59(2):187-97.

[24] Das A, Stöckelhuber KW, Jurk R, Saphiannikova M, Fritzsche J, Lorenz H, Klüppel M, Heinrich G. Modified and unmodified multiwalled carbon nanotubes in high performance solution-styrene–butadiene and butadiene rubber blends. Polymer. 2008;49(24):5276-83.

[25] Rios S, Chicurel R, Del Castillo LF. Potential of particle and fibre reinforcement of tyre tread elastomers. Materials & Design. 2001;22(5):369-74.

[26] Bokobza L, El Bounia NE. Reinforcement effects of multiwall carbon nanotubes in elastomeric matrices: Comparison with other types of fillers. Composite Interfaces. 2008;15(1):9-17.

[27] Ahmadi M, Shojaei A. Reinforcing mechanisms of carbon nanotubes and high structure carbon black in natural rubber/styrene-butadiene rubber blend prepared by mechanical mixing−effect of bound rubber. Polymer International. 2015;64(11):1627-38.

[28] Kalaprasad G, Joseph K, Thomas S, Pavithran C. Theoretical modelling of tensile properties of short sisal fibre-reinforced low-density polyethylene composites. Journal of Materials Science. 1997;32(16):4261-7.

[29] Chon CT, Sun C. Stress distributions along a short fibre in fibre reinforced plastics. Journal of Materials Science. 1980;15(4):931-8.

[30] Tucker III CL, Liang E. Stiffness predictions for unidirectional short-fiber composites: review and evaluation. Composites Science and Technology. 1999;59(5):655-71.

[31] Clyne T. A simple development of the shear lag theory appropriate for composites with a relatively small modulus mismatch. Materials Science and Engineering: A. 1989;122(2):183-92.

[32] Shetty DK. Shear-lag analysis of fiber push-out (indentation) tests for estimating interfacial friction stress in ceramic-matrix composites. Journal of the American Ceramic Society. 1988;71(2):C-107-C-9.

[33] Mondali M, Abedian A, Ghavami A. A new analytical shear-lag based model for prediction of the steady state creep deformations of some short fiber composites. Materials & Design. 2009;30(4):1075-84.

[34] Gao YC, Mai YW, Cotterell B. Fracture of fiber-reinforced materials. Journal of Applied Mathematics and Physic. 1988;39(4):550-72.

[35] Cox H. The elasticity and strength of paper and other fibrous materials. British Journal of Applied Physics. 1952;3(3):72.

[36] Rosen B. Mechanics of Fibre Strengthening in Fibre Composite Materials. ASM, Metals Park, OH. 1960.

[37] Young RJ, Liu M, Kinloch IA, Li S, Zhao X, Vallés C, Papageorgiou DG. The mechanics of reinforcement of polymers by graphene nanoplatelets. Composites Science and Technology. 2018;154:110-6.

[38] Gong L, Kinloch IA, Young RJ, Riaz I, Jalil R, Novoselov KS. Interfacial Stress Transfer in a Graphene Monolayer Nanocomposite. Advanced Materials. 2010;22(24):2694-7.

[39] Mohiuddin TM, Lombardo A, Nair RR, Bonetti A, Savini G, Jalil R, Bonini N, Basko DM, Galiotis C, Marzari N, Novoselov KS. Uniaxial strain in graphene by Raman

spectroscopy: G peak splitting, Grüneisen parameters, and sample orientation. Physical Review B. 2009;79(20):205433.

[40] Li Z, Young RJ, Kinloch IA, Wilson NR, Marsden AJ, Raju APA. Quantitative determination of the spatial orientation of graphene by polarized Raman spectroscopy. Carbon. 2015;88:215-24.

[41] Li Z, Young RJ, Wilson NR, Kinloch IA, Vallés C, Li Z. Effect of the orientation of graphene-based nanoplatelets upon the Young's modulus of nanocomposites. Composites Science and Technology. 2016;123:125-33.

[42] Trappe V, Prasad V, Cipelletti L, Segre PN, Weitz DA. Jamming phase diagram for attractive particles. Nature. 2001;411(6839):772-5.

[43] Fralick BS, Gatzke EP, Baxter SC. Three-dimensional evolution of mechanical percolation in nanocomposites with random microstructures. Probabilistic Engineering Mechanics. 2012;30:1-8.

[44] Baxter SC, Robinson CT. Pseudo-percolation: Critical volume fractions and mechanical percolation in polymer nanocomposites. Composites Science and Technology. 2011;71(10):1273-9.

[45] Nawaz K, Khan U, Ul-Haq N, May P, O'Neill A, Coleman JN. Observation of mechanical percolation in functionalized graphene oxide/elastomer composites. Carbon. 2012;50(12):4489-94.

[46] Liff SM, Kumar N, McKinley GH. High-performance elastomeric nanocomposites via solvent-exchange processing. Nature Materials. 2007;6(1):76.

[47] Noël A, Faucheu J, Chenal J-M, Viricelle J-P, Bourgeat-Lami E. Electrical and mechanical percolation in graphene-latex nanocomposites. Polymer. 2014;55(20):5140-5.

[48] Geethamma V, Thomas S. Diffusion of water and artificial seawater through coir fiber reinforced natural rubber composites. Polymer Composites. 2005;26(2):136-43.

[49] Gwaily S, Badawy M, Hassan H, Madani M. Influence of thermal aging on crosslinking density of boron carbide/natural rubber composites. Polymer Testing. 2003;22(1):3-7.

[50] Obasi HC, Ogbobe O, Igwe IO. Diffusion characteristics of toluene into natural rubber/linear low density polyethylene blends. International Journal of Polymer Science. 2009;2009.

[51] Unnikrishnan G, Thomas S. Diffusion and transport of aromatic hydrocarbons through natural rubber. Polymer. 1994;35(25):5504-10.

[52] Visakh P, Thomas S, Oksman K, Mathew AP. Cellulose nanofibres and cellulose nanowhiskers based natural rubber composites: Diffusion, sorption, and permeation of aromatic organic solvents. Journal of Applied Polymer Science. 2012;124(2):1614-23.

[53] Wei C, Srivastava D, Cho K. Thermal expansion and diffusion coefficients of carbon nanotube-polymer composites. Nano Letters. 2002;2(6):647-50.

[54] Cervenka AJ, Young RJ, Kueseng K. Gravimetric determination of the diffusion characteristics of polymers using small specimens. Journal of Polymer Science Part B: Polymer Physics. 2004;42(11):2122-8.

[55] Flory PJ, Rehner Jr J. Statistical mechanics of cross-linked polymer networks II. Swelling. The Journal of Chemical Physics. 1943;11(11):521-6.

[56] Flory PJ, Rehner Jr J. Statistical mechanics of cross-linked polymer networks I. Rubberlike elasticity. The Journal of Chemical Physics. 1943;11(11):512-20.

[57] Flory PJ. Thermodynamics of high polymer solutions. The Journal of Chemical Physics. 1942;10(1):51-61.

[58] Huggins ML. Thermodynamic properties of solutions of long-chain compounds. Annals of the New York Academy of Sciences. 1942;43(1):1-32.

[59] Treloar LRG. The physics of rubber elasticity: Oxford University Press, USA; 1975.

[60] Young RJ, Lovell PA. Introduction to polymers: CRC press; 2011.

[61] Flory PJ. Network structure and the elastic properties of vulcanized rubber. Chemical Reviews. 1944;35(1):51-75.

[62] Treloar LRG. The swelling of cross-linked amorphous polymers under strain. Transactions of the Faraday Society. 1950;46:783-9.

[63] Kraus G. Swelling of filler-reinforced vulcanizates. Journal of Applied Polymer Science. 1963;7(3):861-71.

[64] Burnside SD, Giannelis EP. Synthesis and properties of new poly (dimethylsiloxane) nanocomposites. Chemistry of Materials. 1995;7(9):1597-600.

[65] Coran AY, Boustany K, Hamed P. Unidirectional fiber–polymer composites: Swelling and modulus anisotropy. Journal of Applied Polymer Science. 1971;15(10):2471-85.

[66] Nardinocchi P, Pezzulla M, Teresi L. Anisotropic swelling of thin gel sheets. Soft Matter. 2015;11(8):1492-9.

[67] Tang Z, Zhang L, Feng W, Guo B, Liu F, Jia D. Rational design of graphene surface chemistry for high-performance rubber/graphene composites. Macromolecules. 2014;47(24):8663-73.

[68] Jose T, Moni G, Salini S, Raju AJ, George JJ, George SC. Multifunctional multi-walled carbon nanotube reinforced natural rubber nanocomposites. Industrial Crops and Products. 2017;105:63-73.

[69] Yaragalla S, Meera A, Kalarikkal N, Thomas S. Chemistry associated with natural rubber–graphene nanocomposites and its effect on physical and structural properties. Industrial Crops and Products. 2015;74:792-802.

Chapter 3. Micromechanics of Reinforcement of a Graphene-based Thermoplastic Elastomer*

* Contributions to the publication (author name order of the publication): Mufeng Liu: experiments, data & theoretical analysis, writing of the manuscript; Dimitrios G. Papageorgiou: guidance to the internal mixer and help with the mixing, proof-reading and discussion of the manuscript; Suhao Li: guidance and discussion of the Raman band shift measurements; Kailing Lin: drawing of Figure 3.7; Ian A. Kinloch & Robert J. Young: final proof-reading and discussion.

3.1 Introduction

Thermoplastic elastomers (TPEs) are a very interesting and versatile family of polymers with an ever-expanding range of applications. TPEs based on thermoplastic vulcanizate blends are considered an interesting class of materials since they combine the melt processability of thermoplastics with the properties of conventional thermoset rubbers [1]. TPEs usually have excellent weatherability, ozone resistance, chemical resistance to oils and abrasion resistance; however, their applications are limited by their relatively poor mechanical properties [2]. In this context, inorganic fillers have been incorporated within the TPEs and enhancements in their mechanical performances have been reported in the literature [3-7]. More recently, since the isolation of monolayer graphene [8] and the discovery of its unique properties, graphene and graphene-related nanomaterials have been employed extensively as reinforcement in elastomers [9].

It has been reported previously that although the intrinsic Young's modulus of monolayer graphene has been found to be very high (~1 TPa) [10, 11], it cannot be fully utilized in bulk nanocomposites, especially in soft materials such as elastomers due to inefficient stress transfer from the low modulus matrix to the high modulus filler by shear at the filler/matrix interface [9, 12-17]. In addition, it has been shown recently that classical micromechanics can be applied for the study of the mechanisms of stress transfer in

polymeric matrices with varying stiffness and a theory was developed, which can predict the modulus of bulk nanocomposites based on the characteristics of the nanoplatelets [15, 17]. The reinforcing mechanism of elastomers reinforced by graphene is different from that of stiff polymers: the normalized modulus (E_c/E_m) of an elastomer/graphene nanocomposite is dependent upon the graphene orientation, the aspect ratio and volume fraction of the filler, while it is independent of the filler modulus [17]. This result suggests that the filler geometry and the processing methods (which in turn affect the nanoscale filler distribution [9, 18]) will eventually determine the mechanical properties of the elastomeric nanocomposites.

In the present work, a comprehensive study of the mechanisms of reinforcement of a TPE by GNPs was undertaken. The composite samples based on a commercially-available TPE (Alcryn®) and GNPs with three different flake sizes were prepared by melt mixing. The microstructure of the injection moulded specimen was studied by quantifying the orientation factor of the fillers with polarised Raman spectroscopy. The mechanical properties of the nanocomposites with different filler loadings were evaluated by tensile testing followed by stress transfer measurements by observing the 2D Raman band shifts of the fillers during *in situ* deformation. Moreover, it applies recently developed theory [17] to the experimental results from tensile testing and correlated the fittings with important geometrical characteristics of the filler, such as the effective aspect ratio. Through the experimental and theoretical analysis, it can be concluded that the enhancement of thermoplastic elastomers with graphene nanoplatelets is effective, and gives considerable potential to develop high-performance engineering plastics, with tuned, application-specific properties.

The information for the matrix material employed in this chapter is provided herein. The first commercial introduction of Alcryn® melt processable rubber (MPR) was announced by Wallace and co-workers of Do Pont in 1985 and described as a single-phase thermoplastic elastomer alloy, based on chlorinated olefin and ethylene interpolymer in which the ethylene polymer component is partially crosslinked *in situ* [19-24]. This TPE can be classified into one of the thermoplastic vulcanizates (TPVs). The principle behind

the technology is that the selection of proper low-T_g ethylene copolymers or terpolymers is blended with PVC, which exhibits a high degree of miscibility.

Based on the Patent US4613533 [25], the polymer blends for the MPR can be either ethylene-vinyl acetate/ polyvinyl chloride (EVA/PVC) or ethylene-*co*-n butyl acrylate-*co*-carbon monoxide/polyvinyl chloride (E-nBA-CO/PVC). For the Alcryn 2000 series, which were designed for injection moulding, the materials are E-nBA-CO (**Fig 3.1 a**) blended with PVC. The blend is completely miscible because the keto group in the ethylene terpolymer is proton-accepting, which can form hydrogen bonds with the α-hydrogen atoms in the PVC as shown in the **Figs 3.1 (b)** and **(c)**.

$$-[-(CH_2-CH_2)_x-(CH_2-CH)_y-(CH_2-CH_2-C-CH_2-CH_2)_z-]_n-$$

$$
\begin{array}{cc}
| & \| \\
C=O & O \\
| & \\
O-(CH_2)_3-CH_3 &
\end{array}
$$
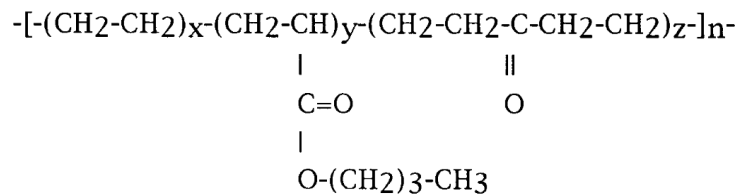
(a)
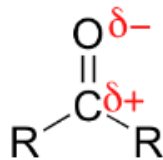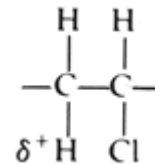
(b)   (c)

Figure 3.1 (a) E-nBA-CO; (b) Polar keto group and (c) PVC showing α-hydrogen.

The polar keto groups enable high miscibility for the blends of E-nBA-CO with PVC and also facilitate the free-radical-induced cross-linking of the ethylene terpolymer [26]. This concept was employed to a dynamic vulcanization process through an internal mixer and an extruder to acquire homogeneous high-volume dispersions of cured E-nBA-CO

terpolymer rubbers (weight fraction around 60%) in the thermoplastic matrix of PVC (weight fraction around 30%). The information in the patent also indicates that in these TPVs, the elastomeric ethylene terpolymer is cross-linked selectively through the addition of a combination of peroxide and bis-maleimide-type free-radical cross-linking agents. This crosslinking process of the E-nBA-CO can be carried out before or concurrently with blending with the PVC. Furthermore, after the crosslinking and blending process, it was proven experimentally that there was no crosslinking in PVC [25].

Alcryn 2265 applies a typical formulation of these MPR products, which includes 60 wt% ethylene-n-butyl acrylate-carbon monoxide (60/30/10) mixed with 30 wt% PVC and 10 wt% non-volatile plasticiser. The plasticiser could be trioctyltrimellitate or polyester oil ('santicizer') [25], which can facilitate the curing process of the ethylene terpolymer rubbers in situ during the mixing of peroxide (p- and m- α,α'-bis(t-butylperoxy) diisopropyl benzene) and a bismaleimide crosslink promoter (m-phenylenediamine-bis-maleimide) [25]. The amount of each crosslinking agent is less than 1% by weight.

The MPR can be processed by conventional processing methods such as extrusion, injection, calendaring and compression moulding. There are different products designed for different processing technologies. Among them, Alcryn 2000 series are designed specifically for injection moulding, which is employed in this chapter. Because the materials are substantially amorphous, there is no significant decrease in viscosity showing crystalline melt point to the hard-segment. The melt flow can be only prompted by a shearing force with elevated temperature [2]. Pseudoplastic flow (shear thinning) is the main mechanism to describe this MPR.

3.2 Experimental Methods

3.2.1 Materials and Preparation

Graphene nanoplatelets (GNPs) with nominal lateral diameters of 5, 10, 25 µm (dimensions claimed by the supplier) and average thicknesses in the range of 6-8 nanometres were purchased from XG Sciences, Inc. Lansing, Michigan, USA and used as received. Three grades of xGnP® M5, M15 and M25 were used. The thermoplastic elastomer, Alcryn® 2265 UT (Unfilled Translucent), which is based on a partially crosslinked chlorinated olefin interpolymer alloy, was purchased from A. Schulman, Inc.

The melt mixing of the composites was undertaken in a Thermo Fisher HAAKE Rheomix internal mixer. The mixing took place at 165 °C and 50 rpm for 5 minutes. The GNP fractions in the nanocomposites were 1%, 5%, 10%, and 20% by weight. The Alcryn nanocomposites in this study are coded based on the type of the matrix, the diameter and weight content of the fillers. For example, the sample code 2265-M15-GNP10, means that the matrix is the Alcryn 2265, the diameter of the GNPs is 15 µm and the weight percentage of the filler is 10 wt%.

The dumbbell-shaped tensile specimens were prepared by injection moulding in a HAAKE Minijet Piston Injection Moulding System. The geometry of the injection moulding system is shown in **Figure 3.2**. The temperatures of the barrel and the mould were set as 185 °C and 30 °C. The injection pressures were 500 bar, 550 bar, 600 bar, 700 bar and 800 bar for the neat polymer and the nanocomposites filled with 1 wt%, 5 wt%, 10 wt% and 20 wt% of GNPs, respectively. The injection pressure was held for 10 seconds followed by post-injection pressure of 200 bar, held for 5 seconds, for all specimens.
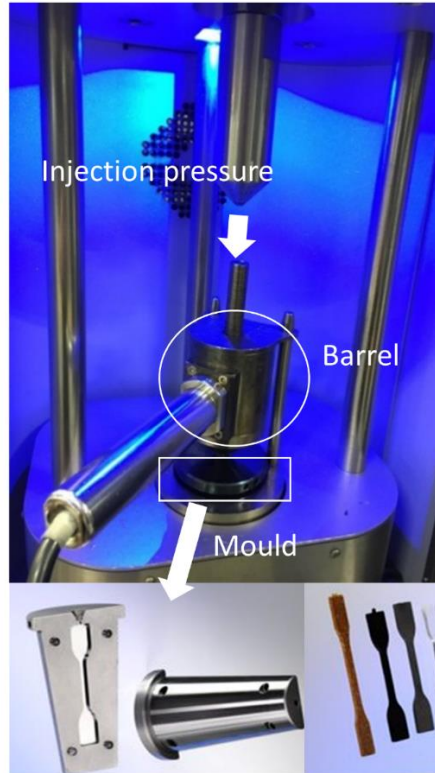
Figure 3.2 Photograph of the injection moulding system with its geometry.

3.2.2 Characterisation of the Nanocomposites

The actual loadings of GNPs in the nanocomposites were obtained by thermogravimetric analysis (TGA) using a TA Q500 TGA instrument. The samples were heated from room temperature up to 600 $^\circ$C under a 50 mL/min flow of N_2 at 10°C/min. Three samples were tested for each material in order to ensure reproducibility of the results.

The morphologies of the fillers, neat polymer and the microstructure of the nanocomposites were examined using scanning electron microscopy (SEM). The samples (GNP powders and cryo-fractured dumbbells) were placed on conductive carbon tapes, which were stuck on aluminium stubs. Subsequently, the coating process was carried out using Au-Pd alloy in order to provide satisfactory conductivity to the samples. The images

were acquired using a high-resolution XL30 Field Emission Gun Scanning Electron Microscope (FEGSEM) at 6 kV.

The XRD diffractograms were obtained from a PANalytical X'Pert3 diffractometer with Cu Kα radiation. The 2-theta angle range was selected from 5° to 90° with a step size of 0.03° and a step time of 180 s operated at 40 kV and 40 mA.

Stress–strain curves were obtained using dumbbell-shaped specimens in an Instron 4301 machine, under a tensile rate of 50 mm·min^{-1} with a load cell of 5 kN. The measurement of the strains was carried out with an extensometer with a gauge length of 20 mm.

Raman spectra were obtained using a Renishaw InVia Raman spectrometer with a laser wavelength of 633 nm and an objective of ×50, which produces a spot size of 1-2 µm. The Raman 2D band shift of the injection moulded samples (gauge length ~ 55 mm) was studied following the application of strain on the nanocomposites with the highest loading of GNPs (20 wt%). The tests were carried out using a mini-tensile rig. The strain was determined by measuring the extension of the two grips with a digital caliper. The Raman laser spot was in the order of 1-2 µm and it was focused on the same point of a single flake on each sample surface. The results were based on 5 composite samples for each type of GNPs, at the highest loading. All the spectra were fitted with a single Lorentzian curve.

The spatial orientation of the GNPs in the composites was determined using the method reported in previous studies [13, 14, 27]. The equipment employed was a 514 nm Raman spectrometer by Renishaw with 'VV' (vertical-vertical) polarisation, in which the incident and scattered radiation were polarised in the same direction. In the test, the laser was aligned perpendicular to the surface of the materials either along *X* or *Z* axis, as shown in **Figure 3.3**. The Raman G bands were recorded as a function of rotation angle (Φ_X, Φ_Z) and the rotation angles were used to estimate the orientation distribution function (ODF) [14, 27]. Regarding the *X*-axis tests, the orientation factor may vary throughout different

regions, since the samples were injection moulded [28]. Hence, the tests were carried out on a number of regions across the cryo-fractured cross-sections of the samples (red dash lines in **Figure 3.3**) to give the variation of the orientation parameter values.
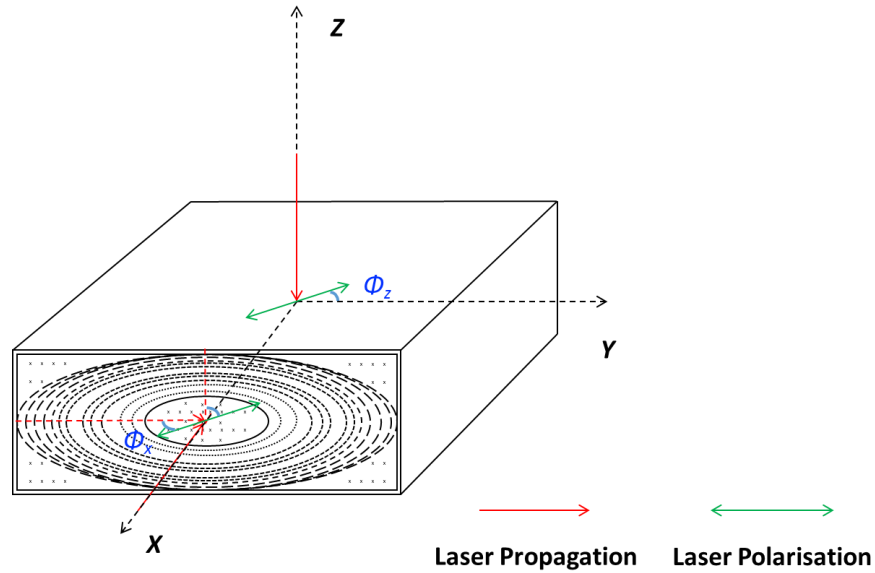
Figure 3.3 Experimental method of spatial orientation test of the GNPs for injection moulded samples.

3.3 Results

3.3.1 Characterisation of the Filler and Matrix

The three types of GNPs were examined by scanning electron microscopy as shown in **Figure 3.4**. It can be seen from (a) to (c) that the flake size increases from M5 to M15 to M25. However, the M15 and M25 GNPs batches seem to include a number of smaller flakes, which may decrease their average lateral size. Another important observation is that folded and looped structures can be found particularly in larger flake samples (**Figure 3.4** d and e). Overall, the three types of fillers display the stacked and agglomerated structure of many-layer graphene. The cryo-fractured cross-section of the neat elastomer can be also seen in **Figure 3.4** (f). Two distinct morphologies can be observed, revealing

the two components in the matrix and indicating that the polymer blend is not completely miscible, as expected from earlier reports [1].
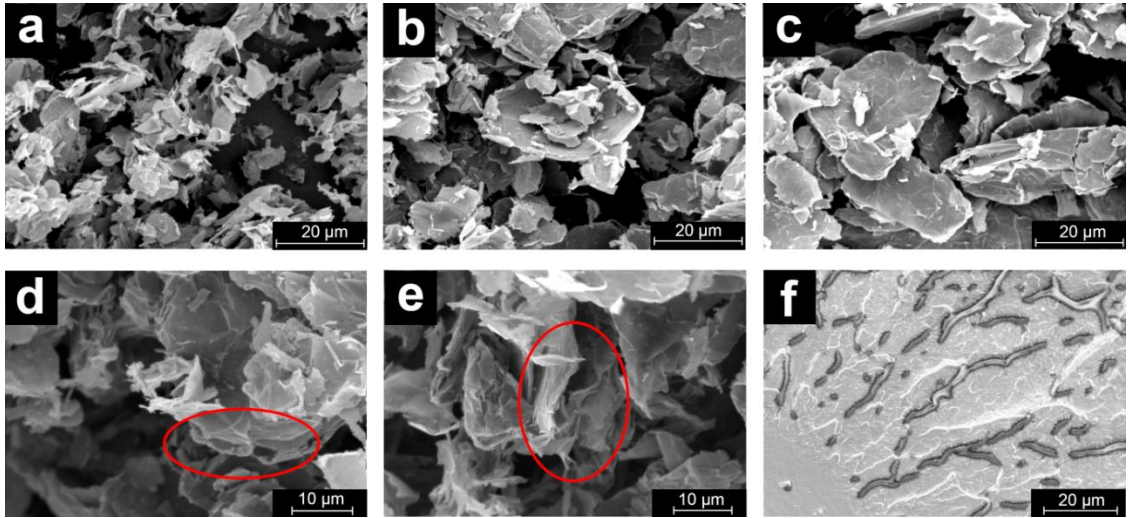
Figure 3.4 SEM images of (a-c) M5, M15 and M25 GNP powders, (d,e) M15 and M25 GNPs showing folded or looped structure and (f) neat elastomer.

The Raman spectra of the GNPs are shown in the **Figure 3.5** (a). The G (~1580 cm^{-1}) and 2D bands (~2680 cm^{-1}) are well defined for all types of the nanoplatelets, consistent with the signature of graphitic structures. The 2D bands are broad and asymmetric suggesting that the nanoplatelets consist of many layers of graphene [10, 29, 30]. Moreover, broad and weak D bands can be observed at ~ 1360 cm^{-1} which is an indication of defects that are present in the structure. The XRD patterns of GNPs are also shown in **Figure 3.5** (b), which display the sharp and strong peaks at $2\theta \approx 26°$ consistent with reflections from the (002) plane of graphite, while weak peaks can be seen at $2\theta \approx 42.1, 44.3$ and $54.4°$ corresponding to reflections from (100), (010) and (004) planes, respectively.
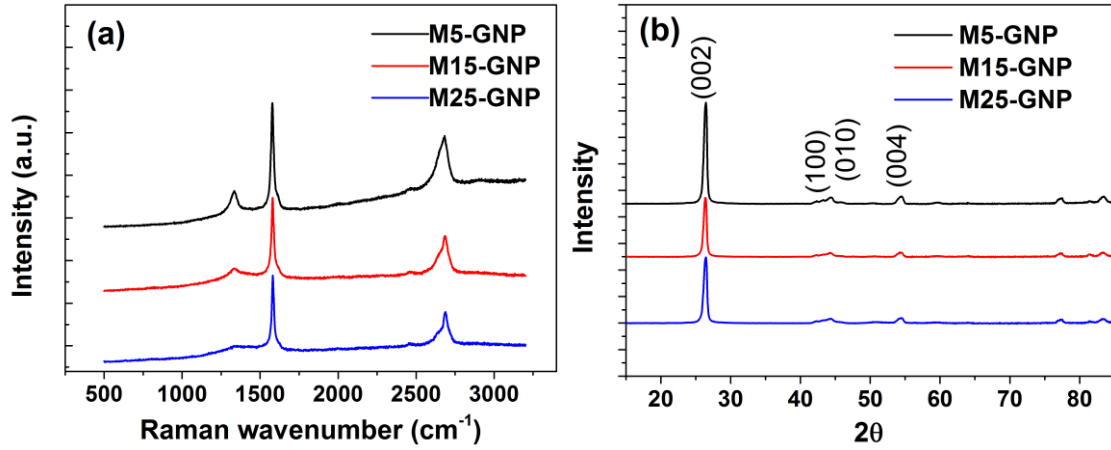
Figure 3.5 (a) Raman spectra and (b) XRD patterns of M5, M15 and M25 GNPs.

3.3.2 Characterisation of the Composites

Thermogravimetric analysis was employed initially to determine the actual volume fractions of the fillers after the preparation procedure. The mass residue and volume fractions of the filler in the prepared composites are given in **Table 3.1**. The volume fraction was calculated by: $V_f = \frac{w_f \rho_m}{w_f \rho_m + (1-w_f)\rho_f}$, where w_f is the mass fraction of the filler, ρ_m ($=1.08$ g/cm^3) and ρ_f ($=2.2$ g/cm^3) are the densities of the matrix and the filler, respectively. It can be seen that the final mass fractions were very close to the nominal mass fractions of the nanocomposites. Representative TGA curves for Alcryn 2265 samples filled with M5, M15 and M25 GNPs are shown in **Figure 3.6** (a-c). **Figure 3.6** (d) shows 2265-M15 TGA curves from 500 to 600 °C, which is used as an example to show the calculation of the mass fractions of the nanocomposites samples. As can be seen from **Figure 3.6** (d), the mass residue of the 2265-neat samples is close to 5% (4.3%), which is the carbonaceous residue of the polymer. For the filled samples, the polymers should also have approximately 5% residue at this temperature. For the nanocomposites samples, the 100% mass at the room temperature is given by the mass fraction of the GNP and the polymer. At 500-600 °C when the polymer is fully degraded, the mass residue is given by the mass fraction of the GNP and the carbonaceous residue of the polymer, which is approximately 5% of the polymer fraction of the nanocomposites. Take the 2265-M15-GNP20 shown in **Figure 3.6** (d) as an example, GNP wt% = 100% - polymer wt%, and

101

(polymer wt%)×4.3% + GNP wt% = mass residue (24.1%). Hence, for this sample, (1-GNP wt%)×4.3% + GNP wt% = 24.1% and therefore the mass fraction of GNP for this sample is calculated to be 20.7%.

Table 3.1 Mass and volume fractions of GNP for each composite sample.

Materials	Mass fraction (%)	GNP volume fraction (%)
2265 neat	0	0
2265-M5-GNP1	1.9 ± 0.04	0.95 ± 0.02
2265-M5-GNP5	5.14 ± 0.18	2.57 ± 0.09
2265-M5-GNP10	11.04 ± 1.32	5.52 ± 0.66
2265-M5-GNP20	21.64 ± 0.10	10.82 ± 0.05
2265-M15-GNP1	1.07 ± 0.03	0.53 ± 0.02
2265-M15-GNP5	5.46 ± 0.06	2.73 ± 0.03
2265-M15-GNP10	12.42 ± 0.06	6.21 ± 0.03
2265-M15-GNP20	20.6 ± 0.40	10.3 ± 0.20
2265-M25-GNP1	0.81 ± 0.15	0.4 ± 0.08
2265-M25-GNP5	4.87 ± 0.59	2.44 ± 0.30
2265-M25-GNP10	9.75 ± 0.21	4.88 ± 0.11
2265-M25-GNP20	20.94 ± 0.31	10.47 ± 0.16

The cross-sectional surfaces of cryo-fractured dumbbell samples were investigated by SEM as shown in **Figure 3.7**. The low magnification images of the composites with highest loading (20 wt%) **Figures 3.7** (a-c) indicate that a uniform distribution of the fillers was achieved even at high filler contents. The observation of different regions of the cross-section, reveals a distinct alignment of the fillers, which was induced by the shear rate distribution during the injection moulding procedure, known as a fountain flow mechanism [28, 31]. The orientation of nanoplatelets due to the fountain flow mechanism in the case of the samples can be seen in **Figure 3.8**. There are regions within the samples with different degrees of orientation of the fillers, due to the variation of shear rate

generated by the combination of the injection pressure and the slightly lower temperature of the mould walls [28, 31].
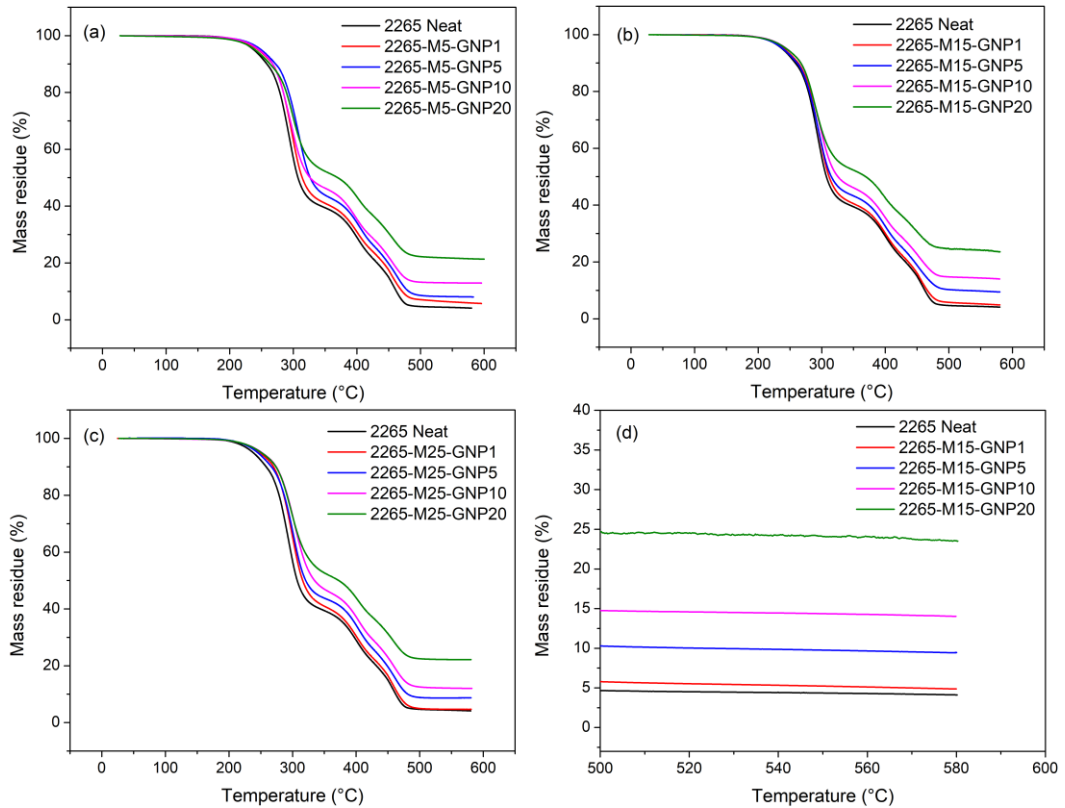
Figure 3.6 Representative TGA curves for Alcryn 2265 samples filled with (a) M5, (b) M15 and (c) M25 GNPs; (d) TGA curves of 2265-M15 samples from 500 to 600 °C.

The high magnification SEM images (**Figures 3.7** d-f) demonstrate the morphologies of the individual flakes within the matrix. Generally, the interface between the matrix and the nanoplatelets is intact, without voids or gaps, which is expected to contribute to a higher reinforcement efficiency. Interestingly, the shorter flakes tend to be flat and embedded in the matrix, as shown in **Figure 3.7** (d), while on the other hand, the larger ones can be seen bent or form looped-folded morphologies as shown in **Figures 3.7** (e) and (f). It is believed that the large flakes retain their morphologies after processing. The looped-folded morphologies, as also shown in **Figures 3.7** (d) and (e) before processing, were formed during the production of the GNPs that introduced high pressure and

temperature. In addition, it can be also seen that the flakes tend to restack and form agglomerates, which will reduce the reinforcing efficiency.
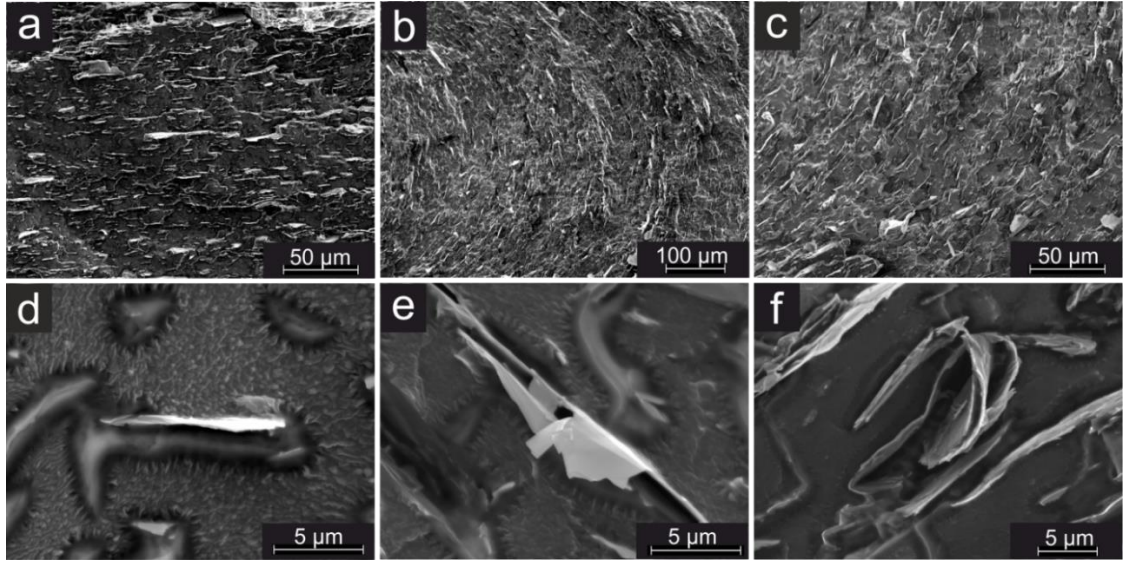
Figure 3.7 SEM images of cryo-fractured cross-section of the injection moulded composites: (a-c) low magnification images of the composites (2265-M5-GNP20) showing preferred orientation of the flakes in accordance with fountain flow mechanism; (e-f) High magnification images of M5, M15 and M25 GNPs in the composites showing the interface between the filler and the matrix and preferred morphologies dependent on the sizes of the fillers.

3.3.3 Polarised Raman Spectroscopy

Since it is obvious from SEM that the flakes have a preferred alignment, it is possible to quantify the orientation factor using polarised Raman spectroscopy [14]. Different regions across the cryo-fractured cross-sections of the samples were studied by using a rotation stage. Because the sample was ~5 mm in width and ~1.5 mm in thickness, the tests were carried out stepwise, every 0.25 mm from the edge to the centre of the cross-sections in the perpendicular direction of the dumbbell surfaces and the test track lines are equidistant and parallel to the two parallel sides of the rectangular cross-sections (red dash lines in both **Figures 3.3 and 3.9**).
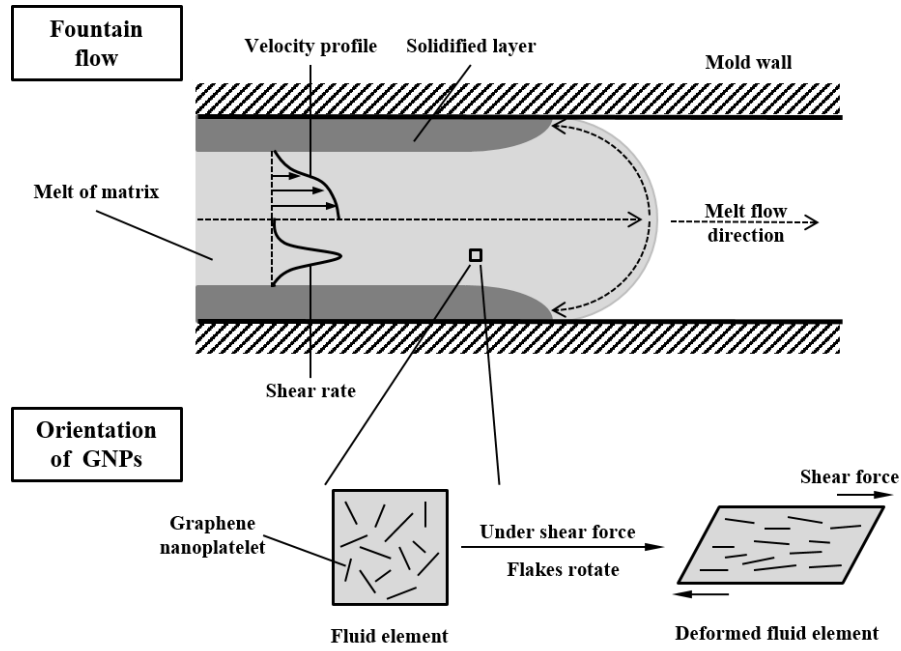
Figure 3.8 Fountain flow mechanism of the injection moulding.
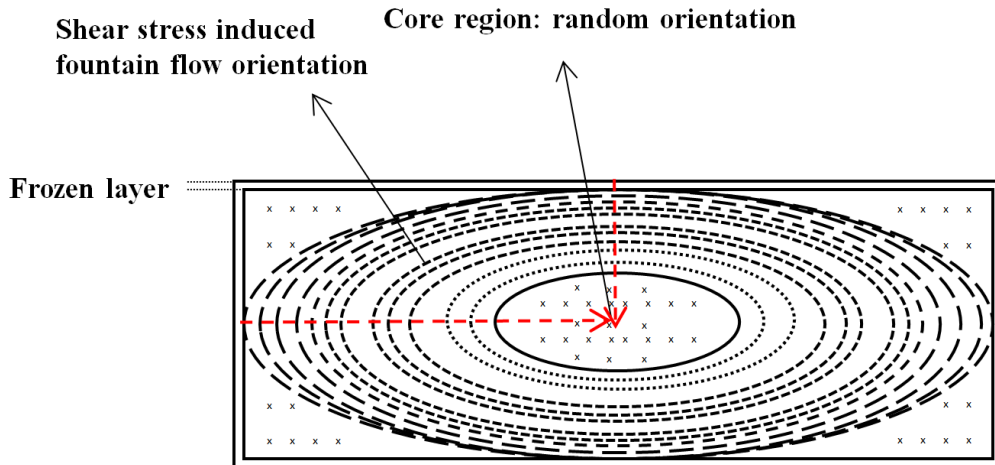
Figure 3.9 Schematic diagram of the flake orientation on the cross-sectional surface for nanocomposites.

From the results shown in **Figure 3.10** (a), it can be seen that when the laser is polarised parallel to the Z axis, there is no change in G band intensity with the rotation of Φ_Z, indicating no preferred orientation. In contrast, the G band intensity decreases from 0° to 90° and subsequently increases from 90° to 180° when the sample is rotated around the

X axis (shown in **Figure 3.10** b for the M5 GNP sample), which is an indication that the flakes tend to be oriented along the *X* axis. The calculated average orientation factor can be used to evaluate the effect of orientation on the reinforcing efficiency of the filler [14, 27]. The $<P_2 (\cos\theta)>$ and $<P_4 (\cos\theta)>$ values described in detail in Refs. [14, 27] are obtained by the *X* axis tests along with the curve fitting using equation (3.1).

$$I_{sample}(\varPhi)=I_o\left\{\frac{8}{15}+\langle P_2(\cos\theta)\rangle(-\frac{16}{21}+\frac{8}{7}\cos^2\varPhi)+\langle P_4(\cos\theta)\rangle(\frac{8}{35}-\frac{8}{7}\cos^2\varPhi+\cos^4\varPhi)\right\} \tag{3.1}$$

where I_o is the amplitude and assuming the surface normals are uniformly distributed around the Z-axis.
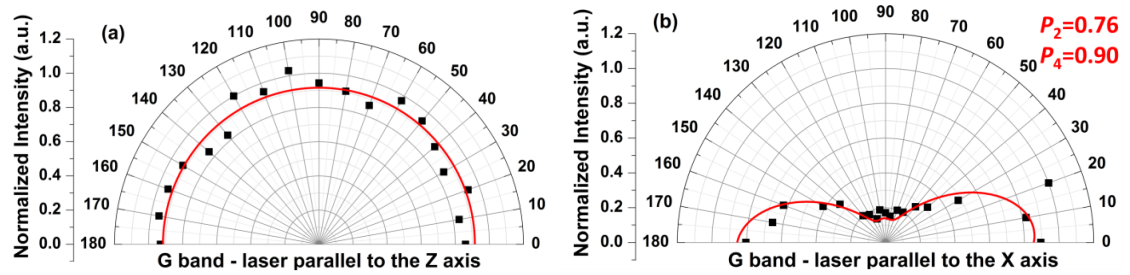
Figure 3.10 Representative fitting of normalized G band intensities parallel to the (a) Z and (b) X axis as a function of rotational angle for M5 GNPs.

Subsequently, the orientation factor η_o is given by:

$$\eta_o=\frac{8}{15}+\frac{8}{21}\langle P_2(\cos\theta)\rangle+\frac{3}{35}\langle P_4(\cos\theta)\rangle \tag{3.2}$$

The orientation factors for all samples were then calculated using equation (3.2), and the results are plotted in **Figure 3.11** (a-c) and listed in **Tables 3.2-3.4**. It is apparent that when moving from the edge to the centre of the cross-section, $<P_2 (\cos\theta)>$ increases and then decreases, which points out the actual variation of the orientation degrees in different regions. The results were consistent for all types of GNPs in this experiment. This trend is also in accordance with the SEM results, presented in **Figures 3.7** (a-c) and the shear rate profile reported in early studies on injection moulded polymer samples [28, 31]. In

this experiment, the calculated average orientation factors are 0.76, 0.69 and 0.62 for M5, M15, and M25, respectively. The orientation factor values clearly imply that the degree of orientation decreases with increasing flake size, due to looped and folded morphologies of the larger diameter flakes, which is in agreement with the results reported by Li *et al.* on GNP-reinforced natural rubbers [13].
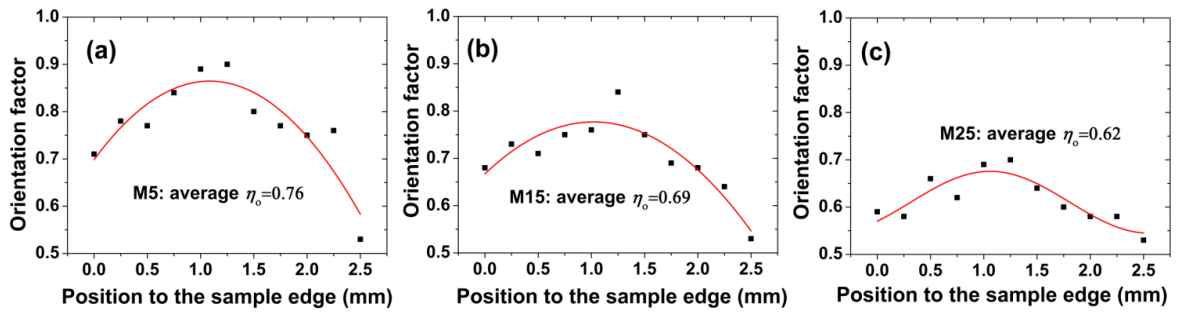
Figure 3.11 Orientation degrees of (a-c) M5, M15 and M25 samples showing variation of the orientation factor against the position of the test spots.

Table 3.2 Orientation factors for M5 samples

Position from the edge of the sample (mm)		P_2	P_4	η_o
	0	0.46	0.1	0.71
	0.25	0.48	0.78	0.78
	0.5	0.46	0.77	0.77
	0.75	0.61	0.92	0.84
	1	0.73	0.89	0.89
Horizontally	1.25	0.76	0.9	0.9
	1.5	0.5	0.88	0.8
	1.75	0.44	0.76	0.77
	2	0.46	0.51	0.75
	2.25	0.45	0.69	0.76
	2.5	0	0	0.53
	0	0.41	0.75	0.75
Vertically	0.25	0.61	0.84	0.84
	0.5	0.64	0.45	0.82
	0.75	0	0	0.53

Table 3.3 Orientation factors for M15 samples.

Position from the edge of the sample (mm)	P_2	P_4	η_o
0	0.24	0.6	0.68
0.25	0.38	0.58	0.73
0.5	0.37	0.45	0.71
0.75	0.46	0.46	0.75
1	0.51	0.41	0.76
Horizontally 1.25	0.62	0.84	0.84
1.5	0.46	0.5	0.75
1.75	0.26	0.69	0.69
2	0.37	0.05	0.68
2.25	0.21	0.31	0.64
2.5	0	0	0.53
0	0.33	0.55	0.71
Vertically 0.25	0.52	-0.06	0.73
0.5	0.42	-0.16	0.68
0.75	0	0	0.53

Table 3.4 Orientation factors for M25 samples.

Position from the edge of the sample (mm)	P_2	P_4	η_o
0	0.289	0.247	0.66
0.25	0.217	0.026	0.62
0.5	0.328	0.345	0.69
0.75	0.334	0.482	0.7
1	0.263	0.081	0.64
Horizontally 1.25	0.156	0.139	0.6
1.5	0.178	-0.038	0.59
1.75	0.125	0.023	0.58
2	0.106	0.094	0.58
2.25	0.125	0.003	0.58
2.5	0	0	0.53
0	0.26	-0.29	0.61
Vertically 0.25	0.138	0.088	0.64
0.5	0.213	0.273	0.59
0.75	0	0	0.53

3.3.4 Mechanical Testing

Tensile testing was used to evaluate the mechanical properties of the materials. The stress-strain behaviour of all injection moulded samples is presented in **Figure 3.12** (a). It can be seen that the addition of GNPs up to ~10 vol% increases the stiffness and tensile strength of the thermoplastic elastomer significantly. Overall, larger flakes are more efficient in increasing the modulus, whereas the smaller flakes contribute to better tensile strength enhancements. It is also apparent that the addition of GNPs results in a reduction of strain at failure.

The initial Young's modulus values are plotted against the volume fractions of the fillers in **Figure 3.12** (b). As expected, in all cases, the modulus increases significantly with increasing GNP content. The modulus values of the composites are up to ~6 times higher (at 20 wt% filler loading) compared with the matrix, indicating the stiffening effect of the fillers. The reinforcement mechanism of graphene in composites is attributed to the interfacial stress transfer from the matrix to the flakes; larger platelets resulting in larger aspect ratio are beneficial for stress transfer on the basis of the well-established shear-lag theory [10, 32].

Tensile strength and strain at failure values are also plotted against GNP volume fractions in **Figure 3.12** (c-d). The tensile strength increases with increasing GNP loading, indicating a strong interaction between the fillers and the matrix. It has been reported that the wrinkled structure of graphene flakes can improve the tensile strength by acting as a crack propagation barrier and improve the mechanical interlocking between the matrix and the filler [33]. It can be clearly seen that the tensile strength enhancement is dependent significantly upon the flake size, particularly at high filler loadings. Tensile strength is known to depend heavily on the dispersion characteristics [15]; therefore these results indicate higher degree of aggregation of larger flakes at higher loadings and looped/folded flake morphologies similar to the ones seen in **Figure 3.7** (e and f). The strain at failure declines significantly with increasing filler fraction. Similar results have been observed

not only for elastomeric nanocomposites but almost all polymer nanocomposites where agglomerated fillers act as failure points during elongation [9].
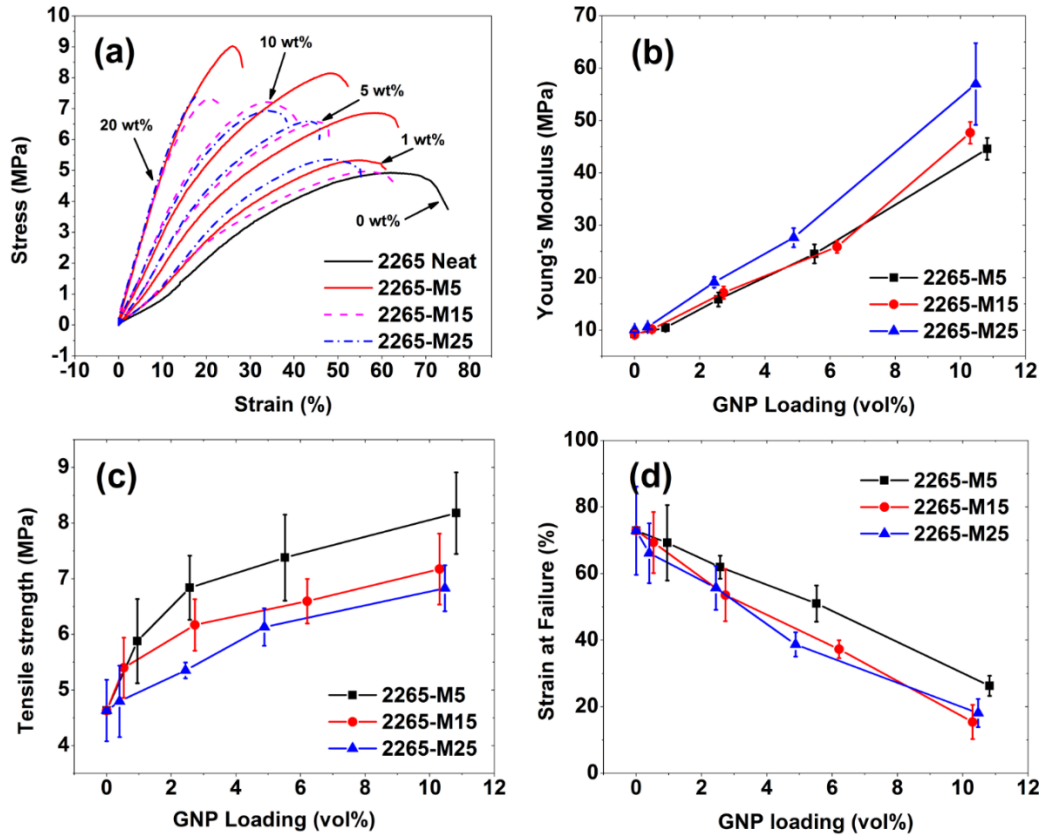
Figure 3.12 (a) Stress-strain curves of the materials; (b-d) Plots of the values of stiffness, tensile strength and strain at failure against volume fractions of the GNPs.

3.3.5 Raman 2D Band Shifts

Raman spectroscopy has been proven to be a very effective technique in assessing the stress transfer efficiency from the matrix to any type of carbon-based reinforcement [10, 12, 13, 15, 17, 34-42]. The samples with the highest amount of filler (20 wt%) were strained *in situ* under a Raman spectrometer and the characteristic shifts of the Raman bands were recorded with increasing strain. The slope of the band shifts at different strain levels represents the stress transfer efficiency between the matrix and the filler. A representative example of the shift of the 2D band for the composite filled with M15

flakes, can be seen in **Figure 3.13** (a) For each composite reinforced by M5, M15 and M25 nanoplatelets, 5 samples were tested, in order to give the average values shown in **Figure 3.13** (b-d). It was shown that the flakes display very low 2D band shifts, with obvious scattering on the linear curve fitting, indicating the significantly lower stress transfer efficiency of this elastomeric material than the stiffer matrices of previous studies [12, 14, 35] but higher than softer matrices such as natural rubber [13]. The small values of the slope indicate the low effective modulus of GNPs within the TPE matrix, compared with pristine graphene (-60 cm^{-1}/% strain for the 2D band that corresponds to a modulus of 1050 GPa) [10, 11]. This is because the interfacial stress transfer efficiency in graphene nanocomposites depends upon the stiffness of the matrix (the effective modulus of graphene increases with increasing stiffness of the matrix), as discussed in a previous study [17].
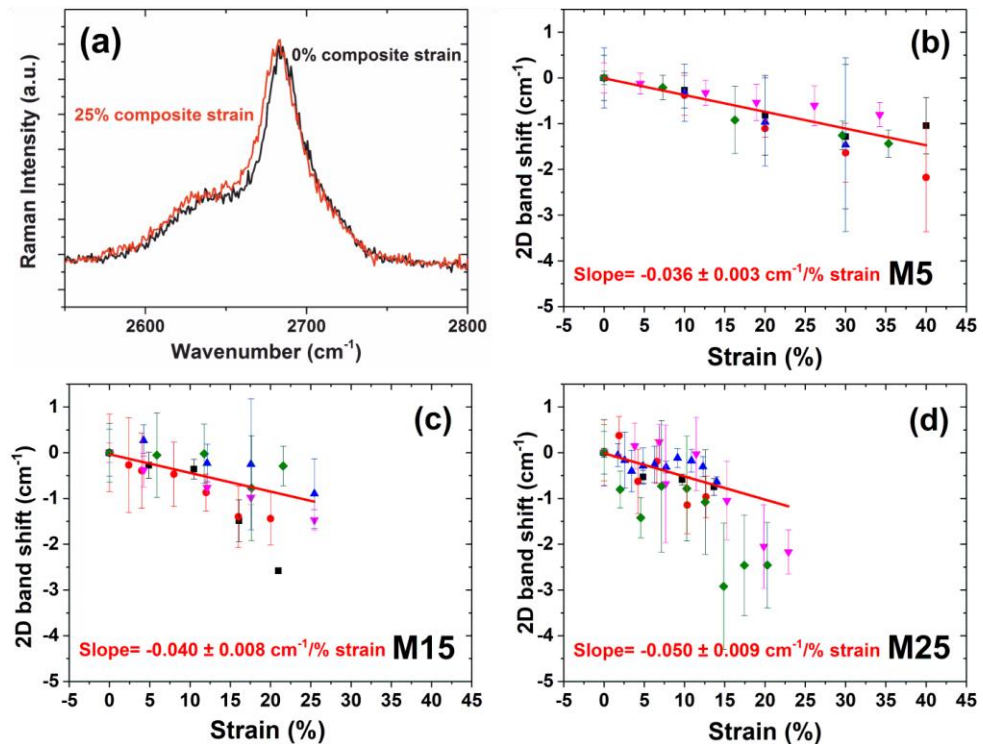
Figure 3.13 (a) Representative 2D Raman bands at 0 and 25% strain; (b-d) 2D Raman band shifts of M5, M15 and M25 flakes respectively against the composite strain. Different colours represent different sets of measurements. The fittings were carried out based on all measurements for each type of GNP.

111

3.4 Discussion

3.4.1 Micromechanics of Reinforcement

The effect of the addition of GNPs upon the stiffness of the elastomer can be evaluated by an equation that was recently developed, which is the result of the simultaneous use of the rule-of-mixtures along with the well-accepted shear-lag theory [17], as reviewed in **Chapter 2, Section 2.1.2**. The modulus of the composite is given by:

$$E_c \approx E_m (1 - V_f + \frac{s^2}{12} \frac{\eta_o}{(1+v)} V_f^2)$$
(3.3)

where V_f is the volume fraction of the filler, E_m and E_f are the Young's Modulus of the matrix and the filler, respectively; s is the aspect ratio of the filler in the composites; η_o is the orientation factor of the GNPs and v is the Poisson's ratio of the matrix. Equation (3.3), same as equation (2.13) in **Chapter 2**, reveals that for soft materials the composite modulus is only dependent on V_f and s^2 and independent of the filler modulus ($E_m > 500$ MPa) [17]. This fact allows us to focus on the effective aspect ratio s_{eff} of the reinforcement, since the formation of agglomerates and the bending/folding of the flakes during processing affects the nanoplatelets critically. The results of the fitting of the experimental data with the above equation can be seen in **Figure 3.11** (a-c), where s_{eff} was the floating parameter. Equation (3.3) has similarities with the equation suggested by the Guth-Gold-Smallwood (GGS) theory [43, 44], as reviewed in **Chapter 2, Section 2.1.1**, in which the modulus of the composites is given by:

$$E_c = E_m (1 + 0.67 f V_f + 1.62 f^2 V_f^2)$$
(3.4)

where f is length/breadth of the platelet-like or rod-like filler, which can be considered analogous to the aspect ratio of the filler. Equation (3.4) is same as equation (2.4) in

Chapter 2. The fitting of the experimental data with the GGS theory can be seen in **Figure 3.14** (d-f).

Both equations fit the experimental results quite well and the effective aspect ratio of the fillers increases systematically from M5 to M15 to M25, attributing better enhancement to the stiffness of the composites. However, the values are significantly lower than the ones expected, which should be in the order of 10^3, based on the dimensions of the nanoplatelets measured in a previous study [17]. The reason for the relatively small values of aspect ratio can be attributed to the restacking and agglomeration of the flakes that is unavoidable to the additional presence of looped and folded flakes in the composites, that can pre-exist in the batches of the nanoplatelets or can also originate from the shear forces applied to the flakes during melt mixing/injection moulding. As shown in **Figure 3.7** (f), the looped/folded flakes can even form hollow structures, resulting in significant reductions of the aspect ratio values.
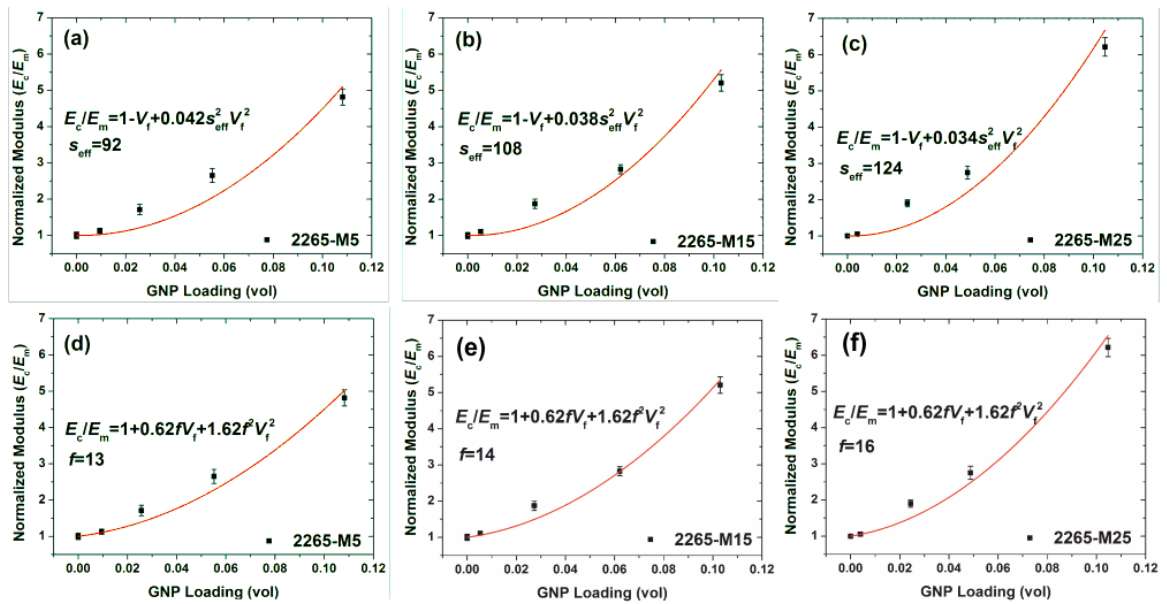
Figure 3.14 Normalized Young's Modulus against the volume fraction of the filler and fitted data using equation (3.3) for (a) 2265-M5, (b) 2265-M15 and (c) 2265-M25 samples; and fitted using equation (3.4) for (d) 2265-M5, (e) 2265-M15 and (f) 2265-M25.

The fitted values of the effective aspect ratio for both equations can be used to evaluate the reinforcing efficiency of the GNPs. Nevertheless, the Guth-Gold-Smallwood theory is based on the effect of pairs of spherical fillers [43, 44], which is an analogy of rod-like fillers, rather than relatively thin nanoplatelets. This is why the fitted aspect ratio *f*, obtained from the GGS equation is significantly lower than that of the GNP flakes. Moreover, from **Figure 3.14** it can be seen that the normalized modulus of the nanocomposites filled with 5 wt% and 10 wt% lie above the expected theoretical values. This observation indicates one simple equation may not be able explain all the results. The phenomenon will be discussed in detail in the next Chapter.

3.4.2 Stress-induced 2D Raman Band Shifts

It was reviewed in **Chapter 1 & 2** that on the basis of the shear-lag theory, for soft matrices reinforced by graphene nanoplatelets, the Young's modulus of the flakes obtained from Raman experiments (E_R) is higher than the filler modulus (E_f) obtained from tensile testing [17]. The Raman modulus of the graphene flakes is given by:

$$E_R = -\frac{d\omega_{2D}}{d\varepsilon} \frac{1050}{-60} \, \text{GPa} \tag{3.5}$$

where $-d\omega_{2D}/d\varepsilon$ is the 2D Raman band shift rate per % composite strain for any type of graphene. The filler modulus from tensile tests, according to the simple rule of mixtures can be calculated by

$$E_f = \frac{E_c - E_m(1 - V_f)}{V_f} \tag{3.6}$$

where V_f is the volume fraction of the filler, E_m and E_c are the Young's modulus of the matrix and the filler, respectively. The theoretical values of E_f and E_R derived by shear lag theory are given by [17],

$$E_{\text{f}} \approx \eta_{\text{o}} \frac{s^2}{12} \frac{1}{1+\nu} \frac{t}{T} E_{\text{m}} \qquad\qquad (3.7)$$

and

$$E_{\text{R}} \approx \eta_{\text{o}} \frac{s^2}{8} \frac{1}{1+\nu} \frac{t}{T} E_{\text{m}} \qquad\qquad (3.8)$$

where t is the thickness of the flake and T is the thickness of the polymer layer surrounding the flake in the model nanocomposite. Equations (3.7) and (3.8) predict that the Raman modulus is higher than the filler modulus obtained from tensile testing that were reviewed in **Chapter 2, Section 2.1.2**. If we take the $E_{\text{R}}/E_{\text{f}}$ ratio from the two equations, then $E_{\text{R}} \approx 1.5 E_{\text{f}}$. The experimental data of E_{R} and E_{f} from the samples with the highest filler contents are all listed in Table 5. The experimentally obtained values of E_{R} and E_{f} reveal that the effective modulus of graphene within this quite soft TPE matrix ($E_{\text{m}} \approx 10$ MPa) is in the order of hundreds of MPa, which is three to four orders of magnitude lower than the intrinsic modulus of monolayer graphene (1050 GPa) [10, 11]. The reason for the low E_{f} and E_{R} values is that the shear modulus of the elastomeric matrix is very low; therefore, the shear stress transferred from the matrix to the flakes through the TPE/GNP interface, according to the shear lag theory, is relatively low [13, 17]. Based on this, even though the absolute enhancement of the mechanical properties of soft materials in terms of percentage is almost always impressive, the superlative mechanical properties of graphene and graphene nanoplatelets are not realised in these systems.

It should also be stated that the Raman band shift experiments were carried out probing flakes axially aligned on the sample surface. This means that the flakes that were tested should be considered nearly perfectly orientated ($\eta_{\text{o}} \approx 1$), whereas the calculated filler modulus E_{f} values have actually taken the orientation factors of the bulk composites into account. Therefore, the actual relationship between experimental E_{R} and E_{f} should be given by,

$$E_R \approx 1.5 E_f / \eta_o \tag{3.9}$$

where η_o is the overall orientation factor of the bulk composites.

The results from the use of the $E_R \approx 1.5 E_f / \eta_o$ relationship show good consistency with the measured E_R values (**Table 3.5**) especially for smaller flakes and the differences between the data can originate either from disoriented flakes that have been tested or due to the rough and wrinkled surface of the nanoplatelets [45]. Another factor of discrepancy can be the length effects that are known to reduce the efficiency of reinforcement from the nanoplatelets. The agreement between the theoretical and experimental values is another indication that the orientation factor calculated from the polarised Raman experiments are very close to reality, for the bulk composites.

Table 3.5 Raman 2D band shift values and the corresponding calculated Raman modulus along with the filler modulus acquired from the tensile testing. E_R and E_f at 20 wt% GNP loading are calculated using equation (3.5) and (3.6), respectively. $1.5 E_f / \eta_o$ is the theoretically calculated E_R (assuming the flake is perfectly aligned) based on equation (3.7), (3.8) and (3.9).

	M5	M15	M25
Band shift (cm^{-1}/% strain)	-0.036 ± 0.003	-0.040 ± 0.005	-0.050 ± 0.006
E_R (MPa)	630 ± 53	700 ± 88	875 ± 105
E_f (MPa)	336 ± 37	383 ± 40	457 ± 111
Theoretical E_R ($1.5 E_f / \eta_o$ (MPa))	663 ± 74	833 ± 87	1106 ± 269

3.5 Conclusion

A thermoplastic elastomer based on amorphous polymer blends (Alcryn®) was prepared successfully by melt mixing with graphene nanoplatelets. The eventual nanocomposites moulded by injection moulding showed homogeneous dispersion along with preferred

orientation of the filler at the axial direction. Raman spectroscopy were used to analyse the interface and found that the stress transfer efficiency is highly dependent upon the shear modulus of the matrix. For elastomers possessing a low shear modulus, the stress transfer is therefore not as efficient as stiff polymer. Analytical models were employed to understand the mechanisms of reinforcement of elastomers by graphene nanoplatelets and indicated that the crucial factors determining the mechanical improvement are orientation, aspect ratio and volume fraction of the filler.

References

[1] Akkapeddi M. Commercial polymer blends. Polymer blends handbook: Springer; 2003. p. 1023-115.

[2] Drobny JG. Handbook of thermoplastic elastomers: Elsevier; 2014.

[3] Costa P, Silva J, Sencadas V, Simoes R, Viana J, Lanceros-Méndez S. Mechanical, electrical and electro-mechanical properties of thermoplastic elastomer styrene–butadiene–styrene/multiwall carbon nanotubes composites. Journal of Materials Science. 2013;48(3):1172-9.

[4] Frogley MD, Ravich D, Wagner HD. Mechanical properties of carbon nanoparticle-reinforced elastomers. Composites Science and Technology. 2003;63(11):1647-54.

[5] Katbab A, Nazockdast H, Bazgir S. Carbon black-reinforced dynamically cured EPDM/PP thermoplastic elastomers. I. Morphology, rheology, and dynamic mechanical properties. Journal of Applied Polymer Science. 2000;75(9):1127-37.

[6] Khan U, May P, O'Neill A, Coleman JN. Development of stiff, strong, yet tough composites by the addition of solvent exfoliated graphene to polyurethane. Carbon. 2010;48(14):4035-41.

[7] Koerner H, Price G, Pearce NA, Alexander M, Vaia RA. Remotely actuated polymer nanocomposites—stress-recovery of carbon-nanotube-filled thermoplastic elastomers. Nature Materials. 2004;3(2):115-20.

[8] Novoselov KS, Geim AK, Morozov SV, Jiang D, Zhang Y, Dubonos SV, Grigorieva IV, Firsov AA. Electric field effect in atomically thin carbon films. Science. 2004;306(5696):666-9.

[9] Papageorgiou DG, Kinloch IA, Young RJ. Graphene/elastomer nanocomposites. Carbon. 2015;95:460-84.

[10] Gong L, Kinloch IA, Young RJ, Riaz I, Jalil R, Novoselov KS. Interfacial stress transfer in a graphene monolayer nanocomposite. Advanced Materials. 2010;22(24):2694-7.

[11] Lee C, Wei X, Kysar JW, Hone J. Measurement of the elastic properties and intrinsic strength of monolayer graphene. Science. 2008;321(5887):385-8.

[12] Ahmad SR, Xue C, Young RJ. The mechanisms of reinforcement of polypropylene by graphene nanoplatelets. Materials Science and Engineering: B. 2017;216:2-9.

[13] Li S, Li Z, Burnett TL, Slater TJ, Hashimoto T, Young RJ. Nanocomposites of graphene nanoplatelets in natural rubber: microstructure and mechanisms of reinforcement. Journal of Materials Science. 2017;52(16):9558-72.

[14] Li Z, Young RJ, Wilson NR, Kinloch IA, Vallés C, Li Z. Effect of the orientation of graphene-based nanoplatelets upon the Young's modulus of nanocomposites. Composites Science and Technology. 2016;123:125-33.

[15] Papageorgiou DG, Kinloch IA, Young RJ. Mechanical properties of graphene and graphene-based nanocomposites. Progress in Materials Science. 2017;90:75-127.

[16] Young RJ, Kinloch IA, Gong L, Novoselov KS. The mechanics of graphene nanocomposites: a review. Composites Science and Technology. 2012;72(12):1459-76.

[17] Young RJ, Liu M, Kinloch IA, Li S, Zhao X, Vallés C, Papageorgiou DG. The mechanics of reinforcement of polymers by graphene nanoplatelets. Composites Science and Technology. 2018;154:110-6.

[18] Lacayo-Pineda J. Filler Dispersion and Filler Networks. Encyclopedia of Polymeric Nanomaterials. 2015:771-6.

[19] De S, Bhowmick AK. Thermoplastic elastomers from rubber-plastic blends: Ellis Horwood; 1990.

[20] Utracki LA. Commercial polymer blends: Springer Science & Business Media; 2013.

[21] Chanda M, Roy SK. Plastics fabrication and recycling: CRC Press; 2008.

[22] De SK, White JR. Rubber technologist's handbook: iSmithers Rapra Publishing; 2001.

[23] Olabisi O, Adewale K. Handbook of thermoplastics: CRC press; 2016.

[24] Legge NR, Holden G, Schroeder H. Thermoplastic elastomers: a comprehensive review. Carl Hanser Verlag, Kolbergerstr 22, D-8000 Munchen 80, FRG, 1987 574. 1987.

[25] Loomis GL, Statz RJ. Thermoplastic elastomeric compositions based on compatible blends of an ethylene copolymer and vinyl or vinylidene halide polymer. Google Patents; 1986.

[26] Akkapeddi M. Commercial Polymer Blends. Polymer Blends Handbook: Springer; 2014. p. 1733-883.

[27] Li Z, Young RJ, Kinloch IA, Wilson NR, Marsden AJ, Raju APA. Quantitative determination of the spatial orientation of graphene by polarized Raman spectroscopy. Carbon. 2015;88:215-24.

[28] Kenig S. Fiber orientation development in molding of polymer composites. Polymer composites. 1986;7(1):50-5.

[29] Ferrari AC, Meyer JC, Scardaci V, Casiraghi C, Lazzeri M, Mauri F, Piscanec S, Jiang D, Novoselov KS, Roth S, Geim AK. Raman spectrum of graphene and graphene layers. Physical review letters. 2006;97(18):187401.

[30] Malard L, Pimenta M, Dresselhaus G, Dresselhaus M. Raman spectroscopy in graphene. Physics Reports. 2009;473(5):51-87.

[31] Tadmor Z. Molecular orientation in injection molding. Journal of Applied Polymer Science. 1974;18(6):1753-72.

[32] Cox H. The elasticity and strength of paper and other fibrous materials. British Journal of Applied Physics. 1952;3(3):72.

[33] Wakabayashi K, Pierre C, Dikin DA, Ruoff RS, Ramanathan T, Brinson LC, et al. Polymer−Graphite Nanocomposites: Effective Dispersion and Major Property Enhancement via Solid-State Shear Pulverization. Macromolecules. 2008;41(6):1905-8.

[34] Deng L, Eichhorn SJ, Kao C-C, Young RJ. The effective Young's modulus of carbon nanotubes in composites. ACS Applied Materials & Interfaces. 2011;3(2):433-40.

[35] Papageorgiou DG, Kinloch IA, Young RJ. Hybrid multifunctional graphene/glass-fibre polypropylene composites. Composites Science and Technology. 2016;137:44-51.

[36] Tanaka F, Okabe T, Okuda H, Ise M, Kinloch IA, Mori T, Young RJ. The effect of nanostructure upon the deformation micromechanics of carbon fibres. Carbon. 2013;52:372-8.

[37] Vallés C, Kinloch IA, Young RJ, Wilson NR, Rourke JP. Graphene oxide and base-washed graphene oxide as reinforcements in PMMA nanocomposites. Composites Science and Technology. 2013;88:158-64.

[38] Vilatela J, Deng L, Kinloch I, Young R, Windle A. Structure of and stress transfer in fibres spun from carbon nanotubes produced by chemical vapour deposition. Carbon. 2011;49(13):4149-58.

[39] Young RJ. Carbon Fibre Composites: Deformation micromechanics analysed using Raman spectroscopy. Structure and Multiscale Mechanics of Carbon Nanomaterials: Springer; 2016. p. 29-50.

[40] Young RJ. Deformation Mechanisms of Carbon Fibres and Carbon Fibre Composites. The Structural Integrity of Carbon Fiber Composites: Springer; 2017. p. 341-57.

[41] Young RJ, Deng L. Carbon Nanotubes and Nanotube-Based Composites: Deformation Micromechanics. Structure and Multiscale Mechanics of Carbon Nanomaterials: Springer; 2016. p. 51-74.

[42] Young RJ, Deng L, Wafy TZ, Kinloch IA. Interfacial and internal stress transfer in carbon nanotube based nanocomposites. Journal of Materials Science. 2016;51(1):344-52.

[43] Guth E. Theory of filler reinforcement. Journal of Applied Physics. 1945;16(1):20-5.

[44] Smallwood HM. Limiting law of the reinforcement of rubber. Journal of Applied Physics. 1944;15(11):758-66.

[45] Li Z, Kinloch IA, Young RJ, Novoselov KS, Anagnostopoulos G, Parthenios J, Galiotis C, Papagelis K, Lu CY, Britnell L. Deformation of wrinkled graphene. ACS Nano. 2015;9(4):3917-25.

Chapter 4. Modelling Mechanical Percolation in Graphene-reinforced Elastomer Nanocomposites[*]

* Contributions to the publication (author name order of the publication): Mufeng Liu: experiments, data analysis, propose of the theory and writing of the manuscript; Ian A. Kinloch & Robert J. Young: final proof-reading and discussion; Dimitrios G. Papageorgiou: help with the mixing, proof-reading and discussion of the manuscript.

4.1 Introduction

Thermoplastic elastomers (TPEs) based on semi-crystalline polymers account for a dominant percentage in the TPE family that utilize physical crosslinks to achieve elastomeric characteristics. They are easier to process than conventional rubbers but are limited by their poor mechanical properties relative to thermoplastics [1].

A number of micromechanical theories have been reviewed in Chapter 2 to describe the reinforcement of polymers by 2D materials. Classical theories such as the Guth-Gold theory [2] based on hydrodynamics and more modern ones, such as the jamming theory [3, 4] based on the percolation phenomenon, have been utilized to explain the stiffening mechanisms in elastomer/graphene composite systems [5, 6]. The corresponding theoretical analysis has shown good consistency with the experimental results [3, 5-9]; nevertheless, some questions still stand when moving from the microscopic to the macroscopic scales in order to explain fully the mechanisms of mechanical enhancement. In Chapter 3, the mechanisms of reinforcement of polymers by graphene nanoplatelets were established showing that for elastomers possessing low shear modulus, the reinforcing efficiency of graphene nanoplatelets is dependent upon the aspect ratio and the volume fraction of the filler, whilst virtually independent of the filler modulus (E_f) [10].

In the present Chapter, an analytical method is developed by the combining shear-lag and the rule-of-mixtures theories, along with the mechanical percolation phenomenon, in an attempt to evaluate the stiffening mechanism in TPE/GNP nanocomposites. A semicrystalline polyether block amide thermoplastic elastomer was employed to prepare nanocomposites with two types of GNPs of different lateral sizes, by melt mixing in an internal mixer. The degree of crystallinity of the matrix and the composites was obtained by differential scanning calorimetry (DSC) and X-ray diffraction (XRD). The microstructure of the nanocomposites was characterised by scanning electron microscopy (SEM), while the mechanical properties were investigated by tensile testing and *in situ* deformation under a Raman spectrometer. A detailed theoretical analysis was carried out to determine the different mechanisms and stages of mechanical reinforcement of the TPE/GNP nanocomposites produced.

4.2 Experimental Methods

4.2.1 Materials and Preparation

A commercially-available thermoplastic elastomer (Pebax® 7033) was purchased from Arkema, Inc. and used as received. Pebax® is a plasticizer-free polyether block amide. Graphene nanoplatelets (GNPs) with nominal lateral sizes of 5 and 25 μm (M5 and M25) (according to the supplier) and average thicknesses in the range of 6–8 nm were purchased from XG Sciences, Inc. Lansing, Michigan, USA and used as received. Composites with 1, 5, 10, and 20% by weight of the GNPs were prepared by melt mixing in a Thermo Fisher HAAKE Rheomix internal mixer at 220 °C and 50 rpm for 10 minutes. The lumps of composites were afterwards injection moulded in a HAAKE Minijet Piston Injection Moulding System in order to prepare dog-bone shaped specimen. Based on the fact that the nanocomposites containing the M25 GNPs displayed higher values of Young's modulus (compared to M5 GNPs), a wide range of composites with various M25 GNP loadings (1, 2.5, 3.3, 5, 6.7, 7.5, 10, 11.1, 12.5, 13.3, 15, 16.6, 17.5, 18.9, 20 wt%) were prepared additionally in order to obtain sufficient data for theoretical analysis and

modelling of the mechanical percolation phenomenon. The samples throughout the chapter will be coded based on the matrix (TPE), the lateral size and the weight content of the filler. For example, TPE-M5-GNP1 refers to the TPE matrix reinforced by 1 wt% of GNPs, whose average lateral size is 5 µm.

The selection of this particular matrix material, Pebax®, is because of its modulus (~400 MPa), which is between conventional elastomers and thermoplastics. The dependence of the reinforcing efficiency of graphene-based 2D materials on the shear modulus of the matrix can therefore be examined further, regarding the previous research [10].

4.2.2 Characterisation of the Nanocomposites

The final filler contents of GNPs in the nanocomposites were evaluated by thermogravimetric analysis (TGA) using a TA Q500 TGA instrument. The samples were heated from 25 °C to 800 °C under a 50 mL/min flow of N_2 at 10 °C/min. Three samples were tested for each material in order to ensure reproducibility of the results.

The XRD diffractograms were obtained using a PANalytical X'Pert3 diffractometer with Cu Kα radiation operated at 40 kV and 40 mA. The 2-theta angle range was selected from 5° to 90° with a step size of 0.03° and a step time of 180 s.

A TA Instruments Q100 DSC was used to investigate the melting and crystallization behaviour. Samples of about 10 mg were heated, cooled and re-heated between -90 and 200 °C using a heating/cooling rate of 10 °C/min, under a nitrogen flow of 50 ml/min.

The morphology of the neat polymer and the microstructure of the nanocomposites were examined using SEM. The images of the cryo-fractured samples were acquired using a high-resolution Philips XL30 Field Emission Gun Scanning Electron Microscope (FEGSEM) operated at 6 kV.

Stress–strain curves were obtained using dumbbell-shaped specimen in an Instron 3365 machine, under a tensile rate of 10 mm·min^{-1} with a load cell of 5 kN, in accordance with the ASTM D638 standard. An extensometer with a gauge length of 20 mm was used to measure the strain precisely.

Raman spectra were obtained using a Renishaw InVia Raman spectrometer with a laser wavelength of 633 nm and a x50 objective lens, which produces a laser spot with a diameter in the order of 1–2 μm. The Raman 2D band shift of the injection moulded samples was studied following the application of strain on the nanocomposites. The strain was applied using a four-point bending rig from 0 to ~ 2.7% and determined by a resistance strain gauge attached to the surface of samples. Spectra were taken every ~0.1 % strain. The Raman spot was focused on the same point of a single flake on each sample surface. All spectra were fitted with a single Lorentzian curve.

The spatial orientation of the nanoplatelets was quantified by polarised Raman spectroscopy. The same method was employed in a previous research work for injection moulded graphene-reinforced nanocomposites [11-13]. The equipment employed was a 514 nm Renishaw Raman spectrometer with 'VV' (vertical-vertical) polarisation, where the incident and scattered radiation were polarised in the same direction. During the experimental procedure, the laser was aligned either perpendicular or parallel to the direction of injection moulding. The intensity of the characteristic Raman G band of graphene nanoplatelets was recorded as a function of rotation angle (Φ) and the rotation angle was subsequently used for the estimation of the orientation distribution function (ODF) [12]. The tests were carried out on a number of positions along the cryo-fractured sections of the samples in order to take into account the variation of orientation across different regions in the samples.

4.3 Results

4.3.1 Volume Fraction and Degree of Crystallinity

The volume fraction of the fillers within the composites was assessed using TGA. The mass residue along with the volume fractions of the filler are given in the **Table 4.1**. The final mass fractions were very close to the nominal mass fractions of the nanocomposites. The volume fraction was calculated by: $V_f = \frac{w_f \rho_m}{w_f \rho_m + (1-w_f)\rho_f}$, where w_f is the mass fraction of the filler, ρ_m (=1.01 g/cm^3) and ρ_f (=2.2 g/cm^3) are the densities of the matrix and the filler, respectively.

Table 4.1 Mass fractions of GNPs determined by TGA for each sample and calculated volume fractions.

Materials	Mass fraction (%)	GNP volume fraction (%)
TPE	0	0
TPE-M5-GNP1	1.10 ± 0.30	0.50 ± 0.14
TPE -M5-GNP5	4.95 ± 0.14	2.31 ± 0.06
TPE -M5-GNP10	9.90 ± 0.14	4.76 ± 0.09
TPE -M5-GNP20	18.28 ± 0.20	9.23 ± 0.18
TPE -M25-GNP1	1.20 ± 0.20	0.55 ± 0.09
TPE -M25-GNP5	5.05 ± 0.03	2.36 ± 0.01
TPE -M25-GNP10	10.51 ± 0.75	5.06 ± 0.34
TPE -M25-GNP20	19.28 ± 0.82	9.79 ± 0.37

The degree of crystallinity of the neat polymer and the nanocomposites was characterised using both XRD and DSC (**Figure 4.1**). In the X-ray diffractograms, the matrix displays only one characteristic peak which is present at $2\theta \approx 21.4°$, showing a reflection from the (001) plane, corresponding to the γ phase of polyamide 12 (PA12) [14]. The XRD patterns of GNPs display a sharp and strong peak at $2\theta \approx 26°$ consistent with reflections from the

(002) plane of graphite. Moreover, the peak of the GNPs remained at the same position with increasing GNP loading, as shown in the insets of **Figure 4.1** (a) and (b). The degree of crystallinity can be calculated by $X_c = A_c/(A_c + A_\alpha)$ for XRD, where A_c and A_α are the areas under the crystalline peaks and amorphous halo, respectively. The results can be seen in **Table 4.2**. In addition, the DSC in **Figure 4.1** (c) results suggest that the melting point (T_m) of all samples is at around 160 °C and the presence of GNPs did not affect the T_m. The degree of crystallinity from DSC was calculated (shown in **Table 4.2**) from the ratio $X_c = \Delta H_f/\Delta H_f^0 \times 100\%$, where ΔH_f is enthalpy of fusion of the sample and ΔH_f^0 is the enthalpy of fusion of 100% crystalline PA12 in Pebax (65 J/g [15]). As can be understood from the application of both techniques, the presence of GNPs did not alter the crystallinity of the matrix significantly.
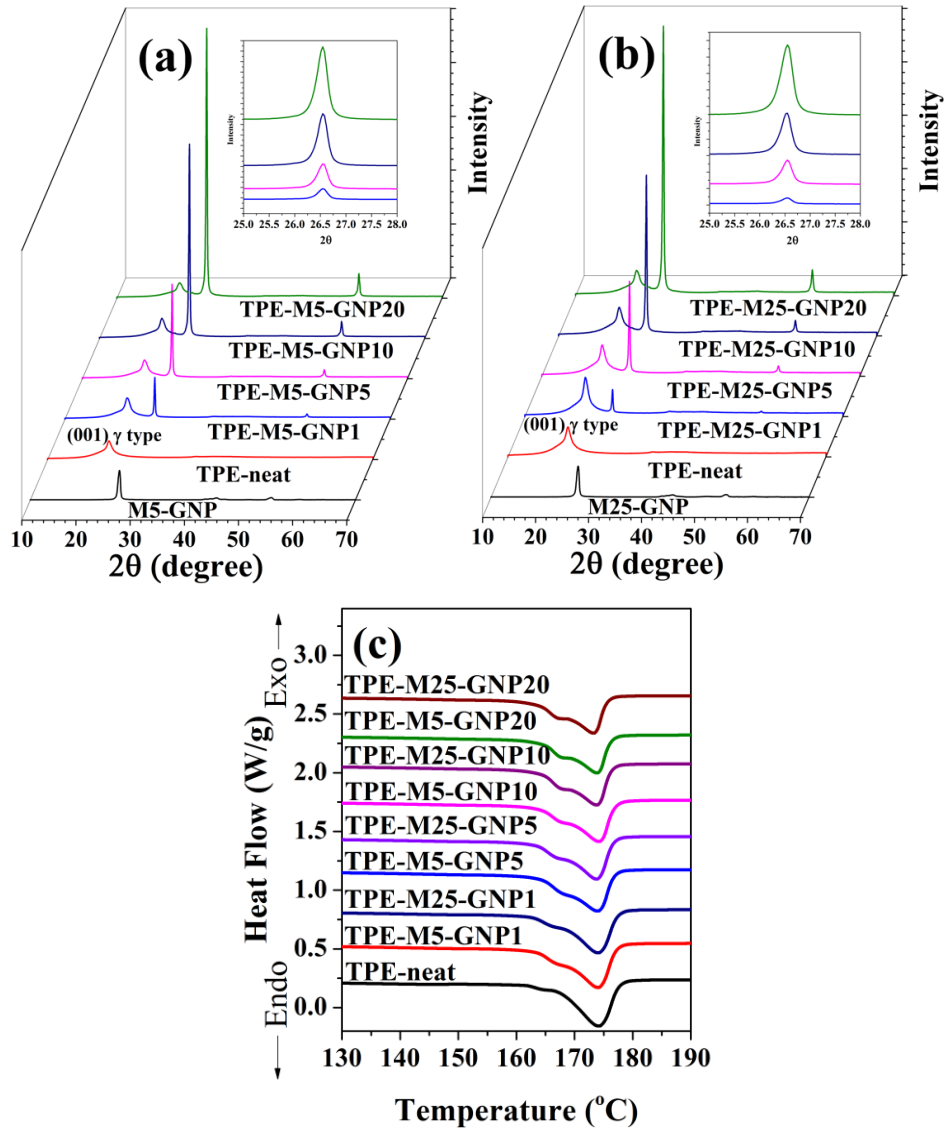
Figure 4.1 XRD patterns of (a) M5 and (b) M25 GNP-reinforced TPE and (c) DSC curves from 120 °C to 190 °C of GNP-reinforced TPE samples. Insets: XRD patterns of GNP1, 5, 10 and 20 showing the GNP characteristic peak at 2θ=26°.

127

Table 4.2 Degree of crystallinity of the neat polymer and composite samples.

Materials	Crystallinity from XRD (%)	Crystallinity from DSC (%)
TPE	46.2 ± 0.5	47.3 ± 0.7
TPE-M5-GNP1	47.4 ± 1.2	47.0 ± 1.3
TPE -M5-GNP5	47.3 ± 0.8	46.9 ± 0.6
TPE -M5-GNP10	46.3 ± 1.2	47.3 ± 0.6
TPE -M5-GNP20	45.4 ± 1.5	47.3 ± 0.4
TPE -M25-GNP1	48.5 ± 1.2	47.2 ± 1.1
TPE -M25-GNP5	47.5 ± 0.8	47.2 ± 0.5
TPE -M25-GNP10	46.6 ± 1.3	47.7 ± 0.3
TPE -M25-GNP20	45.6 ± 1.4	44.7 ± 2.3

4.3.2 Microstructure of the Nanocomposites

The SEM images of cryo-fractured cross-sections of the nanocomposite samples reinforced with M5 GNPs, at different filler fractions, can be seen in **Figure 4.2**. The corresponding images of M25-GNP-reinforced nanocomposites are shown in **Figure 4.3**. It can be seen that a homogeneous dispersion of the flakes was achieved as a result of the mixing procedure. Moreover, the injection moulding procedure attributed a preferred orientation of the flakes in the axial direction of the samples, due to the fountain flow mechanism [11]. Overall, the distance between individual flakes in the vertical direction (the direction of the surface normal of the flakes) in the images, is reduced with increasing filler loading.
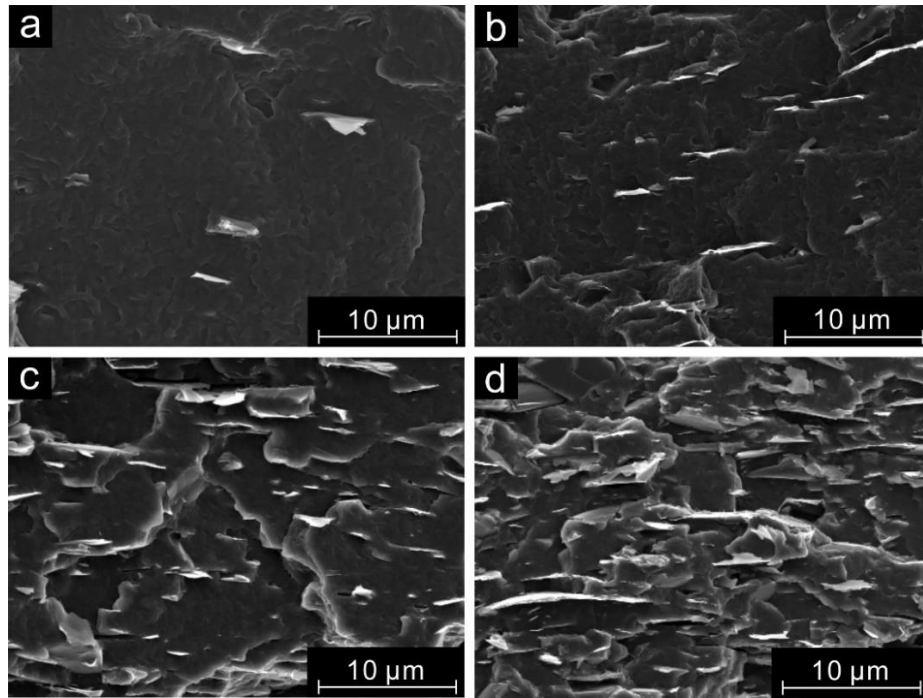
Figure 4.2 SEM images of the composites (a) TPE-M5-GNP1, (b) TPE-M5-GNP5, (c) TPE-M5-GNP10, (d) TPE-M5-GNP20.
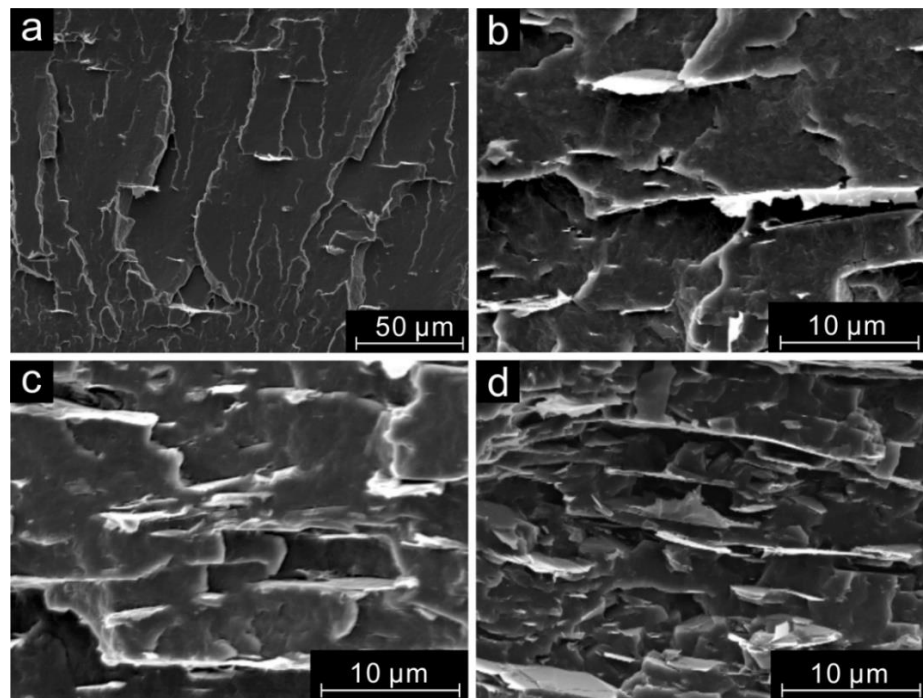
Figure 4.3 SEM images of the composites (a) TPE-M25-GNP1, (b) TPE-M25-GNP5, (c) TPE-M25-GNP10, (d) TPE-M25-GNP20.

A measurement of the distances between neighbouring flakes was carried out based on more than 100 flakes for each sample and shown in **Figure 4.4**. This reduction in inter-flake distance can activate a pronouncedly enhanced mechanical performance, which will be discussed in detail later. It should be pointed out that both batches of GNPs seem to include a number of smaller flakes, which decrease significantly the average lateral size quoted by the manufacturer, as was also identified in a previous work [10].
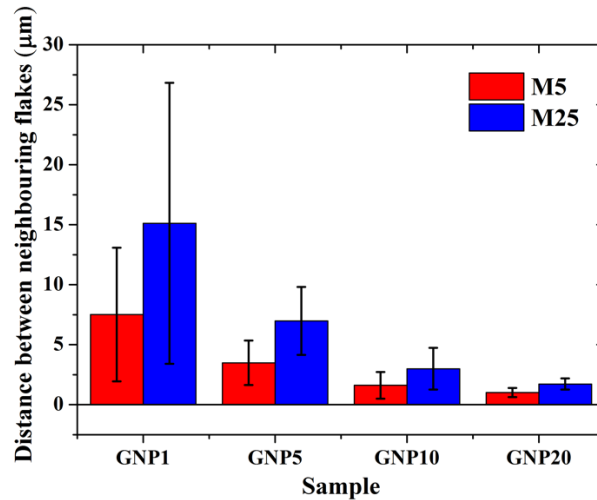
Figure 4.4 Measured distance between flakes in surface normal direction based on SEM.

The high magnification SEM images in **Figure 4.5** reveal flakes wetted by the matrix However, the morphologies of the flakes in the bulk nanocomposites also indicate stacking and the formation of agglomerates among the flakes at higher filler contents that are known to reduce the reinforcing efficiency by subsequently reducing the average aspect ratio of the flakes. In addition, some flakes can be seen forming looped or folded morphologies, similar to the ones observed in **Chapter 3** for a different thermoplastic elastomer matrix [11]. The pre-existing folds of the GNPs can be attributed for the folding and the bending of the nanoplatelets within the nanocomposites.
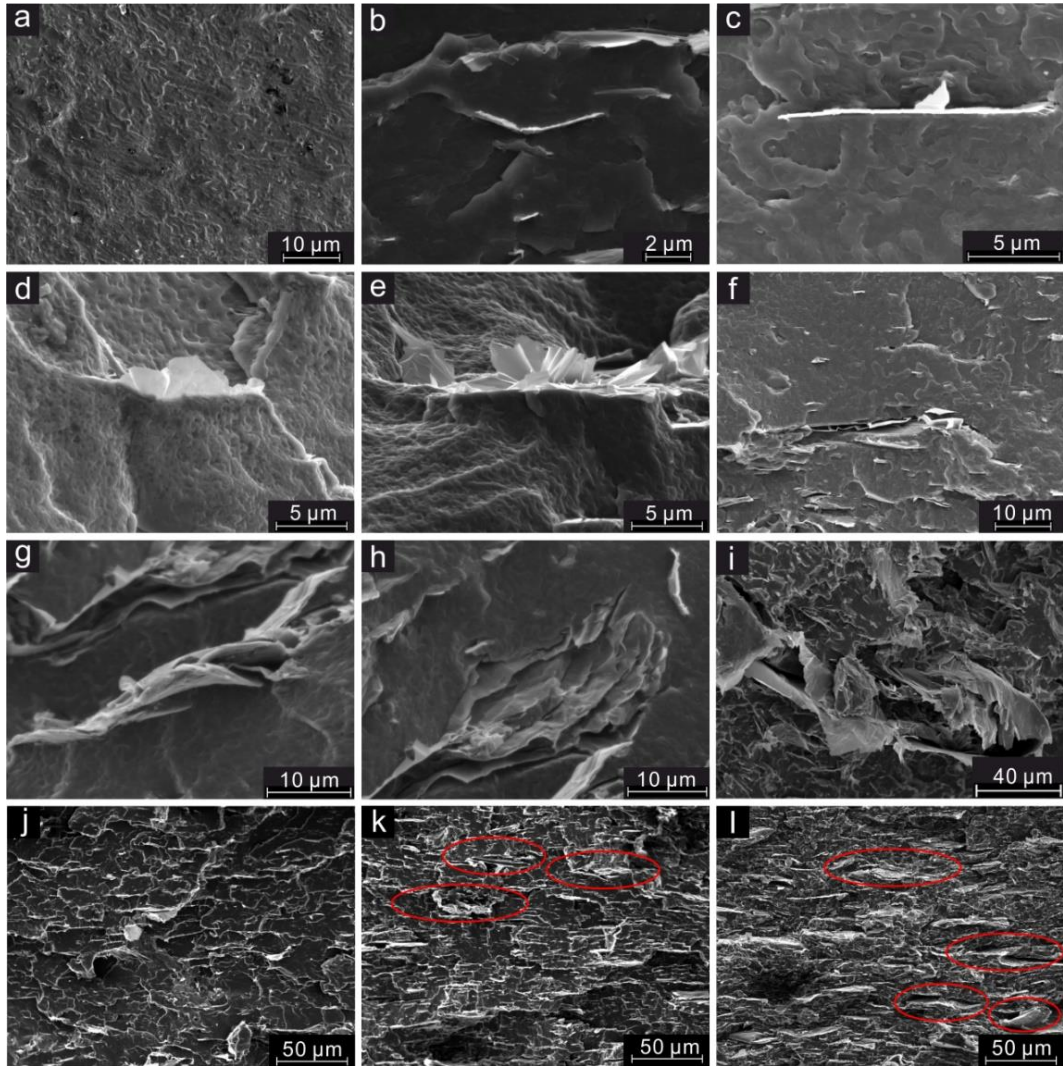
Figure 4.5 SEM images of (a) Neat TPE; (b,c) M5-GNP reinforced composites and (d,e) M25-GNP reinforced composites, respectively showing typical flake/matrix interfaces; (f,g) M5-GNP5 and M25-GNP5 samples showing stacking of the flakes; (h,i) M5-GNP5 and M25-GNP10 samples showing agglomerates;(j-l) Lower magnification SEM micrographs of TPE-M25-GNP5, 10 and 20 showing increasing degree of agglomerates (red circles) with increasing filler loading.

The orientation of the fillers was further investigated using polarised Raman, which enabled the quantification of orientation [13]. The relative parameters obtained by curve fitting of the orientation distribution function (**Figure 4.6**) are listed in **Table 4.3** along with the calculated orientation factors. The calculated orientation factors of 0.76 and 0.68

for M5 and M25 GNP-reinforced composites clearly indicate that the fillers are preferably oriented along the axial direction of the dumbbell samples.
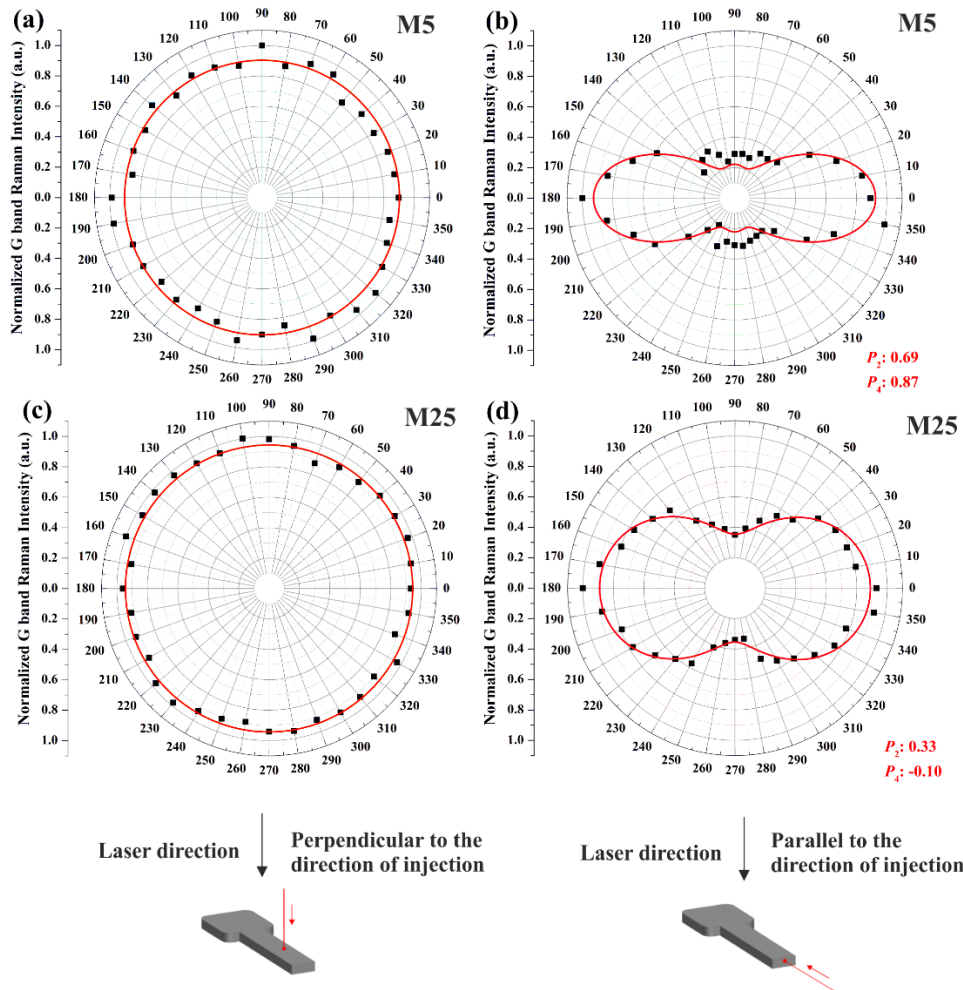
Figure 4.6 Representative Raman G band intensity as a function of angles of incident laser for (a-b) M5-GNP and (c-d) M25-GNP reinforced injection moulded dumbbell samples: (a,c) laser direction perpendicular to the direction of the injection and (b,d) laser direction parallel to the direction of the injection. The direction of the laser is shown in the schematic diagrams: (left)-laser perpendicular to the direction of injection; (right)-laser parallel to the direction of injection. The curve fittings of (b) and (d) were carried out using Equation (3.2) shown in **Chapter 3**.

Table 4.3 P_2, P_4 and orientation factor values obtained from different positions of the cross-section of the dumbbell sample using polarised Raman spectroscopy. P_2 and P_4 values were obtain by curve fitting using Equation 3.1, and orientation factor η_o was calculated by Equation 3.2. The positions that the measurements took place are illustrated by schematic diagrams (same as Figure 3.6 in Chapter 3).

GNP type	Position	P_2	P_4	η_o	Average η_o of measurements for different positions
M5		0.41	-0.01	0.69	
		0.44	0.11	0.71	
		0.62	0.84	0.84	
		0.84	0.93	0.93	
		0.69	0.87	0.87	0.76
		0.61	0.84	0.84	
		0.44	-0.11	0.69	
		0	0	0.53	
M25		0.33	-0.12	0.65	
		0.34	-0.07	0.66	
		0.45	-0.09	0.70	
		0.56	0.72	0.81	
		0.48	-0.20	0.73	0.68
		0.37	-0.06	0.67	
		0.33	-0.10	0.65	
		0	0	0.53	

4.3.3 Tensile Testing

The mechanical properties of the nanocomposites produced were evaluated initially by tensile testing. Typical stress-strain curves of all nanocomposite samples are shown in **Figure 4.7**. It is interesting to observe that the addition of GNPs into the matrix alters the tensile behaviour of the original TPE. More specifically, the yield point shifts to higher stress and lower strain with the increase of the filler loading, indicating that the mobility of the macromolecular chains is restricted [3]. Moreover, the samples with high filler loadings (TPE-M5-GNP10 and TPE-M5-GNP20 for the M5-reinforced composites and TPE-M25-GNP5, TPE-M25-GNP10 and TPE-M25-GNP20 for the M25-reinforced composites) tend to display only elastic deformation. The lateral size of the filler plays an important role in mechanical reinforcement since it determines the interfacial area with the matrix and the stress transfer; however, fillers with large lateral dimensions can form looped/folded morphologies during the mixing procedure, which are known to reduce the effective mechanical properties. It is interesting to see from **Figure 4.7** (a) that the low loadings of M5 GNP (1 wt% and 5 wt%) effectively improved all measured mechanical properties of the matrix including stiffness, yield strength, elongation at break and toughness. At low filler loadings, the polymer surrounding the nanoplatelets is reinforced, whereas the polymer chains located far from the nanoplatelets remain unaffected and retain their flexibility and inherent properties [2]. When the materials are on the verge of fracture during tensile tests, the interfaces between the filler and the matrix absorb the excess energy and therefore the toughness of the material is improved. Comparatively, only the sample filled with 1 wt% of M25 GNP-reinforced TPE (**Figure 4.7 b**) showed improved toughness. This comes as a result of the larger size of the nanoplatelets which form more looped/folded morphologies that reduce the effectiveness of stress transfer. Additionally, the larger nanoplatelet sizes can also lead to the easier formation of agglomerates where failure is initiated during elongation due to stress concentration [16].
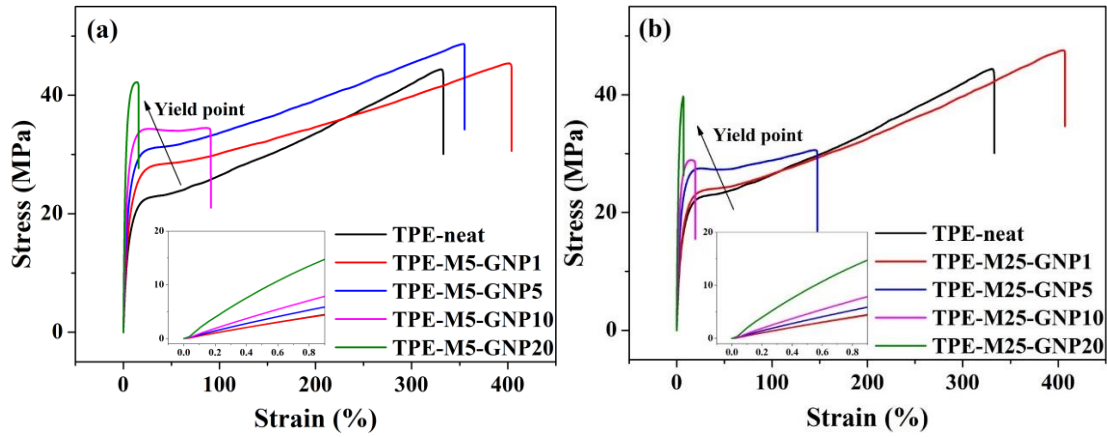
Figure 4.7 Typical stress-strain curves for (a) M5 GNP-reinforced and (b) M25 GNP-reinforced elastomer nanocomposites; the insets are the stress-strain curves at low strain.

The mechanical properties of the nanocomposites are plotted against the volume fractions of the GNPs in **Figures 4.8** (a) and (b). Moreover, the calculation of the filler volume fractions for the composites under study can be found in **Table 4.1** along with the corresponding weight percentage of the fillers. It can be seen that both the yield strength and the tensile modulus increase with increasing filler content, indicating good stress transfer efficiency through shear at the filler-matrix interface. Overall, the M5 GNPs give rise to higher improvements in the yield strength, as a result of their better dispersion and consequently filler-matrix adhesion, while M25 GNPs contribute slightly more to the stiffness of the materials indicating better stress transfer. The differences in the mechanical properties between the samples reinforced with M5 and M25 GNPs are quite small. This comes as a result of the small differences in the lateral sizes of the flakes that have been determined to be in the order of 5.2±3.3 µm and 7.7±4.2 µm, based on a previous publication [10]. As it can be understood, the distinction between the lateral sizes of the two fillers is considerably smaller than the supplier-suggested values of 5 µm and 25 µm since there is a number of small nanoplatelets (<3 µm) that control the average filler size in each batch.

Moreover, it can be seen from **Figures 4.8** (a) and (b) that the plots of the Young's modulus values against the volume fraction of the filler clearly display a super-linear

increase rather than a linear one. This implies that the higher loadings of GNPs exert an additional enhancement in the modulus, compared to the lower loadings. This is consistent with previous findings for different types of elastomer matrices reinforced by 2D materials [3, 5, 6]. Based on this finding, a number of TPE-M25-GNP nanocomposites with various filler loadings were prepared, in order to establish the transitional turning point in the modulus versus loading graph. It can be clearly seen in **Figure 4.8** (c) that the slope of the linear fit of the normalized modulus of the composite against the volume fraction of the filler is significantly higher for loadings above ~ 5 vol% (~10 wt%). Quantitatively, the slope of the data below 5 vol% (~10 wt%) is 24, whereas the corresponding slope for the data above 5 vol% (~10 wt%) is 61. This phenomenon observed for elastomer composites, was defined as 'accelerated stiffening' by Guth and Gold [2], where the rate of the increase of the composite modulus increases with increasing filler volume fractions. Accelerated stiffening has been observed in elastomer composites for a variety of fillers including carbon black [2], clays [3, 6] carbon nanotubes [7] and graphene-based fillers [5, 7, 17-19]. Although theories including the Guth-Gold theory [2] and the jamming theory [3, 4] were employed to analyse this observation [2, 3, 5-7, 9, 11, 17], there is no specific equation with well-defined parameters, able to describe the reinforcing mechanisms of graphene-reinforced elastomer nanocomposites. Hence, a theoretical analysis based on the recently developed shear-lag/rule-of-mixtures theory, where the parameters are well-defined [10], will be carried out in this work and discussed thoroughly in the next sections.
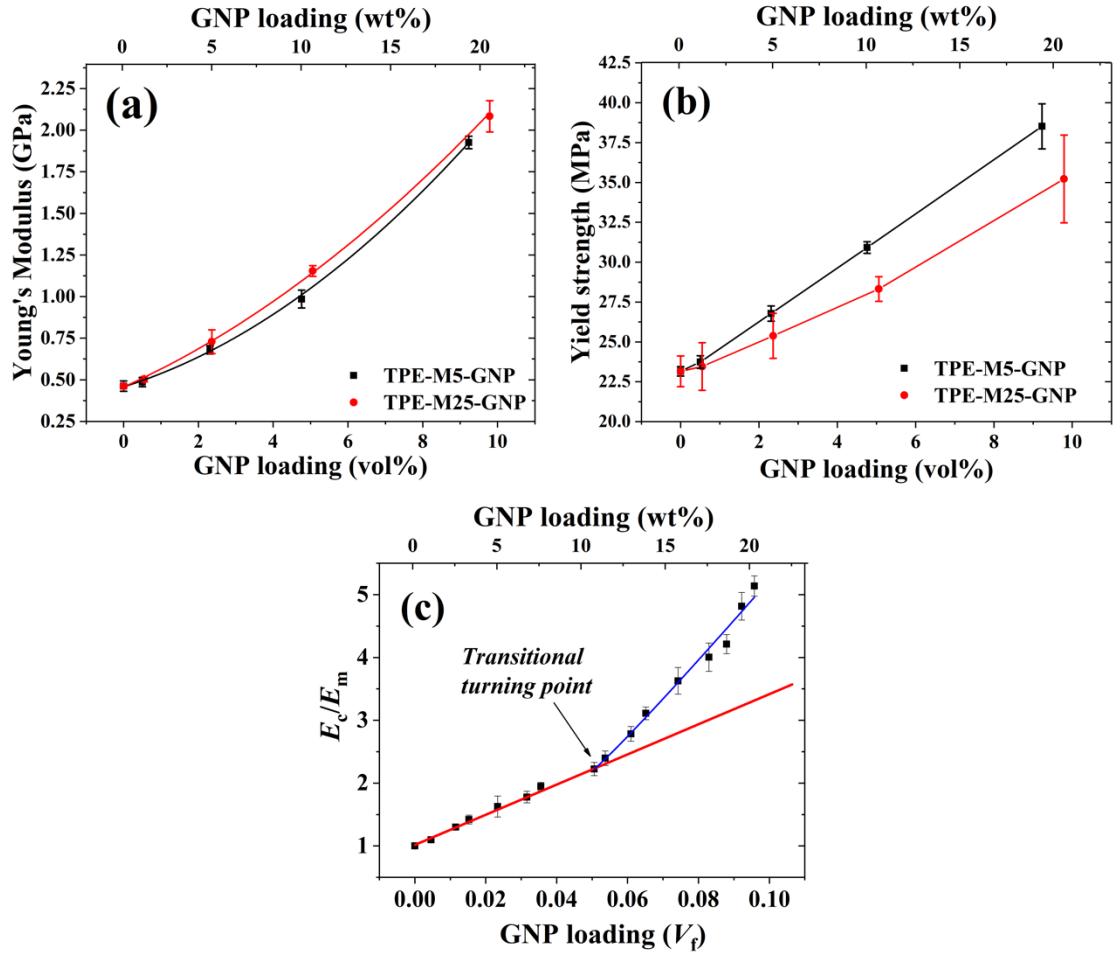
Figure 4.8 (a) Young's modulus and (b) yield strength against volume fractions of the filler (the lines in both (a) and (b) are just a guide to the eye); (c) Young's modulus of the M25-GNP reinforced samples with various filler loadings showing higher reinforcing efficiency at loadings higher than 5 vol% (~10 wt%). Separate linear fittings were performed to show different reinforcing efficiency of the filler. The red line and blue line were the fitting lines with the data points lower than 5 vol% (~10 wt%) and higher than 5 vol% (~10 wt%), respectively.

4.3.4 Raman 2D Band Shift

Raman spectroscopy is a powerful technique that is able to investigate the interfacial stress transfer from a polymer matrix to graphene-related materials [10, 13, 16, 20-24]. The specimen with the highest GNP loading ~10 vol% (20 wt%) were strained using a bending rig *in situ* under a Raman spectrometer and the characteristic shifts of the Raman bands were recorded with increasing composite strain from 0 to ~2.7%. The corresponding results are shown in **Figure 4.9**.

At a strain range from 0 to ~ 1.2 %, the Raman 2D band shifts to lower wavenumbers and the downshift can be fitted linearly in order to obtain the stress transfer efficiency from the matrix to the nanoplatelets [20]. The slope values presented in this work, reveal that the interfacial stress transfer from the matrix to the filler is more efficient compared to a number of softer elastomeric matrices reinforced by GNPs [10, 11, 22], but less efficient compared to stiffer matrices including PP, PMMA and epoxy resins [10, 21, 23, 24]. This is in accordance with a recent study [10] where it can be identified clearly that the filler modulus of graphene in polymer nanocomposites increases almost linearly with increasing matrix modulus.

When the applied load on the specimen was increased from ~1.2% up to ~2.7% strain, the 2D band shift increased and decreased irregularly with increasing strain, indicating a certain degree of relaxation in the specimen [20]. In thermoplastic elastomers, stress relaxation can lead to irreversible disentanglement of the physical crosslinks that are able to support stress for a short period of time [1].
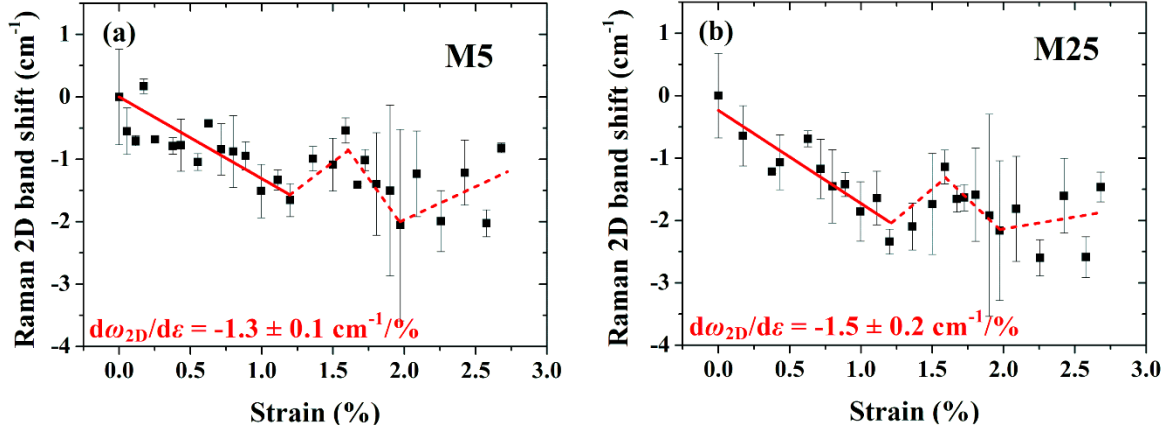
Figure 4.9 Raman 2D band shift against the composites strain of (a) M5 and (b) M25 reinforced TPE composite samples at ~10 vol% (20 wt%) loading of the filler. The solid lines in both (a) and (b) represent the linear fit of the downshift of the 2D Raman band, for strain up to ~1.2%, while the dashed irregular lines for strain higher than 1.2% are an indication of stress relaxation and disentanglement of the physical crosslinks in the TPE matrix.

The filler modulus can be calculated using the initial slope of 2D Raman band shift by the equation: $E_R = -\frac{d\omega_{2D}}{d\varepsilon}\frac{1050}{60}$ GPa [20]. The filler modulus results obtained by Raman measurements (E_R) and tensile testing (E_f) for the samples at the filler content of ~10 vol% (20 wt%) are listed in Table 1. E_f was calculated using the simple rule-of-mixtures [1] on the single data point at ~10 vol% (20 wt%) filler content: $E_c = E_f V_f + E_m(1-V_f)$, where E_f and E_m are the modulus of the filler and the matrix, respectively and V_f is the volume fraction of the filler. It can be seen that the filler modulus measured by the Raman band shift (E_R) is similar to the one obtained from tensile tests (E_f) in the cases of both M5 and M25 reinforced TPE, with E_R being somewhat higher than E_f. The filler modulus determined by tensile testing is based on the overall deformation of the composites. However, during the Raman measurements, the laser spot (in the order of 1-2 µm) generally probes on the centre of the axially-aligned flakes, while the flakes measured are ~5 or ~25 µm. Therefore, the stress at the laser-focused point of the nanoplatelet is higher than the average stress along the flakes, leading to higher filler modulus acquired by Raman measurements (E_R) than the filler modulus determined by tensile testing (E_f) [10].

139

Table 4.4 Raman 2D Band shifts and corresponding Raman modulus values along with theoretical Raman modulus values calculated by $E_R = -\frac{d\omega_{2D}}{d\varepsilon}\frac{1050}{60}$ GPa for both M5 and M25 reinforced TPE composites at the highest filler contents (~10 vol%).

	M5	M25
Band shift (cm^{-1}/% strain)	-1.3 ± 0.1	-1.5 ± 0.2
E_R (GPa)	22.9 ± 1.8	26.3 ± 3.5
E_f (GPa)	16.6 ± 0.6	18.1 ± 1.4

4.4 Discussion

4.4.1 Theoretical Analysis Using Micromechanics

The rule-of-mixtures is a well-accepted theory in the field of polymer composites, used to analyse the mechanics of reinforcement [1]. The Young's modulus of the composites is given by:

$$E_c = E_f V_f + E_m(1 - V_f) \tag{4.1}$$

Based on **Chapters 2 and 3** [10], when elastomers are reinforced by graphene, the E_f is dependent upon the modulus of the matrix, the orientation factor (η_o) and the aspect ratio (s) of the filler [10] as discussed in **Chapter 2, section 2.1.2**, equation (2.12):

$$E_f = \eta_o \frac{s^2}{12} \frac{t}{T} \frac{1}{(1+v)} E_m \tag{4.2}$$

where s is the aspect ratio of the filler; v is the Poisson's ratio of the elastomer. Moreover, t is the thickness of the flake and T is the thickness of a layer of the matrix surrounding

the flake. If we substitute E_f from Equation (4.2), then Equation (4.1) can be rewritten and rearranged into:

$$E_c/E_m = 1 + (\eta_o \frac{s^2}{12} \frac{t}{T} \frac{1}{(1+v)} - 1)V_f \tag{4.3}$$

The key to address the issue of the reinforcing mechanism in graphene-reinforced elastomers is to analyse the parameter t/T in Equation (4.3). If we assume a simple model of a single nanoplatelet inserted in a continuous elastomer matrix, then due to the fact that the macromolecular chains of elastomers are very flexible, the matrix unit located at an infinite distance from the flakes cannot be affected [25]. Therefore, T cannot be infinitely large for an elastomer matrix. More specifically, the value of T is dependent upon the shear modulus of the elastomeric matrix, which relates to the flexibility of the macromolecular chain segment. In this context, we can assume a shear-lag unit for a single flake in the elastomeric matrix as shown in **Figure 4.10** that can be affected by the flake through shear when an external stress is applied. Any part of the matrix located further than T from the flake cannot be affected.
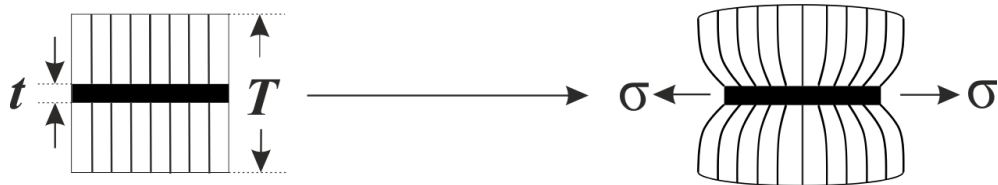
Figure 4.10 (left) Shear-lag stress transfer unit for an individual flake within the elastomer matrix: t is the thickness of the flake and the T is the thickness of the matrix surrounding the flake, which the flake can affect when an external stress is applied; (right) the deformation of the flake and the matrix polymer after application of strain.

The shear-lag unit model illustrates the reinforcement from individual flakes through stress transfer in elastomer nanocomposites. We can now apply the model of multiple shear-lag units into bulk elastomeric nanocomposites. The distribution and behaviour of the shear-lag units in elastomer nanocomposites from low to high filler loadings, when

an external stress is applied, is demonstrated in **Figure 4.11** In this case, it is assumed that all the nanoplatelets are dispersed homogeneously. When the loading of the filler is low (**Figures 4.11** a and b), the flakes are located far enough from each other, making the interaction between shear-lag units impossible. The SEM images of the samples filled with low GNP content, next to the shear-lag unit model, also point towards this direction. In this case, the modulus increase can be attributed to the enhancement from individual flakes, through stress transfer. Hence, the value of t/T is constant and consequently Equation (4.3) shows a linear relationship between the normalized modulus and the volume fraction of the filler. With the increase of V_f, the distance between adjacent shear-lag units becomes closer and they finally coincide with each other. At this critical point, the t/T ratio is equal to the V_f (**Figure 4.11** c). This point can be defined as *the percolation threshold volume fraction* of the filler, V_p. It can be understood with the aid of both the model and the SEM **Figures 4.11** (a-b) that when the volume fraction of the filler is below V_p, the constant parameter, t/T, can be approximated to be equal to V_p. When the filler content increases from the percolation threshold volume fraction of the filler (V_p), to higher filler contents (**Figure 4.11** c and d), the thickness of the matrix surrounding the flake (T) is geometrically reduced due to the smaller distances between the flakes and the parameter t/T in Equation (4.3) can be eventually substituted by V_f. The normalized modulus is then given by:

$$E_c/E_m = 1 - V_f + \eta_o \frac{s^2}{12} \frac{1}{(1+v)} V_f^2 \qquad\qquad (4.4)$$

Assuming the Poisson's ratio of the elastomer is ~0.5 [25], Equation (4.3) for filler contents below the percolation threshold takes the form;

$$E_c/E_m = 1 + (0.056 \eta_o s_{eff}^2 \frac{t}{T} - 1) V_f \qquad \text{for} \qquad V_f < V_p \qquad (t/T = V_p) \qquad (4.5)$$

and Equation (4.4) for filler contents above the percolation threshold can be rewritten as;

$$E_c/E_m = 1 - V_f + 0.056\eta_o s_{eff}^2 V_f^2 \qquad \text{for} \qquad V_f \geq V_p \qquad (4.6)$$

where s_{eff} is the effective aspect ratio of the GNPs in the bulk nanocomposites. The schematic diagrams in **Figure 4.11** were drawn for the case of perfect orientation of the filler, in order to simplify the illustration. If the flakes are not perfectly aligned along the direction of the external force, as they are in this case, then the orientation factor η_o ($8/15 \leq \eta_o < 1$) which can be obtained experimentally [13], should be taken into account.

The proposed Equations (4.5) and (4.6) can describe the reinforcement from GNPs in elastomer-based nanocomposites, while also being able to explain the accelerated stiffening phenomenon with increasing filler content. From low to high filler contents, the reinforcing mechanism of the GNPs in graphene-reinforced elastomer composites can be divided into 3 individual stages:

Stage I: When the filler loading is low and below the percolation threshold volume fraction ($V_f < V_p$), it is considered that the mechanical improvements are dependent upon the performance of the individual flakes, where the parameter t/T takes the constant value of V_p and consequently the normalized modulus shows a linear relationship with V_f, represented by Equation (4.5).

Stage II: With the increase of filler fraction to reach and overcome the percolation threshold ($V_f \gtrsim V_p$), the average distance between nanoplatelets is small enough to enable mechanical reinforcement from both individual fillers and the simultaneous contributions by pairs of fillers. This effect can be expressed quantitatively by a quadratic relationship between E_c/E_m and V_f, as shown in Equation (4.6), while being also able to explain the accelerated stiffening phenomenon in elastomer composites with increasing filler contents [2].
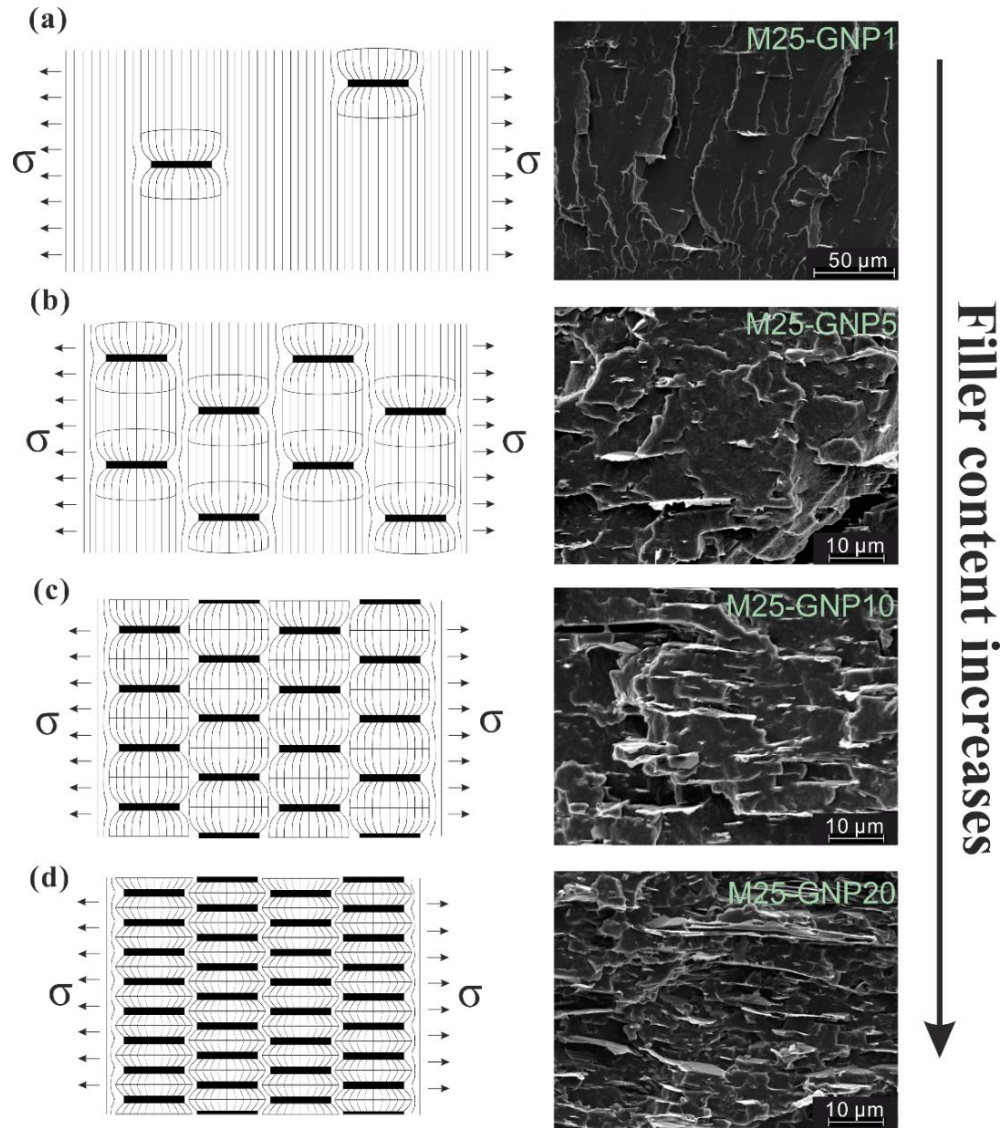
Figure 4.11 Schematic illustration of samples reinforced with different loadings of GNPs (increase from a to d) under external stress, demonstrating the dependence of stress transfer efficiency upon the filler loading in an elastomer matrix, based on shear-lag theory: (a) low filler loading; (b) high filler loading than (a) but below the percolation threshold (both a and b show the reinforcement from individual flakes); (c) filler loading at percolation threshold and (d) filler loading above the percolation threshold showing the formation of the filler network and the enhanced reinforcing efficiency of the flakes due to the reduced distance between individual flakes. The illustration of the distance between the flakes is also suggested by SEM images as shown.

Stage III: When the filler loading is high enough, a number of agglomerates are formed in the nanocomposite and as a result, the reinforcing efficiency is reduced [11, 21, 23]. The influence of agglomeration can be realised quantitatively by the decreased values of the effective aspect ratio, obtained through the fitting of the experimentally obtained modulus data, using Equation (4.6).

4.4.2 Application of the Proposed Theory

The results of the mechanical properties of the nanocomposites were presented in Section 4.3.3 and the fitting of the experimental data using Equations (4.5) and (4.6), was carried out as shown in **Figure 4.12** for the case of perfect orientation. From the normalized modulus values presented in **Figure 4.8** (c), it can be clearly observed that the slopes of the experimental data are different before and after the filler content of 5 vol% (~10 wt%). On this basis, 5 vol% (~10 wt%) was established as the percolation threshold volume fraction of the filler (V_p). The data below 5 vol% (~10 wt%), were fitted by Equation (4.5), where according to the previous discussion, reinforcement depends on stress transfer from individual flakes, while the data above 5 vol% (~10 wt%) were fitted using Equation (4.6), where the matrix is additionally stiffened.

The data points below 5 vol% (~10 wt%) were fitted using a linear line, as suggested by Equation (4.5). The slope has the same value as the factor $[0.056\eta_o s_{\text{eff}}^2(t/T)\text{-}1]$, where t/T ($=V_p$) is 0.05. Assuming the orientation of the flakes is perfect (η_o=1), the effective aspect ratio can be calculated. For the M25 GNPs within the TPE matrix, the value of the effective aspect ratio is 95, as shown in **Figure 4.12** (a). Then, by substituting s_{eff} into Equation (4.6), the fitting of the experimental data is represented by the red curves in **Figures 4.12**. It can be seen that equation (4.6) fits accurately the normalized modulus of the samples filled with ~0.05 – ~0.07 vol (~10-15 wt%). GNPs. The effective aspect ratio (in the order of 100) for M25-GNPs in the bulk composites is relatively low for a 2D material and this can be attributed to the high thickness of the starting material and the presence of a prexisting looped or folded morphology amongst the flakes (**Figure 4.5**).

However, the fitting was not accurate enough for the samples filled with higher GNP loadings, due to the increased number of folded flakes and the unavoidable formation of agglomerates. When adjusting the value of s_{eff} to a slightly lower value (s_{eff}=90), the fitting becomes consistent with the data, as shown by the blue-dashed curves in **Figures 4.12**. For the case of random orientation (η_o=0.53), the same fitting procedure can be carried out for the experimental data, as shown in **Figure 4.12** (b). The fitted value of effective aspect ratio is slightly higher, but still in the order of 100. If we compare **Figure 4.12** (a) with (b), it can be seen that the difference of the fitted aspect ratio values between random and perfect orientation is rather small (90 compared to 132).
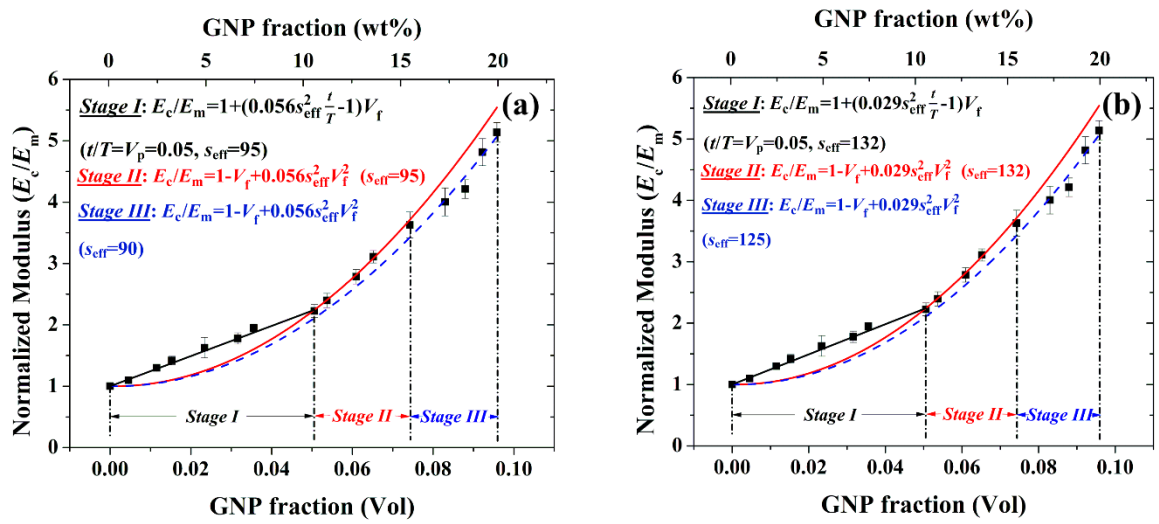
Figure 4.12 Fittings of normalized modulus against volume fraction of the fillers with both Equations (4.5) and (4.6) for M25-GNP reinforced composite samples showing three stages of the reinforcement, assuming (a) perfect orientation of the flakes and (b) random orientation of the flakes. Stage I: reinforcement takes place from individual flakes through stress transfer and the modulus can be fitted with a linear Equation (4.5). Stage II: above the percolation threshold volume fraction, the reinforcement originates from both individual fillers and the simultaneous contributions by pairs of fillers. The effect is described by a quadratic relationship (Equation 4.6). Stage III: higher filler contents lead to the formation of agglomerates; the modulus can still be fitted with Equation 4.6 however the effective aspect ratio (s_{eff}) of the fillers is reduced. The corresponding weight percentage of the filler is shown on the top *X* axis.

4.5 Conclusion

GNP-reinforced semicrystalline thermoplastic elastomers have been prepared successfully by melt mixing. The degree of crystallinity remained constant with the addition of GNPs. SEM images indicate that the dispersion of the GNPs within the matrix is homogeneous, with excellent filler/matrix interfaces in general. A mechanical percolation phenomenon was seen and modelled successfully using micromechanics. It was revealed that GNPs were able to stiffen the elastomers with higher reinforcing efficiency at volume fractions higher than the percolation threshold, owing to the reduction of distances between flakes.

References

[1] Young RJ, Lovell PA. Introduction to polymers: CRC press; 2011.

[2] Guth E. Theory of filler reinforcement. Journal of Applied Physics. 1945;16(1):20-5.

[3] Liff SM, Kumar N, McKinley GH. High-performance elastomeric nanocomposites via solvent-exchange processing. Nature Materials. 2007;6(1):76.

[4] Trappe V, Prasad V, Cipelletti L, Segre P, Weitz DA. Jamming phase diagram for attractive particles. Nature. 2001;411(6839):772.

[5] Nawaz K, Khan U, Ul-Haq N, May P, O'Neill A, Coleman JN. Observation of mechanical percolation in functionalized graphene oxide/elastomer composites. Carbon. 2012;50(12):4489-94.

[6] Ramorino G, Bignotti F, Pandini S, Riccò T. Mechanical reinforcement in natural rubber/organoclay nanocomposites. Composites Science and Technology. 2009;69(7-8):1206-11.

[7] Das A, Kasaliwal GR, Jurk R, Boldt R, Fischer D, Stöckelhuber KW, et al. Rubber composites based on graphene nanoplatelets, expanded graphite, carbon nanotubes and

their combination: a comparative study. Composites Science and Technology. 2012;72(16):1961-7.

[8] Potts JR, Shankar O, Du L, Ruoff RS. Processing–morphology–property relationships and composite theory analysis of reduced graphene oxide/natural rubber nanocomposites. Macromolecules. 2012;45(15):6045-55.

[9] Fernández-d'Arlas B, Corcuera MA, Eceiza A. Comparison between exfoliated graphite, graphene oxide and multiwalled carbon nanotubes as reinforcing agents of a polyurethane elastomer. Journal of Thermoplastic Composite Materials. 2015;28(5):705-16.

[10] Young RJ, Liu M, Kinloch IA, Li S, Zhao X, Vallés C, Papageorgiou DG. The mechanics of reinforcement of polymers by graphene nanoplatelets. Composites Science and Technology. 2018;154:110-6.

[11] Liu M, Papageorgiou DG, Li S, Lin K, Kinloch IA, Young RJ. Micromechanics of reinforcement of a graphene-based thermoplastic elastomer nanocomposite. Composites Part A: Applied Science and Manufacturing. 2018:84-92.

[12] Li Z, Young RJ, Kinloch IA, Wilson NR, Marsden AJ, Raju APA. Quantitative determination of the spatial orientation of graphene by polarized Raman spectroscopy. Carbon. 2015;88:215-24.

[13] Li Z, Young RJ, Wilson NR, Kinloch IA, Vallés C, Li Z. Effect of the orientation of graphene-based nanoplatelets upon the Young's modulus of nanocomposites. Composites Science and Technology. 2016;123:125-33.

[14] Salmoria GV, Paggi RA, Lago A, Beal VE. Microstructural and mechanical characterization of PA12/MWCNTs nanocomposite manufactured by selective laser sintering. Polymer Testing. 2011;30(6):611-5.

[15] Kuo AC. Polymer Data Handbook. 1999.

[16] Papageorgiou DG, Kinloch IA, Young RJ. Mechanical properties of graphene and graphene-based nanocomposites. Progress in Materials Science. 2017;90:75-127.

[17] Araby S, Zaman I, Meng Q, Kawashima N, Michelmore A, Kuan HC, Majewski P, Ma J, Zhang L. Melt compounding with graphene to develop functional, high-performance elastomers. Nanotechnology. 2013;24(16):165601.

[18] Wu C, Huang X, Wang G, Wu X, Yang K, Li S, Jiang P. Hyperbranched-polymer functionalization of graphene sheets for enhanced mechanical and dielectric properties of polyurethane composites. Journal of Materials Chemistry. 2012;22(14):7010-9.

[19] Yang L, Phua SL, Toh CL, Zhang L, Ling H, Chang M, Zhou D, Dong Y, Lu X. Polydopamine-coated graphene as multifunctional nanofillers in polyurethane. RSC Advances. 2013;3(18):6377-85.

[20] Gong L, Kinloch IA, Young RJ, Riaz I, Jalil R, Novoselov KS. Interfacial stress transfer in a graphene monolayer nanocomposite. Advanced Materials. 2010;22(24):2694-7.

[21] Ahmad SR, Xue C, Young RJ. The mechanisms of reinforcement of polypropylene by graphene nanoplatelets. Materials Science and Engineering: B. 2017;216:2-9.

[22] Li S, Li Z, Burnett TL, Slater TJ, Hashimoto T, Young RJ. Nanocomposites of graphene nanoplatelets in natural rubber: microstructure and mechanisms of reinforcement. Journal of Materials Science. 2017;52(16):9558-72.

[23] Papageorgiou DG, Kinloch IA, Young RJ. Hybrid multifunctional graphene/glass-fibre polypropylene composites. Composites Science and Technology. 2016;137:44-51.

[24] Vallés C, Kinloch IA, Young RJ, Wilson NR, Rourke JP. Graphene oxide and base-washed graphene oxide as reinforcements in PMMA nanocomposites. Composites Science and Technology. 2013;88:158-64.

[25] Smallwood HM. Limiting law of the reinforcement of rubber. Journal of Applied Physics. 1944;15(11):758-66.

Chapter 5. Anisotropic Swelling of Elastomers Filled With Aligned 2D Materials[*]

* Contributions to the publication (author name order of the publication): Mufeng Liu: experiments of TPE samples, data analysis, derivation of the equations, propose of the theory and writing of the manuscript; Suhao Li: experiments of NR and NBR samples. Ian A. Kinloch: final proof-reading; Robert J. Young: proof-reading and rephrasing of the manuscript; Dimitrios G. Papageorgiou: proof-reading and discussion of the manuscript.

5.1 Introduction

Crosslinked rubbers swell when they come in contact with liquids. The swelling of rubbers impacts negatively their mechanical properties and ultimately makes the materials lose their serviceability. It is therefore crucial to improve the liquid barrier properties for rubber-based materials to control their swelling behaviour. It was reviewed in **Chapter 2** that carbon black has been used extensively for this purpose and detailed studies were undertaken by Kraus [1]. The theory proposed by Kraus has been shown to be applicable to carbon blacks and other types of spherical fillers [2-4]. Kraus' equation is not applicable in graphene nanocomposites, because the reinforcement from asymmetric fillers is no longer uniform and leads to complexity in the swelling process.

In this present study, a number of different elastomers were compounded with different types of graphene nanoplatelets (GNPs) in order to investigate their swelling behavior in different solvents. In particular it has been found that as a result of the processing methods, most of the GNPs were aligned in the plane of the elastomer sheets and that this produced anisotropic swelling. Some elastomer samples filled with carbon black were also tested in order to compare the swelling characteristics for different filler morphologies. A theoretical analysis has also been carried out based on the Flory-Rehner

theory and the analysis of strain-induced swelling by Treloar, to fully understand the anisotropic swelling of the GNP-filled elastomers and relate this to the mechanical properties of the filled elastomers. Finally, a new equation has been derived, that enables us to assess the reinforcing efficiency of GNPs in the volume swelling of elastomers based on both the aspect ratio and volume fraction of the filler.

5.2 Experimental Methods

5.2.1 Materials and Preparation

A range of different elastomers were selected for this study that include natural rubber (NR), nitrile butadiene rubber (NBR) and a thermoplastic elastomer (TPE). The grade of natural rubber (NR) used was SMR CV60 (Standard Malaysian Rubber, Mooney-Viscosity ML (1+4) of 60 at 100 °C, which was purchased from Astlett Rubber Inc., Oakville, Ontario, Canada and used as received. The nitrile butadiene rubber (NBR) was Nipol® 1052J, supplied by Clwyd Compounders Ltd and used as received. The thermoplastic elastomer, Alcryn® 2265 UT (Unfilled Translucent), which is based on a partially crosslinked chlorinated olefin interpolymer alloy, was purchased from A. Schulman, Inc, and used as received.

Graphene nanoplatelets (xGNP®, Grade-M particles, XG Sciences, Lansing USA) with nominal lateral sizes of 5 μm, 15 μm and 25 μm as quoted by the supplier (designated as M5, M15 and M25, respectively) were used for compounding with the NR, NBR and TPE. The thicknesses of all the flakes were quoted by the manufacturer to be in the range 6 to 8 nm (i.e. around 20 layers of graphene).

High abrasion furnace (HAF) N330 carbon black (CB) supplied by the Berwin Polymer Processing Group, Duckinfield, UK, was employed to mix with NR and NBR. Moreover, all the additives involved in some of the rubber processing, zinc oxide, stearic acid,

TMTD (tetramethylthiuram disulfide), CBS (n-cyclohexyl-2-benzothiazole sulfenamide) accelerator and sulfur were of analytical grade and used as received. Detailed formulations are listed in the **Tables 5.1 and 5.2**.

Table 5.1 Formulation of the NR compounds.

Materials	Loading (phr*)
NR (SMR CV60)	100
Sulfur	3
CBS accelerator	1
Zinc Oxide	3
Stearic acid	2.5
GNP (M5, M15, M25) and N330	5, 10, 15, 20

Table 5.2 Formulation of the NBR compounds.

Materials	Loading (phr*)
NBR Nipol® 1052J	100
Sulfur	2
CBS accelerator	0.5
Zinc Oxide	4
TMTD	0.25
GNP (M15) and N330	5, 10, 15, 20

*"phr" is a preferred used unit in the rubber industry, abbreviation for "parts per hundred rubber".

The solvents used in the analysis of swelling behavior of the elastomer nanocomposites, toluene (anhydrous, 99.8%), cyclohexane (anhydrous, 99.5%) and acetone (anhydrous, 99.9%) were purchased from Sigma-Aldrich Co. Ltd. and used as received. The compounding of NR and NBR was carried out in a two-roll mill at room temperature. The loadings of 5, 10, 15 and 20 phr (parts by weight per hundred parts of rubber) for M5,

M15 and M25 xGNPs and N330 CB were incorporated into NR , while only M15 xGNPs and N330 were mixed with NBR. The melt mixing of the TPE with 3 types of GNPs was carried out in a Thermo Fisher HAAKE Rheomix internal mixer. The mixing took place at 165 °C and 50 rpm for 5 minutes. The GNP loadings (M5, M15 and M25) in the TPE nanocomposites were 1%, 5%, 10%, and 20% by weight (and not phr since no other additives were used with this matrix, see **Table 5.3**).

Table 5.3 Formulation of the TPE nanocomposites.

Materials	Loading (wt%)
TPE (Alcryn® 2265UT)	99, 95, 90, 80
GNP (M5, M15 and M25)	1, 5, 10, 20

The compounds were subsequently cut into small pieces and hot pressed in a metal mould into sheets (~2 mm thick) in a Collin Platen Press (Platen Press P 300 P/M). The vulcanization proceeded at a temperature of 160 °C for 10 minutes under a hydraulic pressure of 30 bar for NR and NBR. For TPE, the moulding took place in the same equipment at 185 °C for 10 minutes. All the moulded elastomer sheets (~2 mm thick) were then stamped into disc-shaped samples with a diameter of around 25 mm for swelling tests and into dumbell samples for tensile tests.

5.2.2 Characterisation

The actual loadings of the fillers in the nanocomposites were determined by thermogravimetric analysis (TGA) using a TA Q500 TGA instrument. The samples were heated from room temperature up to 600 °C under a 50 mL/min flow of N_2 at 10°C /min.

The microstructure of the cryo-fractured elastomer nanocomposites was examined using scanning electron microscopy (SEM). The images were acquired using a high-resolution XL30 Field Emission Gun Scanning Electron Microscope (FEGSEM) operated at 6 kV.

For the swelling studies, the samples were immersed in ~50 mL of solvent. The uptake of solvent was monitored by weighing the samples at intervals following immersion until their weight became constant and equilibrium was established. The dimensions of the samples were also measured using a vernier caliper in both the unswollen state and in the equilibrium swollen state. Different sets of elastomers and nanocomposites were tested in different solvents as listed in **Table 5.4.**

Table 5.4 The nanocomposites and solvents used for swelling measurements.

Matrix	Filler	Loadings	Solvent
NR	GNP (M5, 15, 25)/CB	5, 10, 15, 20 phr	Toluene
NBR	GNP (M15)/CB	5, 10, 15, 20 phr	Toluene, Cyclohexane
TPE	GNP (M5, 15, 25)	1, 5, 10, 20 wt%	Toluene

Tensile testing was undertaken using an Instron 4301 machine with a load cell of 5 kN, for all the samples. At least 5 specimens were tested for each sample. The NR and NBR samples were tested under a tensile rate of 500 mm·min^{-1} in accordance with ASTM 412 standard, while the TPE samples were tested under a tensile rate of 50 mm·min^{-1} in accordance with ASTM 638.

5.3 Results and Discussion

5.3.1 Materials Characterisation

The actual weight fractions of the fillers in the different elastomers were confirmed by TGA and the volume fractions are listed in **Table 5.5**. The volume fraction was calculated by: $V_f = \frac{w_f \rho_m}{w_f \rho_m + (1-w_f)\rho_f}$, where w_f is the mass fraction of the filler, ρ_m (=0.93 g/cm^3, for NR and NBR; =1.08 g/cm^3 for TPE) and ρ_f (=2.2 g/cm^3) are the densities of the matrices and the filler, respectively. The results for TPE have been shown in **Chapter 3**.

Table 5.5 Mass fractions of the fillers in the nanocomposites and calculated volume fractions. The TPE was not in phr since no other additives were used with this matrix.

Materials	Mass fraction (%)	Volume fraction (%)
NR/M5 5 phr	3.55 ± 0.35	1.57 ± 0.15
NR/M5 10 phr	7.10 ± 0.41	3.22 ± 0.18
NR/M5 15 phr	10.64 ± 0.35	4.92 ± 0.15
NR/M5 20 phr	14.19 ± 0.06	6.71 ± 0.03
NR/M15 5 phr	3.18 ± 0.19	1.41 ± 0.08
NR/M15 10 phr	7.34 ± 0.32	3.33 ± 0.14
NR/M15 15 phr	10.76 ± 0.17	4.98 ± 0.07
NR/M15 20 phr	13.31 ± 0.58	6.26 ± 0.25
NR/M25 5 phr	3.70 ± 0.14	1.64 ± 0.06
NR/M25 10 phr	6.88 ± 0.30	3.11 ± 0.13
NR/M25 15 phr	10.21 ± 0.24	4.71 ± 0.10
NR/M25 20 phr	13.21 ± 0.09	6.21 ± 0.04
NR/CB 5 phr	3.64 ± 0.14	1.97 ± 0.08
NR/CB 10 phr	7.44 ± 0.18	4.10 ± 0.10
NR/CB 15 phr	11.27 ± 0.12	6.32 ± 0.06
NR/CB 20 phr	14.67 ± 0.08	8.38 ± 0.04
NBR/M15 5 phr	3.18 ± 0.19	2.00 ± 0.10
NBR/M15 10 phr	7.34 ± 0.32	4.06 ± 0.09
NBR/M15 15 phr	10.76 ± 0.17	5.89 ± 0.07
NBR/M15 20 phr	13.31 ± 0.58	7.64 ± 0.14
TPE/M5 1 wt%	1.9 ± 0.04	0.95 ± 0.02
TPE/M5 5 wt%	5.14 ± 0.18	2.57 ± 0.09
TPE/M5 10 wt%	11.04 ± 1.32	5.52 ± 0.66
TPE/M5 20 wt%	21.64 ± 0.10	10.82 ± 0.05
TPE/M15 1 wt%	1.07 ± 0.03	0.53 ± 0.02
TPE/M15 5 wt%	5.46 ± 0.06	2.73 ± 0.03
TPE/M15 10 wt%	12.42 ± 0.06	6.21 ± 0.03
TPE/M15 20 wt%	20.6 ± 0.40	10.3 ± 0.20
TPE/M25 1 wt%	0.81 ± 0.15	0.4 ± 0.08
TPE/M25 5 wt%	4.87 ± 0.59	2.44 ± 0.30
TPE/M25 10 wt%	9.75 ± 0.21	4.88 ± 0.11
TPE/M25 20 wt%	20.94 ± 0.31	10.47 ± 0.16

The microstructures of the filled materials were characterised by SEM of cryo-fractured sections of the sheets as shown in **Figure 5.1.** It can be seen from **Figure 5.1 (a-c)** that the GNPs appear edge-on protruding from the fracture surfaces with a high degreee of alignment in the plane of the elastomer sheets as a consequence of the compression moulding technique employed. On the other hand, the NR sample filled with carbon black shows carbon black clusters of submicron sizes within a relatively smooth surface of the cross-section of the sample, as seen from **Figure 5.1 (d)**. Typical fracture surfaces for other filler (GNP and CB) loadings and sizes of the nanocomposites showing similar characteristics are also presented in **Figures 5.2 and 5.3**.
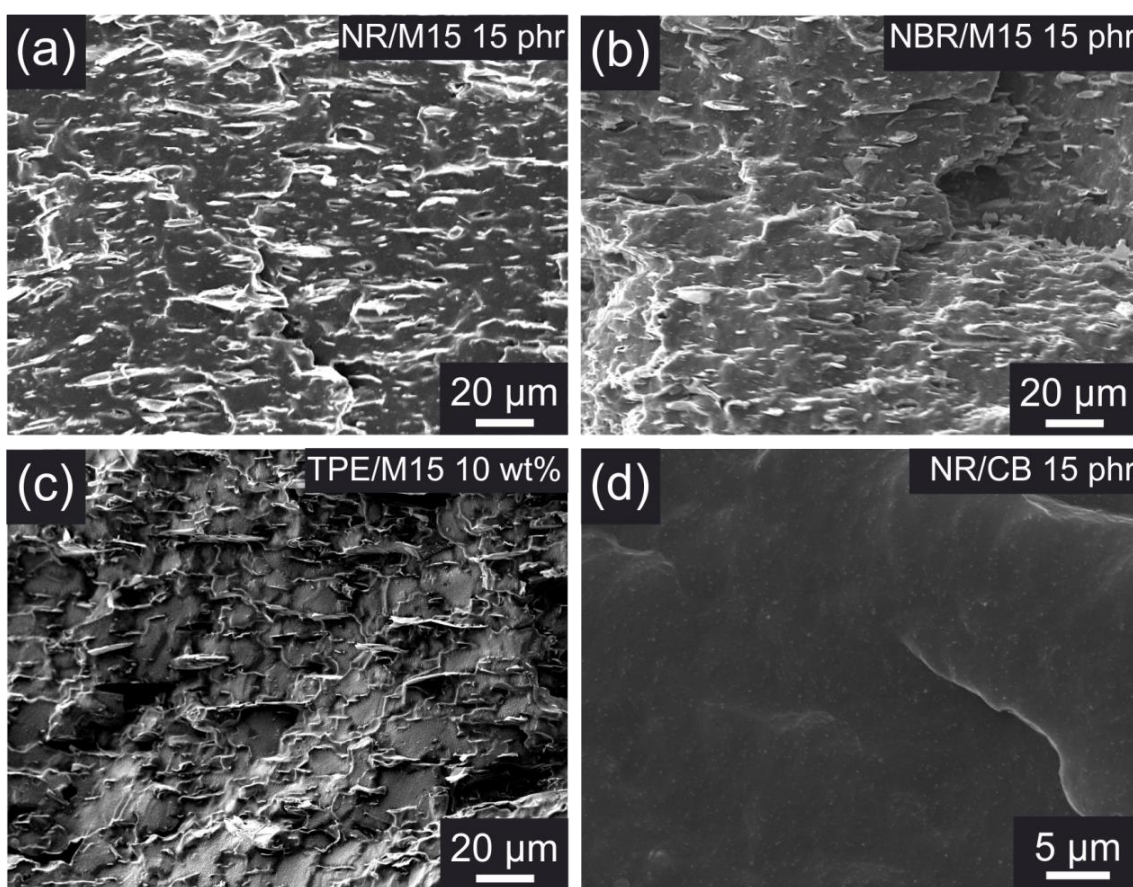
Figure 5.1 The microstructure of GNP filled nanocomposites samples: (a) NR/M15 15 phr; (b) NBR/M15 15 phr; (c) TPE/M15 10 wt% and (d) NR/CB 15 phr.
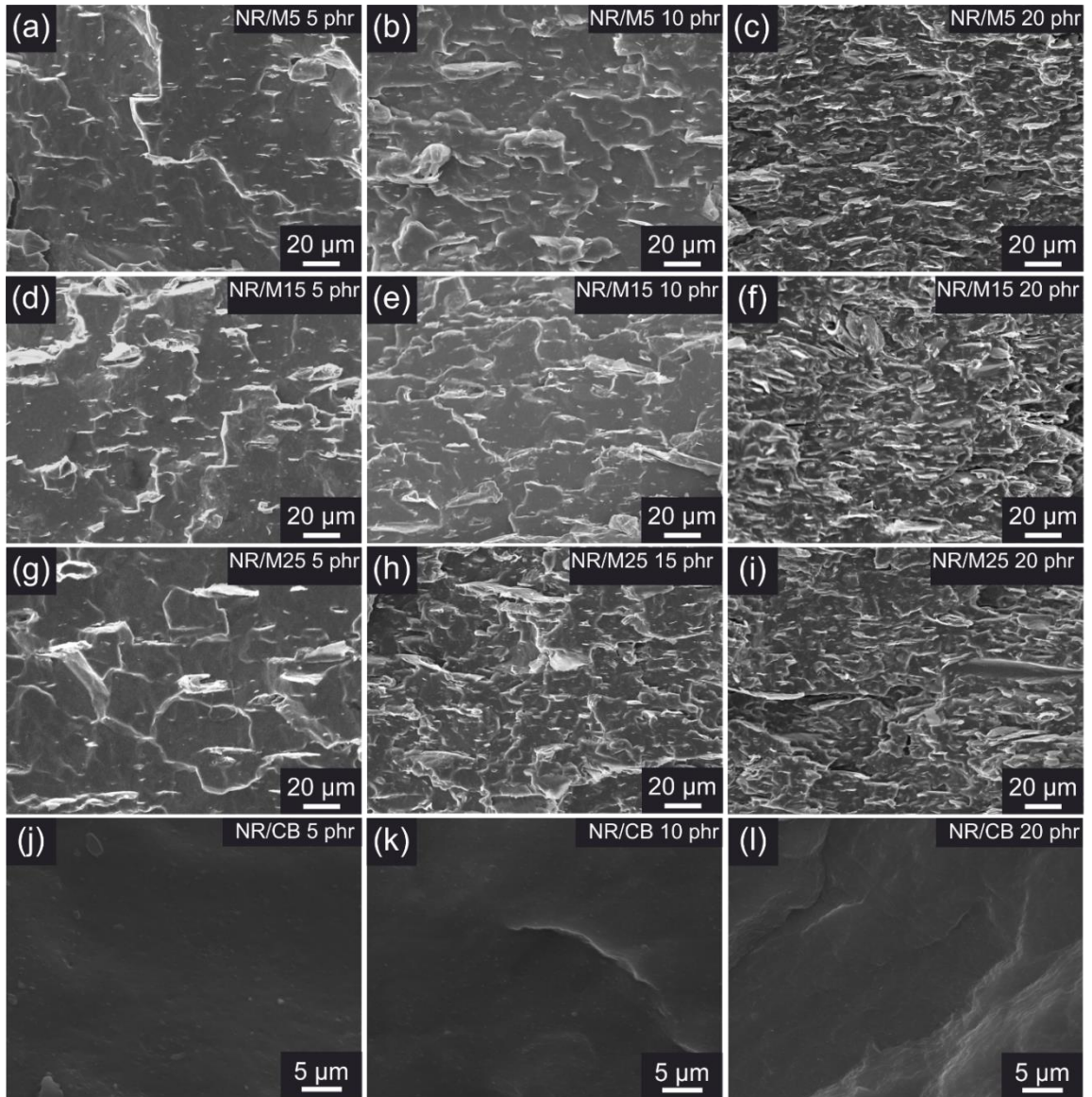
Figure 5.2 SEM micrographs showing microstructures of cross-sectional surfaces of the nanocomposites samples: (a-c) NR/M5-5, 10 and 20 phr, (d-f) NR/M15-5, 10 and 20 phr, (g-i) NR/M25-5, 15 and 20 phr and (j-l) NR/CB-5, 10 and 20 phr.
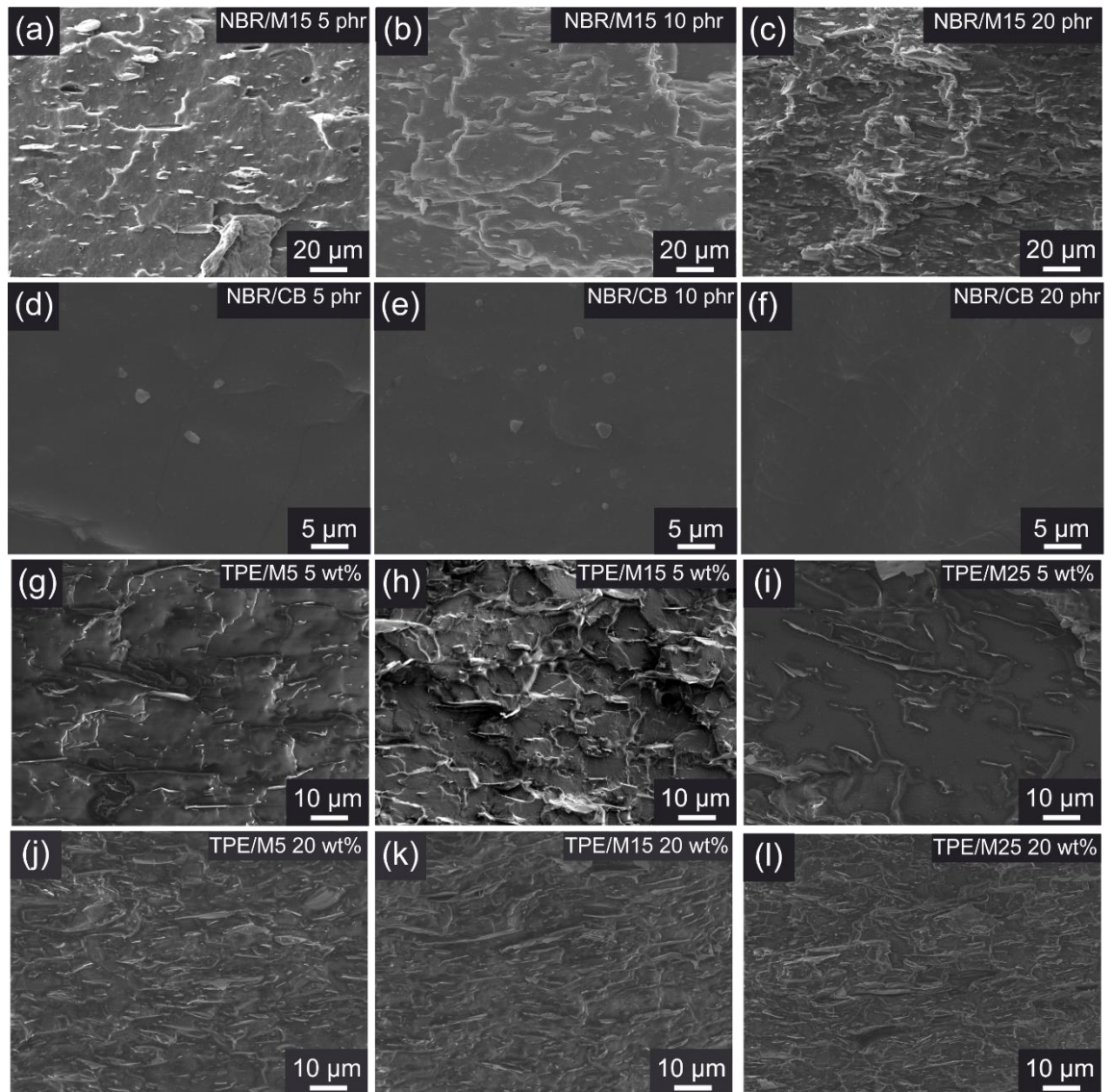
Figure 5.3 SEM micrographs showing microstructures of cross-sectional surfaces of the nanocomposites samples: (a-c) NBR/M15-5, 10 and 20 phr, (d-f) NBR/CB-5, 10 and 20 phr, (g-i) TPE reinforced by 5 wt% of M5, M15 and M25 GNPs and (j-l) TPE reinforced by 20 wt% of M5, M15 and M25 GNPs.

5.3.2 Dimensional Swelling

The mass uptake is defined as $M(t) = \frac{W(t) - W(0)}{W(0)}$, where $W(0)$ and $W(t)$ are the weight of dry samples and the weight measured at time t, respectively. The equilibrium of the swelling processes was indicated by the plateau of the curves of $M(t)$ against time. The mass uptake data for four representative samples are shown in **Figure 5.4** and the mass uptake data for all samples tested is shown in **Figure 5.5**.
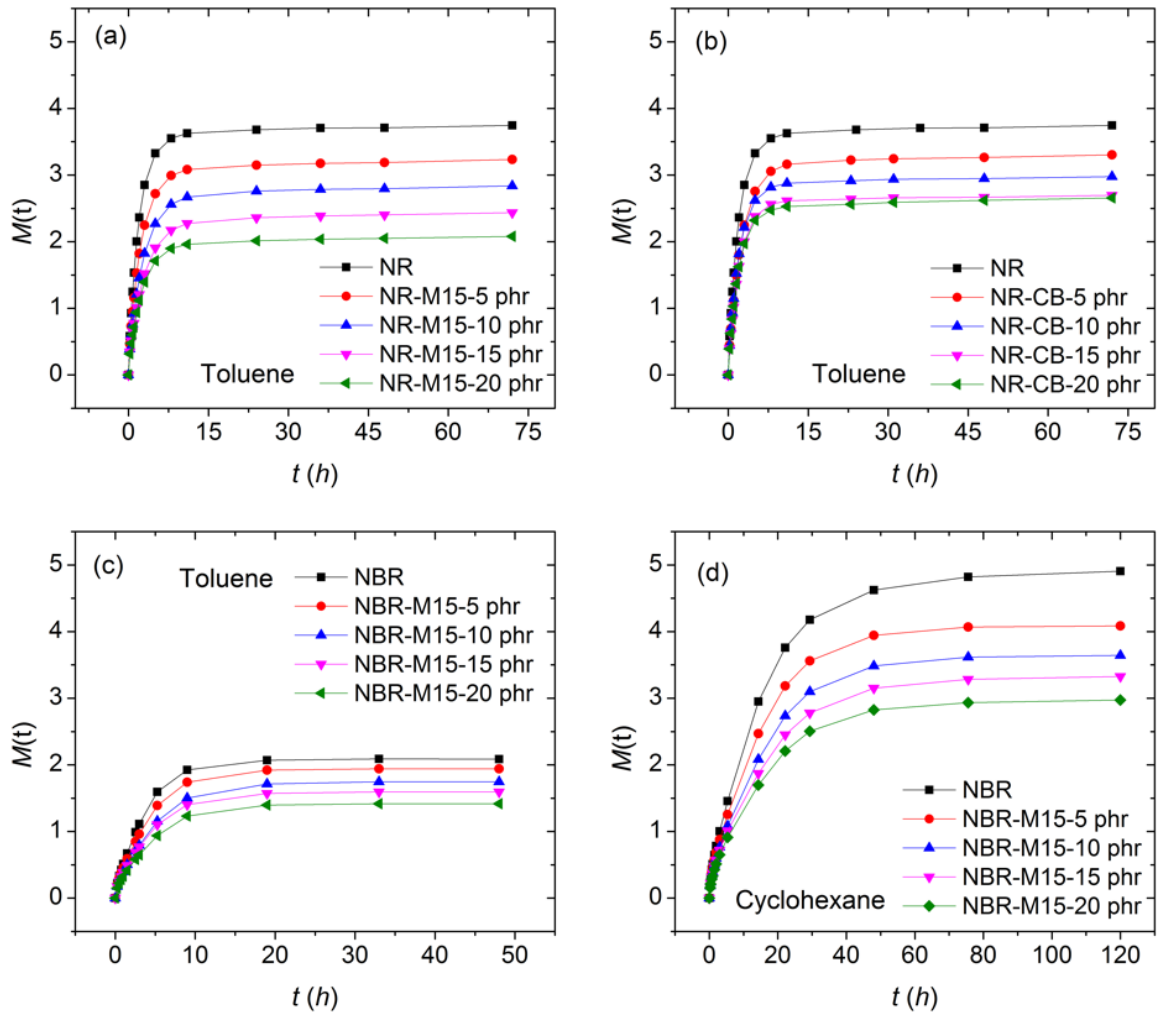
Figure 5.4 Mass uptake of toluene against time of the measurements for the nanocomposites samples: (a) NR-M15, (b) NR-CB, (c) NBR-M15; mass uptake of toluene against time of (d) NBR-M15.

159
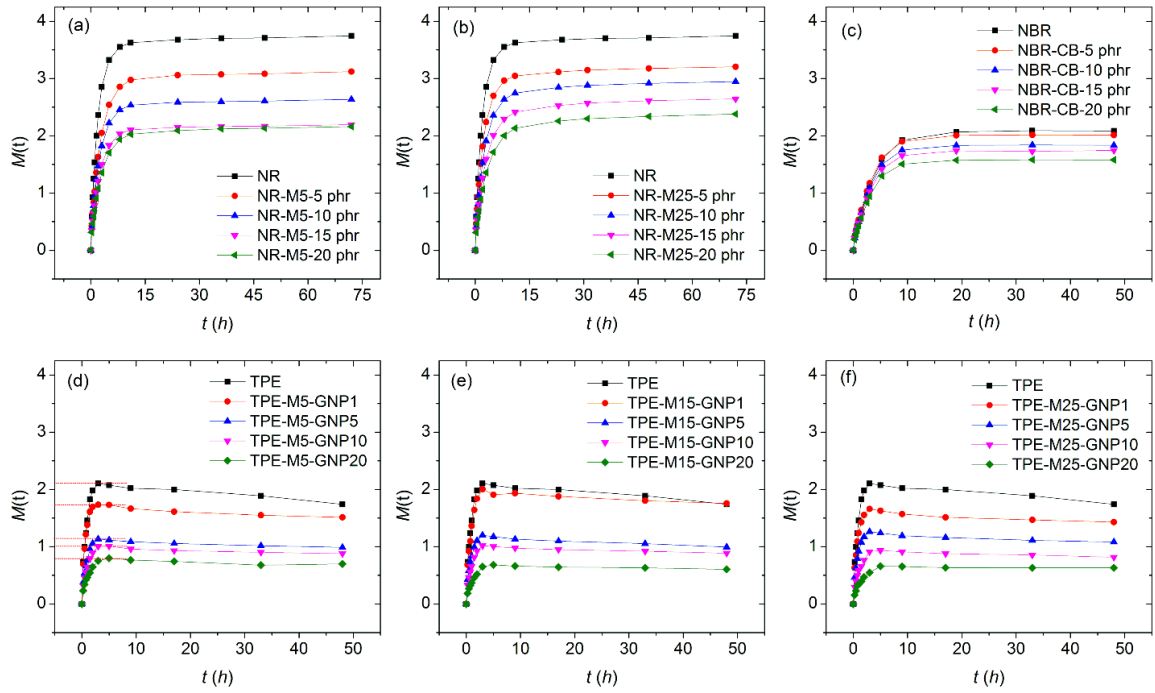
Figure 5.5 Mass uptake of toluene against time of the measurements for the nanocomposites samples: (a) NR-M5, (b) NR-M25, (c) NBR-CB, (d) TPE-M5, (e) TPE-M15 and (f) TPE-M25. For TPE in (d-f), the materials were dissolved slowly in toluene and therefore, the highest M(t) was taken for the saturation point for each material, as an example highlighted in (d).

The measurements of the sample dimensions were carried out both upon the unswollen samples and also after the swelling process reached equilibrium. **Figure 5.6** shows the swelling ratios of the volume, diameter and thickness at the equilibrium plotted against the volume fraction of filler, for the four respresentative samples: NR reinforced by **(a)** M15 GNPs and **(b)** carbon black immersed in toluene, and **(c)** NBR reinforced by M15 GNPs swollen in toluene and **(d)** cyclohexane. The swelling ratios for all the samples studied are shown in **Figure 5.7**. It is apparent that the addition of both GNPs and carbon black (CB) into the elastomers leads to a reduction of the volume swelling ratio (V_e/V_0) and therefore improved the liquid barrier properties of the elastomers. If we compare **Figure 5.6 (a)** with **(b)**, it can be seen that the GNPs reinforced natural rubber more efficiently than carbon black. This is attributed to the higher aspect ratio of the GNPs that

formed a larger interfacial area per volume (specific interfacial area) than the carbon black nanoparticles in the nanocomposites.

When the elastomers started swelling, the GNPs provided a higher restraining force than CB to reduce the swelling ratio.[1] However, the GNP-reinforced elastomers swelled anisotropically, while the CB-filled materials swelled more or less isotropically. More specifically, as shown in **Figure 5.6 (a)**, both the diameter (d_e/d_0) and thickness (h_e/h_0) swelling ratios of the unfilled natural rubber were similar (~1.70) at equilibrium. With increasing GNP loading, the diameter (in-plane) swelling ratio decreased, whereas the thickness (out-of-plane) swelling ratio increased. Such a phenomenon is believed to take place due to the in-plane orientation of the nanoplatelets, which originated from the compression moulding process.[5] The microstructure of both thermoset rubbers and thermoplastic elastomers shown in the SEM graphs in **Figure 5.1-5.3** clearly demonstrates the preferred in-plane orientation of the flakes. In addition, in a previous study [5], the high degree of orientation of the GNPs in rubber/GNP nanocomposites has been characterised using advanced techniques including polarised Raman spectroscopy (reviewed in **Chapter 2**) and X-ray computed tomography (CT) scans. The in-plane-aligned nanoplatelets carried the stress from the in-plane direction of the nanocomposites and hence restrained efficiently the diameter swelling. It is interesting to note, however, that the GNP-filled rubbers displayed higher thickness swelling ratio than the unfilled rubber, similarly to what has already been reported for fibre-filled rubbers.[6, 7] Similar anisotropic swelling behaviour can be observed in **Figure 5.6 (c)** and **(d)** for GNP-filled NBR, swollen in different solvents (toluene and cyclohexane).

From **Figure 5.6** it can also be concluded that the swelling ratio also depends on the types of both matrix and solvent. **Figures 5.6 (a)** and **(c)** show the swelling behaviours in toluene of both NR and NBR reinforced by M15 GNP. The volume swelling ratio of NBR-M15 samples is clearly lower than NR-M15 samples. When the solvent is changed to cyclohexane, the NBR-M15 samples exhibited greater volume swelling ratio than in toluene, which can be realised by comparing **Figures 5.6 (c)** and **(d)**. This phenomenon

will be explained in the next section on the basis of the statistical mechanics approach proposed by Flory and Rehner.[8, 9]

It should also be noted that the lateral size of the GNPs plays a role in improving the liquid barrier properties of the nanocomposites. It can be seen in **Figure 5.7** that both NR and TPE nanocomposites filled with the M25 GNPs showed lower volume (V_e/V_0) and diameter (d_e/d_0) swelling ratios than the samples filled with M5 GNPs. This is because the larger flakes possess higher aspect ratio that is beneficial for effective stress transfer, and therefore they are able to restrain the swelling of the elastomers more efficiently.[10]
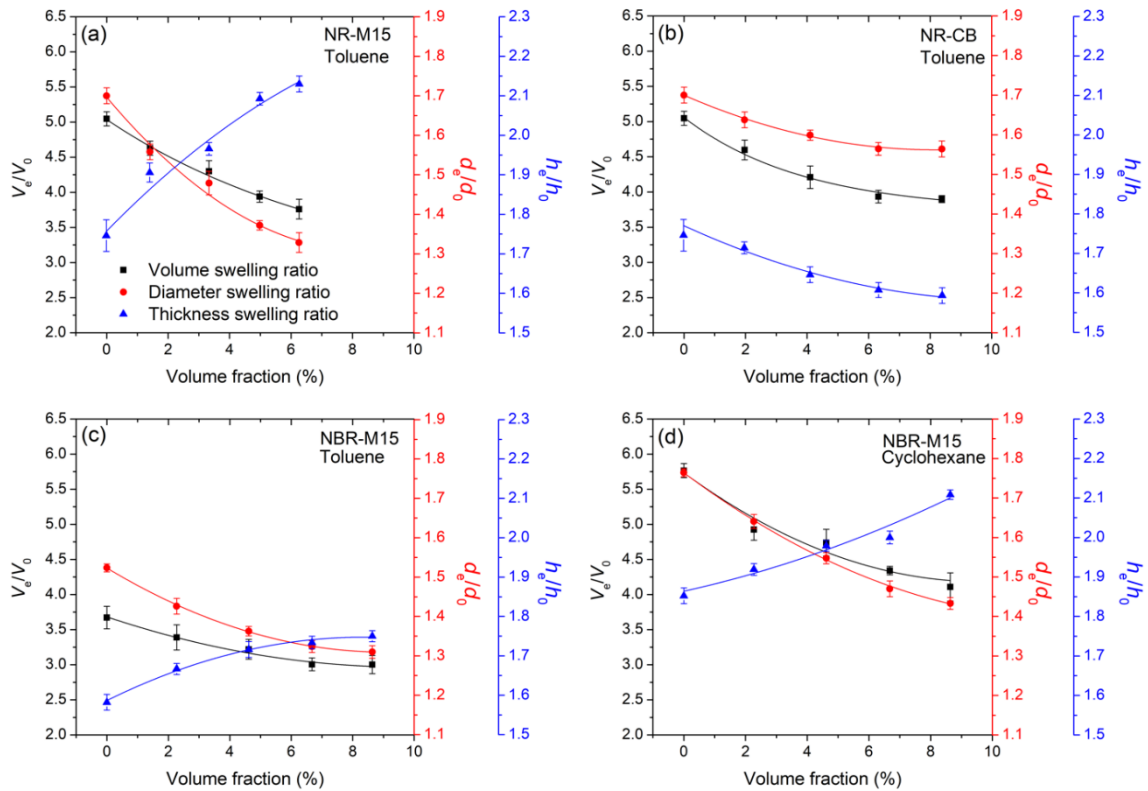
Figure 5.6 Swelling ratio at the equilibrium of the volume (V_e/V_0), diameter (d_e/d_0) and thickness (h_e/h_0) against the volume fraction of the filler for (a) NR-M15-GNP nanocomposites swollen in toluene, (b) NR-CB nanocomposites swollen in toluene, (c) NBR-M15-GNP nanocomposites swollen in toluene and (d) NBR-M15-GNP nanocomposites swollen in cyclohexane. The lines are a guide to the eye.
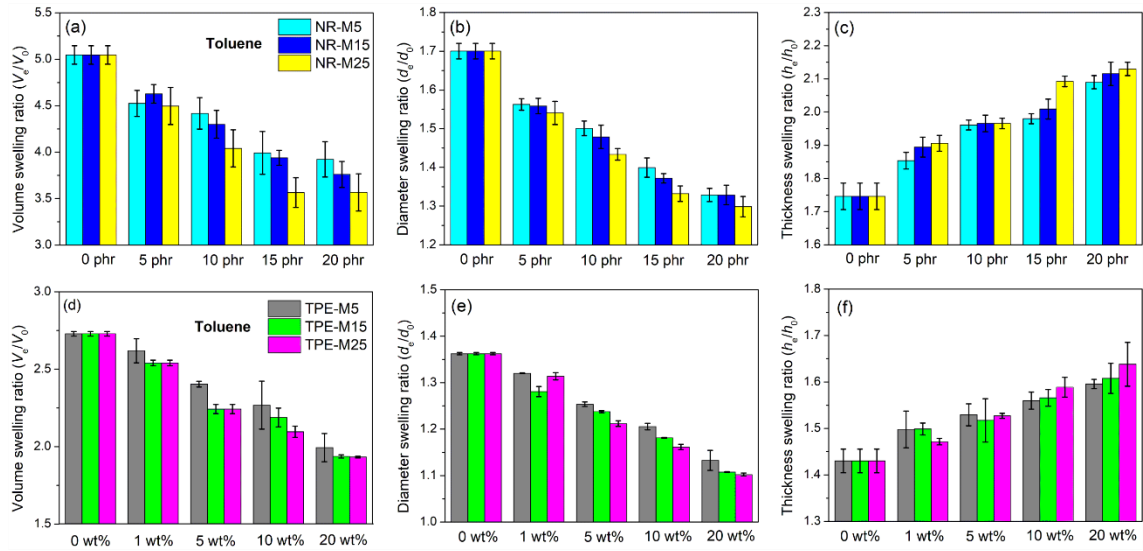
Figure 5.7 Swelling ratio at the equilibrium of the volume (V_e/V_0), diameter (d_e/d_0) and thickness (h_e/h_0) against the volume fraction of the filler for (a-c) NR-M5, NR-M15 and NR-M25 nanocomposites and (d-f) TPE-M5, TPE-M15 and TPE-M25 nanocomposites swollen in toluene to compare the reinforcing efficiency for different lateral size of the flakes. As can be seen, the larger flakes (M25), performed more efficiently than M15 than M25 in constraining the volume swelling and the dimeter swelling for both samples, assuming the crosslinking density of the samples is not changed significantly by the addition of GNPs.

5.3.3 Theoretical Analysis of Anisotropic Swelling

A theoretical analysis of the anisotropic swelling of the filled elastomers is undertaken based on the Flory-Rehner and Treloar's studies of rubber elasticity [8, 9, 11]. The equations that have been derived enable us to determine and predict the anisotropic swelling of elastomers reinforced by oriented-GNPs and to understand how nanoplatelets reinforce elastomers biaxially. The principle of the theory is shown in **Figure 5.8**, where the dimensional changes of the swollen rubber are linked to the change of solvent uptake. Assuming that the volumes of rubber and solvent in the swollen material are additive, the volume fraction of the solvent in the swollen rubber is given by

$$\phi_1 = \frac{n_1 v_1}{n_1 v_1 + n_2 v_2} \tag{5.1}$$

and the volume fraction of the rubber in the swollen sample is

$$\phi_2 = \frac{n_2 v_2}{n_1 v_1 + n_2 v_2} \tag{5.2}$$

where n_1 and n_2 are the respective numbers of moles of the solvent and the elastomer in the swollen gel at equilibrium; v_1 and v_2 are the molar volumes of the solvent and the elastomer, respectively [8, 12]; These volume fractions can also be related to the change in dimensions of the disc-shaped sample during swelling and in particular the volume fraction of rubber in the swollen material at equilibrium is given by

$$\phi_2 = \frac{\frac{\pi}{4} d_0^2 h_0}{\frac{\pi}{4} d_e^2 h_e} \tag{5.3}$$

where d_0 and d_e are the diameters of the disc at unswollen and equilibrium swollen state, while h_0 and h_e are the thickness of the disc at unswollen and equilibrium swollen state. These parameters can be seen in **Figure 5.8 (a)**. The volume swelling ratio is also equal to the reciprocal of the volume fraction of rubber in the swollen material since

$$\frac{\frac{\pi}{4} d_e^2 h_e}{\frac{\pi}{4} d_0^2 h_0} = (d_e/d_0)^2 \, (h_e/h_0) = 1/\phi_2 \tag{5.4}$$

164
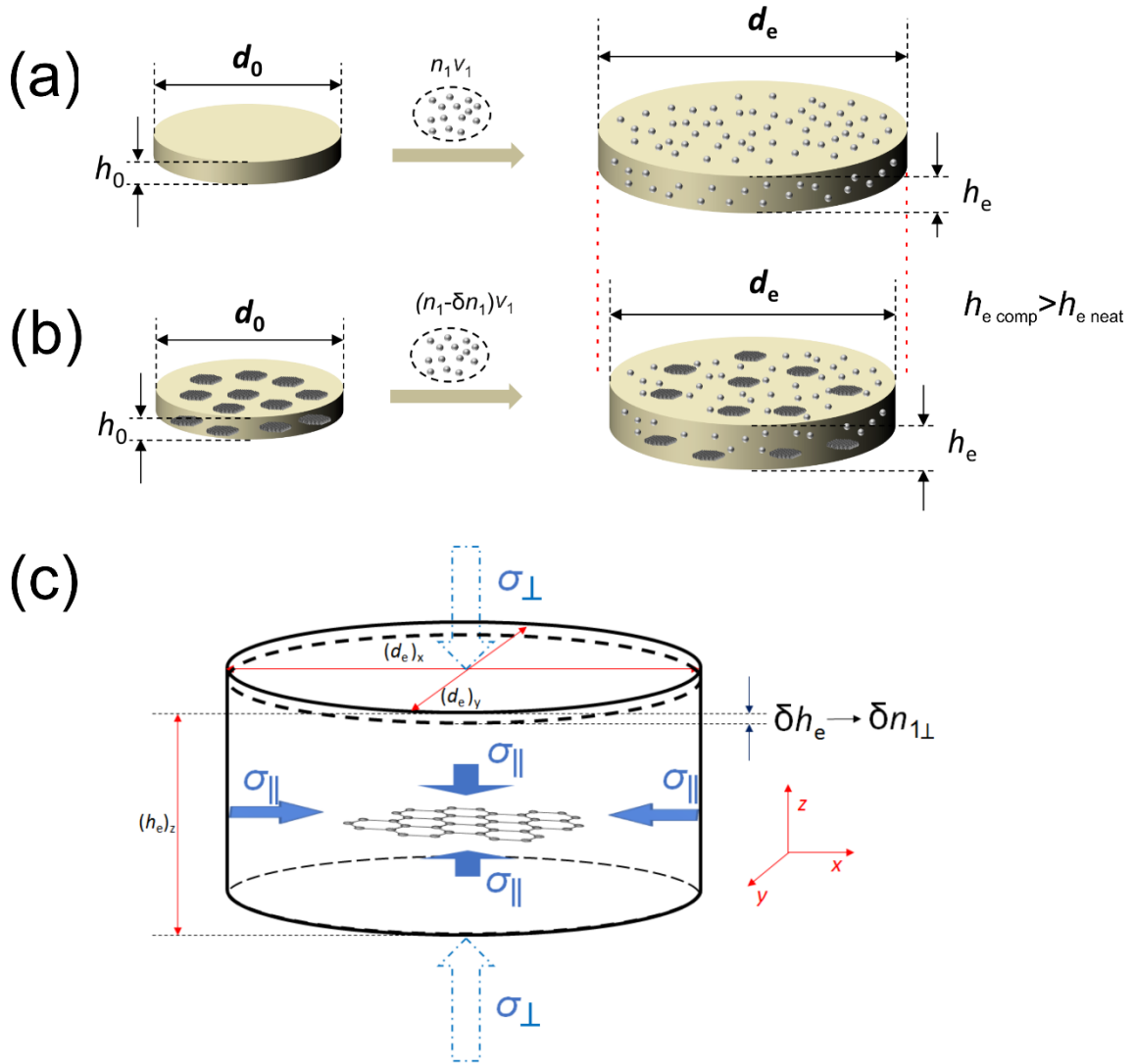
Figure 5.8 (a) Schematic diagram of the swelling of an unfilled elastomer and (b) an elastomer filled with biaxially-aligned 2D materials, where d_0 and d_e are the diameters at the unswollen state and at the equilibrium of swelling, respectively; n_1 is the number of moles of the absorbed solvent molecules, v_1 is the molar volume of the solvent, δn_1 is the change of moles of the solvent absorbed by the elastomer after addition of GNPs. (c) Schematic diagram of the swollen state of the GNP-filled elastomer, where $\sigma_\perp$ and $\sigma_\parallel$ are the stresses contributed by the GNPs at the cross-plane and in-plane directions, respectively. The principal axes x, y, z have been defined in the figure. The diameters of the discs, $(d_e)_x$ and $(d_e)_y$, and the thickness of the disc, $(h_e)_z$, were used order to express the 3-dimensional deformation of swelling process, where $(d_e)_x$ and $(d_e)_y$ should be equal.

The addition of GNPs leads to a reduction of the volume of solvent uptake of $\delta n_1 v_1$ as the result of biaxial (in-plane) stress transfer from the matrix to the nanoplatelets (**Figure 5.8b**). It is assumed that the overall force contributed by the filler gives rise to constraint of the elastomers during swelling that leads to the reduction of the number of moles of solvent uptake by δn_1. If we consider that the reduction of solvent uptake is caused by a combination of the overall in-plane and out-of-plane forces, then the in-plane force will reduce the solvent uptake by $\delta n_{1\parallel} v_1$ and the out-of-plane force reduces the solvent uptake by $\delta n_{1\perp} v_1$. As illustrated in **Figure 5.8 (c)**, the out-of-plane stress ($\sigma_\perp$) from the GNPs contributes an overall constraining force on the area of the circular plane ($\frac{\pi}{4} d_e^2$) at the equilibrium of $\sigma_\perp \frac{\pi}{4} d_e^2$, resulting in a reduction of the thickness at equilibrium of δh_e, and consequently a reduction of the number of moles of solvent uptake by $\delta n_{1\perp}$. Hence, the work done by the out-of-plane force is given by

$$\delta W_\perp = \sigma_\perp \frac{\pi}{4} d_e^2 \cdot \delta h_e \tag{5.5}$$

Based on the relationship between δh_e and $\delta n_{1\perp}$ shown in equation (4), equation (5) can be expressed as

$$\delta W_\perp = \sigma_\perp \cdot \delta n_{1\perp} v_1 \tag{5.6}$$

Figure 5.8 (c) shows the constraining effect of in-plane-aligned nanoplatelets on the swelling in the out-of-plane direction, where the swelling process involves only a small degree of deformation of the elastomer. In this case, the change in the Helmholtz free energy $\Delta A_\perp$ (for this small reduction of thickness of δh_e) is considered to be equal to the work done by the force, $\delta W_\perp$ [12]. At constant temperature and pressure, considering that the net volume (liquid and elastomer) change is zero during swelling, the work done ($\delta W_\perp$) gives a change (δ) in the Gibbs free energy of the swelling process ($\Delta G_\perp$). Thus,

$$\delta \Delta G_\perp = \Delta A_\perp = \delta W_\perp = \sigma_\perp \delta n_{1\perp} v_1 \tag{5.7}$$

In the process of swelling for a crosslinked polymer network, the Gibbs free energy change (ΔG) should be a combination of the free energy of dilution (ΔG_{mix}) and the free energy of elastic deformation (ΔG_{def}) of the materials from the unswollen network to the equilibrium swollen state, such that $\Delta G = \Delta G_{mix} + \Delta G_{def}$ [8, 12, 13]. In terms of partial differentials, equation (5.7) can then be written as

$$\left(\frac{\partial \Delta G}{\partial n_1}\right)_{(d_e)_x (d_e)_y} = \sigma_\perp v_1 = \frac{\partial \Delta G_{mix}}{\partial n_1} + \left(\frac{\partial \Delta G_{def}}{\partial n_1}\right)_{(d_e)_x (d_e)_y} \tag{5.8}$$

where $\partial \Delta G_{mix} / \partial n_1$ is free energy of mixing (dilution) from uncrosslinked unswollen state to the crosslinked equilibrium state [13]. The subscripts $(d_e)_x$ and $(d_e)_y$ represent the in-plane diameters in different principal axes as illustrated in **Figure 5.8 (c).**

The Flory-Huggins theory gives [13],

$$\frac{\partial \Delta G_{mix}}{\partial n_1} = RT_K \left[\ln\left(1 - \phi_2\right) + \phi_2 + \chi \phi_2^2 \right] \tag{5.9}$$

where R is the gas constant, T_K is the thermodynamic temperature, and χ is a dimensionless parameter which is dependent upon the polymer-solvent interaction. The term ΔG_{def} refers to the free energy of elastic deformation of the materials from unswollen network to the equilibrium swollen state. According to the theory of rubber elasticity for the deformation of Gaussian network [8], for a disc-shape sample with a volume of ($\frac{\pi}{4} d_0^2 h_0$) we have for equilibrium swelling,

$$\Delta G_{def} = \frac{\pi}{4} d_0^2 h_0 \frac{\rho R T_K}{2M_c} \left[\left(\frac{d_e}{d_0}\right)_x^2 + \left(\frac{d_e}{d_0}\right)_y^2 + \left(\frac{h_e}{h_0}\right)_z^2 - 3 \right] \tag{5.10}$$

where ρ is the density of the elastomer and M_c is the molar mass of the network chains between crosslinks. The subscripts *x*, *y* and *z* represent the principal axes as in **Figure 5.8 (c)**, where $(d_e/d_0)_x$ should be equal to $(d_e/d_0)_y$. Combining equation (10) with equations (2 and 3), the partial differential equation (8) can be solved to give:

$$\left(\frac{\partial \Delta G_{\text{def}}}{\partial n_1}\right)_{(d_e)_x (d_e)_y} = \left(\frac{\partial \Delta G_{\text{def}}}{\partial h_e}\right)\left(\frac{\partial h_e}{\partial n_1}\right)_{(d_e)_x (d_e)_y} = \frac{\rho R T_K}{M_c}\frac{h_e}{h_0}\frac{v_1}{(d_e/d_0)^2} = \frac{\rho R T_K}{M_c}v_1\phi_2\left(\frac{h_e}{h_0}\right)^2 \tag{5.11}$$

Subsequently, by combining equations (5.8), (5.9) and (5.11), the stress from the GNPs in the out-of-plane direction $(\sigma_\perp)$ is given by

$$\sigma_\perp = \frac{R T_K}{v_1}\left[\ln\left(1-\phi_2\right)+\phi_2+\chi\phi_2^2\right] + \frac{\rho R T_K}{M_c}\phi_2\left(\frac{h_e}{h_0}\right)^2 \tag{5.12}$$

and if we substitute equation (5.4) into (5.12)

$$\sigma_\perp = \frac{R T_K}{v_1}\left[\ln\left(1-\phi_2\right)+\phi_2+\chi\phi_2^2\right] + \frac{\rho R T_K}{M_c\phi_2}\left(\frac{d_e}{d_0}\right)^{-4} \tag{5.13}$$

As suggested from the results in **Figure 5.6 and 5.7**, the swelling in the out-of-plane direction (thickness) was not restrained by GNPs but actually became higher than that of the unfilled elastomer. Hence, we can assume that the nanoplatelets are able to reinforce only in the in-plane directions of the nanocomposite discs during the swelling process and the elastomer is not subjected to any mechanical constraint from the GNPs in the out-of-plane direction. The stress given by the flakes in the out-of-plane direction $(\sigma_\perp$, shown in **Figure 5.8c**) is therefore assumed to be 0. Consequently, the original Flory-Rehner equation is modified for the case of in-plane aligned GNP reinforced elastomers to give

$$\left[\ln\left(1-\phi_2\right)+\phi_2+\chi\phi_2^2\right] + \frac{\rho v_1}{M_c}\left(\frac{h_e}{h_0}\right)^2\phi_2 = 0 \tag{5.14}$$

or expanding the logarithm term

$$\frac{\rho v_1}{M_c} = \left(\frac{1}{2} - \chi\right) \left(\frac{h_e}{h_0}\right)^{-2} \phi_2 \tag{5.15}$$

and

$$[\ln(1-\phi_2) + \phi_2 + \chi\phi_2^2] + \frac{\rho v_1}{M_c(d_e/d_0)^4 \phi_2} = 0 \tag{5.16}$$

or expanding the logarithm term

$$\frac{\rho v_1}{M_c} = \left(\frac{1}{2} - \chi\right) \left(\frac{d_e}{d_0}\right)^4 \phi_2^3 \tag{5.17}$$

Equation (5.16) mirrors the dependence of biaxial strain on the volume swelling ratio for rubbers swollen in solvents under biaxial tension suggested by Treloar [11]. For unfilled elastomers with uniform structures, isotropic swelling is expected. In this case we have (based on equation (5.4)) $d_e/d_0 = h_e/h_0 = (1/\phi_{2\,neat})^{1/3}$ and both equations (5.15) and (5.17) lead to the well-accepted Flory-Rehner theory [8, 13],

$$\rho v_1/M_c \approx \left(\frac{1}{2} - \chi\right) (1/\phi_{2\,neat})^{-5/3} \tag{5.18}$$

where $(1/\phi_{2\,neat})$ is the volume swelling ratio of a neat elastomer (as ϕ_2 is the volume fraction of the elastomer of the swollen gel at the equilibrium of swelling).

By combining equation (5.18) with equations (5.15) and (5.17), we obtain the final equations for the diameter and thickness swelling ratios of elastomers reinforced with oriented 2D materials,

$$d_{e}/d_{0}=(1/\phi_{2\,\text{neat}})^{-5/12}\,(1/\phi_{2})^{3/4} \tag{5.19}$$

$$h_{e}/h_{0}=(1/\phi_{2\,\text{neat}})^{5/6}\,(1/\phi_{2})^{-1/2} \tag{5.20}$$

where $(1/\phi_{2})$ is the overall volume swelling ratio for nanocomposites. When the material is a neat polymer, equations (5.19) and (5.20) are transformed to $d_{e}/d_{0}=h_{e}/h_{0}=(1/\phi_{2\,\text{neat}})^{1/3}$, and the swelling of the materials obeys the equation for isotropic swelling (equation 5.18).

Equations (5.19) and (5.20) are able to predict the dependence of the in-plane and out-of-plane dimensional swelling ratios on the volume swelling ratio for elastomers reinforced by 2D materials, assuming that the fillers are well-oriented in-plane. The products (d_{e}/d_{0}) and (h_{e}/h_{0}) are the respective swelling ratios in the in-plane (diameter) and cross-plane (thickness) directions at equilibrium. It is very important to point out that the newly-derived equation (20) for the thickness swelling ratio predicts an increasing trend with decreasing volume swelling ratio, in agreement with the experimental results reported in **Figure 5.6 (a,c,d) and 5.7**. The products $(1/\phi_{2\,\text{neat}})^{-5/12}$ and $(1/\phi_{2\,\text{neat}})^{5/6}$ contain the information upon the polymer-solvent interaction χ, while based on equation (5.18), other parameters including the density of polymer ρ, the molar volume of solvent v_{1} and the molar mass between crosslinks M_{c} cancel out and so does not affect the difference between in-plane and out-of-plane swelling.

5.3.4 Application of the Anisotropic Swelling Theory

The application of equations (5.19) and (5.20) to the experimental results for various combinations of rubber/filler/solvent are shown in **Figure 5.9 (a-e)**. It can be seen that the theoretical predictions demonstrate excellent consistency with the anisotropic swelling behavior of different elastomers filled with graphene nanoplatelets, while the samples were tested in 2 different solvents including toluene and cyclohexane. For the neat polymer, as highlighted (with a blue arrow) in **Figure 5.9 (a)**, the intersection of the two curves of equations (5.19) and (5.20) represents the theoretical dependence of d_e/d_0 and h_e/h_0 on the volume swelling ratio ($1/\phi_2$), where $d_e/d_0=h_e/h_0=(1/\phi_2)^{1/3}$. As for the experimental results, the diameter and thickness swelling ratios of the neat polymer showed a slight difference compared to the theoretical values. This can be attributed to a small degree of orientation of the chains of the amorphous polymer that was induced during compression moulding [14, 15]. With increasing filler loading, the volume and the diameter swelling ratios were reduced; however, an increase of the thickness swelling ratio was observed as shown in **Figure 5.9 (a)**. Almost identical swelling behaviours were revealed for all other types of elastomers filled with graphene nanoplatelets and swollen in different solvents (**Figure 5.9 b-e**). Regarding the CB-filled samples (NR and NBR matrices), the dimensional swelling should be isotropic, since carbon black is a spherical filler. Therefore, a theoretical curve based on the relationship: $d_e/d_0=h_e/h_0=(1/\phi_2)^{1/3}$ is plotted in **Figure 5.9 (f)**. The experimental results again exhibit excellent consistency with the theory.

From the analysis of the experimental results and the application of the newly-proposed equations, the anisotropic swelling phenomenon in elastomers reinforced by aligned 2D materials is quantified, where the thickness swelling ratio increases with increasing filler loading. The physical meaning of this phenomenon is that the macromolecular network of the elastomers should be treated as incompressible, with a Poisson's ratio of ~0.5 [12]. In the process of swelling under small strains, the deformation of the rubber networks can be modelled by that of a Gaussian network (equation 5.10) [8, 9, 12, 13]. In this case, when a biaxial strain is applied in the two principal axes of a material, there is a

consequential Poisson strain along the other principal axis. For the nanocomposites in the present study, it can be understood that the graphene nanoplatelets enabled the application of a biaxial constraining strain on the elastomer matrices during swelling by in-plane shear stress (equivalent to lateral compression). As a consequence, this resulted in increasing strain in the out-of-plane axis. Since increased solvent uptake can be induced by increasing tensile strain [12], it can be understood that the elastomers absorbed less solvent in the directions where the GNPs are oriented (in-plane), and on the other hand, absorbed more solvent in the direction perpendicular to the filler orientation (out-of-plane) experiencing the Poisson strain.

The essential reason leading to the increased out-of-plane swelling (with more loadings of GNPs oriented in-plane), can be attributed to the orientation of the rubber network struture due to the addition of aligned GNPs. Since the hot press resulted in in-plane orientation of the GNPs, it can be understood easily that the polymer network at the interface region can be oriented in-plane. The counter-intuitive phenomenon found by Treloar [11, 12] is that the swelling ratio of a rubber increases under tensile force, where the tension given to the rubber distorts the network structure and opens more gap (free volume) of the network along the direction of the applied force. For the case of oriented 2D materials filled elastomers, the 2D materials can also distort the 3D network structures of the rubber. In the in-plane direction, the polymer networks are oriented at the filler/matrix interfaces, where swelling is hindered; on the other hand, the network aligned in the perpendicular direction without contact to the filler can have more free volume, resulting in solvent segragation in different directions and therefore greater degree of swelling ratio in the out-of-plane direction.
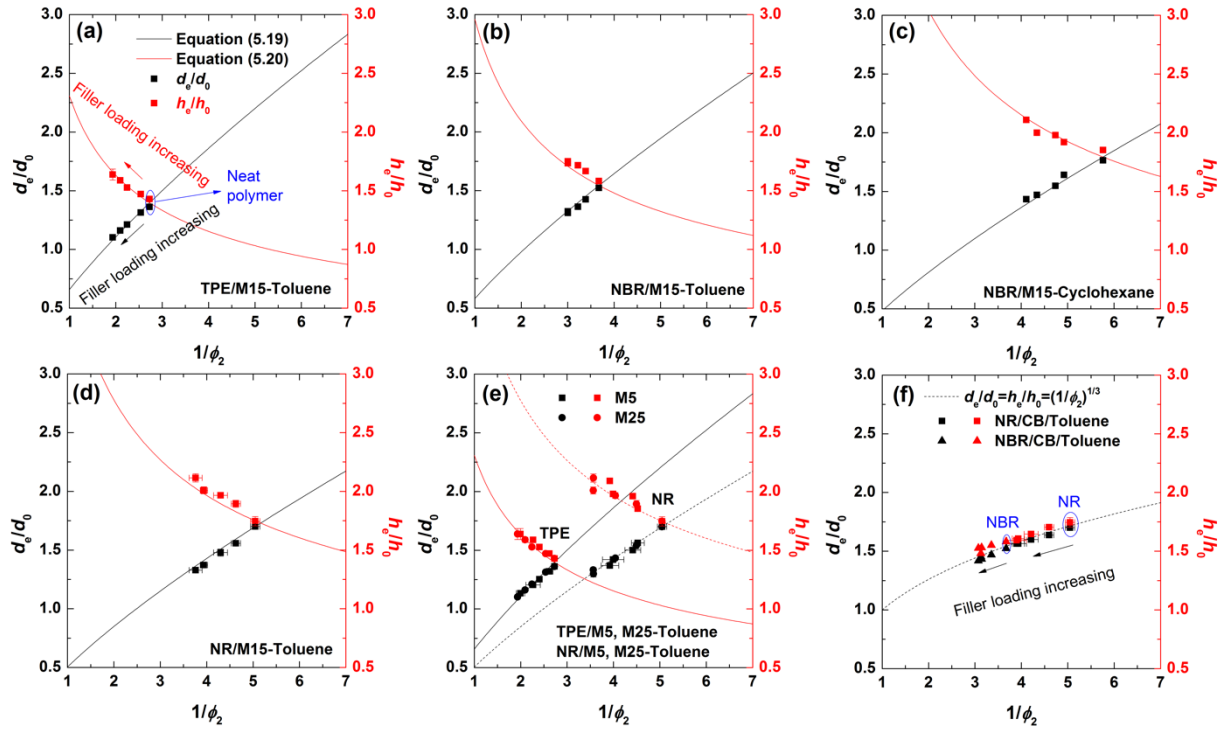
Figure 5.9 The dependence of dimensional swelling ratios (d_e/d_0, h_e/h_0) on volume swelling ratios ($1/\phi_2$) for the samples (a) TPE/M15 GNP in toluene, (b) NBR/M15 GNP in toluene, (c) NBR/M15 in cyclohexane, (d) NR/M15 in toluene, (e) TPE/M5, TPE/M25 GNP and NR/M5, NR/M25 GNP in toluene and (f) NR/CB and NBR/CB in toluene, plotted with theoretical predictions.

5.3.5 Reinforcing Efficiency of the GNP

The anisotropic swelling induced by GNP orientation was analysed successfully. It is possible to quantify the individual parameters of the GNPs that determine the swelling ratio of the nanocomposites. In order to achieve this, the anisotropic modulus and anisotropic swelling of the nanocomposites are examined comparatively.

The osmotic (swelling) pressure (Π) from the solvent to the elastomers is given by [12],

$$\Pi = -(\,RT_K/v_1\,)\ln(\,p/p_0\,) \tag{5.21}$$

where R is the gas constant, T_K is the Kelvin temperature, v_1 is the molar volume of the pure liquid, p is the vapour pressure of the liquid component in equilibrium with the mixture (swollen rubber) and p_0 is the saturation vapour pressure of pure liquid. The swelling pressure is dependent only upon the type of the solvent and defined as the pressure that keeps an elastomer swollen at equilibrium [12]. Hence, the swelling pressures from the solvent to the swollen elastomer should be the same for either the parallel ($\Pi_\parallel$) or perpendicular ($\Pi_\perp$) directions, relative to the GNP orientation (in-plane). For small strains in the swelling process

$$\Pi_\parallel = \Pi_\perp = E_\parallel \varepsilon_\parallel = E_\perp \varepsilon_\perp \tag{5.22}$$

where $E_\parallel$ and $E_\perp$ are the uniaxial moduli of the nanocomposites parallel (*x* or *y*) and perpendicular (*z*) to the filler orientation, respectively, and $\varepsilon_\parallel$ and $\varepsilon_\perp$ are the corresponding strains at equilibrium of swelling. Replacing the swelling strains with the swelling ratios, we have,

$$\frac{E_\parallel}{E_\perp} \simeq \frac{h_e/h_0 - 1}{d_e/d_0 - 1} \tag{5.23}$$

The same relationship was also obtained by Coran *et al*. for rubber/carbon fibre composites under swelling [6]. The stiffness parallel to the filler orientation ($E_\parallel$) is related to the modulus values measured parallel to the rubber sheets, which can be considered as the modulus of the composites (E_c). The stiffness perpendicular to the filler orientation can be considered equal to the stiffness of the neat matrix (E_m), since it was found that the GNPs did not constrain the swelling in the out-of-plane direction. Hence, theoretically, we should have $\frac{E_c}{E_m} \approx \frac{E_\parallel}{E_\perp} \approx \frac{h_e/h_0 - 1}{d_e/d_0 - 1}$. A similar method to link the results of mechanical tests to swelling testing was also carried out by Goettler *et al*. [16] To examine this relationship,

174

the mechanical properties were obtained by tensile tests and the stress-strain curves are presented in **Figure 5.10**. The modulus values for all the samples are listed in **Table 5.6**.
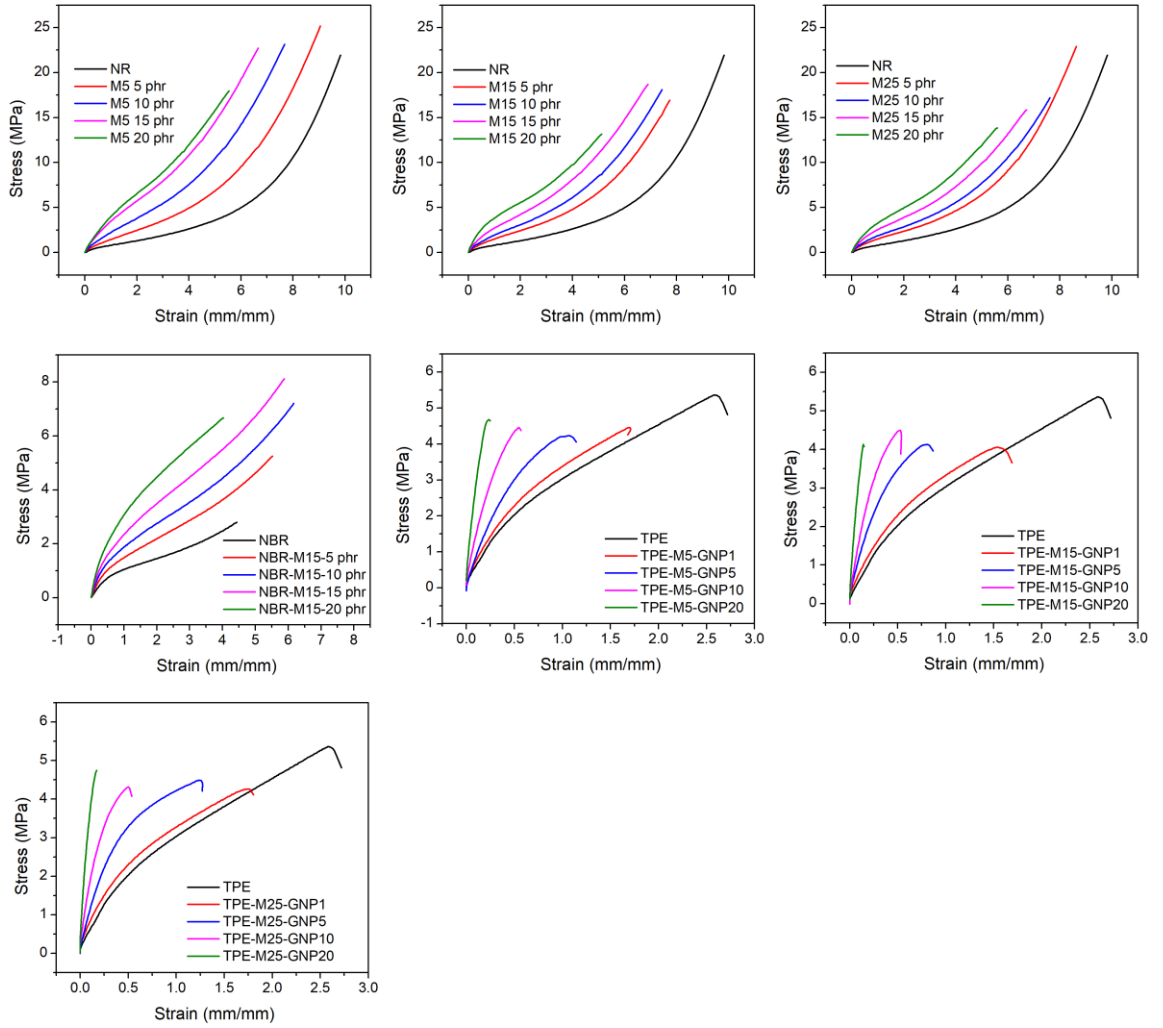
Figure 5.10 Representative stress-strain curves of all samples.

Table 5.6 The modulus values obtained from tensile tests. Since swelling only involves small strain, the moduli were acquired by linear fittings on the stress-strain curves below the swelling strains (<70% strain for NR and NBR, <30% strain for TPE), rather than taking 100% modulus as suggested by ASTM D412 for rubber vulcanizates.

Materials	Modulus (MPa)
NR	0.66 ± 0.03
NR-M5-5 phr	1.00 ± 0.01
NR-M5-10 phr	1.34 ± 0.02
NR-M5-15 phr	1.86 ± 0.04
NR-M5-20 phr	2.37 ± 0.04
NR-M15-5 phr	0.98 ± 0.03
NR-M15-10 phr	1.26 ± 0.08
NR-M15-15 phr	1.80 ± 0.05
NR-M15-20 phr	2.26 ± 0.03
NR-M25-5 phr	1.09 ± 0.04
NR-M25-10 phr	1.50 ± 0.04
NR-M25-15 phr	1.98 ± 0.06
NR-M25-20 phr	2.43 ± 0.04
NBR	0.73 ± 0.04
NBR-M15-5 phr	1.02 ± 0.04
NBR-M15-10 phr	1.30 ± 0.04
NBR-M15-15 phr	1.58 ± 0.07
NBR-M15-20 phr	1.79 ± 0.05
TPE	4.31 ± 0.11
TPE-M5-1 wt%	5.43 ± 0.20
TPE-M5-5 wt%	7.58 ± 0.13
TPE-M5-10 wt%	11.70 ± 0.40
TPE-M5-20 wt%	20.00 ± 0.42
TPE-M15-1 wt%	5.49 ± 0.17
TPE-M15-5 wt%	8.44 ± 0.32
TPE-M15-10 wt%	13.11 ± 0.74
TPE-M15-20 wt%	23.07 ± 0.72
TPE-M25-1 wt%	5.38 ± 0.36
TPE-M25-5 wt%	9.21 ± 0.32
TPE-M25-10 wt%	13.66 ± 0.74
TPE-M25-20 wt%	26.47 ± 0.72

The swelling strain ratios $(\frac{h_e/h_0\text{-}1}{d_e/d_0\text{-}1})$ obtained from swelling tests are plotted in **Figure 5.11** against the corresponding normalized modulus (E_c/E_m) for representative elastomer/GNP nanocomposites at different GNP loadings. It can be seen that the datapoints lie predominantly on the line with a slope of 1, indicating a linear relationship between the values of swelling strain ratios and the normalized moduli. Therefore, we can assume that equation (5.23) is applicable for the study of elastomer/GNP nanocomposite samples.
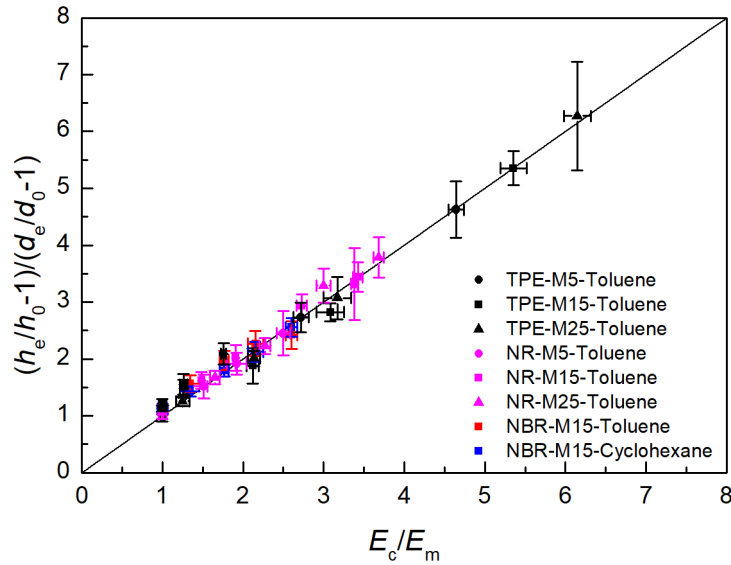
Figure 5.11 The swelling strain ratios [$(h_e/h_0\text{-}1)/(d_e/d_0\text{-}1)$] against the normalized modulus (E_c/E_m) obtained from tensile tests for all the samples.

The dimensional swelling ratios (d_e/d_0, h_e/h_0) can be substituted by equations (5.19) and (5.20). Hence, a theoretical relationship between the volume swelling ratio and the modulus of the nanocomposites (E_c/E_m) can be developed,

$$\frac{(1/\phi_{2\,\text{neat}})^{5/6}(1/\phi_2)^{-1/2}\text{-}1}{(1/\phi_{2\,\text{neat}})^{-5/12}(1/\phi_2)^{3/4}\text{-}1} = \frac{E_c}{E_m} \tag{5.24}$$

Based on previous research, the normalized modulus (E_c/E_m) of an elastomer reinforced by 2D materials is dependent upon the aspect ratio (s), the orientation factor (η_o) and the

filler volume fraction (V_f), while it is independent of the stiffness of the filler [10, 17]. For the swelling properties, since the filler particles are well aligned, the orientation factor (η_o) of the filler can be set equal to 1, in accordance with the experimental results in Section 5.3.2 and theoretical analysis in Section 5.3.3 and 5.3.4. Therefore,

$$\frac{(1/\phi_{2\,\text{neat}})^{5/6}(1/\phi_2)^{-1/2}-1}{(1/\phi_{2\,\text{neat}})^{-5/12}(1/\phi_2)^{3/4}-1}=1-V_f+0.056s^2V_f^2 \tag{5.25}$$

Equation (5.25) provides a relationship between the volume swelling ratio ($1/\phi_2$) and the filler parameters (aspect ratio and volume fraction). Quite importantly, it is clear that with increasing filler aspect ratio (M25>M15>M5) and increasing volume fraction, the swelling ratio ($1/\phi_2$) should be reduced, which is in agreement with the results shown in **Figure 5.12.** It is also interesting that equation (5.25) shows that the swelling behavior depends only on the volume fraction and aspect ratio of the filler, *s* but not upon its Young's modulus. This is because 2D fillers such as GNPs are effectivley infinitely stiff compared with the elastomer matrix [10].
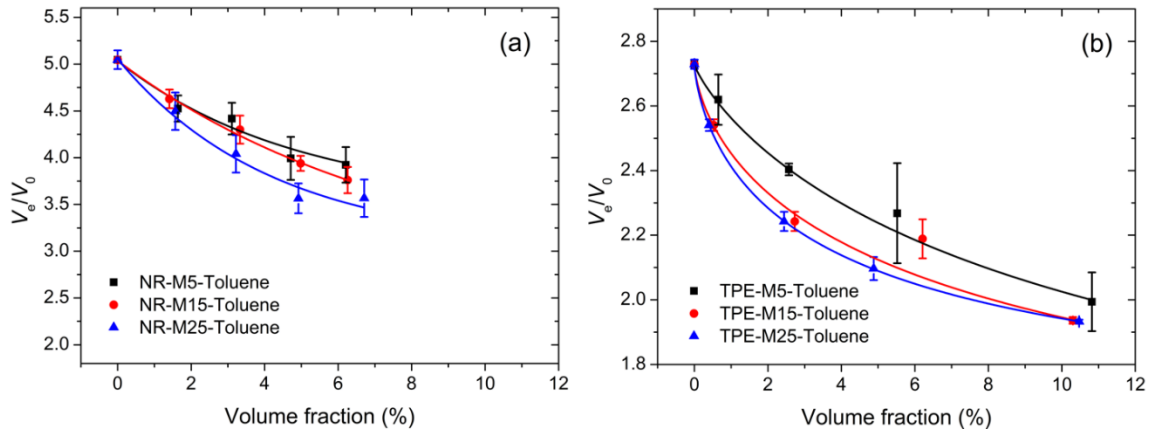
Figure 5.12 Volume swelling ratio (V_e/V_0) against volume fraction of the GNPs for (a) NR and (b) TPE, reinforced by M5, M15 and M25 GNPs. The increasing aspect ratio of the filler results in reducing volume swelling of the nanocomposites.

5.4 Conclusions

In this work, a number of elastomers were filled with different graphene nanoplatelets and carbon blacks to study the swelling behaviour of the nanocomposites in solvents. Both GNPs and CB were able to restrain the volume swelling ratio of the materials. It was found that the restraining efficiency of GNPs was higher than CB in volume swelling, as a result of the high aspect ratio of GNPs that created higher interfacial area per volume. It has been demonstrated that the compression moulding process clearly contributed to the in-plane orientation of the GNPs in the elastomer sheets, leading to anisotropic swelling of the nanocomposites. The swelling measurements revealed that the GNPs only reinforced the materials in the in-plane directions while no enhancement was found in the cross-plane direction. Moreover, the dimensional swelling ratio in the cross-plane direction became even greater with increasing GNP filler loading. Elastomers reinforced by carbon blacks, however, swelled isotropically due to the symmetric (spherical) shape of the filler. A simple theory was proposed to understand and quantify the anisotropic swelling. Micromechanical models were also introduced explaining the key factors controlling the swelling reinforcement.

References

[1] Kraus G. Swelling of filler-reinforced vulcanizates. Journal of Applied Polymer Science. 1963;7(3):861-71.

[2] Boonstra B. Role of particulate fillers in elastomer reinforcement: a review. Polymer. 1979;20(6):691-704.

[3] Burnside SD, Giannelis EP. Synthesis and properties of new poly (dimethylsiloxane) nanocomposites. Chemistry of Materials. 1995;7(9):1597-600.

[4] Huang J-C, Zhu Z-k, Yin J, Qian X-f, Sun Y-Y. Poly (etherimide)/montmorillonite nanocomposites prepared by melt intercalation: morphology, solvent resistance properties and thermal properties. Polymer. 2001;42(3):873-7.

[5] Li S, Li Z, Burnett TL, Slater TJ, Hashimoto T, Young RJ. Nanocomposites of graphene nanoplatelets in natural rubber: microstructure and mechanisms of reinforcement. Journal of Materials Science. 2017;52(16):9558-72.

[6] Coran AY, Boustany K, Hamed P. Unidirectional fiber–polymer composites: Swelling and modulus anisotropy. Journal of Applied Polymer Science. 1971;15(10):2471-85.

[7] Nardinocchi P, Pezzulla M, Teresi L. Anisotropic swelling of thin gel sheets. Soft Matter. 2015;11(8):1492-9.

[8] Flory PJ, Rehner Jr J. Statistical Mechanics of Cross-Linked Polymer Networks II. Swelling. The Journal of Chemical Physics. 1943;11(11):521-6.

[9] Flory PJ, Rehner Jr J. Statistical mechanics of cross-linked polymer networks I. Rubberlike elasticity. The journal of chemical physics. 1943;11(11):512-20.

[10] Young RJ, Liu M, Kinloch IA, Li S, Zhao X, Vallés C, et al. The mechanics of reinforcement of polymers by graphene nanoplatelets. Composites Science and Technology. 2018;154:110-6.

[11] Treloar LRG. The swelling of cross-linked amorphous polymers under strain. Transactions of the Faraday Society. 1950;46:783-9.

[12] Treloar LRG. The physics of rubber elasticity: Oxford University Press, USA; 1975.

[13] Young RJ, Lovell PA. Introduction to polymers: CRC press; 2011.

[14] Saito H, Inoue T. Chain orientation and intrinsic anisotropy in birefringence-free polymer blends. Journal of Polymer Science Part B: Polymer Physics. 1987;25(8):1629-36.

[15] Mitchell G. A wide-angle X-ray study of the development of molecular orientation in crosslinked natural rubber. Polymer. 1984;25(11):1562-72.

[16] Li P, Goettler L, Hamed P. Anisotropy of composites: Mechanical and solvent-swelling characteristics. Journal of Elastomers & Plastics. 1978;10(1):59-77.

180

[17] Liu M, Papageorgiou DG, Li S, Lin K, Kinloch IA, Young RJ. Micromechanics of reinforcement of a graphene-based thermoplastic elastomer nanocomposite. Composites Part A: Applied Science and Manufacturing. 2018;110:84-92.

Chapter 6. Diffusion and Biaxial Reinforcing Mechanisms of Graphene-based Elastomer Nanocomposites[*]

* Contributions to the publication (author name order of the publication): Mufeng Liu: experiments, data analysis, propose of the theory and writing of the manuscript; Ian A. Kinloch & Robert J. Young: final proof-reading and discussion; Dimitrios G. Papageorgiou: proof-reading and discussion of the manuscript.

6.1 Introduction

Since the swelling of elastomers in a solvent is related to the mechanical behaviour of the specimen [1, 2] the reinforcement of the filler in an elastomer composite regarding liquid barrier properties is believed to be through constraining deformation and relative studies can be seen in Chapter 5. Raman spectroscopy has been proven to be a powerful technique in characterising interfacial stress transfer from a polymer matrix to graphene-based materials, normally under uniaxial tension [3-6]. Kueseng and Jacob [7] studied a series of elastomer composites reinforced by carbon nanotubes (CNTs) and found that the characteristic Raman bands (G and 2D band) of the CNTs displayed a blue shift after the sample was aged in water. This implies that it should be possible to also use Raman spectroscopy to follow the reinforcing mechanisms of graphene during the swelling of an elastomer nanocomposite.

In this work, a comprehensive study of the diffusion of toluene into TPE nanocomposites reinforced by graphene nanoplatelets (GNPs) has been undertaken. Three types of GNPs with different lateral dimensions (M5, M15 and M25) were incorporated into a thermoplastic elastomer (Alcryn®) by melt mixing. Raman spectroscopy was employed for the first time to monitor the in-plane, strain-induced 2D band shifts during the de-

swelling process, in order to explore the mechanism of reinforcement by GNPs in the elastomer nanocomposites.

6.2 Experimental Methods

6.2.1 Materials and Preparations

Samples used and the preparation methods were the TPE nanocomposites sample employed in Chapter 5 filled with three types of GNPs (M5, M15 and M25).

6.2.2 Characterisations

The actual loadings of GNPs in the nanocomposites were obtained by thermogravimetric analysis (TGA) using a TA Q500 TGA instrument. The samples were heated from room temperature up to 600 $^\circ$C at 10°C/min under a 50 mL/min flow of N_2.

Dynamic mechanical analysis (DMA) using a TA Q800 DMA instrument was employed to study the glass transition temperature of the neat polymer and the nanocomposites reinforced by GNPs. The hot-pressed elastomer samples with thickness of 1.5 mm were cut to 40 mm $\times$ 5 mm rectangular strips and were tested under tension between -90 °C and 50 °C.

The swelling tests were undertaken using toluene (purity of 99.8%, Sigma-Aldrich). The weight, diameter and thickness of the samples were measured after immersion in toluene for 0, 15, 30, 45, 60, 90, 120, 180, 300, 540, 1020, 1980 and 2880 minutes. At least 3 specimens were measured for each sample.

The morphologies of the neat polymer and the microstructure of the nanocomposites were examined using scanning electron microscopy (SEM). The cryo-fractured cross-sections

of the samples were coated using an Au-Pd alloy in order to provide satisfactory conductivity to the samples. The images were acquired using a high-resolution Tescan Mira 3 Field Emission Gun Scanning Electron Microscope (FEGSEM) at 5 kV.

Polarised Raman spectroscopy was employed to evaluate the spatial orientation of the filler in the matrix. A similar method was used in previous studies [3, 4, 8, 9]. The equipment was a 514 nm Raman spectrometer by Renishaw with 'VV' (vertical-vertical) polarisation, in which the incident and scattered radiation were polarised in the same direction. The laser was aligned perpendicular to the surface of the materials either along the axis of in-plane or cross-plane section. The intensity of the Raman G bands were recorded as a function of the rotation angle to enable estimation of the orientation distribution function (ODF) [9].

Raman spectroscopy was also employed to measure the in-plane strain-induced 2D band shifts. Raman spectra were acquired using a Renishaw InVia Raman spectrometer with a laser wavelength of 633 nm and an objective of 50×, which produces a spot size of 1–2 μm. Ideally, it would have been best to follow the band shifts of the GNPs in the nanocomposites during swelling in toluene. In practice, this proved to be difficult and it was decided to follow the band shifts during the de-swelling of swollen specimens during natural evaporation of the solvent. The Raman 2D band shifts of the swollen nanocomposite samples (after 3 hours immersion in toluene) with the highest loading of GNPs (20 wt%) was first measured. The in-plane strain, determined by measuring the diameter of the disc-shape samples with a digital calliper, reduced with time of exposure the air and the change in band position was determined. The Raman laser spot was focused on the same point of a single flake on each sample surface. The results were based on 3 composite samples for each type of GNP, at the highest loading. All spectra were fitted with a single Lorentzian curve.

6.3 Results and Discussion

6.3.1 Microstructure and Orientation of the Filler

The microstructure of the materials was characterised by SEM as shown in **Figure 6.1**. It can be seen that the fillers are well-dispersed and well-oriented (**Figure 6.1,** a-c) in the elastomer as a result of the preparation procedure for loadings up to 20 wt%. The GNPs appear to be well wetted by the elastomer as suggested by the high magnification images in **Figure 6.1** (d-f) and so the interface between the matrix and the flakes can be considered satisfactory. The preparation of graphene-reinforced elastomer nanocomposites by melt mixing followed by injection/compression moulding, usually leads to the in-plane orientation of the filler in the matrix due to the shear and compression involved [3, 4].

Polarised Raman spectroscopy was employed to quantify the degree of orientation the graphene nanoplatelets in the matrix. The specific method was also utilized in a number of previous studies upon GNP-reinforced polymers [3, 4, 8, 9]. The dependence of the Raman intensity on the angle of incident laser in both in-plane and cross-plane is shown in the **Figure 6.1** (g and h). When the Raman laser was perpendicular to the cross-plane direction, the intensity of the G band remained unchanged with varying polarisation angles. However, when the polarised laser was parallel to the in-plane direction, the angular dependence of the Raman intensity of the G band on the polarisation angle is quite different. In this case the G band Raman intensity decreases from 0° to 90° (and 180° to 270°) and then increases from 90° to 180° (and 270° to 360°).

In this work, the formation of the in-plane orientation of the flakes is believed due to the compression force in the cross-plane z direction (shown in the **Figure 6.2** a) that gave rise to a preferred in-plane orientation (x-y plane) of the flakes (shown in **Figure 6.2**, b and c). The preferred in-plane alignment of the filler leads to anisotropic reinforcement, where the mechanical properties of the samples in the in-plane direction (x-y plane) are improved.
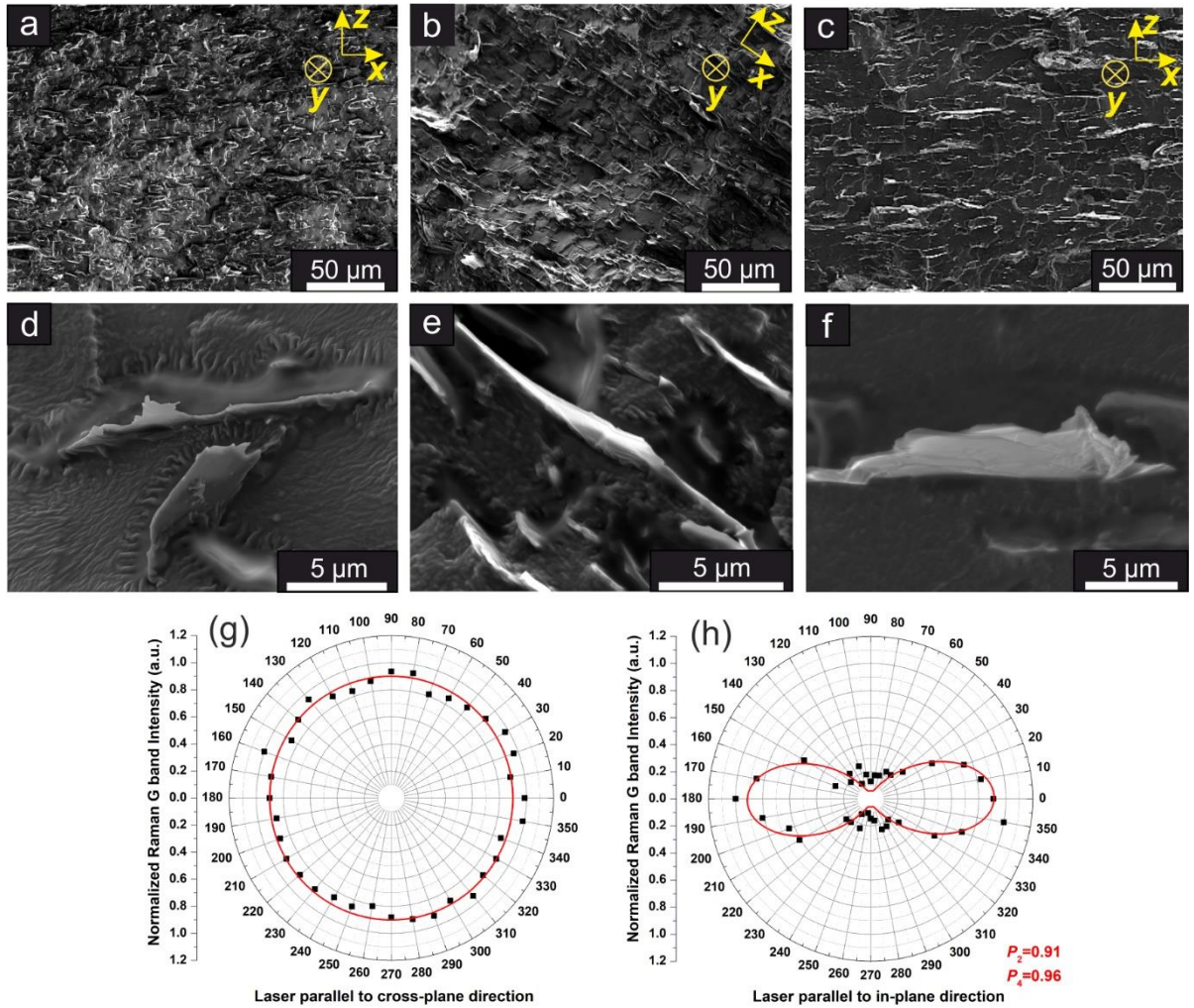
Figure 6.1 Microstructure of the nanocomposites and filler orientation. (a-c) Low magnification SEM images of cryo-fractured cross-sectional surface of the elastomer nanocomposite sheets (20 wt% of M5, M15 and M25 GNP-reinforced nanocomposites, respectively) showing good dispersion of the filler; (d-e) High magnification SEM images of individual M5, M15 and M25 GNP flakes embedded in the nanocomposites showing good wetting. The dependence of normalized Raman G band intensity on the angle of the incident laser parallel to (g) the cross-plane direction and (h) the in-plane direction, measured for an M5 GNP-reinforced TPE at the highest loading (20 wt%).
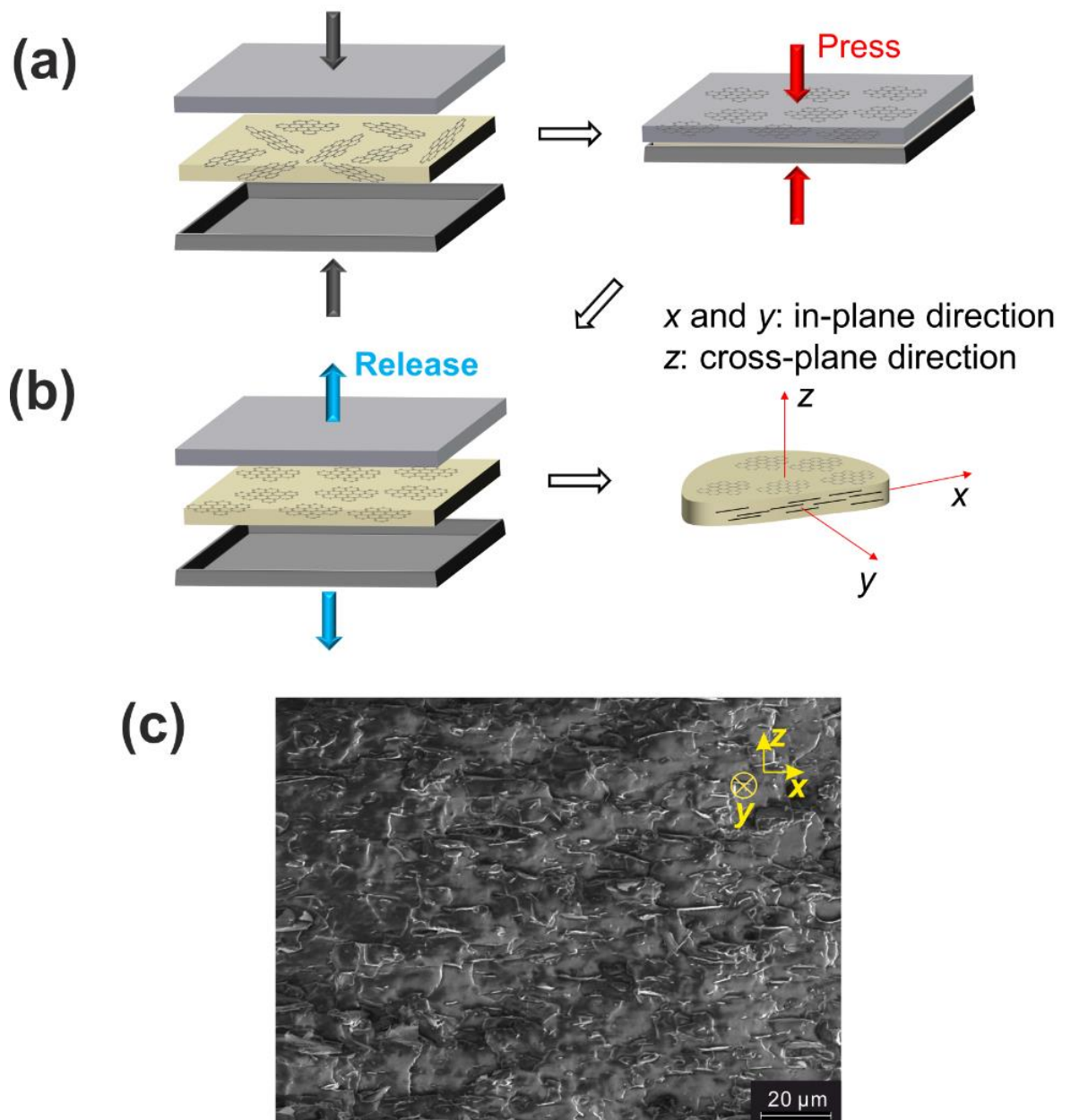
Figure 6.2 Formation of the in-plane filler orientation. (a) Schematic diagram of the formation of in-plane oriented GNPs from randomly oriented GNPs in the nanocomposites under compression in the hot press; (b) Schematic diagram of the in-plane orientation of the GNP flakes in a molded composite sheet, where x, y and z axes are defined; (c) SEM image of cryo-fractured cross-section of the composite sheet showing in-plane orientation with x, y and z axes based on (c).

The quantification of the in-plane flake orientation can be accomplished by curve fitting using the following Equation for the in-plane direction data [9]:

$$I_{sample}(\Phi) = I_O \left\{ \frac{8}{15} + \langle P_2(\cos\theta) \rangle \left(-\frac{16}{21} + \frac{8}{7}\cos^2\Phi \right) + \langle P_4(\cos\theta) \rangle \left(\frac{8}{35} - \frac{8}{7}\cos^2\Phi + \cos^4\Phi \right) \right\} \quad (6.1)$$

where I_o is the amplitude and assuming the surface normals are uniformly distributed around the cross-plane axis. The orientation factor for the in-plane reinforcement is then given by:

$$\eta_o = \frac{8}{15} + \frac{8}{21}\langle P_2(\cos\theta) \rangle + \frac{3}{35}\langle P_4(\cos\theta) \rangle \quad (6.2)$$

Similar method was applied in chapter 3 and 4 for injection moulded samples. Herein, the calculation of the orientation factor is to use the G band Raman intensities tested from 0° to 360°, where the G band intensities were collected when a sample (or the laser) was rotated every 10°. Then, the highest value of the G band intensity was used to normalize all the data points. After the normalization, a set of data (I_{sample}/I_o) for a sample are ready to be fitted using equation (6.1) to obtain the P_2 and P_4 values, where Φ is the rotation angle. An example of the fitting results can be seen in **Figure 6.1** (g) and (h). Afterwards, the obtained P_2 and P_4 values can be put into equation (6.2) to give the orientation factor. The orientation factors for the nanocomposite samples for this work at the highest filler loading (20 wt%) were quantified: $\eta_{oM5}=0.89$, $\eta_{oM15}=0.84$ and $\eta_{oM25}=0.80$. Generally, η_o should be between 0.53 (random orientation) and 1 (perfect in-plane orientation). Therefore, it can be concluded that the GNPs are well oriented in the in-plane direction in the elastomer sheets.

6.3.2 Diffusion of the Solvent

The elastomeric matrix and the nanocomposite specimen were immersed in toluene and measurements of the swollen specimen were performed in order to investigate the relative

mass uptake *M*, and the diffusion coefficient *D*. For well-defined, small, plate-like specimens (with a diameter of at least 10× the thickness), the relative mass uptake *M(t)* determined gravimetrically with exposure times is given by [10]:

$$M(t) = \frac{W(t) - W(0)}{W(0)} \tag{6.3}$$

where *W(t)* is the weight of a specimen after an exposure time *t* and *W(0)* is calculated theoretically by determining the intercept of the linear fitting of *W(t)* against $t^{1/2}$ at *t*=0, in order to reduce any systematic error involved in gravimetry [10]. The diffusion coefficient, *D*, can then be determined by [10], as reviewed in **Chapter 2, Section 2.3.1**:

$$\frac{4M(\infty)}{h\sqrt{\pi}}\sqrt{D} = \frac{M_2 - M_1}{\sqrt{t_2} - \sqrt{t_1}} \tag{6.4}$$

where *h* is the thickness of the samples and *M(∞)* is the mass uptake at the saturation point of the absorption.

The relative mass uptake *M(t)* as a function of $t^{1/2}$ for the elastomer composites reinforced by three types of GNPs is shown in **Figure 6.3** (a-c). At the beginning of exposure time, the small molecules of the solvent were absorbed into the materials leading to an increase of *M(t)*. Afterwards, the curves form a plateau at $t^{1/2} \approx 100$ ($s^{1/2}$), which indicates the saturation of the absorption phenomenon. The elastomer used in this study is based on a thermoplastic vulcanizate, where only a small percentage of the macromolecular chains are chemically crosslinked [11]. Hence, the relative mass uptake *M(t)* is found to decrease slightly after reaching the maximum *M(t)* values at $t^{1/2} \approx 100$, due probably to slow dissolution of the polymer. In this work, the *M(∞)* values are defined for consistency as the maximum *M(t)* values for all measurements.

From **Figure 6.3**, it can be seen that $M(\infty)$ is significantly reduced with increasing filler content, exhibiting an effective restriction of the ultimate solvent uptake with the introduction of GNPs. When a neat polymer is exposed in a solvent, the small molecules of the solvent can diffuse into the free volume, making the polymer swell in three dimensions, until equilibrium between the stress in the reinforcement and the volume swelling is achieved. When a filler is incorporated into the matrix, the internal stress caused by the swelling of the matrix can be transferred from the matrix to the filler by shear at the filler/matrix interface, which allows the filler to partially carry the load and eventually restrain the overall mass uptake of the materials.
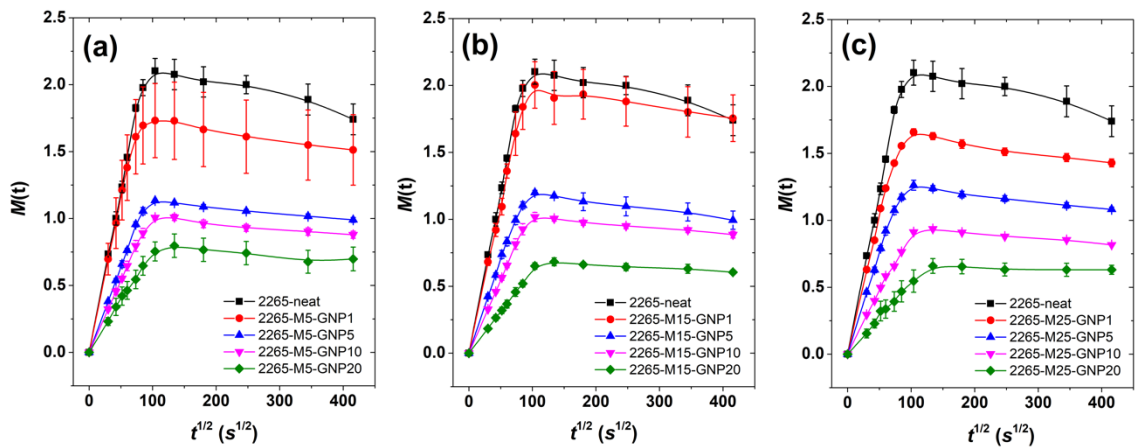
Figure 6.3 Results of mass uptake and geometric swelling. (a-c) The mass uptake against the square root of time for the samples of M5, M15 and M25 reinforced elastomers, respectively. This figure is identical to Figure 5.5 (d-f) in **Chapter 5**, where the materials were dissolved slowly in toluene after saturation of swelling and therefore, the highest $M(t)$ was taken for the saturation point for each material.

The diffusion coefficient (D) (**Table 6.1**, values calculated from Equations 6.1 and 6.2) indicates the rate of solvent diffusion. It is highest for the neat elastomer and decreases with increasing loadings for each size of GNPs. It can also be seen that for a given GNP loading it decreases with increasing GNP diameter, going from M5 to M15 to M25 for both the 10 wt% and 20 wt% GNP-reinforced nanocomposites. This behaviour is the result of nanoconfinement of the macromolecular chains of TPE due to the presence of

GNPs that can be also confirmed by dynamic mechanical thermal analysis (DMTA). It can be clearly seen in **Figure 6.4** that the glass transition temperature (T_g) increases with increasing filler loading as suggested by the shift of the major peak of the loss factor curves towards higher temperatures. This indicates a decrease of the mobility of the TPE macromolecules with increasing temperature and filler content (results also listed in **Table 6.2**).

Table 6.1 Results of diffusion coefficient. The volume fraction determined by TGA and the diffusion coefficient of toluene into the nanocomposites evaluated by the swelling tests. Diffusion coefficient values were calculated from equation 6.1 and 6.2.

2265-M5		2265-M15		2265-M25	
GNP loading (vol%)	$D\ (\times 10^{-5})$ (mm^2/s)	GNP loading (vol%)	$D\ (\times 10^{-5})$ (mm^2/s)	GNP loading (vol%)	$D\ (\times 10^{-5})$ (mm^2/s)
0	9.89 ± 1.21	0	9.89 ± 1.21	0	9.89 ± 1.21
0.65	9.40 ± 0.45	0.53	9.22 ± 0.13	0.40	9.60 ± 1.14
2.57	9.12 ± 0.26	2.73	9.17 ± 0.07	2.44	9.06 ± 0.02
5.52	8.42 ± 1.13	6.21	7.66 ± 0.16	4.88	7.62 ± 0.01
10.82	7.66 ± 0.27	10.3	6.78 ± 0.05	10.47	5.95 ± 1.03
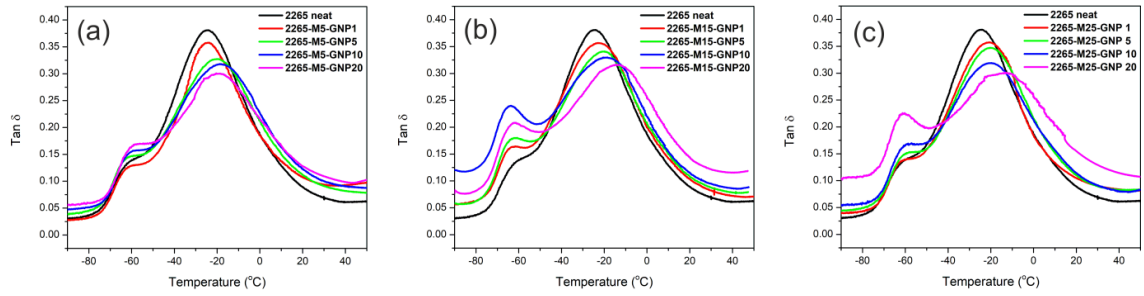
Figure 6.4 (a-c) The loss factor (tan δ) determined using dynamic mechanical analysis (DMA) of M5, M15 and M25 GNP reinforced elastomers from -90 °C to 50 °C, showing the glass transition temperature (temperature at the major peak) of the materials increases with increasing filler content.

Table 6.2 Glass transition temperature values determined by DMA for all the materials including neat elastomer and nanocomposites with filler loadings of 1, 5, 10 and 20 weight percent.

GNP loading (wt%)	T_g (°C) M5	T_g (°C) M15	T_g (°C) M25
0	-24.5	-24.5	-24.5
1	-24.1	-22.7	-21.0
5	-20.5	-20.3	-19.9
10	-18.8	-18.8	-19.9
20	-18.9	-13.9	-12.7

6.3.3 Biaxial Deformation-induced Raman Band Shift

Since in-plane reinforcement by the graphene nanoplatelets was realized from the swelling measurements in **Chapter 5**, a further study of the shear stress transfer was carried out by evaluating the Raman band shifts during de-swelling. When a swollen specimen is taken out from the solvent and exposed in the air, the solvent molecules tends to evaporate from it. This causes the strain in the GNPs to reduce and consequently the internal stress at the filler/matrix interface also decreases. Such a process allowed us to monitor the blue shift of the characteristic 2D Raman band of the GNPs, as shown in **Figure 6.5** (a). In this experiment, only the nanocomposites with the highest filler loading (20 wt% of the GNP) were examined, since the high filler loading made the volatilization of the solvent slow enough to allow the Raman spectra to be captured. The Raman spectra of the GNPs and the diameters of the composite specimens were recorded simultaneously. The peak positions of the 2D band are plotted against strain in **Figure 6.5** (b-d). It can be seen that the Raman 2D band shifts to higher wavenumbers with the decrease of the in-plane strain in the nanocomposites. Generally, larger flakes give higher 2D band shift per strain, which is in agreement with the diffusion and swelling results reported previously. The reason for this is that for short platelets embedded in a matrix, stress transfer takes place at the edge of the flakes and increases from the edges towards the centre, along the nanoplatelets [6]. The data in **Figure 6.5** (b-d) indicate the better reinforcement by the larger nanoplatelets in M15 and M25 showing increasingly-higher values of $-d\omega_{2D}/d\varepsilon$, and therefore higher effective biaxial modulus (**Figure 6.5** e).

The assessment of the in-plane reinforcement of the GNPs can be achieved by analysing the band shift values listed in **Table 6.3**. The effective modulus of graphene in the elastomer matrix under biaxial deformation can be calculated by [6]:

$$E_{\text{eff}} = -\frac{d\omega_{2D}}{d\varepsilon} \cdot \frac{E_{\text{biaxial}}}{(\partial\omega_{2D}/\partial\varepsilon)_{\text{biaxial-ref}}} \text{ GPa} \tag{6.5}$$

where -dω_{2D}/dε is the 2D Raman band shift per composite strain, $E_{biaxial}$ is the biaxial modulus of monolayer graphene measured by pressurized graphene "balloons", which is equal to 2400 GPa as reported by Lee *et al.* [12] and $(\partial\omega_{2D}/\partial\varepsilon)_{biaxial-ref}$ is the 2D Raman band shift rate of monolayer graphene under controlled biaxial deformation, which is equal to -148 cm^{-1}/% strain, according to the work of Androulidakis *et al.* [13]. The effective modulus values of the GNPs in the elastomer matrix for this work were calculated using equation (6.5) and are listed in **Table 6.3**.
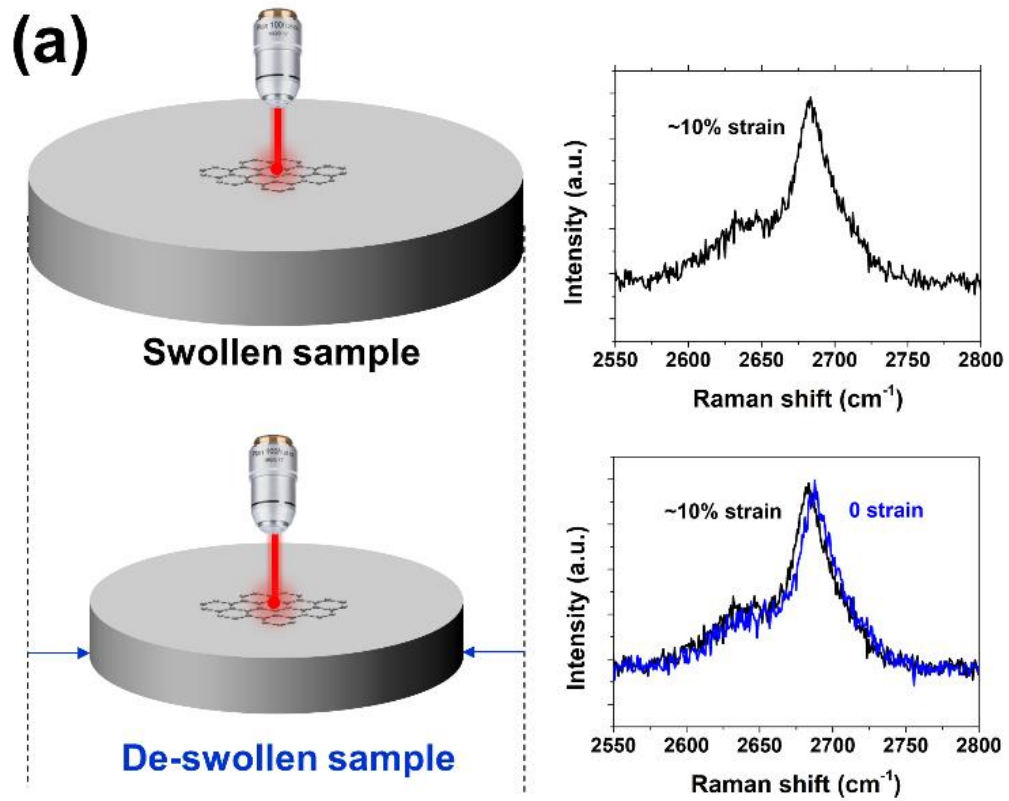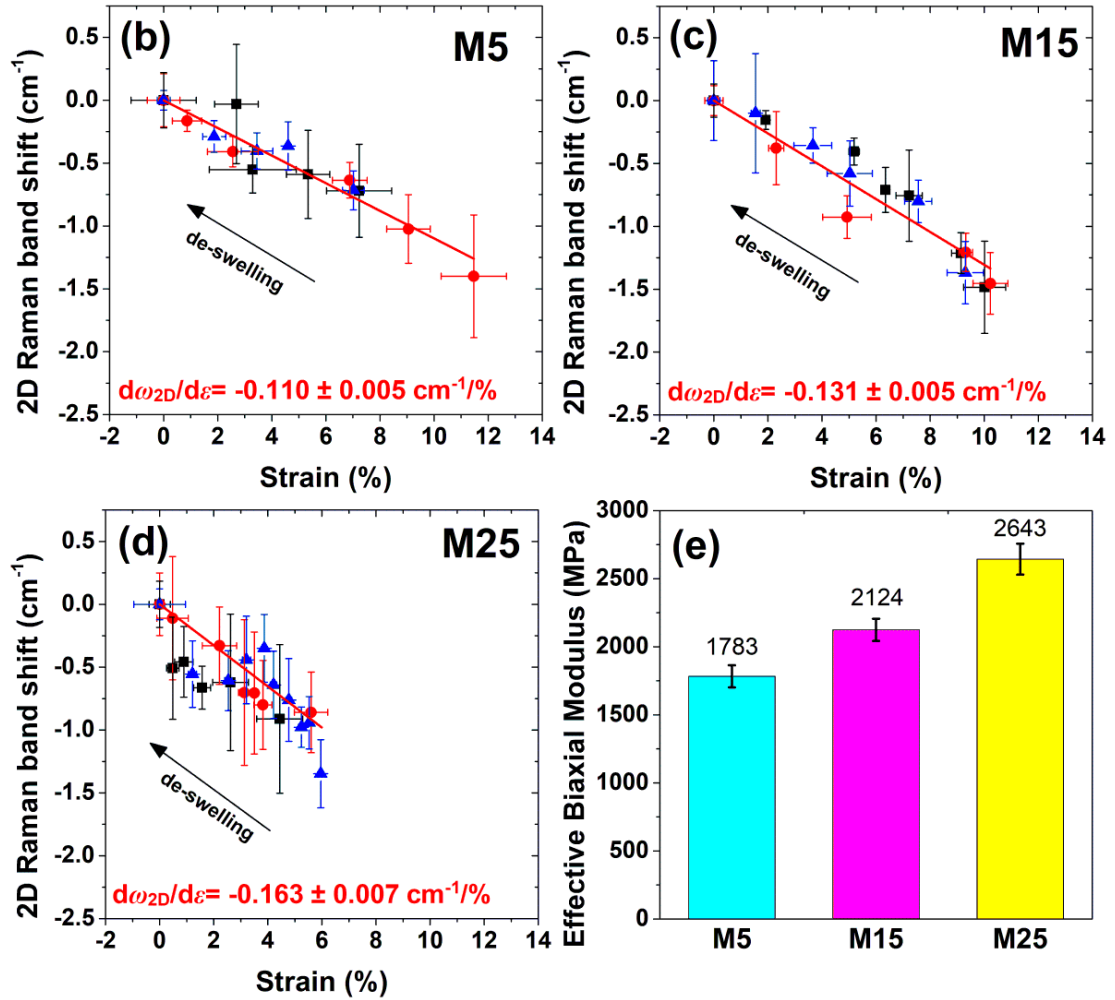
Figure 6.5 Raman band shift during de-swelling. (a) Schematic diagram of the measurement of the 2D Raman band shift with an example of spectra at different in-plane strains. The in-plane strain here is given by $\varepsilon_{\text{in-plane}}=(d_{\text{swollen}}-d_{\text{dry}})/d_{\text{dry}}$, where d_{swollen} is the diameter of the swollen samples, and d_{dry} is the diameter of the dried samples after immersion in the toluene and dried in the air rather than the original diameter before immersed in the solvent. (b-d) Raman 2D band shift of M5, M15 and M25 GNPs as a function of the corresponding strains during the swelling, respectively. The continuous lines are linear fits to the experimental data. (e) Effective biaxial modulus of M5, M15 and M25 GNP flakes calculated from Raman 2D band shift (b-d) using equation (6.5).

The theoretical effective modulus of the filler measured by Raman band shifts (E_R) and based on the shear-lag theory for uniaxial deformation is given by [6]:

$$E_{\text{R biaxial}} = \eta_\text{o} \frac{s^2}{8} \frac{1}{1+v_{\text{matrix}}} \frac{t}{T} E_\text{m} \tag{6.6}$$

where η_o is the orientation factor of the filler, s is the aspect ratio of the measured flake, v_{matrix} is the Poisson's ratio of the matrix, t is the thickness of the flake and T is the thickness of the polymer layer surrounding the flake in the model nanocomposite and E_m is the modulus of the matrix. It should be pointed out that equation (6.6) shows that the effective modulus of the filler depends principally upon the Young's modulus of the matrix, E_m, the nanoplatelet aspect ratio, s and thickness, t.

For the biaxial deformation in this work, the modulus of the matrix is given by $E_\text{m}/(1-v_{\text{matrix}})$, since the stresses ($\sigma_\text{x}$ and σ_y) and strains (ε_x and ε_y) along the principal axes are equal. In addition, both the nanoplatelets and the matrix were under biaxial deformation during the de-swelling process. Hence, the theoretical effective biaxial modulus of the filler measured by Raman band shift is given by:

$$E_{\text{R biaxial}} = \eta_\text{o} \frac{s^2}{8} \frac{1}{1+v_{\text{matrix}}} \frac{1}{1-v_{\text{matrix}}} \frac{1}{1-v_{\text{graphene}}} \frac{t}{T} E_\text{m} \tag{6.7}$$

The Poisson's ratio of elastomers is generally considered to be approaching 0.5 [14]. The Poisson's ratio of graphitic materials is a matter of debate as it ranges widely in the literature from 0.16 to 0.43 [15-24], mainly on the basis of theoretical predictions. Hence, it can be inferred theoretically that $E_{\text{R biaxial}}/E_{\text{R uniaxial}}$ should be in the range of 2.4 to 3.5. It can be seen (**Table 6.3**) that the biaxial deformation gives an effective modulus of the GNPs close to the one that was expected, based on the ratio $E_{\text{R biaxial}}/E_{\text{R uniaxial}}$ (average values around 3) for all three types of GNPs (listed in **Table 6.3**). From equation (6.7) we are able to calculate the Poisson's ratio of the graphene nanoplatelets, which ranges from 0.33 to 0.35. This result is also consistent with the Poisson's ratio of carbon nanotubes

196

(0.34), determined using the local density approximation model [25]. Furthermore, Zhao *et al.* [16] computed the Poisson's ratio of graphene to be around 0.30, by utilizing a molecular structural mechanics model. The accurate value could only be realised experimentally by nanoscale measurements, determining the axial and transverse strain simultaneously, which is very hard to achieve. Hereby, it can be provided with a rather accessible route to measure the Poisson's ratio of the graphene substances indirectly by introducing micromechanical theories that can be employed in polymer nanocomposites along with the use of in-situ Raman spectroscopy.

Table 6.3 Calculated properties from Raman 2D band shift. Raman 2D band shift and the calculated effective modulus for M5, M15 and M25 GNPs under both uniaxial and biaxial deformation are listed, where $d\omega_{2D}/d\varepsilon$ is the Raman 2D band shift per strain and E_R is the effective modulus of the GNPs measured by Raman band shift and calculated by the equation (6.5).

	M5	M15	M25
Diameter (μm) [6]	5.2±3.3	6.6±4.1	7.7±4.2
$d\omega_{2D}/d\varepsilon$ (cm^{-1}/%)(uniaxial) [4]	-0.036±0.003	-0.040±0.005	-0.050±0.006
E_R (MPa)(uniaxial) [4]	630±53	700±88	875±105
$d\omega_{2D}/d\varepsilon$ (cm^{-1}/%)(biaxial)	-0.110±0.005	-0.131±0.005	-0.163±0.007
E_R (MPa)(biaxial)	1783±81	2124±81	2643±114
E_R (bi)/ E_R (uni)	2.99±0.50	3.07±0.50	3.09±0.50
Average Poisson's Ratio	0.33	0.35	0.35

6.4 Conclusion

The orientation of the GNP flakes was characterised regarding compression moulded nanocomposites sheets in this chapter and showed highly preferred orientation of the nanoplatelets in-plane. The study of Raman 2D band shifts during the de-swelling process has directly demonstrated that the mechanism of biaxial deformation is interfacial stress

transfer from the matrix to the GNPs and hence further solidified the theory of anisotropic swelling that was proposed in **Chapter 5**.

References

[1] Boyce MC, Arruda EM. Swelling and mechanical stretching of elastomeric materials. Mathematics and Mechanics of Solids. 2001;6(6):641-59.

[2] Kraus G. Swelling of filler-reinforced vulcanizates. Journal of Applied Polymer Science. 1963;7(3):861-71.

[3] Li S, Li Z, Burnett TL, Slater TJ, Hashimoto T, Young RJ. Nanocomposites of graphene nanoplatelets in natural rubber: microstructure and mechanisms of reinforcement. Journal of Materials Science. 2017;52(16):9558-72.

[4] Liu M, Papageorgiou DG, Li S, Lin K, Kinloch IA, Young RJ. Micromechanics of reinforcement of a graphene-based thermoplastic elastomer nanocomposite. Composites Part A: Applied Science and Manufacturing. 2018;110:84-92.

[5] Papageorgiou DG, Kinloch IA, Young RJ. Mechanical properties of graphene and graphene-based nanocomposites. Progress in Materials Science. 2017;90:75-127.

[6] Young RJ, Liu M, Kinloch IA, Li S, Zhao X, Vallés C, Papageorgiou DG. The mechanics of reinforcement of polymers by graphene nanoplatelets. Composites Science and Technology. 2018;154:110-6.

[7] Kueseng K, Jacob K. Natural rubber nanocomposites with SiC nanoparticles and carbon nanotubes. European Polymer Journal. 2006;42(1):220-7.

[8] Papageorgiou DG, Kinloch IA, Young RJ. Hybrid multifunctional graphene/glass-fibre polypropylene composites. Composites Science and Technology. 2016;137:44-51.

[9] Li Z, Young RJ, Wilson NR, Kinloch IA, Vallés C, Li Z. Effect of the orientation of graphene-based nanoplatelets upon the Young's modulus of nanocomposites. Composites Science and Technology. 2016;123:125-33.

[10] Cervenka AJ, Young RJ, Kueseng K. Gravimetric determination of the diffusion characteristics of polymers using small specimens. Journal of Polymer Science Part B: Polymer Physics. 2004;42(11):2122-8.

[11] Akkapeddi M. Commercial polymer blends. Polymer Blends Handbook. 2003:1023-115.

[12] Lee JU, Yoon D, Cheong H. Estimation of Young's modulus of graphene by Raman spectroscopy. Nano Letters. 2012;12(9):4444-8.

[13] Androulidakis C, Koukaras EN, Parthenios J, Kalosakas G, Papagelis K, Galiotis C. Graphene flakes under controlled biaxial deformation. Scientific Reports. 2015;5:18219.

[14] Pritchard RH, Lava P, Debruyne D, Terentjev EM. Precise determination of the Poisson ratio in soft materials with 2D digital image correlation. Soft Matter. 2013;9(26):6037-45.

[15] Cost JR, Janowski KR, Rossi RC. Elastic properties of isotropic graphite. The Philosophical Magazine: A Journal of Theoretical Experimental and Applied Physics. 1968;17(148):851-4.

[16] Zhao P, Shi G. Study of Poisson ratios of single-walled carbon nanotubes based on an improved molecular structural mechanics model. Computers Materials and Continua. 2011;22(2):147.

[17] Blakslee O, Proctor D, Seldin E, Spence G, Weng T. Elastic constants of compression-annealed pyrolytic graphite. Journal of Applied Physics. 1970;41(8):3373-82.

[18] Treacy MJ, Ebbesen T, Gibson J. Exceptionally high Young's modulus observed for individual carbon nanotubes. Nature. 1996;381(6584):678.

[19] Yakobson BI, Brabec C, Bernholc J. Nanomechanics of carbon tubes: instabilities beyond linear response. Physical Review Letters. 1996;76(14):2511.

[20] Lu JP. Elastic properties of carbon nanotubes and nanoropes. Physical Review Letters. 1997;79(7):1297.

[21] Tsai JL, Tu JF. Characterizing mechanical properties of graphite using molecular dynamics simulation. Materials & Design. 2010;31(1):194-9.

[22] Hemmasizadeh A, Mahzoon M, Hadi E, Khandan R. A method for developing the equivalent continuum model of a single layer graphene sheet. Thin Solid Films. 2008;516(21):7636-40.

[23] Huang Y, Wu J, Hwang K-C. Thickness of graphene and single-wall carbon nanotubes. Physical Review B. 2006;74(24):245413.

[24] Caillerie D, Mourad A, Raoult A. Discrete homogenization in graphene sheet modeling. Journal of Elasticity. 2006;84(1):33-68.

[25] Tu ZC, Ouyang ZC. Single-walled and multiwalled carbon nanotubes viewed as elastic tubes with the effective Young's moduli dependent on layer number. Physical Review B. 2002;65(23):233407.

Chapter 7. Conclusions and Suggestions for Future Work

7.1 Conclusions

7.1.1 Micromechanics of Reinforcement of a Graphene-based Thermoplastic Elastomer

A series of GNP-reinforced thermoplastic elastomers have been successfully prepared by melt mixing. The SEM images suggested that the dispersion of the GNPs is quite homogeneous, while the alignment of the fillers is induced by shear during the injection moulding procedure. The interface between the nanoplatelets and the matrix is most of the time intact, while looped and folded morphologies can be found for larger flakes, which are expected to affect their intrinsic properties. Polarised Raman spectroscopy has been employed to quantify the orientation factor of the injection moulded samples and it was shown that the orientation profile throughout the cross-section was consistent with the trend of the shear rate profile from injection moulding. Larger flakes have lower degree of orientation, again as a result of looped or folded structures.

The mechanical properties from tensile tests revealed that the introduction of GNPs into the TPE gave rise to significant improvements in its stiffness (6 times higher, up to 10 vol% loading) and strength compared to the matrix. Overall, the larger flakes contribute to better enhancements in the stiffness while smaller flakes lead to a higher increase of strength. The modulus values were studied with an equation derived by analytical methods and described in detail in previous work, by combining the shear lag theory with the well-accepted rule-of-mixtures. It was revealed that the composite modulus has a quadratic relationship with the volume fraction of the filler and depends heavily on the aspect ratio of the filler, which is similar as the classical Guth-Gold theory [1]. The effective aspect ratio is found to be of the order of 100. Finally, both the filler modulus from the tensile testing and Raman modulus of the bulk composites measured by 2D band

shifts were found to be lower compared to composites based on stiff polymers but higher than those based on very soft matrices (i.e. natural rubber) due to different shear modulus of the materials. The experimental data have also been analysed and show a good consistency with theory.

It can be concluded that the reinforcement efficiency of the GNPs on a thermoplastic elastomer matrix is highly dependent on the filler geometry and also the processing method. The improvements of the stiffness and strength, to a large extent, rely on the effective aspect ratio of the flakes. The processing method, on the other hand, affects the dispersion, orientation and further intercalation of the filler significantly, which is of a great significance in determining the filler geometry in the bulk nanocomposites. The composites produced show great promise in terms of their mechanical properties and can be considered as high-performance engineering plastics that can be attractive to a number of high-tech industries such as automobile or aerospace, as well as their possible use in conventional consumer goods.

7.1.2 Modelling Mechanical Percolation in Graphene-Reinforced Elastomer Nanocomposites

The mechanical properties obtained from tensile testing suggested that the stiffness and yield strength are both significantly enhanced. It was clearly exhibited that after the percolation threshold volume fraction, the modulus of the composites presents a superlinear increase, compared to the linear increase observed at low filler contents. The filler modulus measured by Raman band shifts showed similar, but slightly higher values than the filler modulus determined by tensile testing. Finally, the consistency of the newly-derived Equations (4.5) and (4.6) with the experimental data has manifested the applicability of the combined shear-lag/rule-of-mixtures theory proposed here, on the reinforcement mechanisms of elastomer/GNP nanocomposites. The three stages of reinforcement from low to high volume fraction of the filler have been clearly identified. Similar analysis methods, considering the mechanical percolation in graphene-based

elastomer nanocomposites have been introduced before [2-5], by using either hydrodynamics [1] or the jamming theory [6, 7]. However, an obvious advantage of the theory proposed here, is the accurate interpretation of the percolation of tensile modulus, for the specific case of elastomer nanocomposites reinforced by 2D materials with well-defined parameters.

7.1.3 Anisotropic Swelling of Elastomers Filled with Aligned 2D materials

A simple and effective theory has been developed for the comprehensive study of anisotropic swelling for elastomer nanocomposites reinforced by in-plane-oriented graphene nanoplatelets. The newly-derived equations are able to accurately predict anisotropic dimensional swelling in both principal axes parallel and perpendicular to the filler orientation, independent of the type of elastomers, GNPs or solvents. The theory of anisotropic swelling can also be combined with the mechanical properties of the nanocomposites measured by tensile tests, in order to assess the reinforcing efficiency of the GNPs to the elastomers, in comparison to their swelling behaviours. The use of micromechanical theories enabled us to relate our observations to measurable physical parameters of the fillers and a correlation between anisotropic swelling and mechanical properties was successfully established. Through the comprehensive experimental and theoretical analysis presented in this study, it can be concluded that the use of 2D materials (such as graphene) can enable the tailoring of the swelling characteristics of an elastomeric matrix. This can have very important implications in highly demanding elastomer-based applications such as seals operating in liquid environments, rapid gas decompression seals and O-rings and gaskets for the chemical, petroleum, automotive and aerospace industries.

7.1.4 Diffusion and Biaxial Reinforcing Mechanisms of Graphene-based Elastomer Nanocomposites

The anisotropic swelling was modelled assuming 2D materials as a reinforcement rather than an initiator of physical crosslinks. This assumption was proven valid due to the

revealed Raman 2D band shift of the flakes during de-swelling process of the samples. The orientation and diffusion coefficient were also reported to fully characterise the liquid barrier properties of TPE-based nanocomposites reinforced by graphene.

Good liquid barrier properties are imperative for elastomers, due to their wide applications in a liquid environment including seals, gaskets, hoses/bonded flexible pipes and joints, valve sleeves and others. From the analysis of experimental results, it was shown that GNPs exhibit a high reinforcing efficiency in the swelling of elastomers and the orientation of the fillers is of vital importance for the control of swelling in different directions. This work along with the Chapter 5 can act as a guideline for the evaluation of the mechanisms of reinforcement, the factors affecting function performance and the prediction of the modes of deterioration in swollen GNP-elastomer nanocomposites, so that end users can continue to use nanocomposite elastomeric components often to completion of design life. As can be easily understood, the introduction of graphene-related materials into elastomers can bring benefits and enhanced properties for a number of practical applications.

7.1.5 Experimental hurdles

This thesis has dealt with a number of common analyses of polymers. However, some of the experiments are introduced particularly for GNP-filled polymer nanocomposites, such as polarised Raman spectroscopy and *in-situ* Raman band shift under uniaxial tension or biaxial deformation (de-swelling). These two measurements are particularly difficult to carry out and therefore the hurdles of these tests are described and explained more specifically.

7.1.5.1 Polarised Raman spectroscopy

Throughout the experiment chapters (3, 4, 5 and 6), polarised Raman spectroscopy has been used to quantify the orientation of the GNPs in the polymer matrices. The principle

is to find the angular dependence of the Raman band intensities on the rotation angles. For this experiment, it is crucial to use cryo-fractured cross-sections of the samples rather than tensile fractures. The most difficult operation is to focus on the same point on the same flake before and after the sample is rotated. When the laser is focused on different locations, even if the focused location is moved by a micron scale, it is possible to give different intensities and Raman spectra. In this case, the measurement should be carried out again to give valid data.

It is also important to do preliminary tests on the flake morphologies (optical microscopy) before the polarised Raman measurements is undertaken. Sometimes, the flakes can give folded or bent edges (such as **Figure 3.7** e), possibly due to the liquid nitrogen breaking, which can give invalid results for the characterisation of the orientation of the fillers. The selected flakes should be ideally edge-on protruding without bent edges, such as **Figure 3.7** (d).

The characterisation is significantly time-consuming since many spectra have to be taken. For a measurement of a single flake, the sample has to be rotated from 0° to 360°, while every time the same point of the sample in a micron scale has to be relocated and checked. For a nanocomposite sample, the measurements have to be undertaken many times (~15 flakes) in order to give a statistical result of the orientation factor.

7.1.5.2 Raman band shift under tension or de-swelling

Raman *in-situ* band shift has been an important evidence of stress transfer from the elastomeric matrices to the GNP flakes, which is the theoretical basis of Chapter 3, 4 and 6. There are a large number of Raman band shift experiments using bending of stiff polymer substrates such as PMMA, where graphene can be deposited on the top and the strain of the substrate can be given by a resistance strain gauge. For Raman *in-situ* band shift on an elastomer matrix, the experiment is more difficult to carry out.

First, the control and determination of the steady strain is very difficult. A specific tensile rig was made to give efficient grip of the elastomer. However, when holding the strain for the Raman measurements, the elastomers can go through stress relaxation quickly, which affects the results. To prevent this from happening, the flake should be located very quickly (from thousands of flakes on the sample surface) every time after the strain is applied.

An essential reason for this experiment to be time-consuming is that the measurement is very easy to fail. For each sample, only one flake can be selected and characterised. Due to the fact that some of the flakes might not have a good interface to the matrix, the Raman band might not shift with the corresponding strain. Hence, a lot of invalid measurements were carried out that took the time but did not give any result.

The Raman band shift for elastomers under strain is quite low and difficult to observe. It can give different curve wavenumber within an error of 1 cm^{-1} (fitted with Lorentzian curve), when Raman spectra are taken on the same point on the same flake for several times. However, in this case, the spectra would not show any visible difference. In order to prove the existence of strain-induced Raman band shift, representative spectra are necessary to be present, which should show visible band shift from the spectra at different strain, such as the **Figure 3.13** and **Figure 6.5**.

7.2 Suggestions for Future Work

7.2.1 Mechanical Reinforcement of Elastomers by 2D Materials

It was shown in Chapter 3&4 that modelling with micromechanics based on shear-lag and rule-of-mixtures is satisfying for understanding the reinforcing mechanism. A number of different fillers with same or similar two-dimensional geometries are expected to reinforce elastomers and confirm the theory, such as GO, hBN, MoS$_2$ and other types of

graphene (rather than GNPs), etc. The mechanical percolation modelling proposed in Chapter 4 could be further investigated using more types of elastomers.

Elastomers, owing to their special mechanical properties, can be employed for wide ranges of applications, from simple ones such as seals for windows to components of electronics to high-end applications such as aerospace. It could be very promising to use 2D materials to improve other mechanical properties of elastomers, such as abrasion resistance, tear resistance, compression set, and resilience. Therefore, the new theories and analytical techniques developed in this thesis could be employed and expanded widely. In addition, high-end applications of elastomers could involve different working conditions such as elevated temperature. The temperature dependence of the mechanical properties of graphene/elastomer nanocomposites may be a promising topic, since graphene can induce nanoconfinement (Chapter 6) that could reduce the loss of mechanical reinforcement with increasing temperature.

In this thesis, the study of mechanics was based mostly on thermoplastic elastomers. The rheological behaviour of the graphene/elastomer nanocomposites, therefore, can be a key factor, influencing the difficulty of the processing. The mechanical behaviour of the molten state of the TPE nanocomposites under torsional or shear stress could be an interesting topic for further study, while a comparison study between 2D fillers and 1D/0D fillers (such as CNT and CB) could give suggestions on how different geometry of the fillers could affect the viscosity of the molten TPEs.

7.2.2 Transport Properties

Transport properties such as barrier, thermal and electrical properties are interesting for elastomer materials. So far, only swelling and liquid diffusion of GNP-reinforced elastomers were studied in Chapter 5&6. The modelling of the anisotropic swelling still needs more elastomers, 2D materials and solvents to confirm it. Gas barrier properties are

also crucial for applications of elastomers and should be studied. One of the reasons is that the failure of seals or O-rings can be caused frequently by rapid gas decompression.

Thermal and electrical conductivities are highly dependent upon the dispersion and orientation of the GNPs and are also interesting properties that could expand the application of graphene additives in nanocomposites. Raman spectroscopy has shown powerful in characterising mechanical reinforcement in this thesis. Therefore, it is interesting to employ Raman spectroscopy in conjunction with thermal and electrical conductivity measurements, since graphene/elastomer nanocomposites have shown piezoresistive behaviour with high sensitivity [8].

7.2.3 Development of Theories

The properties of graphene depend on its quality and grade (lateral size, number of layers, defects, etc). There are some high-end applications, such as rubbers in aerospace, that require the elastomers to withstand extreme temperatures, high stresses and aggressive fluid. As such, some molecular-level modifications of the elastomer using graphene with high quality (such as *in situ* polymerisation with functionalised graphene) could be useful to improve the properties of the elastomers significantly. For engineering applications or commodities, the improvement of the properties of rubbers can be accomplished using relatively cheap GNPs such as the materials employed in this work. The proposed theories in this thesis were also based on GNPs and commercially available elastomers. In the extreme case, however, when a low content of high-quality graphene can alter the properties of an elastomer significantly, with or without chemical functionalisation, the proposed theories in this thesis can be examined again and might not be able to explain the reinforcement. Therefore, potential modifications of the theories might be carried out when the case of the nanocomposites changes significantly.

References

[1] Guth E. Theory of filler reinforcement. Journal of Applied Physics. 1945;16(1):20-5.

[2] Araby S, Zaman I, Meng Q, Kawashima N, Michelmore A, Kuan HC, Majewski P, Ma J, Zhang L. Melt compounding with graphene to develop functional, high-performance elastomers. Nanotechnology. 2013;24(16):165601.

[3] Das A, Kasaliwal GR, Jurk R, Boldt R, Fischer D, Stöckelhuber KW, Heinrich G. Rubber composites based on graphene nanoplatelets, expanded graphite, carbon nanotubes and their combination: a comparative study. Composites Science and Technology. 2012;72(16):1961-7.

[4] Fernández-d'Arlas B, Corcuera MA, Eceiza A. Comparison between exfoliated graphite, graphene oxide and multiwalled carbon nanotubes as reinforcing agents of a polyurethane elastomer. Journal of Thermoplastic Composite Materials. 2015;28(5):705-16.

[5] Nawaz K, Khan U, Ul-Haq N, May P, O'Neill A, Coleman JN. Observation of mechanical percolation in functionalized graphene oxide/elastomer composites. Carbon. 2012;50(12):4489-94.

[6] Liff SM, Kumar N, McKinley GH. High-performance elastomeric nanocomposites via solvent-exchange processing. Nature Materials. 2007;6(1):76.

[7] Trappe V, Prasad V, Cipelletti L, Segre P, Weitz DA. Jamming phase diagram for attractive particles. Nature. 2001;411(6839):772.

[8] Boland CS, Khan U, Ryan G, Barwich S, Charifou R, Harvey A, Backes C, Li Z, Ferreira MS, Möbius ME, Young RJ, Coleman JN. Sensitive electromechanical sensors using viscoelastic graphene-polymer nanocomposites. Science. 2016;9;354(6317):1257-60.